VERLAG DER TECHNISCHEN UNIVERSITÄT GRAZ

Christoph Irrenfried

Convective turbulent near wall heat transfer at high Prandtl numbers

A modelling approach based on Direct Numerical Simulations and experiments

CES 37

MONOGRAPHIC SERIES TU GRAZ
COMPUTATION IN ENGINEERING AND SCIENCE

Christoph Irrenfried

Convective turbulent near wall heat transfer at high Prandtl numbers

Monographic Series TU Graz

Computation in Engineering and Science

Monographic Series TU Graz

Computation in Engineering and Science Volume 37

Christoph Irrenfried

Convective turbulent near wall heat transfer at high Prandtl numbers

A modelling approach based on Direct Numerical Simulations and experiments

---

This work is based on the dissertation *"DNS and experimentally based modelling of convective turbulent near wall heat transfer at high Prandtl numbers"*, presented at Graz University of Technology, Institute of Fluid Mechanics and Heat Transfer in 2019.

Supervisor: Steiner, Helfried (Graz University of Technology)
Reviewer: Pecnik, Rene (Delft University of Technology)

Cover photo	Vier-Spezies-Rechenmaschine by courtesy of the Gottfried Wilhelm Leibniz Bibliothek – Niedersächsische Landesbibliothek Hannover
Cover layout	Christina Fraueneder, TU Graz Stefan Schleich, TU Graz
Print	DATAFORM Media Ges.m.b.H.

Verlag der Technischen Universität Graz
www.tugraz-verlag.at

Print
ISBN 978-3-85125-724-3

E-Book
ISBN 978-3-85125-725-0
DOI 10.3217/978-3-85125-724-3

Zusammenfassung

Eine große Herausforderung für die numerische Simulation von turbulenten Strömungen stellen die mitunter stark unterschiedlichen Dicken der laminaren Unterschicht der Geschwindigkeit und Enthalpie dar. Die Annahme der Reynolds-Analogie zwischen Geschwindigkeit und Enthalpie, welche für die meisten thermischen Randbedingungen in Reynolds Averaged Navier-Stokes (RANS) Simulationen getroffen wird, muss daher mit zunehmender molekularer Prandtl Zahl immer mehr in Frage gestellt werden.

Diese Problematik wird in der vorliegenden Arbeit mittels Direct Numerical Simulation (DNS) von Strömungen mit relativ hohen Prandtl Zahlen, bis zu $\mathrm{Pr} = 50$ und unter Berücksichtigung von temperaturabhängigen Stoffwerten untersucht. Um auch die kleinsten thermalen Strukturen, welche nahe der Wand auftreten, numerisch auflösen zu können, muss das numerische Rechengitter nahe der Wand stark verfeinert werden. Der Einfluss der Variation der Stoffwerte auf die Strömungsgrößen wird durch Vergleiche mit Simulationen basierend auf konstanten Stoffwerten verdeutlicht. Weiters ermöglicht die DNS einen sehr detailreichen Einblick in den turbulenten Wärme- und Impulstransport nahe der Wand. Es konnte gezeigt werden, dass trotz des Anstieges der mittleren molekularen Prandtl Zahl im Fall veränderlichen Stoffwerte, die effektive Dicke der diffusiven thermischen Unterschicht beträchtlich zunimmt. Eine Analyse der turbulenten Budgets bewies, dass dieses Aufdicken der Untersicht der Reduktion des turbulenten radialen Impulsaustausches zugeschrieben werden kann.

Alle Ergebnisse werden mit Messungen verglichen, welche auf einem speziell für diese Problemstellung entwickelten und gebauten Prüfstand durchgeführt wurden. Die ausgezeichnete Übereinstimmung der Simulationswerte für den Strömungs-Widerstandsbeiwert und die Nusselt Zahl mit den Messungen, unterstreicht die hohe Zuverlässigkeit der DNS Ergebnisse.

Weiters wurden, aufbauend auf den generierten Daten, zwei weithin etablierten thermischen Randbedingungen, basierend auf der P-Funktion bzw. einem einfachen Zwei- Schichtes Modell, validiert und weiterentwickelt. Außerdem werden, basierend auf den DNS-Erkenntnissen, Modifikationen vorgeschlagen, welche geeignete Untermodelle für die turbulente Prandtl Zahl, die turbulente Viskosität, sowie eine verbesserte Beschreibung des Verhältnisses zwischen totaler Schubspannung und Wärmestromdichte liefern. Die resultierende adaptierte Modellformulierung stellt einen Ansatz dar, welcher den Enthalpieverlauf über den gesamten radialen Bereich beschreiben kann. Dieser spannt sich von der diffusiven Unterschicht, bis zur "inertial subrange". Darüber hinaus, wird der Einfluss der temperatur abhängigen Stoffwerte mit guter Genauigkeit berücksichtigt. Der Vergleich der Modellvorhersagen für den Reibungskoeffizient und die Nusselt Zahl zeigt eine gute Übereinstimmung mit den DNS-Ergebnissen, sowie auch mit Messungen weit außerhalb des mittels DNS simulierbaren Betriebsbereich, wodurch die sehr umfassende Anwendbarkeit dieses Modells bestätigt wird.

Abstract

The numerical simulation of turbulent heat transfer at high molecular Prandtl numbers is still strongly challenged by disparate thicknesses of the viscous sublayer for velocity and enthalpy. The widely used standard model assumptions for the prescription of the thermal boundary conditions in Reynolds Averaged Navier-Stokes (RANS) type simulations become increasingly questionable for high molecular Prandtl numbers, as the Reynolds analogy between the momentum and the heat transfer breaks down.

The present work addresses this issue by performing Direct Numerical Simulation (DNS) for relatively high molecular Prandtl number, up to $\mathrm{Pr} = 50$, including temperature- dependent fluid properties. In order to capture numerically the small thermal structures occurring in the near wall layer, the numerical resolution requires a strongly refined computational mesh. The alteration of all flow quantities, due to varying fluid properties is extensively examined by a comparison against results from DNS with constant fluid properties. The DNS further gives an very detailed insight into turbulent heat and momentum transfer near the wall. It turned out that, although the variable fluid property cases are associated with a higher bulk molecular Prandtl number due to the increasing viscosity towards the colder center, the effective thickness of diffusive sublayer still thickens. The turbulent budgets, demonstrated that the observed thickening of the diffusive sublayer could be mainly attributed to a reduced radial turbulent transport of momentum.

All DNS results are further validated against measurements, obtained on a test facility, specially designed and constructed for the considered problem. The agreement of the simulated skin-friction coefficients and Nusselt numbers with the experiments is excellent, indicating the high reliability of the present DNS results.

This DNS database was utilized for the evaluation and further development of two popular modeling approaches for RANS-type thermal boundary condition, the so-called P-function and a simple two-layer model. Based on the DNS results, various modifications for either approach are proposed, providing in particular appropriate submodels for the turbulent Prandtl number, the eddy viscosity, and incorporating an analytical solution for the flux ratio of the total shear stress and the total heat flux. The resulting modified formulations were shown to be, capable of describing the enthalpy variation over the whole radial domain, spanning from the diffusive sublayer to the inertial subrange. Additionally, the model also accounts reasonably well for the effect of temperature-dependent material properties. The comparison of the model predictions for the skin-friction coefficient and the Nusselt number shows good agreement with the DNS results as well as the experimental data, which covers also Reynolds numbers not amenable to DNS, indicating the wide applicability of the proposed model.

Contents

Nomenclature

Latin symbols

Symbol	Description	Dimension
a	thermal diffusivity	$\mathrm{m^2\,s^{-1}}$
a_T	eddy diffusivity	$\mathrm{m^2\,s^{-1}}$
A_ρ, B_ρ	constant for density-temperature equation	$\mathrm{kg\,m^{-3}}, \mathrm{kg\,m^{-3}\,K^{-1}}$
A_c, B_c	constant for specific heat-temperature equation	$\mathrm{J\,kg^{-1}\,K^{-1}}, \mathrm{J\,kg^{-1}\,K^{-2}}$
A_λ, B_λ	constant for thermal conductivity-temperature equation	$\mathrm{W\,m^{-1}\,K^{-1}}, \mathrm{W\,m^{-1}\,K^{-2}}$
A_μ, B_μ, C_μ	constant for dynamic viscosity-temperature equation	$\mathrm{Pa\,s}, \mathrm{K}, \mathrm{K}$
A, b, B, C, k_m, k_h	constant	$-$
c_p	specific heat capacity	$\mathrm{J\,kg^{-1}\,K^{-1}}$
c_f	skin-friction coefficient	$-$
D	diameter	m
h	enthalpy	$\mathrm{J\,kg^{-1}}$
$\mathcal{H}$	discretized term in non-dimensional energy equation	$-$
k	turbulent kinetic energy	$\mathrm{J\,kg^{-1}}$
L	length	m
l_m	mixing length	m
$\dot{m}$	mass flow rate	$\mathrm{kg\,s^{-1}}$
$\mathcal{M}$	discretized term in non-dimensional momentum equation exluding pressure	$-$

Symbol	Description	Dimension
p	pressure	Pa
P	P-function	–
$\dot{Q}$	heat flux	W
p_j	heat flux vector	$\mathrm{W\,m^{-2}}$
$\dot{p}_Q$	heat source	$\mathrm{W\,m^{-3}}$
r_u	radius at cell face	m
r_p	radius at cell center	m
t	time	s
T	temperature	K
T_τ	friction temperature	K
u_i, u, v, w	velocity component	$\mathrm{m\,s^{-1}}$
w_τ	friction velocity	$\mathrm{m\,s^{-1}}$
V	volume	$\mathrm{m^3}$
$y^+_{c,m}$	momenum boundary distance between viscous and turbulent layer	–
$y^+_{c,th}$	thermal boundary distance between viscous and turbulent layer	–
x_i, r, φ, z	radial, azimuthal and axial direction	m

Greek symbols

Symbol	Description	Dimension
α	heat transfer coefficient	$\mathrm{W\,m^{-2}\,K^{-1}}$
$\alpha_c, \beta_c, \gamma_c, \delta_c, \epsilon_c$	model coefficient	–
$\beta, \beta_\theta, \beta_\chi$	constant	–
γ	model parameter	–
Γ	blending function for velocity	–
Γ_χ	blending function for enthalpy	–
δ_{ij}	Kronecker delta	–
δ_m	momentum boundary layer thickness	m
δ_{th}	thermal boundary layer thickness	m
δ_{th}	momentum thickness	m
Δ	grid spacing	–
χ	relative enthalpy	$\mathrm{J\,kg^{-1}}$
ϵ	dissipation of turbulent kinetic energy	$\mathrm{m^2\,s^{-3}}$
η	Kolmogorov micro length scale	m
η_{th}	Batchelor micro length scale	m
κ	von Kármán constant	–
λ	thermal conductivity	$\mathrm{W\,m^{-1}\,K^{-1}}$
μ	dynamic viscosity	$\mathrm{Pa\,s}$
μ_T	eddy viscosity	$\mathrm{Pa\,s}$
ν	kinematic viscosity	$\mathrm{m^2\,s^{-1}}$
θ	relative temperature	K
ρ	density	$\mathrm{kg\,m^{-3}}$
π	relative pressure	Pa
Φ_h^{n-1}	discretized source term in non-dimensional energy equation	–
Φ_u^{n-1}	discretized source term in non-dimensional momentum equation	–
Ψ_μ	viscous dissipation	$\mathrm{W\,m^{-3}}$
τ_{ij}	stress tensor	$\mathrm{N\,m^{-2}}$

Subscripts

Symbol	Description
$()_i$	vector
$()_{ij}$	tensor
b	bulk mean value
BW	bandwidth
D	based on bulk values
δ	based on momentum thickness
$crit$	critical
lam	laminar
in	quantity at inflow position
m	momentum
μ	based on local viscosity
0	reference
th	thermal
tot	total
$turb$	turbulent
w	wall
∞	at $y \to \infty$

Superscripts

Symbol	Description
$()^*$	non-dimensionalized
$()^+$	representation in wall-coordinates
$n, n+1$	iteration in time
$\overline{()}$	Reynolds average
$\widehat{()}$	Favre average
$()'$	fluctuation component of Reynolds average
$()''$	fluctuation component of Favre average

Non-dimensional parameters

Symbol	Description	Definition
Nu	Nusselt number	$\frac{\alpha D}{\lambda}$
Pr	molecular Prandtl number	$\frac{\nu \rho c_p}{\lambda}$
Pr_T	turbulent Prandtl number	$\frac{\mu_T \rho}{a_T}$
Pe_T	tubulent Peclet number	$\frac{\nu_T}{\nu}\mathrm{Pr}$
Re	bulk Reynolds number	$\frac{D \rho \overline{w}}{\mu}$
Re_{δ_2}	momentum thickness Reynolds number	$\frac{\delta_2 \overline{w}_\infty}{\nu_b}$
Re_τ	friction Reynolds number	$\frac{D \rho w_\tau}{\mu}$

Abbreviations

DNS	Direct numerical simulation
FFT	Fast Fourier Transformation
iFFT	inverse Fast Fourier Transformation
LES	Large eddy simulation
CFD	Computational fluid dynamics
RANS	Reynolds Averaged Navier-Stokes equations
MPI	Message Passing Interface
CFL	Courant–Friedrichs–Lewy condition
rms	Root mean square

1 INTRODUCTION

Turbulent heat transport in pipe flows is a major topic in many industrial engineering applications. The majority of the employed fluids are of high molecular Prandtl number like organic cooling liquids, or oils. Although much computational and experimental research work has been devoted to this highly relevant subject, it is still a very challenging task to model the turbulent convective heat transport of such liquids. An additional problem arises, as the operation point is often located in the intermediate range between the laminar and the fully turbulent flow regime, where it is generally very hard to develop universal model descriptions. The principle aim of this thesis is to provide a comprehensive and detailed insight into the forced convective heat transfer and the underlying mechanisms for particularly these fluids and flow conditions.

In wall bounded flow, the near wall region essentially determines the exchange of momentum and heat between the fluid and the wall. Inside this region the flow is highly affected by the viscous forces, so that the flow structures differ significantly from those in the turbulent core region. Figure 1.1 shows typical hydraulically and thermally fully developed velocity and temperature profiles of a pipe flow, heated with a constant wall heat flux for several molecular Prandtl numbers. With increasing molecular Prandtl number, the thermal resistance near the wall increases, implying a decreasing boundary layer thickness $\delta_{th} << \delta_m$, and therefore a shift of the essential convective and conductive transport mechanisms closer to the wall.

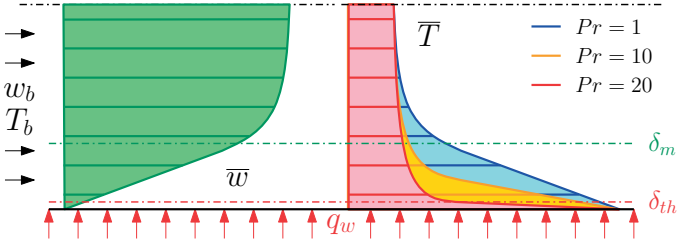

Figure 1.1: Velocity and temperature profiles

In order to capture numerically the small thermal structures occurring in the near wall layer, the numerical resolution requires a strongly refined computational mesh. This makes the computational costs unacceptably high, especially for the complex geometries often

considered in industrial applications. For such applications the typically followed Computational Fluid Dynamics (CFD) approach is to apply Reynolds-averaged Navier-Stokes (RANS) simulations using wall function models. According to this concept only the fully turbulent core region of the flow is simulated, while the near wall region is described using analytic wall functions. Various state-of-the-art wall functions are reviewed in this thesis, pointing out their capabilities and deficits. These standard approaches mostly introduce the turbulent Prandtl number to relate the thermal eddy diffusivity to the eddy viscosity. The setting of this parameter significantly determines the thermal boundary conditions. Therefore, the turbulent Prandtl number plays a prominent role in the literature review given below. Any further advancement of the modelling towards a better prediction of the real fluid behavior requires good insight into the relevant physical effects down to the smallest dynamic and thermal length scales. The hereby required high level of description suggests the method of Direct Numerical Simulation (DNS) as most powerful approach.

1.1 Literature survey

The majority of previous DNS studies considered heated channel flows at fairly low Prandtl numbers near unity and constant thermophysical properties. One of the first attempts was made by Kim and Moin (1987), who considered a flow with a friction Reynolds number $\mathrm{Re}_\tau = 180$ (based on the wall shear stress velocity and the channel half-width) and molecular Prandtl numbers less than two. Although the near wall resolution provided by their numerical mesh was fairly coarse (the distance of the first grid point near the wall in wall-units was $y^+ > 1$), a moderate increase of the turbulent Prandtl number towards the wall could be still observed for the case $\mathrm{Pr} = 2$. Based on the near-wall variation of turbulence quantities obtained from these DNS results, Antonia and Kim (1991) approximated the near-wall variation of the turbulent Prandtl number using Taylor series expansions. Their actually derived expansions, however, implied no dependence of the eddy diffusivity on the molecular Prandtl number near the wall. The inferred independence of the turbulent Prandtl number of the molecular Prandtl near the wall was clearly contradicted by various later DNS studies. Kawamura et al. (1998) did similar DNS simulations of a turbulent heated channel flow on refined meshes and for slightly higher molecular Prandtl number, up to $\mathrm{Pr} = 5$. The near wall resolution of these DNS was similar to that of Kim and Moin (1987), first grid point near the wall at $y^+ > 1$, and the obtained results also indicated an increase of the turbulent Prandtl number towards the wall for molecular Prandtl numbers above unity. A further investigation on the passive scalar transport in the vicinity of the wall, for high Prandtl number between $\mathrm{Pr} = 1$ up to $\mathrm{Pr} = 10$, was published by Na and Hanratty (2000) considering fully developed turbulent flow in a channel at $\mathrm{Re}_\tau = 150$ (based on the channel half-width). These simulations were carried out on different numerical meshes to verify the independence of the results of the resolution. As an important output, this study showed the limits of the frequently assumed analogy between momentum and

scalar transport close to the wall. The effect of the thermal wall boundary condition was studied by Tiselj et al. (2001b). This study compared the isoflux and isothermal boundary condition for a turbulent channel flow with $\mathrm{Re}_\tau = 170$ (based on the channel half-width) assuming alternatively Prandtl numbers $\mathrm{Pr} = 1$ and $\mathrm{Pr} = 5.4$. For the case with isoflux boundary condition, associated with invariant wall heat flux $q_w = const.$, the temperature fluctuations at the wall do not vanish as it is in the case for the isothermal boundary condition, associated with invariant wall temperature $T_w = const$. In the isoflux case the persistent temperature fluctuations throughout to the wall cause the turbulent Prandtl number to vanish for $y^+ \to 0$. In a further publication, Tiselj et al. (2001a) presented DNS results for the same geometry, yet for a Prandtl number variation from $\mathrm{Pr} = 0.71$ up to $\mathrm{Pr} = 7$, and a friction Reynolds number $\mathrm{Re}_\tau = 150$. Following the mesh resolution requirements proposed by Na and Hanratty (2000), these simulations were done on a coarser mesh than in the precursor study. Additionally, for further investigating the heat transfer in close proximity to the wall, the flow field simulation was coupled with an unsteady simulation of the conduction inside the heated solid wall structure. It was demonstrated, how the magnitude of the temperature fluctuations in the wall structure depend on two particular parameters, the thermal effusivity and the wall thickness. One of the first attempts of DNS of turbulent heated pipe flow was made by Piller (2005). The flow conditions assumed a Reynolds number $\mathrm{Re}_\tau = 360$ (based on the pipe diameter) and Prandtl number of 0.71. Three different thermal wall boundary conditions were considered, isoflux, isothermal, and a mixed type boundary condition. The results confirmed the vanishing turbulent Prandtl number at the wall for the isoflux case and an considerable increase of Pr_T towards unity at the wall for the isothermal case. Furthermore, comparing the against corresponding data for channel flow revealed that the thermal fluctuations are slightly more intense for the pipe geometry. For little higher Prandtl numbers, up to $\mathrm{Pr} = 1$, Redjem-Saad et al. (2007) published DNS results on the same geometry and Reynolds number. The case with unity molecular Prandtl number did not reveal any increase of the turbulent Prandtl number towards the wall similar to previous DNS of channel flow at this Prandtl number. Aside from the heat transfer simulations for high Prandtl number, Schwertfirm and Manhart (2007) presented DNS simulations of a passive scalar transport in a turbulent channel for very high Schmidt numbers up to $\mathrm{Sc} = 49$. A very fine computational mesh had to be employed in order to resolve all scales of the scalar field. In order to reduce the computational effort, a hierarchical mesh algorithm was employed which solves the Navier-Stokes equations on a twice as coarse mesh as that used for the passive scalar transport. Regarding the turbulent Schmidt number, the increase towards the wall is clearly visible. Wu and Moin (2008) did extensive DNS on a turbulent pipe flow on a very fine mesh. This study, however, does not take the transport of thermal energy into account. The results of this well resolved simulations are still applied in this thesis for the validation of the velocity field predicted by the DNS of the present work. DNS simulations with higher molecular Prandtl number where presented by Kozuka et al. (2009) for a turbulent channel flow with high spatial resolution. The highest considered Prandtl number was $\mathrm{Pr} = 10$ and two Reynolds numbers were assumed $\mathrm{Re}_\tau = 180$ and $\mathrm{Re}_\tau = 395$ (based on the channel half-width). The DNS re-

sults for the radial variations of the mean temperature obtained for the different Reynolds and Prandtl were analyzed, showing decreasing non-dimensional bulk temperatures for increasing Reynolds numbers. By comparing the temperature variation against the empirical correlation of Kader (1981) a rather good agreement was shown for the cases with the higher Reynolds number, yet the differences increased with increasing Pr. The analysis of the higher-order showed once more the near wall increase of the turbulent Prandtl number for a molecular Prandtl number above unity. Due to the very fine mesh resolution near the wall, it is even possible to predict fairly accurately the asymptotic wall value of Pr_T. It was shown, that, except for the asymptotically approached near-wall value, the profiles for the different considered Prandtl number cases can be merged by scaling the wall distance with the conductive sublayer thickness as obtained from a formulation proposed by Shaw and Hanratty (1977) dependent on the viscous sublayer thickness and the molecular Prandtl number. Moreover, the comparison of the near wall asymptotic of Pr_T for the the different Reynolds number cases indicated only a minor Reynolds number dependency.

An important focus of this thesis is on the impact of temperature depending material properties on the flow conditions and heat transfer. Due to its relevance in various technical applications the effect of the variation of the material properties has also been investigated in various previous studies in literature.
Lee et al. (2013) performed DNS of turbulent boundary layers with temperature-depending viscosity in order to investigate the influence of wall heating on the skin-friction coefficient. The considered fluid was water with a reference Prandtl number $\mathrm{Pr} = 5.4$ and a momentum thickness Reynolds number $Re_{\delta_2} = 1240$. It was shown that the skin-friction coefficient can be considerably decreased by the heating. In addition, the decreasing viscosity towards the wall caused the production term in the turbulent kinetic energy budget to decrease due to a reduction of the Reynolds shear stress while the near wall dissipation was increased. Zonta et al. (2012) investigated the effect of a temperature-dependent viscosity on forced convection in a channel flow with a heated and a cooled wall. The reference Prandtl number for this study was set to $\mathrm{Pr} = 3$ and based on the mean temperature between the heated and the cooled wall. It is clearly shown, that on the hot side of the channel, corresponding to low viscosity, the turbulence is damped while the velocity gradient is increased. The damped turbulence is also reflected by reduction in the production and dissipation terms in the turbulent energy budgets.
The more recent study of Patel et al. (2015) conducted a DNS based investigation of the effect of temperature-dependent density and viscosity on turbulence in channels in low Mach number approximation. It was shown that the Van-Driest transformed velocity and the second order statistics are strong functions of the semi-local wall coordinate, defined with the local values of the density and viscosity. A similar scaling approach was introduced for the temperature in Patel et al. (2017), who showed that the results with different Reynolds number can be collapsed, for unity Prandtl number. For non-unity Prandtl number the scaling had to be extended dependent on the Prandtl number.
Nemati et al. (2016) carried out DNS of heat transfer in forced convection in a turbulent

pipe flow at super-critical pressure, accounting for the very strong variation of all relevant thermophysical fluid properties. They considered a thermally developing pipe flow, heated with constant wall heat flux. The reference conditions were set at the inlet with $\mathrm{Re}_\tau = 360$ and $\mathrm{Pr} = 3$. As a major effect of the strong variation of the temperature-dependent material properties the author observed a reduction in kinetic energy, which further caused a deterioration in heat transfer.

Due to the excessively high computational costs of DNS simulations, they are generally not applicable to technically relevant flows involving mostly too high Reynolds numbers. For such flows, it is common to carry out RANS-type simulations instead, using the well established standard wall-function models for prescribing dynamic and thermal wall boundary conditions. In this thesis two different popular thermal wall modelling approaches will be investigated and further advanced using DNS data. On the one hand, it investigates the rather simple two-layer approach, which essentially splits the boundary layer into two separate sublayers, a diffusive near wall layer and the fully turbulent inertial sublayer. Kader (1981) further proposed a blending between these two sub-layers yielding a smooth transition from one to the other. Most commercial CFD codes prescribe the dynamic and thermal wall boundary conditions, which are essentially based on this idea. The other approach is the so-called P-function approach for describing the logarithmic temperature profile inside the inertial subrange. This concept essentially relates the total shear stress to the total heat flux and integrates the temperature over the axial velocity. This yields a temperature formulation depending on the axial velocity, the bulk turbulent Prandtl number and the P-function. The P-function basically represents the thermal resistance of the diffusive sublayer dependent on the molecular Prandtl number. In literature many formulations for the P-function or equivalent expressions can be found, e.g., in the work of Kármán (1939), Hofmann (1940), Spalding (1967), Jayatilleke (1969), Kader and Yaglom (1972), Malin (1987). The most popular representation among these are the analytically based formulation of Spalding (1967), and its empirical extension of Jayatilleke (1969). Spalding (1967) applied several simplifying assumptions to finally obtain an analytical solution for the P-function. These simplifications essentially consist in approximating the near wall variation of the eddy viscosity with a Taylor series expansion, and in using an invariant turbulent Prandtl number set to its bulk value $Pr_T = Pr_{T,\infty}$. Their actual setting significantly determines the resulting description of the thermal wall boundary conditions. Much research work has been therefore devoted to the modelling of these two key parameters. Regarding the eddy viscosity, it is commonly known that the most popular approach, the mixing-length ansatz of Van Driest (1956), yields incorrect near wall asymptotics, predicting a dependence $\nu_T \sim y^{+4}$. Therefore, Grifoll and Giralt (2000) proposed a modification to the damping coefficient as used in the original mixing length formulation, essentially enforcing the analytically as well as DNS proven y^{+3}-dependency of ν_T in close proximity to the wall.
It has become rather common, to assume the turbulent Prandtl number as constant, setting it to the value of the bulk turbulent Prandtl number $\mathrm{Pr}_{T,\infty}$ approached in the limit of high

$y^+ \gg 1$. This simplifying assumption is certainly contradicted by many of the DNS studies cited above. Especially for molecular Prandtl numbers well above unity, the near-wall variation of the turbulent Prandtl number needs to be suitably modelled to obtain an accurate description of the thermal boundary conditions. In literature, basically three different modeling approaches for the turbulent Prandtl number can be found, a purely empirical, a purely analytical and experimentally adapted analytical (semi-empirical) models. For the purely empirical turbulent Prandtl number models, the approach of Graeber (1970) can be considered as a typical representative. This model is exclusively dependent on the molecular Prandtl number and is based on various heat transfer measurements on different geometries for a variety or Re_τ and Pr. Due to the full independence of the wall distance, this approach is not capable of prescribing an increase of the turbulent Prandtl number towards the wall, as indicated by the DNS studies cited above. Among the semi-empirical models, the formulation of Cebeci (1973) produces a similar near wall variation of the turbulent Prandtl number as the DNS results indicate. The underlying idea of this model is to model the eddy diffusivity in a similar manner as the eddy viscosity based on Van Driest (1956) mixing length formulation. In a following study, Na and Habib (1973) extended this approach with an additional molecular Prandtl number dependency of the model coefficients. Although the model prescribes qualitatively correct an increase of the turbulent Prandtl number towards the wall, this increase is quantitatively underpredicted. A very promising turbulent Prandtl number model was proposed by Kays and Crawford (1980). This experimentally adapted analytical model is based on the analytical consideration of conductive heat transfer in thermal eddies, relying on an idea proposed by Jenkins (1951). The model is further tuned using experimental data of Hollingsworth et al. (1989), who performed measurements for a fully turbulent boundary layer in a free-surface channel flow with zero pressure gradient and $\mathrm{Pr} = 5.9$. The resulting model imposes, on the one hand, a constant bulk turbulent Prandtl number $\mathrm{Pr}_{T,\infty}$, approached remote from the wall and, on the other hand, prescribes the increase of Pr_T near the wall as indicated by the DNS.
Basically, none of the above mentioned wall-function model include a variation of temperature-dependent material properties. Petukhov (1970) derived correlations for the skin-friction coefficient and the Nusselt number based on analytical considerations, including thermophysical fluid properties. It was concluded, that in order to improve the prescription of either coefficients, the ratio of the wall and the bulk Prandtl number raised to some power needs to be included to account for the material property variation.

The considerable restrictions, which arise from the high computational costs of DNS on the one hand, and, from the simplifying assumptions typically required by analytical approaches on the other hand, suggest heated channel flow experiments as a feasible alternative. This is especially the case, when considering very high Prandtl number fluids with temperature-dependent material properties. Certain typical restrictions apply to the experimental approach as well, in that it hardly ever delivers a detailed spatially resolved description of the heated near wall region. The available experimental techniques rather

measure only global mean quantities like the bulk temperature, the heat transfer coefficients and Nusselt numbers delivered therefrom. Providing these characteristic parameters of the heat transfer over a wide range of Reynolds and Prandtl numbers, experiments still represent a very useful tool, not only for verifying computational predictions but also for validating and calibrating empirical model correlations. Well established representations of the latter, such as the Nusselt number correlations of Sleicher and Rouse (1975) or Gnielinski (1995), are often used themselves for evaluating CFD data. This may also include DNS results obtained at Reynolds numbers close to or inside the transition regime between laminar and fully turbulent flow, even though both of the popular Nusselt number correlations mentioned above are exclusively valid for the fully turbulent regime. In order to reduce the well-known deficits of the original Gnielinski correlation in the transition regime, Gnielinski (2002) himself proposed a linear superposition of a laminar and a fully turbulent Nusselt number contribution for predicting better the corresponding low Reynolds number range. However, when comparing against measurements especially at high Prandtl numbers, see e.g., Morris and Whitman (1928), Sherwood (1932), the extended correlation still tends to under-predict the experimental values. This may be also due to the fact, that the data employed by Gnielinski (1995) for deriving and calibrating his Nusselt number correlation is rather old, especially the experimental data considering high molecular Prandtl numbers and Reynolds number in the intermediate regime between laminar and fully turbulent flow. One of the more recent attempts to measure the Nusselt number for these conditions was made by Ghajar and Tam (1994), whose concept for heating the test section was also used in the experimental facility designed in the present work. The temperature-dependent variation of the thermophysical fluid properties is mostly included into the empirical correlation in terms of a correction factor. Gnielinski (2002), follows here a well established approach including the ratio of the wall and the bulk Prandtl number raised to some power.

1.2 Objectives and thesis outline

The present thesis essentially targets four major goals.

The first goal is a detailed DNS based analysis of the near wall heat and momentum transfer of a turbulent heated pipe flow with a special focus on high molecular Prandtl number effects, considering molecular Prandtl number well above unity.

The second goal is to investigate the effect of temperature-depending real fluid properties on the transport of momentum and heat. For this purpose temperature-dependent material properties, typically met with heat transfer oils were considered in the DNS.

The detailed insight into the near wall momentum and heat transfer provided by the DNS is the basis for the third goal, which attempts to assess the scope of state-of-the-art boundary conditions. Two of the most popular approaches are considered, a simple two-layer

model and the P-function approach originally proposed by Spalding (1967). All assumptions and simplifications are reviewed and assessed against the available DNS data-base. Possible improvements for both, alternative thermal boundary conditions shall be derived and validated against the DNS data.

The fourth goal of this thesis is the validation of all computational results, predicted by the DNS and the RANS boundary condition models, with experimental data. Due to the lack of adequate literature data for the here considered high molecular Prandtl number flow, appropriate validation data shall be acquired in own dedicated experiments. For this purpose, a test bench capable of producing equivalent boundary conditions as considered in the DNS was designed. Various measurements series with varying Reynolds and Prandtl number were carried out. Since these measurements cover a very wide range of Reynolds and Prandtl numbers, the scope of the further developed models for the thermal boundary conditions can be also assessed for operating conditions, which are not accessible to DNS.

This thesis is divided into seven main chapters:

- Chapter 1: Introduction
  Motivation for the present study and comprehensive literature survey.
- Chapter 2: Mathematical description
  The governing differential conservation equations are shown, and a short overview of the derivation of the standard wall-models is presented as well.
- Chapter 3: Direct numerical simulation
  Gives an overview of the numerical approach used for the DNS, consisting of the meshing strategy, the temporal- and spatial-integration as well as the prescribed boundary conditions for the constant and the real fluid property cases.
- Chapter 4: Experiments
  This chapter starts with the description of the utilized fluid. It follows a description of the experimental setup and measuring procedure. Finally, in the end the measurement results are discussed and compared to the Gnielinski (2002) correlation.
- Chapter 5: DNS analysis
  The obtained DNS results for all considered cases are presented and analyzed as well as validated against the experimental data.
- Chapter 6: Near wall model
  The classical two-layer approach and the P-function approach Spalding (1967) are reviewed and compared against the DNS results. Possible weaknesses are identified and DNS based improvements and extensions are proposed. The modified approaches are validated against the DNS results in order to evaluate the improvements.

- Chapter 7: Summary and Conclusions
  Summary of all experimental and computational findings as well as an overview of the possible model improvements.

2 MATHEMATICAL DESCRIPTION

For investigating computationally the problem of heated or cooled flows the conservation equations of mass, momentum and energy have to be solved. The conservation equations of mass and momentum are the so-called Navier-Stokes equations, which can be written in a conservative formulation as

$$\frac{\partial \rho}{\partial t} + \frac{\partial \rho u_i}{\partial x_i} = 0 \tag{2.1}$$

$$\frac{\partial \rho u_i}{\partial t} + \frac{\partial \rho u_i u_j}{\partial x_j} = -\frac{\partial p}{\partial x_i} + \frac{\partial \tau_{ij}}{\partial x_j}. \tag{2.2}$$

The conservation equation of thermal energy, written in terms of enthalpy $h = e + p/\rho$, reads

$$\frac{\partial \rho h}{\partial t} + \frac{\partial \rho u_j h}{\partial x_j} = -\frac{\partial q_i}{\partial x_i} + \frac{\partial p}{\partial t} + u_j \frac{\partial p}{\partial x_j} + \Psi_\mu + \dot{q}_Q. \tag{2.3}$$

The viscous stress tensor (τ_{ij}) is written as

$$\tau_{ij} = \mu \left(\frac{\partial u_i}{\partial x_j} + \frac{\partial u_j}{\partial x_i} \right) - \mu \frac{2}{3} \delta_{ij} \frac{\partial u_k}{\partial x_k}, \tag{2.4}$$

and the viscous dissipation (Ψ_μ) reads,

$$\Psi_\mu = \mu \left(\frac{\partial u_i}{\partial x_j} + \frac{\partial u_j}{\partial x_i} \right) \frac{\partial u_i}{\partial x_j} - \frac{2}{3} \mu \left(\frac{\partial u_k}{\partial x_k} \right)^2. \tag{2.5}$$

Assuming a Newtonian fluid, the dynamic viscosity μ is a pure material property independent of the flow-induced deformation. Furthermore, applying Fourier's law, the heat flux vector (q_i) can be rewritten as

$$q_i = -\lambda \frac{\partial T}{\partial x_i}. \tag{2.6}$$

The flow is assumed as incompressible in the limit of low Mach numbers. This implies that the density can only vary with the temperature due to thermal expansion, but not with pressure. In the cases with variable material properties the thermo-physical properties of the fluid are assumed as dependent on the temperature according to the experimentally measured data of the considered liquid. Therefore, the material derivative of the pressure and viscous dissipation are neglected in the energy equation.

2.1 Turbulent flow

A turbulent flow is characterized by irregular and chaotic fluctuations of all flow quantities. Turbulent flow occurs at Reynolds numbers which exceed a certain critical limit, the so-called critical Reynolds number Re_{crit}. Beyond this critical limit, which depends on the considered flow configuration, the inertial forces dominate over the viscous forces resulting in highly unstable flow conditions. The inertial forces are represented in the momentum equation (2.2) by the nonlinear advective terms on the left-hand side. In the turbulent flow regime the viscous forces represented in equations (2.2) by the diffusive terms on the right-hand side are too weak to dampen the fluctuating turbulent motion.

2.1.1 Laminar-turbulent transition

As mentioned above the laminar-turbulent transition depends on the Reynolds number written in case of a pipe flow as

$$\mathrm{Re}_D = \frac{\overline{w}_b D}{\nu}, \tag{2.7}$$

where $\overline{w}_b$ denotes the volumetric flow rate equivalent mean bulk velocity.

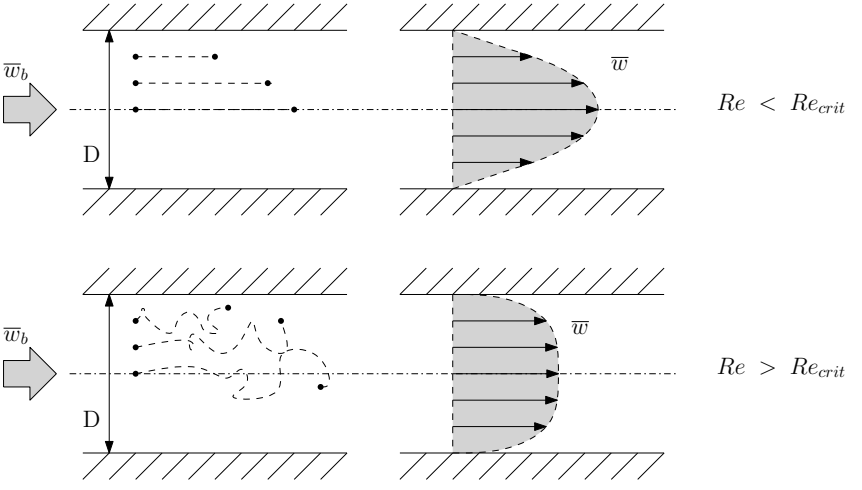

Figure 2.1: Laminar and turbulent pipe flow.

If the Reynolds number exceeds the critical Reynolds number, the flow becomes unstable. This means that any arbitrarily small perturbation is increased so that the flow finally changes from a laminar into a turbulent state. For example, the critical Reynolds number is around 2300 in the case of cylindrical pipe flow.

In the upper part of figure 2.1, a laminar pipe flow can be seen, where the particle trajectories are parallel to the wall. The lower sub-figure shows a typical turbulent state, where the instantaneous velocity components are strongly fluctuating, so that the particles move in a chaotic way. Due to this irregular motion, the pressure drop increases and is roughly proportional to the second power of the bulk velocity in comparison to the laminar flow, where the pressure drop varies linearly with the bulk velocity.

2.2 Computation of turbulent flow

The majority of technical flow applications are in the turbulent regime. Since turbulent flow is characterized by a random, unsteady, three-dimensional motion, all variables vary in all three spatial dimensions and in time. Such a flow can be described using statistical methods, which is generally based on ensemble averages.

Ensemble averages

An ensemble represents the number of realizations of a flow variable in a turbulent flow. In the theoretical limit of an infinite number of realizations, the ensemble average becomes the real statistical average, generally termed Reynolds averaged mean value. Assuming N as number of realizations, the Reynolds averaged mean value of an arbitrary flow quantity ψ is defined as

$$\langle \psi \rangle = \lim_{N \to \infty} \frac{1}{N} \sum_{n=1}^{N} \psi^{(n)}$$

Based on this statistical average, Reynolds (1895) proposed to decompose each flow variable into a mean $\langle \psi \rangle$ and a fluctuation ψ' written as

$$\psi = \langle \psi \rangle + \psi'. \tag{2.8}$$

Assuming statistically stationary flow the ensemble average obtained in the limit of an infinite number of ensembles does not depend on the time, so that

$$\langle \psi \rangle \neq f(t). \tag{2.9}$$

It follows that the statistical mean value can be also obtained as temporal average defined as

$$\langle \psi \rangle = \overline{\psi} = \lim_{\vartheta \to \infty} \frac{1}{\vartheta} \int_0^{\vartheta} \psi(t) dt,$$

2.2.1 Length scales and energy cascade

By visualizing a statistically stationary turbulent flow, coherent structures, so-called turbulent eddies of different sizes can be identified. These eddies can be characterized by determining the auto- and cross-correlation as

$$R_{ij}(\vec{x}, \zeta, t) = \langle u_i(\vec{x}, t) u_j(\vec{x} + \zeta, t) \rangle = \overline{u_i(\vec{x}, t) u_j(\vec{x} + \zeta, t)}, \tag{2.10}$$

R_{ij} can be non-dimensionalised with corresponding standard deviation $std(u_i)$, reading

$$\rho_{ij}(\vec{x}, \zeta, t) = \frac{\overline{u_i(\vec{x}, t) u_j(\vec{x} + \zeta, t)}}{std(u_i(\vec{x}, t)) std(u_j(\vec{x} + \zeta, t))}, \tag{2.11}$$

which basically quantifies the statistical relationship between the fluctuations at different locations. Furthermore, the correlation coefficient ρ_{ij} can be used to measure the average size of turbulent coherent structures in terms of an integral length scale, defined as

$$\mathcal{L}_{ij}^{\vec{x}} = \int_0^{\infty} \rho_{ij}(\vec{x}, \zeta, t) d\zeta. \tag{2.12}$$

In case of isotropic turbulence, the integral length scale of equation (2.12) becomes $\mathcal{L}_{ij}^{\vec{x}} = \mathcal{L}$ and the diagonal elements of R_{ij}, representing the velocity fluctuations magnitudes are essentially the same for all directions. Therefore, these fluctuations can be characterized by a single scalar, namely the turbulent kinetic energy

$$k = \frac{1}{2} \overline{u_i' u_i'}. \tag{2.13}$$

The largest turbulent eddies are typically characterized by the characteristic geometrical length scale of the flow configuration. Their size is comparable to the integral length $\mathcal{L}$, and they contain the major part of the turbulent kinetic energy k of the flow, yet tend to break up, where their kinetic energy is transferred to smaller eddies. This energy cascade successively transfers kinetic energy to smaller eddies, until the eddy size reaches the dissipative range, where they are dissipated by viscous forces. Figure 2.2 shows this cascading

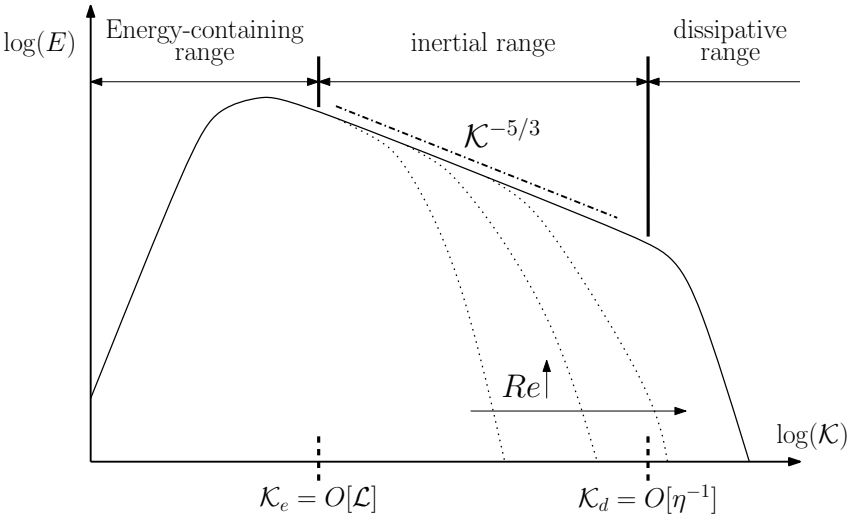

Figure 2.2: Turbulent energy spectrum $E(\mathcal{K},t)$

process in terms of the turbulent energy spectrum dependent on to the wave-number $\mathcal{K}$, where

$$k = \int_0^\infty E(\mathcal{K},t)d\mathcal{K}. \tag{2.14}$$

This spectrum basically distinguishes the "Energy-containing range" with the upper limit of $\mathcal{K}_e$ where the turbulent kinetic energy is produced by the large scale motion dependent on the actually considered flow configuration, the independent "Inertial range", where the energy is transferred to smaller ans smaller eddies with negligible viscous losses, and the "Dissipative range", where the viscous effects become dominant. According to Kolmogorov, the energy transfer rate remains constant in the inertial range. Consequently, the transport change of kinetic energy at large scale, which is estimated as

$$\epsilon_\mathcal{L} = \frac{u_\mathcal{L}^2}{\mathcal{L}/u_\mathcal{L}} \tag{2.15}$$

has to be equal to the energy finally dissipated at the Kolmogorov length scale

$$\epsilon_\mathcal{L} \approx \bullet = \frac{u_\eta^2}{\eta/u_\eta}. \tag{2.16}$$

Thus, the dissipation rate ϵ determines the energy transfer in the inertial range. Based on dimensional arguments the turbulent energy spectrum can be shown to depend on the wave number in the inertial range as $E(\mathcal{K},t) \propto \mathcal{K}^{-5/3}$, as indicated in figure 2.2. The lower limit of the dissipative range is $\mathcal{K}_d$ is associated with the Kolmogorov length-scale η, defined as

$$\eta = \left(\frac{\nu^3}{\epsilon}\right)^{1/4}, \tag{2.17}$$

which represents the size of the smallest eddies. Eddies smaller than the Kolmogorov length scale dissipate to thermal energy. Batchelor (1959) correlated the Kolmogorov micro length to smallest thermal coherent structures, dependent on the molecular Prandtl number as

$$\eta_{th} = \left(\frac{a^2\nu}{\epsilon}\right)^{1/4} = \frac{\eta}{\sqrt{\mathrm{Pr}}}, \tag{2.18}$$

with a being the thermal diffusivity.

2.2.2 Direct numerical simulation

DNS represents the most accurate approach for solving numerically the conservation equations (2.1) - (2.3). It solves the discretized equations directly without any modelling. Therefore, no averaging, or modelling assumptions (aside from the spacial and temporal discretization) are applied, this method basically attempts to capture numerically all physically relevant length scales, down to the Kolmogorov length scale (η). As a consequence, the computational mesh has to satisfy stringent resolution requirements to describe appropriately the smallest turbulent structures. For isotropic turbulence, this requires a grid with a minimum number of mesh cells based on the bulk Reynolds number, estimated as

$$N_{min} \geq \mathrm{Re}_D^{9/4}.$$

This inherently limits the applicability of DNS to rather low Reynolds numbers and mainly simple geometries. Therefore, DNS is unfeasible particularly for most technically relevant problems which are often associated with high Reynolds numbers and complex geometry. These flows are in general rather computed with Reynolds-averaged Navier-Stokes equations (RANS) approach. Nevertheless, the major benefits of DNS are the unsurpassed accuracy of the obtained results and the delivered detailed insight into the underlying principles of all flow relevant mechanism, making it a powerful tool for model development and validation.

2.2.3 Reynolds-averaged Navier-Stokes equations

In RANS, a statistical ensemble averaging procedure is applied to the conservation equations (2.1) - (2.3). The flow quantities are considered statistical random variables is time

and space, whose statistics is characterized by ensemble averages accordingly to Reynolds and Favre decomposition. In the case of varying density, the velocity components, the enthalpy, and the temperature are Favre-averaged, whereas the fluid-properties, pressure, viscous stresses, and heat fluxes are Reynolds averaged. When applying Reynolds averaging to an arbitrary quantity, its instantaneous value can be decomposed into a mean $\overline{\psi}$ and a fluctuating ψ' part, as

$$\psi(t;r,\varphi,z) = \overline{\psi}(r,\varphi,z) + \psi'(t;r,\varphi,z),$$

with $\overline{\psi'} = 0$. Applying the density-weighted Favre averaging instead, the decomposition reads

$$\psi(t;r,\varphi,z) = \widehat{\psi}(r,\varphi,z) + \psi''(t;r,\varphi,z),$$

where the mean part $\widehat{\psi}$ is defined as $\widehat{\psi} = \overline{\rho\psi}/\overline{\rho}$, resulting in $\overline{\rho\psi''} = 0$.

Introducing this decomposition into the conservation equation for mass, momentum and energy, the so-called RANS-type transport equations are obtained. Assuming low Mach number flow, they read

$$\frac{\partial\overline{\rho}}{\partial t} + \frac{\partial\overline{\rho}\widehat{u}_i}{\partial x_i} = 0 \tag{2.19}$$

$$\frac{\partial\overline{\rho}\widehat{u}_i}{\partial t} + \frac{\partial\overline{\rho}\widehat{u}_i\widehat{u}_j}{\partial x_j} = -\frac{\partial\overline{p}}{\partial x_i} + \frac{\partial\overline{\tau_{ij}}}{\partial x_j} - \frac{\partial\overline{\rho u_i'' u_j''}}{\partial x_j} \tag{2.20}$$

$$\frac{\partial\overline{\rho}\widehat{h}}{\partial t} + \frac{\partial\overline{\rho}\widehat{u}_j\widehat{h}}{\partial x_j} = -\frac{\partial\overline{q_j}}{\partial x_j} - \frac{\partial\overline{\rho u_j'' h''}}{\partial x_j} \tag{2.21}$$

with the averaged viscous shear stress and averaged heat flux defined as

$$\overline{\tau_{ij}} = \overline{\mu}\left(\frac{\partial\overline{u_i}}{\partial x_j} + \frac{\partial\overline{u_j}}{\partial x_i}\right) + \overline{\mu'\left(\frac{\partial u_i'}{\partial x_j} + \frac{\partial u_j'}{\partial x_i}\right)} - \overline{\mu}\frac{2}{3}\delta_{ij}\frac{\partial\overline{u_k}}{\partial x_k} - \overline{\mu'\frac{2}{3}\delta_{ij}\frac{\partial u_k'}{\partial x_k}} \tag{2.22}$$

and

$$\overline{q_j} = -\overline{\lambda}\frac{\partial\overline{T}}{\partial x_j} - \overline{\lambda'\frac{\partial T'}{\partial x_j}}. \tag{2.23}$$

respectively.

The two additional term on the right-hand-side of equation (2.20) and (2.21) are a turbulent stress tensor and a turbulent heat flux vector, respectively. It is further possible to derive a conservation equation for these turbulent stresses and fluxes. The resulting stress tensor equation, or "Reynolds stress" equation then reads

$$\frac{\partial \overline{\rho u_i'' u_j''}}{\partial t} = C_{ij} + P_{ij} + T_{ij} + \Pi_{ij} + \Psi_{ij} + D_{ij} + \epsilon_{ij} + E_{ij} \tag{2.24}$$

with

$$C_{ij} = -\frac{\partial \widehat{u_k} \overline{\rho u_i'' u_j''}}{\partial x_k} \tag{2.25}$$

$$P_{ij} = -\overline{\rho u_j'' u_k''} \frac{\partial \widehat{u_i}}{\partial x_k} - \overline{\rho u_i'' u_k''} \frac{\partial \widehat{u_j}}{\partial x_k} \tag{2.26}$$

$$T_{ij} = -\frac{\partial \overline{\rho u_i'' u_j'' u_k''}}{\partial x_k} \tag{2.27}$$

$$D_{ij} = \left[\frac{\partial \overline{\tau_{ik}' u_j''}}{\partial x_k} + \frac{\partial \overline{\tau_{jk}' u_i''}}{\partial x_k} \right] \tag{2.28}$$

$$\Pi_{ij} = -\frac{\partial \overline{p' u_j''}}{\partial x_i} - \frac{\partial \overline{p' u_i''}}{\partial x_j} \tag{2.29}$$

$$\Psi_{ij} = \overline{p' \left[\frac{\partial u_j''}{\partial x_i} + \frac{\partial u_i''}{\partial x_j} \right]} \tag{2.30}$$

$$\epsilon_{ij} = -\left[\overline{\tau_{ik}' \frac{\partial u_j''}{\partial x_k}} + \overline{\tau_{jk}' \frac{\partial u_i''}{\partial x_k}} \right] \tag{2.31}$$

$$E_{ij} = \left[\overline{u_j''} \frac{\partial \overline{\tau_{ik}}}{\partial x_k} + \overline{u_i''} \frac{\partial \overline{\tau_{jk}}}{\partial x_k} \right] - \overline{u_j''} \frac{\partial \overline{p}}{\partial x_i} - \overline{u_i''} \frac{\partial \overline{p}}{\partial x_j} \tag{2.32}$$

where, C_{ij} is the mean convection, P_{ij} the production, T_{ij} the turbulent diffusion, Π_{ij} the pressure diffusion, Ψ_{ij} the pressure dilatation, D_{ij} the viscous diffusion, ϵ_{ij} the dissipation and E_{ij} is an additional term due to the varying fluid properties. The stress fluctuation appearing in equations (2.28), (2.31) and (2.32) is computed as

$$\tau_{ij}' = \tau_{ij} - \overline{\tau_{ij}}, \tag{2.33}$$

following from the Reynolds decomposition, where τ_{ij} is the instantaneous shear stress. Substituting the individual components of the mean averaged shear stress $\overline{\tau_{ij}}$ shown in equation (2.22) into equation (2.33) yields

$$\begin{aligned} \tau_{ij}' =& \mu \left(\frac{\partial u_i}{\partial x_j} - \frac{\partial u_j}{\partial x_i} \right) - \left[\overline{\mu} \left(\frac{\partial \overline{u_i}}{\partial x_j} + \frac{\partial \overline{u_j}}{\partial x_i} \right) + \overline{\mu' \left(\frac{\partial u_i'}{\partial x_j} + \frac{\partial u_j'}{\partial x_i} \right)} \right] \\ & - \frac{2}{3} \delta_{ij} \left[\mu \frac{\partial u_k}{\partial x_k} - \left(\overline{\mu} \frac{\partial \overline{u_k}}{\partial x_k} + \overline{\mu' \frac{\partial u_k'}{\partial x_k}} \right) \right]. \end{aligned} \tag{2.34}$$

The conservation equation for enthalpy variance reads

$$\frac{1}{2} \frac{\partial \overline{\rho h''^2}}{\partial t} = -C_h + P_h + T_h + D_h + \epsilon_h + E_h \tag{2.35}$$

$$C_h = \frac{\partial \widehat{u}_j \overline{\rho h''^2}}{\partial x_j} \tag{2.36}$$

$$D_h = \left[\frac{\partial \overline{q'_j h''}}{\partial x_j} \right] \tag{2.39}$$

$$P_h = -\overline{\rho u''_j h''} \frac{\partial \widehat{h}}{\partial x_j} \tag{2.37}$$

$$\epsilon_h = -\left[\overline{q'_j \frac{\partial h''}{\partial x_j}} \right] \tag{2.40}$$

$$T_h = -\frac{\partial \overline{\rho u''_j h''^2}}{\partial x_j} \tag{2.38}$$

$$E_h = \left[\overline{h''} \frac{\partial \overline{q_j}}{\partial x_j} \right] \tag{2.41}$$

where, C_h is the mean convection, P_h the production, T_h the turbulent diffusion, D_h the molecular diffusion, ϵ_h the dissipation and E_h additional contribution due to the fluid property fluctuations. The heat flux fluctuation appearing in equations (2.39) and (2.40) reads

$$q'_j = q_j - \overline{q}_j. \tag{2.42}$$

For the turbulent contribution of the heat flux $\overline{\rho u''_j h''}$, present in the production term of equation (2.35), the conservation equation reads

$$\frac{\partial \overline{\rho u''_i h''}}{\partial t} = C_{qi} + P_{qi} + T_{qi} + \Pi_{qi} + D_{qi} + \epsilon_{qi} + E_{qi} \tag{2.43}$$

with

$$C_{qi} = \frac{\partial \widehat{u}_j \overline{\rho u''_i h''}}{\partial x_j} \tag{2.44}$$

$$D_{qi} = \left[\frac{\partial \overline{\tau'_{ij} h''}}{\partial x_j} - \frac{\partial \overline{q'_j u''_i}}{\partial x_j} \right] \tag{2.47}$$

$$P_{qi} = -\overline{\rho u''_j h''} \frac{\partial \widehat{u}_i}{\partial x_j} - \overline{\rho u''_i u''_j} \frac{\partial \widehat{h}}{\partial x_j} \tag{2.45}$$

$$\Pi_{qi} = -\overline{h'' \frac{\partial p'}{\partial x_i}} \tag{2.48}$$

$$T_{qi} = -\frac{\partial \overline{\rho u''_i u''_j h''}}{\partial x_j} \tag{2.46}$$

$$\epsilon_{qi} = -\left[\overline{\tau'_{ij} \frac{\partial h''}{\partial x_j}} - \overline{q'_j \frac{\partial u''_i}{\partial x_j}} \right] \tag{2.49}$$

$$E_{qi} = \left[\overline{h''} \frac{\partial \overline{\tau_{ij}}}{\partial x_j} - \overline{u''_j} \frac{\partial \overline{q_j}}{\partial x_j} \right] - \overline{h''} \frac{\partial \overline{p}}{\partial x_i} \tag{2.50}$$

where, C_{qi} is the mean convection, P_{qi} the production, T_{qi} the turbulent diffusion, Π_{qi} the enthalpy pressure diffusion, D_{qi} the molecular diffusion, ϵ_{qi} the dissipation and E_{qi} is an additional term due to the varying fluid properties.

Closure problem

If a three-dimensional problem is considered, there are 14 unknown variables (three mean velocity components, the mean pressure, the mean temperature, and nine turbulent stresses

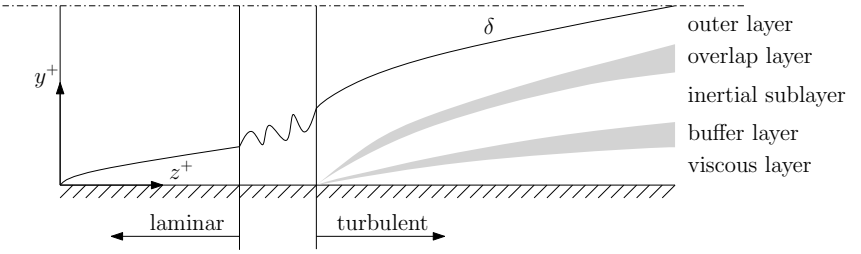

Figure 2.3: The structure of the turbulent velocity boundary layer.

and heat fluxes represented by the non-linear fluctuation terms), but only five equations (continuity (eq. (2.19)), three momentum (eq. (2.20)) and the thermal energy equation (eq. (2.21))) available to solve the problem. This lack of equations is called "closure problem". It is noted that including the transport equations for the turbulent stresses and fluxes, as given above by equations (2.24) and (2.43), respectively, would not solve this problem, because these equations introduce further unclosed higher-order terms on their rhs. Therefore, turbulence models are needed to provide closure for the equations by relating the non-linear turbulent momentum and heat flux terms to the mean values. In channel flows a reliable modelling of these fluxes requires some insight into their behavior near the wall. The main focus of this thesis is on the near wall behavior of the most relevant turbulent stresses and heat fluxes. The influence of these turbulent fluxes on the momentum and heat transfer inside a turbulent boundary layer will be discussed in the following subsections.

2.3 Turbulent boundary layer

A turbulent flow is generally characterized by very intense advective transport of momentum and energy. However, in the proximity of non-moving walls, the flow decelerates due to the non-slip condition and a velocity boundary layer is formed. Consequently, inside the boundary layer, the local Reynolds number is reduced, implying a decrease in the turbulent stresses and an increase in the viscous stresses. Several sub-layers can be distinguished based on the dominating stress. Figure 2.3 shows a typical development of a velocity boundary layer, starting at the entrance, where the flow is laminar, followed by the transition and the fully turbulent flow. Beside the boundary layer thickness, Tennekes and Lumley (1972) introduced a characteristic viscous scale $\frac{\nu}{w'}$, which characterizes the boundary layer. Consequently, with this two length scales the before mentioned sub-layers can be further distinguished, see figure 2.4.

- Inner layer:
  Located closest to the wall and dominated by viscous forces. It consists of the viscous sub-layer and the buffer layer.

- Inertial sub-layer:
  This represents an intermediate layer far enough from the solid wall that the viscous forces can be neglected and the flow is controlled by the turbulent contribution.

- Outer layer:
  This layer is essentially determined by the outer flow conditions, affecting the boundary layer thickness δ.

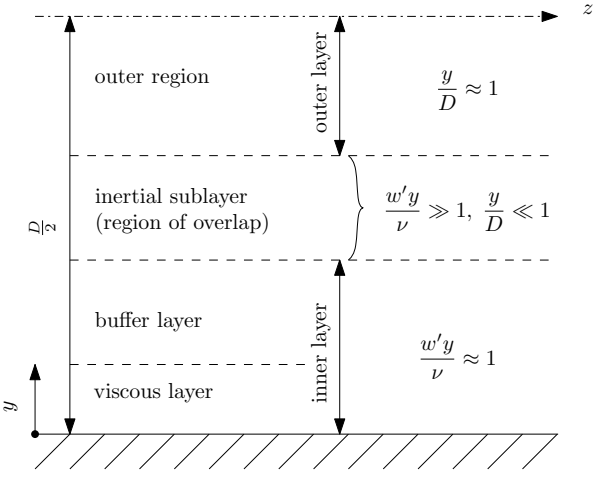

Figure 2.4: Regions of a turbulent boundary layer.

The same applies for the temperature, where the heat fluxes are in analogy to the shear stresses. The characteristic length scales of the momentum boundary layer are related to the characteristic length scales of the thermal boundary through the molecular Prandtl number Pr and the turbulent Prandtl number Pr_T. In the framework of Prandtl's mixing length theory, the turbulent Prandtl number basically represents the ratio of the turbulent mixing length of momentum ℓ_m to the turbulent mixing length of heat, both mixing lengths are mostly assumed as roughly equal, which implies a setting for the turbulent Prandtl number near unity $\mathrm{Pr}_T \approx 1$. The molecular Prandtl number is basically a material constant defined as the ratio of diffusivity of momentum to the thermal diffusivity, relating the molecular diffusive transport of momentum to the molecular conductive transport of

heat.

$$\mathrm{Pr} = \frac{c\mu}{\lambda} = \frac{\nu}{a} = \frac{\text{diffusivity of momentum}}{\text{thermal diffusivity}} \tag{2.51}$$

Applying an order-of-magnitude analysis to the non-dimensionalized boundary layer equations for a convective laminar flow along a heated (or cooled) wall it can be shown that the molecular Prandtl number measures the relative thickness of the thermal boundary layer to the velocity boundary layer according to

$$\frac{\delta_T^2}{\delta^2} = O\left(\frac{1}{\mathrm{Pr}}\right). \tag{2.52}$$

The stream-wise development of the boundary layer thickness along a flat plate is exemplary shown for different Prandtl numbers in figure 2.5.
The relation (2.52) is, strictly speaking, only valid in laminar flow. It can be, however, extended to the turbulent flow as well, where it applies to the relative thicknesses of the viscous and diffusive sub-layers.

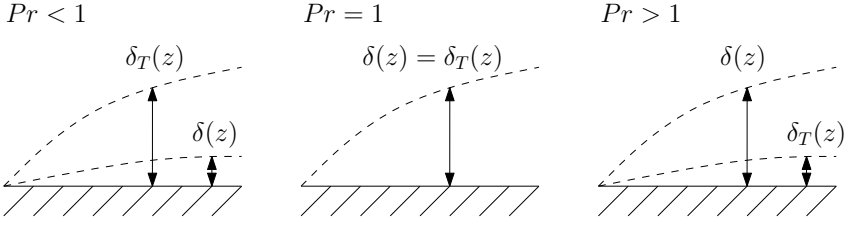

Figure 2.5: Velocity and thermal boundary layers with different molecular Prandtl numbers.

2.4 Fully developed heated turbulent pipe flow

The computational investigation of this thesis considers the particular case of fully developed turbulent circular pipe flow. Such an axisymmetric wall-bounded flow is most conveniently described by the Navier-Stokes and the energy equations, generally given in equations (2.1) - (2.3), rewritten in cylindrical coordinates, as:

- continuity equation

$$\frac{\partial \rho}{\partial t} + \frac{1}{r}\frac{\partial (r\rho u)}{\partial r} + \frac{1}{r}\frac{\partial (\rho v)}{\partial \varphi} + \frac{\partial (\rho w)}{\partial z} = 0 \tag{2.53}$$

- momentum equation into the radial direction

$$\begin{aligned}\frac{\partial \rho u}{\partial t}+\frac{1}{r}\frac{\partial (r\rho uu)}{\partial r}+\frac{1}{r}\frac{\partial (\rho uv)}{\partial \varphi}-\frac{\rho v^2}{r}+\frac{\partial (\rho uw)}{\partial z}=\\ -\frac{\partial p}{\partial r}+\left[\frac{1}{r}\frac{\partial (r\tau_{rr})}{\partial r}+\frac{1}{r}\frac{\partial \tau_{r\varphi}}{\partial \varphi}-\frac{\tau_{\varphi\varphi}}{r}+\frac{\partial \tau_{rz}}{\partial z}\right]\end{aligned} \tag{2.54}$$

- momentum equation into the azimuthal direction

$$\begin{aligned}\frac{\partial \rho v}{\partial t}+\frac{1}{r}\frac{\partial (r\rho vu)}{\partial r}+\frac{1}{r}\frac{\partial (\rho vv)}{\partial \varphi}+\frac{\rho vu}{r}+\frac{\partial (\rho vw)}{\partial z}=\\ -\frac{1}{r}\frac{\partial p}{\partial \varphi}+\left[\frac{1}{r}\frac{\partial (r\tau_{\varphi r})}{\partial r}+\frac{\tau_{\varphi r}}{r}+\frac{1}{r}\frac{\partial \tau_{\varphi\varphi}}{\partial \varphi}+\frac{\partial \tau_{\varphi z}}{\partial z}\right]\end{aligned} \tag{2.55}$$

- momentum equation into the axial direction

$$\begin{aligned}\frac{\partial \rho w}{\partial t}+\frac{1}{r}\frac{\partial (r\rho wu)}{\partial r}+\frac{1}{r}\frac{\partial (\rho wv)}{\partial \varphi}+\frac{\partial (\rho ww)}{\partial z}=\\ -\frac{\partial p}{\partial z}+\left[\frac{1}{r}\frac{\partial (r\tau_{zr})}{\partial r}+\frac{1}{r}\frac{\partial \tau_{z\varphi}}{\partial \varphi}+\frac{\partial \tau_{zz}}{\partial z}\right]\end{aligned} \tag{2.56}$$

The energy equation:

$$\begin{aligned}\frac{\partial \rho h}{\partial t}+\frac{1}{r}\frac{\partial (r\rho hu)}{\partial r}+\frac{1}{r}\frac{\partial (\rho hv)}{\partial \varphi}+\frac{\partial (\rho hw)}{\partial z}=\\ -\left[\frac{1}{r}\frac{\partial (rq_r)}{\partial r}+\frac{1}{r}\frac{\partial \left(q_\varphi\right)}{\partial \varphi}+\frac{\partial \left(q_z\right)}{\partial z}\right]\end{aligned} \tag{2.57}$$

The viscous stresses are written as

$$\tau_{rr}=\mu\left[2\frac{\partial u}{\partial r}-\frac{2}{3}\left\{\underline{\nabla}\cdot\underline{v}\right\}\right] \tag{2.58}$$

$$\tau_{\varphi\varphi}=\mu\left[2\left(\frac{1}{r}\frac{\partial v}{\partial \varphi}+\frac{u}{r}\right)-\frac{2}{3}\left\{\underline{\nabla}\cdot\underline{v}\right\}\right] \tag{2.59}$$

$$\tau_{zz}=\mu\left[2\frac{\partial w}{\partial z}-\frac{2}{3}\left\{\underline{\nabla}\cdot\underline{v}\right\}\right] \tag{2.60}$$

$$\tau_{r\varphi}=\tau_{\varphi r}=\mu\left[r\frac{\partial}{\partial r}\left(\frac{v}{r}\right)+\frac{1}{r}\frac{\partial u}{\partial \varphi}\right] \tag{2.61}$$

$$\tau_{\varphi z}=\tau_{z\varphi}=\mu\left[\frac{\partial v}{\partial z}+\frac{1}{r}\frac{\partial w}{\partial \varphi}\right] \tag{2.62}$$

$$\tau_{zr}=\tau_{rz}=\mu\left[\frac{\partial w}{\partial r}+\frac{\partial u}{\partial z}\right]. \tag{2.63}$$

and the heat fluxes read

$$q_r = -\lambda \frac{\partial T}{\partial r} \tag{2.64}$$

$$q_\varphi = -\frac{\lambda}{r} \frac{\partial T}{\partial \varphi} \tag{2.65}$$

$$q_z = -\lambda \frac{\partial T}{\partial z} \tag{2.66}$$

In the DNS the discretized representations of these equations need to be solved directly. Assuming hydraulically and thermally fully developed flow allows for comparatively short axial extensions of the computational domain. This computationally less expensive shorter domain is applicable due to the axial periodicity, which can be assumed in a fully developed case for the velocity components as well as the fluctuations of the dynamic pressure and the thermodynamic state variables around suitably defined reference values. The introduction of these relative fluctuations produces two source terms of axial momentum and energy in the respective conservation equations, as will be shown below.

2.4.1 Dynamically fully developed flow

Assuming dynamically fully developed flow conditions the ensemble averaged conservation equation of the axial momentum equation (2.56) is reduced to

$$0 = -\frac{\partial \overline{p}}{\partial z} + \frac{1}{r} \frac{\partial}{\partial r} \left(r \, \tau_{tot} \right). \tag{2.67}$$

with

$$\tau_{tot} = \overline{\tau}_{rz} + \overline{\rho u w}. \tag{2.68}$$

Since the mean pressure gradient does not depend on the radial coordinate, the integration of equation (2.67) yields

$$0 = -\frac{r}{2} \frac{\partial \overline{p}}{\partial z} + \overline{\tau}_{tot}, \tag{2.69}$$

Equation (2.69) can be evaluated at the wall with $\tau_{tot}|_{D/2} = -\tau_w$ (see figure 2.6), resulting in

$$\frac{\partial \overline{p}}{\partial z} = -\frac{4 \, \tau_w}{D}. \tag{2.70}$$

Integrating this equation results in

$$\overline{p}(z) = \overline{p}_{in} - \frac{4 \, \tau_w}{D} \, z, \tag{2.71}$$

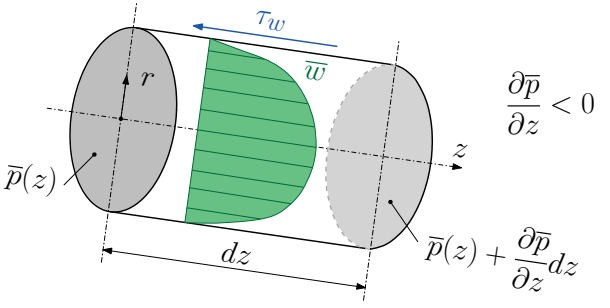

Figure 2.6: Shear stress and axial pressure gradient in a cylindrical pipe flow

which basically represents the axial variation of the mean pressure, reflecting the constant axial drop of mean pressure due to the drag, as schematically shown in figure 2.6.

A suitable decomposition for the pressure is introduced as

$$p(t;r,\varphi,z) = \overline{p}(z) + \pi(t;r,\varphi,z). \tag{2.72}$$

where the component π is periodic in the axial direction. Incorporating this decomposition into the conservation equation of momentum (2.54)-(2.56) finally yields

- momentum equation into the radial direction

$$\begin{aligned} \frac{\partial \rho u}{\partial t} + \frac{1}{r}\frac{\partial (r\rho uu)}{\partial r} + \frac{1}{r}\frac{\partial (\rho uv)}{\partial \varphi} - \frac{\rho v^2}{r} + \frac{\partial (\rho uw)}{\partial z} = \\ -\frac{\partial \pi}{\partial r} + \left[\frac{1}{r}\frac{\partial (r\tau_{rr})}{\partial r} + \frac{1}{r}\frac{\partial \tau_{r\varphi}}{\partial \varphi} - \frac{\tau_{\varphi\varphi}}{r} + \frac{\partial \tau_{rz}}{\partial z}\right] \end{aligned} \tag{2.73}$$

- momentum equation into the azimuthal direction

$$\begin{aligned} \frac{\partial \rho v}{\partial t} + \frac{1}{r}\frac{\partial (r\rho vu)}{\partial r} + \frac{1}{r}\frac{\partial (\rho vv)}{\partial \varphi} + \frac{\rho vu}{r} + \frac{\partial (\rho vw)}{\partial z} = \\ -\frac{1}{r}\frac{\partial \pi}{\partial \varphi} + \left[\frac{1}{r}\frac{\partial (r\tau_{\varphi r})}{\partial r} + \frac{\tau_{\varphi r}}{r} + \frac{1}{r}\frac{\partial \tau_{\varphi\varphi}}{\partial \varphi} + \frac{\partial \tau_{\varphi z}}{\partial z}\right] \end{aligned} \tag{2.74}$$

- momentum equation into the axial direction

$$\begin{aligned} \frac{\partial \rho w}{\partial t} + \frac{1}{r}\frac{\partial (r\rho wu)}{\partial r} + \frac{1}{r}\frac{\partial (\rho wv)}{\partial \varphi} + \frac{\partial (\rho ww)}{\partial z} = \\ -\frac{\partial \pi}{\partial z} + \frac{4}{D}\frac{\tau_w}{} + \left[\frac{1}{r}\frac{\partial (r\tau_{zr})}{\partial r} + \frac{1}{r}\frac{\partial \tau_{z\varphi}}{\partial \varphi} + \frac{\partial \tau_{zz}}{\partial z}\right] \end{aligned} \tag{2.75}$$

These equations describe a dynamically fully developed turbulent flow, allowing for the prescription of periodic boundary conditions for the velocities u, v and w, and the pressure fluctuation π.

2.4.2 Thermally fully developed flow

The thermal boundary condition considered in this thesis prescribes an uniform wall heat flux, causing the fluid temperature to increase along the axial direction. This continuous heat-up would, on the first sight, exclude the assumption of axial periodicity for the thermal state variables. However, axial periodicity can be still provided by relating the thermal variables to appropriate reference values. Figure (2.7) shows the variation of the bulk and wall enthalpy in the thermal entrance length and in the fully developed region. The axial distance, until a flow reaches a fully developed state, is generally termed "entrance length", and basically depends on the Reynolds and the molecular Prandtl number.

The bulk enthalpy represents a cross-sectional average, defined as

$$h_b = \frac{1}{\dot{m}} \int_A \rho(r) w(r) h(r) \mathrm{d}A, \tag{2.76}$$

with the mass flow rate $\dot{m}$ defined as

$$\dot{m} = \int_A \rho(r) w(r) \mathrm{d}A. \tag{2.77}$$

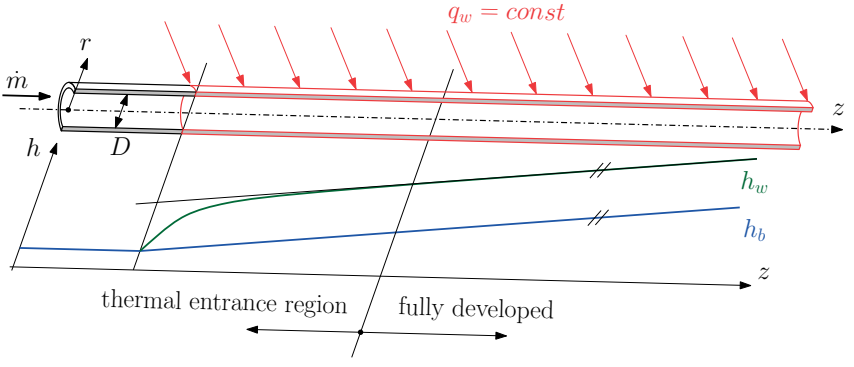

Figure 2.7: Enthalpy variation in the thermal entrance region and in the fully turbulent region

The fully developed region is evidently characterized by a constant difference between the enthalpy at the wall and the bulk enthalpy,

$$h_w - h_b = \text{const.}. \tag{2.78}$$

This implies that the enthalpy fluctuations relative to $h_w(z)$, or $h_b(z)$, are statistically homogeneous in the axial direction. Thus, introducing the decomposition

$$h(t;r,\varphi,z) = \overline{h}_w(z) - \chi(t;r,\varphi,z), \tag{2.79}$$

and

$$T(t;r,\varphi,z) = \overline{T}_w(z) - \theta(t;r,\varphi,z) \tag{2.80}$$

into the conservation equation of energy, equation (2.57), yields a transport equation for the relative enthalpy χ, which is written as

$$\begin{aligned} \rho\frac{\partial\chi}{\partial t} + \rho\frac{1}{r}\frac{\partial(r\chi u)}{\partial r} + \rho\frac{1}{r}\frac{\partial(\chi v)}{\partial\varphi} + \rho\frac{\partial(\chi w)}{\partial z} = \\ \left[\frac{1}{r}\frac{\partial}{\partial r}\left(r\lambda\frac{\partial\theta}{\partial r}\right) + \frac{1}{r}\frac{\partial}{\partial\varphi}\left(\frac{\lambda}{r}\frac{\partial\theta}{\partial\varphi}\right) + \frac{\partial}{\partial z}\left(\lambda\frac{\partial\theta}{\partial z}\right)\right] + \rho w\frac{\mathrm{d}h_w}{\mathrm{d}z}. \end{aligned} \tag{2.81}$$

In consistence with the statistical homogeneity of χ in the axial direction, axial periodicity is imposed as respective boundary condition,

$$\begin{aligned} \chi(r,\varphi,z) &= \chi(r,\varphi,z+L), \\ \theta(r,\varphi,z) &= \theta(r,\varphi,z+L), \end{aligned} \tag{2.82}$$

and Dirichlet boundary conditions are imposed at the wall $r = D/2$: $\chi = 0$ and $\theta = 0$, essentially assuming zero fluctuations $T'_w = 0$ and $h'_w = 0$ at the wall.

The assumption of fully developed flow is associated with a constant relative bulk enthalpy χ_b, as already stated above in equation (2.78). This implies for the axial derivatives

$$\frac{\mathrm{d}h_w}{\mathrm{d}z} = \frac{\mathrm{d}h_b}{\mathrm{d}z}. \tag{2.83}$$

The axial derivative of the bulk enthalpy can be obtained based on a global energy balance for a differential cylindrical element of the length $\mathrm{d}z$, written as

$$\dot{m}\left(\frac{\mathrm{d}h_b}{\mathrm{d}z}\mathrm{d}z\right) = q_w D\pi\mathrm{d}z, \tag{2.84}$$

yielding

$$\frac{\mathrm{d}h_b}{\mathrm{d}z} = \frac{q_w D\pi}{\dot{m}}. \tag{2.85}$$

Introducing (2.83) and (2.85) into the balance equation of energy (2.81) yields

$$\begin{aligned} &\frac{\partial \chi}{\partial t} + \frac{1}{r}\frac{\partial (r\chi u)}{\partial r} + \frac{1}{r}\frac{\partial (\chi v)}{\partial \varphi} + \frac{\partial (\chi w)}{\partial z} - \chi\,(\underline{\nabla}\cdot\underline{v}) = \\ &\frac{1}{\rho}\left[\frac{1}{r}\frac{\partial}{\partial r}\left(r\lambda\frac{\partial \theta}{\partial r}\right) + \frac{1}{r}\frac{\partial}{\partial \varphi}\left(\frac{\lambda}{r}\frac{\partial \theta}{\partial \varphi}\right) + \frac{\partial}{\partial z}\left(\lambda\frac{\partial \theta}{\partial z}\right)\right] + w\frac{q_w D\pi}{\dot{m}}. \end{aligned} \tag{2.86}$$

Solving equation (2.86) for χ further provides the local temperature $T(t;r,\varphi,z)$, and the corresponding relative value $\theta = T_w - T$, using the integral

$$\chi = \int_{T}^{T_w(z)} c_p(\tilde{T})\mathrm{d}\tilde{T}. \tag{2.87}$$

The computation of the wall temperature $T_w(z)$, which is used here as upper boundary, invokes again the assumption of fully developed flow and the consistently assumed axially invariance of the material properties. Fully developed flow implies a constant mean heat transfer coefficient, such that the axial derivative of Newton's ansatz for the mean wall heat flux

$$\overline{q}_w = \alpha\,(T_w - T_b) \tag{2.88}$$

yields

$$\frac{\mathrm{d}T_w}{\mathrm{d}z} = \frac{\mathrm{d}T_b}{\mathrm{d}z}, \tag{2.89}$$

for the presently considered constant wall heat flux $\overline{q}_w = \text{const.}$. The axial derivative of the bulk temperature can be related to the bulk enthalpy through

$$\frac{\mathrm{d}T_b}{\mathrm{d}z} = \frac{1}{\langle c_p\rangle}\frac{\mathrm{d}h_b}{\mathrm{d}z}, \tag{2.90}$$

introducing a global average for the specific heat capacity. According to its definition

$$\langle c_p\rangle = \frac{1}{\langle T_w\rangle - \langle T_b\rangle}\int_{\langle T_b\rangle}^{\langle T_w\rangle} c_p\,(T)\,\mathrm{d}T = \frac{\chi_b}{\langle T_w\rangle - \langle T_b\rangle}, \tag{2.91}$$

this quantity represents a global average over the whole computational domain, and is computed from the bulk enthalpy difference χ_b and the axial averages $\langle T_b \rangle$ and $\langle T_w \rangle$. The latter is determined from

$$\langle T_w \rangle = (T_{w,out} + T_{w,in}) \frac{1}{2}. \tag{2.92}$$

The integration of (2.89) with (2.90) yields

$$T_w(z) = T_w|_{z=L} - \frac{q_w D \pi}{\dot{m} \langle c_p \rangle} (L - z) \tag{2.93}$$

to be substituted into (2.91). The wall temperature at the exit, $T_w|_{z=L}$, represents the reference temperature, T_0, and is therefore a known input into (2.93).

In consistence with the assumption of axially invariant material properties the temperature, which is used for computing their radial and azimuthal variations according to the material laws of the fluid, must not depend on the axial direction either. This is assured by evaluating the integral in (2.87) using an axially averaged wall temperature $\langle T_w \rangle$ as upper boundary instead of the local value $T_w(z)$.

2.4.3 Total shear stress

Based on the previously shown considerations, it is furthermore possible to find an analytical expression for the total shear stress. This is done by rearranging equation (2.67) and replacing the mean pressure gradient with equation (2.70), so that the spatial variation of the total shear stress reads

$$\tau_{tot} = -\tau_w \frac{2\,r}{D} \tag{2.94}$$

2.4.4 Total heat flux

The same consideration can be made for the total heat flux. For a dynamically and thermally fully developed pipe flow the, ensemble averaged equation of axial momentum is written as

$$0 = -\frac{1}{r} \frac{\partial}{\partial r} (r\, q_{tot}) + \overline{\rho}\widehat{w} \frac{q_w D \pi}{\dot{m}}. \tag{2.95}$$

Integrating equation (2.95) and rearranging yields the radial variation of the total heat flux

$$q_{tot} = \frac{1}{r} \frac{q_w D \pi}{\dot{m}} \int_{\tilde{r}=0}^{r} \tilde{r}\, \overline{\rho}\widehat{w}\, d\tilde{r}, \tag{2.96}$$

with the density and the axial velocity varying depending on the radial position.

2.4.5 Non-dimensional representation

For the sake of a most universal description of the fluid dynamics, the DNS solves the conservation equations for mass (eq. (2.53)), momentum (eqs. (2.73)-(2.75)) and enthalpy (eq. (2.86)) in non-dimensionalized representation. The governing equations are non-dimensionalized introducing the quantities

$$r^* = \frac{r}{D} \qquad u_i^+ = \frac{u_i}{w_\tau} \qquad \pi^+ = \frac{\pi}{\rho {w_\tau}^2} \qquad \rho^* = \frac{\rho}{\rho_0}$$

$$t^* = \frac{t w_\tau}{D} \qquad \theta^+ = \frac{\theta}{T_\tau} \qquad \tau_{ij}^+ = \frac{\tau_{ij}}{\tau_w} \qquad c_p^* = \frac{c_p}{c_{p,0}}$$

$$z^* = \frac{z}{D} \qquad \chi^+ = \frac{\chi}{h_\tau} \qquad q_i^+ = \frac{q_i}{q_w} \qquad \lambda^* = \frac{\lambda}{\lambda_0}$$

$$\underline{\nabla}^* = \frac{\underline{\nabla}}{D} \qquad \dot{m}^* = \frac{\dot{m}}{\rho_w w_\tau D^2 \pi} \qquad \mu^* = \frac{\mu}{\mu_0}$$

with the friction velocity, friction temperature and friction enthalpy being defined as

$$w_\tau = \sqrt{\frac{\tau_0}{\rho_0}} \qquad T_\tau = \frac{q_w}{\rho_0 c_{p,0} w_\tau} \qquad h_\tau = c_{p,0}\, T_\tau$$

and "0" denoting values based on the reference temperature T_0. This leads to the following non-dimensional conservation equations in cylindrical coordinates

- continuity equation

$$\frac{\partial \rho^*}{\partial t^*} + \frac{1}{r^*}\frac{\partial r^* \rho^* u^+}{\partial r^*} + \frac{1}{r^*}\frac{\partial \rho^* v^+}{\partial \varphi} + \frac{\partial \rho^* w^+}{\partial z^*} = 0 \tag{2.97}$$

- momentum equation into the radial direction

$$\begin{aligned} \frac{\partial \rho^* u^+}{\partial t^*} + \frac{1}{r^*}\frac{\partial (r^* \rho^* u^+ u^+)}{\partial r^*} + \frac{1}{r^*}\frac{\partial (\rho^* u^+ v^+)}{\partial \varphi} - \frac{\rho^* {v^+}^2}{r^*} + \frac{\partial (\rho^* u^+ w^+)}{\partial z^*} = \\ -\frac{\partial \pi^*}{\partial r^*} + \frac{1}{\mathrm{Re}_{\tau,0}}\left[\frac{1}{r^*}\frac{\partial (r^* \tau_{rr}^+)}{\partial r^*} + \frac{1}{r^*}\frac{\partial \tau_{r\varphi}^+}{\partial \varphi} - \frac{\tau_{\varphi\varphi}^+}{r^*} + \frac{\partial \tau_{rz}^+}{\partial z^*}\right] \end{aligned} \tag{2.98}$$

- momentum equation into the azimuthal direction

$$\begin{aligned} \frac{\partial \rho^* v^+}{\partial t^*} + \frac{1}{r^*}\frac{\partial (r^* \rho^* v^+ u^+)}{\partial r^*} + \frac{1}{r^*}\frac{\partial (\rho^* v^+ v^+)}{\partial \varphi} + \frac{\rho^* v^+ u^+}{r^*} + \frac{\partial (\rho^* v^+ w^+)}{\partial z^*} = \\ -\frac{1}{r^*}\frac{\partial \pi^*}{\partial \varphi} + \frac{1}{\mathrm{Re}_{\tau,0}}\left[\frac{1}{r^*}\frac{\partial (r^* \tau_{\varphi r})}{\partial r^*} + \frac{\tau_{\varphi r}^+}{r^*} + \frac{1}{r^*}\frac{\partial \tau_{\varphi\varphi}^+}{\partial \varphi} + \frac{\partial \tau_{\varphi z}^+}{\partial z^*}\right] \end{aligned} \tag{2.99}$$

- momentum equation into the axial direction

$$\frac{\partial \rho^* w^+}{\partial t^*} + \frac{1}{r^*}\frac{\partial (r^* \rho^* w^+ u^+)}{\partial r^*} + \frac{1}{r^*}\frac{\partial (\rho^* w^+ v^+)}{\partial \varphi} + \frac{\partial (\rho^* w^+ w^+)}{\partial z^*} = -\frac{\partial \pi^*}{\partial z^*} + 4 + \frac{1}{\mathrm{Re}_{\tau,0}}\left[\frac{1}{r^*}\frac{\partial (r^* \tau_{zr}^+)}{\partial r^*} + \frac{1}{r^*}\frac{\partial \tau_{z\varphi}^+}{\partial \varphi} + \frac{\partial \tau_{zz}^+}{\partial z^*}\right] \tag{2.100}$$

- energy equation:

$$\frac{\partial \chi^+}{\partial t^*} + \frac{1}{r^*}\frac{\partial (r^* \chi^+ u^+)}{\partial r^*} + \frac{1}{r^*}\frac{\partial (\chi^+ v^+)}{\partial \varphi} + \frac{\partial (\chi^+ w^+)}{\partial z^*} - \chi^+ \left(\underline{\nabla}^* \cdot \underline{v}^+\right) = \frac{1}{\rho^* \,\mathrm{Re}_{\tau,0}\,\mathrm{Pr}_0}\left[\frac{1}{r^*}\frac{\partial \left(r^* q_r^+\right)}{\partial r^*} + \frac{1}{r^*}\frac{\partial \left(q_\varphi^+\right)}{\partial \varphi} + \frac{\partial \left(q_z^+\right)}{\partial z^*}\right] + \frac{w^+}{\dot{m}^*} \tag{2.101}$$

- viscous stresses

$$\tau_{rr}^+ = \mu^*\left[2\frac{\partial u^+}{\partial r^*} - \frac{2}{3}\left\{\underline{\nabla}^* \cdot \underline{v}^+\right\}\right] \tag{2.102}$$

$$\tau_{\varphi\varphi}^+ = \mu^*\left[2\left(\frac{1}{r^*}\frac{\partial v^+}{\partial \varphi} + \frac{u^+}{r^*}\right) - \frac{2}{3}\left\{\underline{\nabla}^* \cdot \underline{v}^+\right\}\right] \tag{2.103}$$

$$\tau_{zz}^+ = \mu^*\left[2\frac{\partial w^+}{\partial z^*} - \frac{2}{3}\left\{\underline{\nabla}^* \cdot \underline{v}^+\right\}\right] \tag{2.104}$$

$$\tau_{r\varphi}^+ = \tau_{\varphi r}^+ = \mu^*\left[r^*\frac{\partial}{\partial r^*}\left(\frac{v^+}{r^*}\right) + \frac{1}{r^*}\frac{\partial u^+}{\partial \varphi}\right] \tag{2.105}$$

$$\tau_{\varphi z}^+ = \tau_{z\varphi}^+ = \mu^*\left[\frac{\partial v^+}{\partial z^*} + \frac{1}{r^*}\frac{\partial w^+}{\partial \varphi}\right] \tag{2.106}$$

$$\tau_{zr}^+ = \tau_{rz}^+ = \mu^*\left[\frac{\partial w^+}{\partial r^*} + \frac{\partial u^+}{\partial z^*}\right]. \tag{2.107}$$

- heat fluxes

$$q_r^+ = -\lambda^*\frac{\partial \theta^+}{\partial r^*} \tag{2.108}$$

$$q_\varphi^+ = -\frac{\lambda^*}{r^*}\frac{\partial \theta^+}{\partial \varphi} \tag{2.109}$$

$$q_z^+ = -\lambda^*\frac{\partial \theta^+}{\partial z^*} \tag{2.110}$$

The non-dimensional parameters appearing in equation (2.97) - (2.101) are the wall friction Reynolds number and molecular Prandtl number, defined as
$\mathrm{Re}_{\tau,0} = \dfrac{D\, w_\tau}{\nu_0}$, and $\mathrm{Pr}_0 = \dfrac{\nu_0\, \rho_0\, c_{p,0}}{\lambda_0}$, respectively.

2.5 Material properties

Some restrictions had to be observed in the choice of a suitable working fluid. On the one hand, the fluid had to provide sufficiently high molecular Prandtl numbers well above unity, representing the Prandtl number range of oils. On the other hand, the molecular Prandtl must not exceed the limits imposed by the numerical resolution requirements to be accessible to DNS. Figure 2.8 gives an overview of the typical Prandtl number range of various fluids. The molecular Prandtl number range of oils is rather wide due to the different areas of application. The presently considered oil (Shell Heat Transfer Oil S2) is a "heat transfer oil" typically employed in heat exchanges, where the lubrication is of secondary importance, so that the Prandtl number varies within a moderate range, which is still quite far from unity.

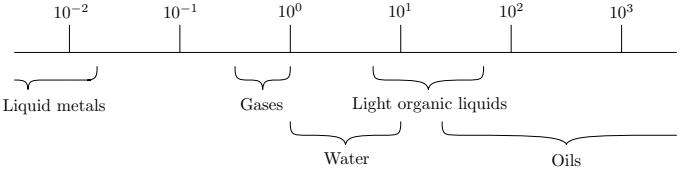

Figure 2.8: Range of Prandtl numbers.

The material properties of the considered oil show a strong temperature dependency. The oil manufacturer provided information about the temperature dependency of the density (ρ), thermal conductivity (λ), specific heat capacity (c_p) and dynamic viscosity (μ). Comparative measurements were performed as well, and simplified temperature-dependent functions were fitted to these data. In the following, a short overview of these measurements and the derived functional temperature dependencies are shown.

2.5.1 Density

The density was measured with the so-called "Oscillating U-tube" method, where the fluid is pumped into a tube which is excited and the resulting oscillation frequency is used to determine the density. The temperature dependence based on the measurements reads

$$\rho = A_\rho + B_\rho T = 1045 - 0.616\,T \qquad [\mathrm{kg\,m^{-3}}] \quad (2.111)$$

The line is shown together with the underlying data in figure 2.9.

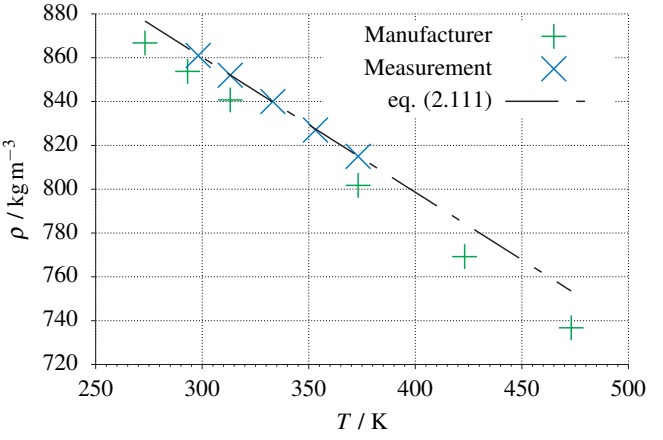

Figure 2.9: Density vs. temperature

2.5.2 Specific heat capacity

The specific heat capacity was measured with the "Dynamical scanning calorimety", which basically relates the transient heat-up of the sample to that of a known reference material to compute the specific heat capacity. Due to some inconsistencies in the repeatability of the measurements for the present oil (indicated by the large error bars in figure 2.10), the temperature dependence was rather based on the manufacturer data and reads

$$c_p = A_c + B_c T = 0.818 + 3.664\text{E}-3\,T \quad [\text{J kg}^{-1}\,\text{K}^{-1}] \quad (2.112)$$

2.5.3 Thermal conductivity

The thermal conductivity was obtained based on the measured density, specific heat capacity and thermal diffusivity. Therefore, due to the already mentioned uncertainties in the measurements of the specific heat capacity, the temperature dependence of the thermal conductivity was purely based on the manufacturer data as well. It reads

$$\lambda = A_\lambda + B_\lambda T = 0.157 - 7.328\text{E}-5\,T \quad [\text{W m}^{-1}\,\text{K}^{-1}] \quad (2.113)$$

and is shown in Figure 2.11.

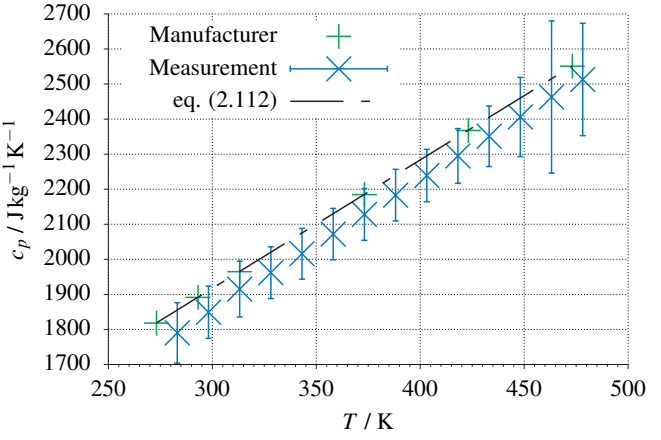

Figure 2.10: Specific heat capacity vs. temperature

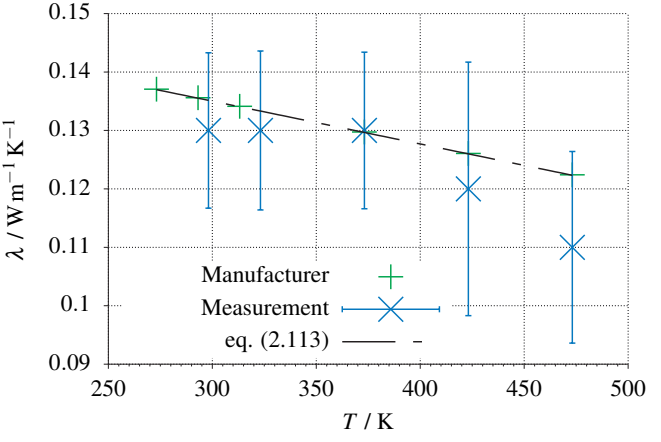

Figure 2.11: Thermal conductivity vs. temperature

2.5.4 Dynamic viscosity

The dynamic viscosity was measured with a "Stabinger viscometer", which basically determines the dynamic viscosity from speed and torque measurements. The obtained tem-

perature dependence reads

$$\mu = A_\mu \exp\left(\frac{B_\mu}{T + C_\mu}\right) = 5.894\text{E}-5 \exp\left(\frac{857.4}{T - 172.2}\right). \quad [\text{Pa s}] \quad (2.114)$$

It reproduces the data points very well, as seen from Figure 2.12.

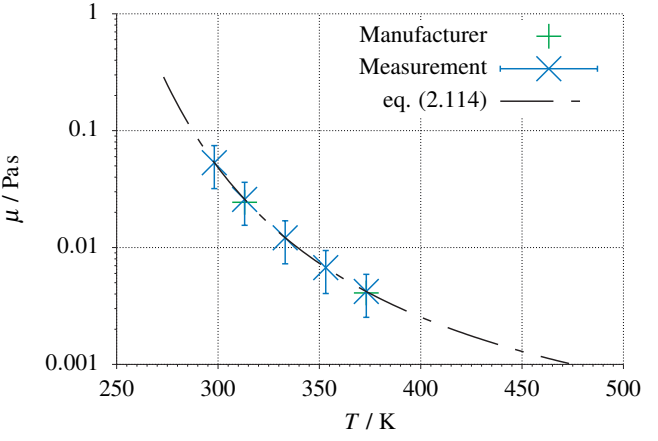

Figure 2.12: Dynamic viscosity vs. temperature

2.5.5 Molecular Prandtl number

The molecular Prandtl number is straight-forwardly computed based on the measured material properties as

$$\text{Pr} = \frac{\nu}{a} = \frac{\mu c_p}{\lambda}. \quad [-] \quad (2.115)$$

Figure (2.13) plots the molecular Prandtl number over the temperature. Regarding simulation costs of DNS, the highest computationally affordable Prandtl number is roughly assumed around $\text{Pr} \approx 50$. This corresponds to an oil temperature around $T \cong 400\text{K}$ as seen from Figure 2.13. The presently performed DNS with therefore always consider operating conditions, which cover a temperature range beyond this level, ensuring a maximum Prandtl number around $\text{Pr} \approx 50$ or less.

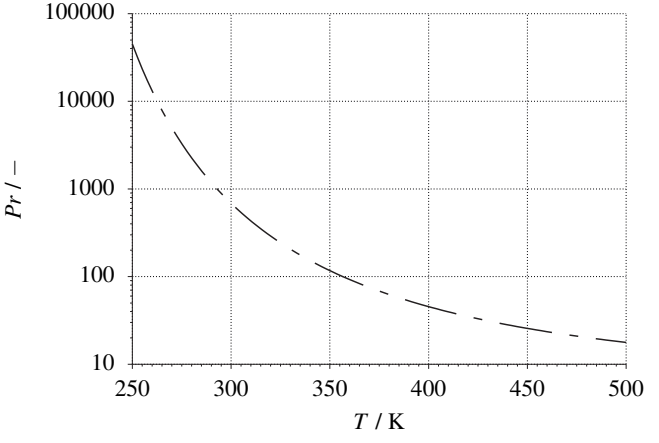

Figure 2.13: Molecular Prandt number vs. temperature

3 DIRECT NUMERICAL SIMULATION

In this chapter the numerical procedure, which is used to solve directly the conservation equations (2.97) - (2.101) will be discussed in detail. Two versions of an incompressible, flow solver, written in cylindrical coordinates, were used for the simulations. On the one hand a solver capable of including temperature-dependent fluid properties, and on the other hand, a solver prescribing constant fluid properties. Both versions are written in FORTRAN and parallelized with MPI.

3.1 Computational mesh

This thesis investigates a cylindrical pipe flow configuration with an axial length of five diameters, which is assumed to be sufficient to capture the largest coherent structures in the

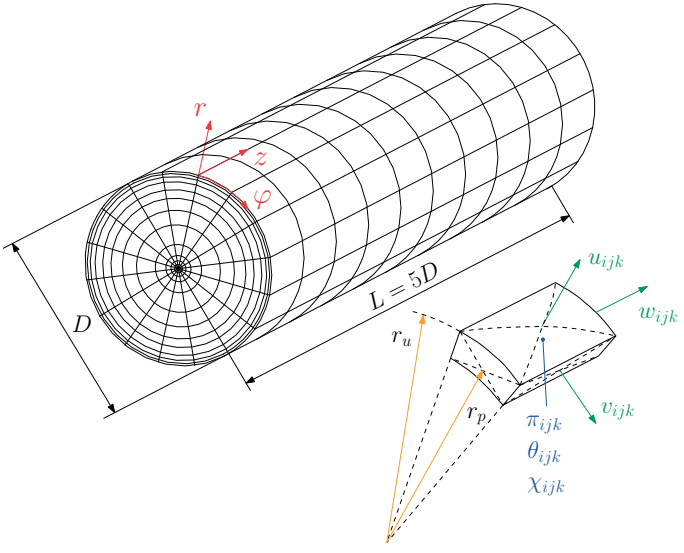

Figure 3.1: Computational grid

streamwise direction. The considered computational domain is shown in figure 3.1, where r is the radial, φ the azimuthal, and z the streamwise direction, with the corresponding velocity components u, v, and w, respectively. The velocity components are located on the cell faces, whereas all scalar quantities are stored in the center of the cell, consistent with a staggered grid setting.

For a DNS the computational mesh has to be sufficiently fine to capture all relevant processes and phenomena. Near the solid wall the flow structures are generally the smallest, especially, when considering the thermal structures whose size decreases with increasing molecular Prandtl number, according to equation (2.18). Therefore, the mesh has to be the finest near the wall, which was achieved by radially clustering the mesh towards the wall.

Preliminary DNS studies further showed that decreasing the cell size near the center notably improves the predictions at the centerline singularity. For this reason, an additional radial mesh clustering is applied towards the center. The employed meshing strategy is based on Vinokur (1983) and will be briefly shown in the following. The first step is to prescribe the desired radial size of the first cell next to the wall, and the next to center, Δr_w and Δr_c, respectively. The so-called stretching function, based on the radial index i, where $i = 0$ represents the center and $i = i_{max}$ the wall is defined as

$$\zeta(i) = \frac{1}{2}\left[1 + \frac{\tanh\left(\delta\left(i/i_{max} - 0.5\right)\right)}{\tanh\left(\delta/2\right)}\right]. \tag{3.1}$$

The stretching factor δ, which is introduced to provide certain prescribed cell sizes at the radial boundaries, is defined by the following equation

$$\frac{\sinh(\delta)}{\delta} = \frac{1}{i_{max}\sqrt{\Delta r_w \Delta r_c}}. \tag{3.2}$$

Using the stretching function (3.1) the radius of each cell face can be obtained as

$$r_u(i) = \frac{\zeta(i)}{2\left[A + (1-A)\zeta(i)\right]} \tag{3.3}$$

with the parameter A defind as

$$A = \frac{\sqrt{\Delta r_w}}{\sqrt{\Delta r_c}}. \tag{3.4}$$

Applying such a mesh clustering approach essentially adapts the cell sizes to resolve the locally varying Kolmogorov micro length scale η (equation (2.17)), and the Batchelor micro length scale η_{th} (equation (2.18)) circumventing a costly global reduction of all cells.

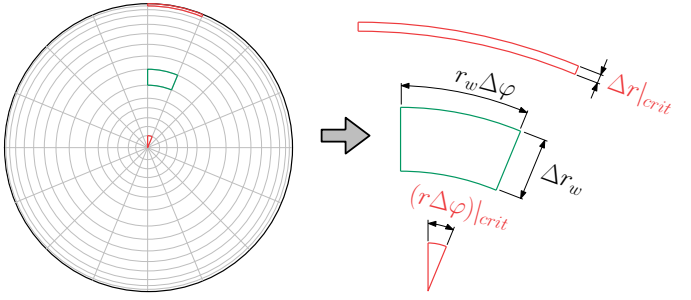

$$\Delta r|_{crit} < \Delta r_w, r_w\Delta\varphi < (r\Delta\varphi)|_{crit}$$

Figure 3.2: Critical cells sizes

Since the presently considered high molecular Prandtl numbers lead to low values of the Batchelor micro length scale, the high resolution requirements can only be met with local mesh refinement. The very small cell size restricts the maximum allowable time-step to guarantee a stable computation which can be determined from the so-called Courant-Friedrichs-Lewy (CFL) condition introduced by Courant et al. (1928). Figure 3.2 schematically shows a double-sided radially clustered mesh with smallest cells highlighted in red. The shortest edges of the computational cells are denoted here as "critical" because their length essentially limits the time-step. At the wall due to the extensive radial clustering, the radial extension of the cell is the critical restricting length, whereas near the center, the azimuthal extension is critical. These two particular constraints were the reason for applying an implicit integration to certain terms of the governing equations in order to ensure a feasible time-step size.

3.2 Numerical solution procedure

The presently considered flow is incompressible with temperature-dependent fluid properties according to the variations shown in section 2.5. The corresponding conservative partial differential equations in non-dimensional form, seen in equation (2.97)-(2.101) are written in cylindrical coordinates and discretized in space applying a 4^{th} order accurate finite volume method. In the following, all involved steps in the numerical scheme are presented and discussed in detail. For convenience, the superscripts introduced in the previous chapters, indicating non-dimensional quantities, will be skipped.

3.2.1 Time integration

There exist various techniques which can be employed to numerically integrate the governing equations in time. For incompressible low Mach number flow with significant isobaric density fluctuations, the predictor-corrector projection scheme, as applied in Najm et al. (1998) and Boersma (1998) has become fairly popular. However, as seen from the variation of the density with the temperature in figure 2.9, the density of the working liquid only weakly varies in the considered temperature range. For this reason, a one-step projection method was chosen, more precisely, a semi-implicit Adams-Bashforth fractional-step method. Such a scheme is widely used to solve the incompressible Navier-Stokes equations with constant density, e.g. Kim and Moin (1985). It was originally proposed by Chorin (1967) and basically splits the time integration of the momentum equation into two sub-steps. In the first sub-step, the momentum fluxes are predicted neglecting the pressure force term. In the successive correction step, the pressure gradient is used to correct the predicted momentum fluxes, such that they satisfy the continuity equation. The required pressure field is computed from a Poisson equation derived from enforcing the conservation of mass in the momentum equation.

At the beginning of each integration step, the enthalpy conservation equation (2.101) is solved. The resulting enthalpy yields the temperature on the new time level, which is further used to update the fluid properties when considering their temperature dependency. The enthalpy is integrated in time combining explicit and implicit schemes. While the fluxes into the axial direction are always treated explicitly, applying a second order accurate Adams-Bashforth scheme, the radial fluxes and the azimuthal fluxes are mutually integrated implicitly in the intervals $r_w < r < D/2$, and $0 \leq r \leq r_w$, respectively. The radius r_w, which basically determines the relative length of these intervals, denotes the radial position with the largest radial grid size Δr_{max}, following from the applied radial clustering, as schematically shown in figure 3.2. Switching the implicitly treated directions dependent on the radial interval allows for a significantly larger time-step than a fully explicit scheme, while the additional computational costs to be spent in the implicit solution procedure are still acceptable. The formulation used to obtain the new enthalpy at time-level $n+1$ reads

- $0 < r < r_w$

$$\begin{aligned}
&\frac{\chi^{n+1}-\chi^n}{\Delta t} = \\
&\frac{3}{2}\left[-\frac{1}{r}\frac{\partial r\chi u}{\partial r}-\frac{\partial \chi w}{\partial z}+\frac{1}{\mathrm{Re}_{\tau,w}\mathrm{Pr}_w}\left\{\frac{1}{r}\frac{\partial (rq_r)}{\partial r}+\frac{\partial (q_z)}{\partial z}\right\}+\chi\,(\underline{\nabla}\cdot\underline{v})\right]^{n-1} \\
&-\frac{1}{2}\left[-\frac{1}{r}\frac{\partial r\chi u}{\partial r}-\frac{\partial \chi w}{\partial z}+\frac{1}{\mathrm{Re}_{\tau,w}\mathrm{Pr}_w}\left\{\frac{1}{r}\frac{\partial (rq_r)}{\partial r}+\frac{\partial (q_z)}{\partial z}\right\}+\chi\,(\underline{\nabla}\cdot\underline{v})\right]^{n} \\
&+\frac{1}{2}\left\{-\left[\frac{1}{r}\frac{\partial \chi v}{\partial \varphi}\right]^{n}-\left[\frac{1}{r}\frac{\partial \chi v}{\partial \varphi}\right]^{n+1}\right\} \\
&+\left[\frac{1}{\mathrm{Re}_{\tau,w}\mathrm{Pr}_w}\frac{1}{r}\frac{\partial (q_\varphi)}{\partial \varphi}\right]^{n+1} \\
&+\Phi_h^{n-1}
\end{aligned} \tag{3.5}$$

- $r_w < r < D/2$

$$\begin{aligned}
&\frac{\chi^{n+1}-\chi^n}{\Delta t} = \\
&\frac{3}{2}\left[-\frac{1}{r}\frac{\partial \chi v}{\partial \varphi}-\frac{\partial \chi w}{\partial z}+\frac{1}{\mathrm{Re}_{\tau,w}\mathrm{Pr}_w}\left\{\frac{1}{r}\frac{\partial (q_\varphi)}{\partial \varphi}+\frac{\partial (q_z)}{\partial z}\right\}+\chi\,(\underline{\nabla}\cdot\underline{v})\right]^{n-1} \\
&-\frac{1}{2}\left[-\frac{1}{r}\frac{\partial \chi v}{\partial \varphi}-\frac{\partial \chi w}{\partial z}+\frac{1}{\mathrm{Re}_{\tau,w}\mathrm{Pr}_w}\left\{\frac{1}{r}\frac{\partial (q_\varphi)}{\partial \varphi}+\frac{\partial (q_z)}{\partial z}\right\}+\chi\,(\underline{\nabla}\cdot\underline{v})\right]^{n} \\
&+\frac{1}{2}\left\{-\left[\frac{1}{r}\frac{\partial r\chi u}{\partial r}\right]^{n}-\left[\frac{1}{r}\frac{\partial r\chi u}{\partial r}\right]^{n+1}\right\} \\
&+\left[\frac{1}{\mathrm{Re}_{\tau,w}\mathrm{Pr}_w}\frac{1}{r}\frac{\partial (rq_r)}{\partial r}\right]^{n+1} \\
&+\Phi_h^{n-1}
\end{aligned} \tag{3.6}$$

The last term Φ_h^{n-1} in equation (3.5) and (3.6) corresponds to the source-term, enforcing axial periodicity for the variable χ, assuming thermally fully developed flow conditions, corresponding to the last term in equation (2.101). The fluid properties are updated with the enthalpy-equivalent temperature T^{n+1} and yield the fluid properties on the new time level (e.g. ρ^{n+1}).

After the integration of the enthalpy difference χ, the momentum equations are integrated using the fractional-step method. In the first sub-step, the prediction step, the intermediate

flux field $(\rho u_i)^\star$ is predicted using the same combined explicit/implicit scheme used to obtain the enthalpy. It is written as

- $0 < r < r_w$

$$\frac{(\rho u)^\star - (\rho u)^n}{\Delta t} = \tag{3.7}$$
$$\frac{3}{2}\left[-\frac{1}{r}\frac{\partial r\rho uu}{\partial r} + \frac{\rho v^2}{r} - \frac{\partial \rho uw}{\partial z} + \frac{1}{\mathrm{Re}_{\tau,w}}\left\{\frac{1}{r}\frac{\partial r\tau_{rr}}{\partial r} - \frac{\tau_{\varphi\varphi}}{r} + \frac{\partial \tau_{rz}}{\partial z}\right\}\right]^{n-1}$$
$$-\frac{1}{2}\left[-\frac{1}{r}\frac{\partial r\rho uu}{\partial r} + \frac{\rho v^2}{r} - \frac{\partial \rho uw}{\partial z} + \frac{1}{\mathrm{Re}_{\tau,w}}\left\{\frac{1}{r}\frac{\partial r\tau_{rr}}{\partial r} - \frac{\tau_{\varphi\varphi}}{r} + \frac{\partial \tau_{rz}}{\partial z}\right\}\right]^{n}$$
$$+\frac{1}{2}\left\{-\left[\frac{1}{r}\frac{\partial \rho uv}{\partial \varphi}\right]^n - \left[\frac{1}{r}\frac{\partial \rho uv}{\partial \varphi}\right]^{n+1}\right\}$$
$$+\left[\frac{1}{\mathrm{Re}_{\tau,w}}\frac{1}{r}\frac{\partial \tau_{r\varphi}}{\partial \varphi}\right]^{n+1}$$

$$\frac{(\rho v)^\star - (\rho v)^n}{\Delta t} = \tag{3.8}$$
$$\frac{3}{2}\left[-\frac{1}{r}\frac{\partial r\rho vu}{\partial r} - \frac{\rho vu}{r} - \frac{\partial \rho vw}{\partial z} + \frac{1}{\mathrm{Re}_{\tau,w}}\left\{\frac{1}{r}\frac{\partial r\tau_{\varphi r}}{\partial r} + \frac{\tau_{\varphi r}}{r} + \frac{\partial \tau_{\varphi z}}{\partial z}\right\}\right]^{n-1}$$
$$-\frac{1}{2}\left[-\frac{1}{r}\frac{\partial r\rho vu}{\partial r} - \frac{\rho vu}{r} - \frac{\partial \rho vw}{\partial z} + \frac{1}{\mathrm{Re}_{\tau,w}}\left\{\frac{1}{r}\frac{\partial r\tau_{\varphi r}}{\partial r} + \frac{\tau_{\varphi r}}{r} + \frac{\partial \tau_{\varphi z}}{\partial z}\right\}\right]^{n}$$
$$+\frac{1}{2}\left\{-\left[\frac{1}{r}\frac{\partial \rho vv}{\partial \varphi}\right]^n - \left[\frac{1}{r}\frac{\partial \rho vv}{\partial \varphi}\right]^{n+1}\right\}$$
$$+\left[\frac{1}{\mathrm{Re}_{\tau,w}}\frac{1}{r}\frac{\partial \tau_{\varphi\varphi}}{\partial \varphi}\right]^{n+1}$$

$$\frac{(\rho w)^\star - (\rho w)^n}{\Delta t} = \tag{3.9}$$
$$\frac{3}{2}\left[-\frac{1}{r}\frac{\partial r\rho wu}{\partial r} - \frac{\partial \rho ww}{\partial z} + \frac{1}{\mathrm{Re}_{\tau,w}}\left\{\frac{1}{r}\frac{\partial r\tau_{zr}}{\partial r} + \frac{\partial \tau_{zz}}{\partial z}\right\}\right]^{n-1}$$
$$-\frac{1}{2}\left[-\frac{1}{r}\frac{\partial r\rho wu}{\partial r} - \frac{\partial \rho ww}{\partial z} + \frac{1}{\mathrm{Re}_{\tau,w}}\left\{\frac{1}{r}\frac{\partial r\tau_{zr}}{\partial r} + \frac{\partial \tau_{zz}}{\partial z}\right\}\right]^{n}$$
$$+\frac{1}{2}\left\{-\left[\frac{1}{r}\frac{\partial \rho wv}{\partial \varphi}\right]^n - \left[\frac{1}{r}\frac{\partial \rho wv}{\partial \varphi}\right]^{n+1}\right\}$$
$$+\left[\frac{1}{\mathrm{Re}_{\tau,w}}\frac{1}{r}\frac{\partial \tau_{z\varphi}}{\partial \varphi}\right]^{n+1}$$
$$+\Phi^{n-1}$$

- $r_w < r < D/2$

$$\frac{(\rho u)^\star - (\rho u)^n}{\Delta t} = \tag{3.10}$$
$$\frac{3}{2}\left[-\frac{1}{r}\frac{\partial \rho uv}{\partial \varphi} + \frac{\rho v^2}{r} - \frac{\partial \rho uw}{\partial z} + \frac{1}{\mathrm{Re}_{\tau,w}}\left\{\frac{1}{r}\frac{\partial \tau_{r\varphi}}{\partial \varphi} - \frac{\tau_{\varphi\varphi}}{r} + \frac{\partial \tau_{rz}}{\partial z}\right\}\right]^{n-1}$$
$$-\frac{1}{2}\left[-\frac{1}{r}\frac{\partial \rho uv}{\partial \varphi} + \frac{\rho v^2}{r} - \frac{\partial \rho uw}{\partial z} + \frac{1}{\mathrm{Re}_{\tau,w}}\left\{\frac{1}{r}\frac{\partial \tau_{r\varphi}}{\partial \varphi} - \frac{\tau_{\varphi\varphi}}{r} + \frac{\partial \tau_{rz}}{\partial z}\right\}\right]^{n}$$
$$+\frac{1}{2}\left\{-\left[\frac{1}{r}\frac{\partial r\rho uu}{\partial r}\right]^{n} - \left[\frac{1}{r}\frac{\partial r\rho uu}{\partial r}\right]^{n+1}\right\}$$
$$+\left[\frac{1}{\mathrm{Re}_{\tau,w}}\frac{1}{r}\frac{\partial r\tau_{rr}}{\partial r}\right]^{n+1}$$

$$\frac{(\rho v)^\star - (\rho v)^n}{\Delta t} = \tag{3.11}$$
$$\frac{3}{2}\left[-\frac{1}{r}\frac{\partial \rho vv}{\partial \varphi} - \frac{\rho vu}{r} - \frac{\partial (\rho vw)}{\partial z} + \frac{1}{\mathrm{Re}_{\tau,w}}\left\{\frac{1}{r}\frac{\partial \tau_{\varphi\varphi}}{\partial \varphi} + \frac{\tau_{\varphi r}}{r} + \frac{\partial \tau_{\varphi z}}{\partial z}\right\}\right]^{n-1}$$
$$-\frac{1}{2}\left[-\frac{1}{r}\frac{\partial \rho vv}{\partial \varphi} - \frac{\rho vu}{r} - \frac{\partial \rho vw}{\partial z} + \frac{1}{\mathrm{Re}_{\tau,w}}\left\{\frac{1}{r}\frac{\partial \tau_{\varphi\varphi}}{\partial \varphi} + \frac{\tau_{\varphi r}}{r} + \frac{\partial \tau_{\varphi z}}{\partial z}\right\}\right]^{n}$$
$$+\frac{1}{2}\left\{-\left[\frac{1}{r}\frac{\partial r\rho vu}{\partial r}\right]^{n} - \left[\frac{1}{r}\frac{\partial r\rho vu}{\partial r}\right]^{n+1}\right\}$$
$$+\left[\frac{1}{\mathrm{Re}_{\tau,w}}\frac{1}{r}\frac{\partial r\tau_{\varphi r}}{\partial r}\right]^{n+1}$$

$$\frac{(\rho w)^\star - (\rho w)^n}{\Delta t} = \tag{3.12}$$
$$\frac{3}{2}\left[-\frac{1}{r}\frac{\partial \rho wv}{\partial \varphi} - \frac{\partial \rho ww}{\partial z} + \frac{1}{\mathrm{Re}_{\tau,w}}\left\{\frac{1}{r}\frac{\partial \tau_{z\varphi}}{\partial \varphi} + \frac{\partial \tau_{zz}}{\partial z}\right\}\right]^{n-1}$$
$$-\frac{1}{2}\left[-\frac{1}{r}\frac{\partial \rho wv}{\partial \varphi} - \frac{\partial \rho ww}{\partial z} + \frac{1}{\mathrm{Re}_{\tau,w}}\left\{\frac{1}{r}\frac{\partial \tau_{z\varphi}}{\partial \varphi} + \frac{\partial \tau_{zz}}{\partial z}\right\}\right]^{n}$$
$$+\frac{1}{2}\left\{-\left[\frac{1}{r}\frac{\partial r\rho wu}{\partial r}\right]^{n} - \left[\frac{1}{r}\frac{\partial r\rho wu}{\partial r}\right]^{n+1}\right\}$$
$$+\left[\frac{1}{\mathrm{Re}_{\tau,w}}\frac{1}{r}\frac{\partial r\tau_{zr}}{\partial r}\right]^{n+1}$$
$$+\Phi^{n-1}$$

The last term in equations (3.9) and (3.12) represents the momentum source-term, which enforces axial periodicity of the momentum fluxes, assuming dynamically developed flow. The momentum flux field predicted from the projection step does not satisfy the continuity equation. The conservation of mass is enforced by applying a pressure-correction, defined as

$$\begin{bmatrix} \dfrac{(\rho u)^{n+1}-(\rho u)^{\star}}{\Delta t} \\ \dfrac{(\rho v)^{n+1}-(\rho v)^{\star}}{\Delta t} \\ \dfrac{(\rho w)^{n+1}-(\rho w)^{\star}}{\Delta t} \end{bmatrix} = - \begin{bmatrix} \dfrac{1}{r}\dfrac{\partial (r\pi^{n+1})}{\partial r} \\ \dfrac{1}{r}\dfrac{\partial \pi^{n+1}}{\partial \varphi} \\ \dfrac{\partial \pi^{n+1}}{\partial z} \end{bmatrix}, \tag{3.13}$$

The pressure required for the gradient on rhs of equation (3.13) is computed from the poisson equation

$$\begin{aligned} \frac{1}{\Delta t}\left[\left\{ \frac{1}{r}\frac{\partial r\rho u}{\partial r} + \frac{1}{r}\frac{\partial \rho v}{\partial \varphi} + \frac{\partial \rho w}{\partial z} \right\}^{n+1} - \left\{ \frac{1}{r}\frac{\partial r\rho u}{\partial r} + \frac{1}{r}\frac{\partial \rho v}{\partial \varphi} + \frac{\partial \rho w}{\partial z} \right\}^{\star} \right] \\ = -\frac{1}{r}\frac{\partial}{\partial r}\left(r\frac{\partial \pi^{n+1}}{\partial r} \right) - \frac{1}{r^2}\frac{\partial^2 \pi^{n+1}}{\partial \varphi^2} - \frac{\partial^2 \pi^{n+1}}{\partial z^2}, \end{aligned} \tag{3.14}$$

which is obtained by applying the divergence to the complementary part of the truncated momentum equations (3.7) - (3.12) given above.

The first term on the left side of the poisson equation (3.13) represents the divergence of the mass fluxes at the new time level $n+1$. Incorporating the mass conservation equation (2.97), written at time level $n+1$

$$\frac{\partial \rho^{n+1}}{\partial t} + \left\{ \frac{1}{r}\frac{\partial r\rho u}{\partial r} + \frac{1}{r}\frac{\partial \rho v}{\partial \varphi} + \frac{\partial \rho w}{\partial z} \right\}^{n+1} = 0, \tag{3.15}$$

yields

$$\begin{aligned} \frac{1}{\Delta t}\left[\frac{\partial \rho^{n+1}}{\partial t} - \left\{ \frac{1}{r}\frac{\partial r\rho u}{\partial r} + \frac{1}{r}\frac{\partial \rho v}{\partial \varphi} + \frac{\partial \rho w}{\partial z} \right\}^{\star} \right] \\ = -\frac{1}{r}\frac{\partial}{\partial r}\left(r\frac{\partial \pi^{n+1}}{\partial r} \right) - \frac{1}{r^2}\frac{\partial^2 \pi^{n+1}}{\partial \varphi^2} - \frac{\partial^2 \pi^{n+1}}{\partial z^2}. \end{aligned} \tag{3.16}$$

The temporal derivative of the density in equation (3.16) can be determined from the temporal gradient of the temperature, accounting for the thermophysical fluid behavior, as will

be shown in a following section in detail. The second term is the divergence of the momentum flux field obtained from the projection-step equations (3.7) and (3.12). The poisson equation is solved using a direct solver. The substitution of the resulting pressure into equation (3.13), finally yields the new momentum fluxes $(\rho u)^{n+1}$, $(\rho v)^{n+1}$ and $(\rho w)^{n+1}$, which satisfies the conservation of mass given by (3.15).

The final step computes the new velocity field by dividing the new momentum flux obtained from (3.13) by the new density

$$u^{n+1} = \frac{(\rho u)^{n+1}}{\rho^{n+1}} \tag{3.17}$$

$$v^{n+1} = \frac{(\rho v)^{n+1}}{\rho^{n+1}} \tag{3.18}$$

$$w^{n+1} = \frac{(\rho w)^{n+1}}{\rho^{n+1}}. \tag{3.19}$$

3.2.2 Discretisation in space

The governing partial differential equations are discretized in space using the finite volume method. This method essentially solves the conservation equations integrated over the finite volumes of the computational cells, where the volume integral over the divergence terms are transformed into surface integrals, which generally reads

$$\int_V \frac{\partial \psi_k}{\partial x_k} dV = \oint_S \psi_k n_k dS, \tag{3.20}$$

Figure 3.3 exemplarily shows three adjacent volumes. For the discretized balance of surface fluxes according to rhs of equation (3.20), the face values $\psi_{i+1/2}$ and $\psi_{i-1/2}$ have to be determined from the known volumetric averages $\overline{\psi}_{i-1}, \overline{\psi}_i, \overline{\psi}_{i+1}$, etc.. In order to achieve high spatial overall accuracy, a 4^{th} order accurate approach, based on Lemos et al. (2012), was chosen for this purpose. This approach basically approximates the required values at the cell faces using Taylor-series expansions, which consistently reproduce the volumetric averages $\overline{\psi}_{i-}$ and $\overline{\psi}_{i+}$ given in the neighboring volumes. In the following, this 4^{th} order accurate concept will be exemplary shown for a 1-dimensional disretization, as sketched in figure 3.3, where the bars indicate cell averaged values $\overline{\psi}_i$.

The ansatz proposed by Lemos et al. (2012) determines the face volumes as a linear combination of the very next four cell averaged values, written as

$$\psi_{i+\frac{1}{2}} = a\overline{\psi}_{i-1} + b\overline{\psi}_i + c\overline{\psi}_{i+1} + d\overline{\psi}_{i+2}. \tag{3.21}$$

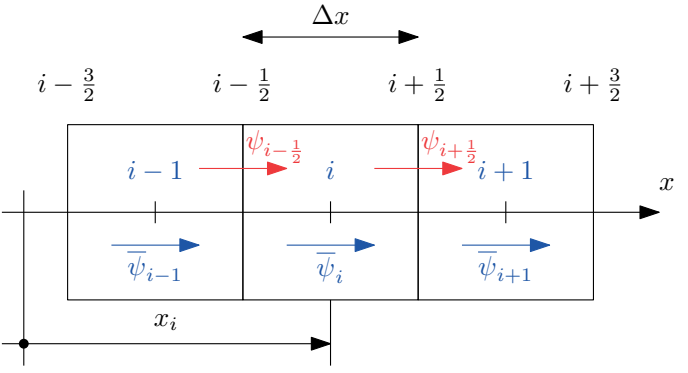

Figure 3.3: 1-dimensional discretisation

The coefficients a,b,c and d are determined by approximating the spatial variation of ψ with a Taylor series expansion of 4^{th} order accuracy around the position of the cell face, written as

$$\psi(x) \cong \psi_{i+1/2} + \left.\frac{\partial \psi}{\partial x}\right|_{i+1/2} (x - x_{i+1/2}) + \left.\frac{\partial^2 \psi}{\partial x^2}\right|_{i+1/2} \frac{(x-x_{i+1/2})^2}{2} + \left.\frac{\partial^3 \psi}{\partial x^3}\right|_{i+1/2} \frac{(x-x_{i+1/2})^3}{6} + \mathcal{O}(4). \tag{3.22}$$

Using this expansion for the computation of the cell averaged quantities on rhs of equation (3.21), i.e.,

$$\overline{\psi}_{i\pm k} = \frac{1}{x_{i+\frac{2k+1}{2}} - x_{i+\frac{2k-1}{2}}} \int_{i+\frac{2k-1}{2}}^{i+\frac{2k+1}{2}} \psi(x) dx, \; k = -1, 0, 1, 2 \tag{3.23}$$

yields, upon equating the terms with the same derivatives, a linear system of equations to be solved for the coefficients a, b, c and d.

Figure 3.4 exemplarily shows the case for a variation assumed as

$$\psi(x) = 10 - 15x - 15x^2 + 5x^3 \tag{3.24}$$

represented by the green line. The step-shaped function denotes the corresponding volume averages. It is clearly visible that the approach of Lemos et al. (2012) approximates the face values of $x_{i\pm 1/2}$ very well. This high level of accuracy is not achievable using a second or fourth-order Lagrangian polynomial interpolation of the cell averages, generally written

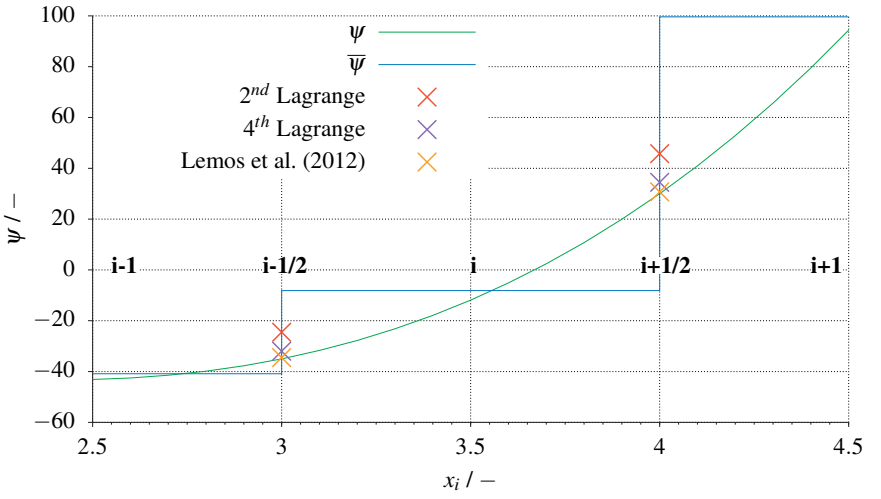

Figure 3.4: 1-dimentional discretisation

for the order $\alpha+\beta+1$ as

$$\overline{\psi}_{i+\frac{1}{2}} \cong \sum_{k=i-\alpha}^{i+\beta} \overline{\psi}_k \prod_{\substack{j=i-\alpha \\ k\neq j}}^{i+\beta} \frac{x_{i+\frac{1}{2}} - x_j}{x_k - x_j} \tag{3.25}$$

whose approximations are shown in figure 3.4 as well.

In the two directions with equidistant grid spacing, the azimuthal and axial, the coefficients used for spatial discretisation, is the same for all cells, while they vary with the radius for the radial discretization, due to the clustering.

3.2.3 Temporal density gradient

The temporal gradient of the density appearing in equation (3.15) is often approximated using a backwards second-order accurate Taylor series expansion, written as

$$\frac{\partial \rho^{n+1}}{\partial t} \approx \frac{3\rho^{n+1} - 4\rho^n + \rho^{n-1}}{2\Delta t}. \tag{3.26}$$

The numerical errors of this approach may become considerably high, especially for small time steps, resulting in an overall low accuracy. For this reason an alternative was used in the present simulations. Using the functional dependence of the density on the temperature, shown in equation (2.111), the temporal density gradient can expressed in terms of the time derivative of the temperature as

$$\frac{\partial \rho^{n+1}}{\partial t} = \underbrace{\frac{\partial \rho}{\partial T}}_{B_\rho} \frac{\partial T^{n+1}}{\partial t}. \tag{3.27}$$

This temporal temperature gradient at time $(n+1)$ is obtained as the rhs of equations (3.5) and (3.6) at time leves $(n+1)$, divided by c_p, respectively.

3.2.4 Boundary conditions

The boundary conditions are implemented with the ghost node method, which basically extends the inner flow field at the boundaries by additional cells. Due to the 4^{th} order accurate spacial discretisation, two additional ghost cells are needed in order to prescribe the boundary conditions with the same accuracy, when using a central-discretisation scheme. For the radial direction, only one additional ghost cell was assumeds requiring a backwards-discretisation scheme.

The actually prescribed boundary conditions (BC) for the different boundaries will be described and discussed in the following.

Wall BC

At the wall, the no-slip condition is assumed for all velocity components. For the thermal boundary condition, a uniform time averaged wall heat flux $\langle q_w \rangle = \text{const.}$ and zero enthalpy fluctuations $\chi'' = 0$ are prescribed. The prescription of no-slip condition for the velocities for all time levels, can be incorporated into equation (3.13), resulting in

$$\left.\frac{\partial \pi^{n+1}}{\partial r}\right|_{r=D/2,\varphi,z} = 0, \tag{3.28}$$

employed as boundary condition of π at the wall.

Centerline BC

At the centerline, the "center singularity", due to the vanishing radial coordinate $r \to 0$ poses a mathematical problem. The φ and z - momentum transfer are essentially not affected by the center singularity due to the presently used staggered grid configuration, so that the area of the radially inner face of the first near-center cell is zero, as seen from figure 3.5, while the center singularity is an issue for the radial momentum transfer. For all independent flow-quantities Neumann boundary conditions are prescribed at $r = 0$, which is realized by a consistent setting at the ghost nodes. For the radial velocity component, the value on the opposite side of the center is used for the interpolation of the ghost node value (denoted by *gn*), reading

$$u_{gn} = \frac{u_{i,j,k} - u_{i,j+\pi,k}}{2}, \tag{3.29}$$

as highlighted in figure 3.5. All other quantities, which are allocated at the center of the first cell, v, w, π and χ, use a von Neumann zero-gradient formulation for the ghost node, generally written as

$$\psi_{gn} = \psi_{i,j,k}. \tag{3.30}$$

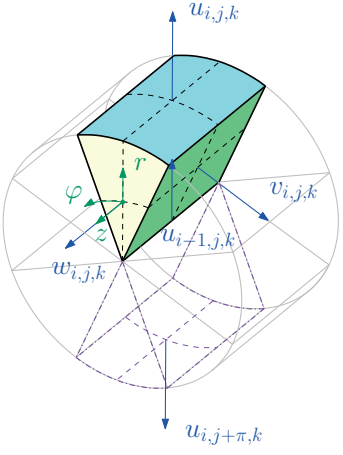

Figure 3.5: Boundary conditions at the centerline

Axial BC

As shown in section 2.4, where the relative pressure and the relative enthalpy have been introduced, being defined as difference to the cross-sectional mean and the value at the wall, respectively, the flow can be considered axially periodic. This implies for all dependent variables u, v, w, π and χ

$$\psi(r,\varphi,z=0) = \psi(r,\varphi,z=L). \tag{3.31}$$

Azimuthal BC

The considered cylindrical geometry allows to prescribe a periodic boundary condition in this direction, generally written as

$$\psi(r,\varphi,z) = \psi(r,\varphi+2\pi,z), \tag{3.32}$$

for all dependent variables.

3.2.5 Axial decomposition of computational domain for parallel processing

In order to reduce the total simulation time, the flow field is split into axial pipe parts. For each subdomain, the conservation equations are solved in parallel according to the procedure shown in section 3.2.1, always followed by a shifting operation, where the ghost nodes are updated with the new values of the neighboring subdomains. This procedure is graphically shown in figure 3.6. The gray arrows indicate the shifting of the data for updating the ghost nodes. Using MPI each axial subdomain is assigned to a CPU (node).

3.2.6 Fluid properties

The fluid properties have to be updated at each time level after solving the transport equation of enthalpy, as defined in (3.5) and (3.6). This requires to relate at first the enthalpy to the temperature, which is then further used as input into the temperature-dependent material properties, as described by equations (2.111) to (2.115). The local temperature can be determined from the local enthalpy differences, as obtained from (3.5) and (3.6), incorporating the temperature-dependent specific heat capacity (equation (2.112)) into equation (2.87), yielding

$$\chi = h_w - h = \int_T^{T_w} c_p(\tilde{T})d\tilde{T} = \int_T^{T_w} A_c + B_c\tilde{T}\; d\tilde{T}. \tag{3.33}$$

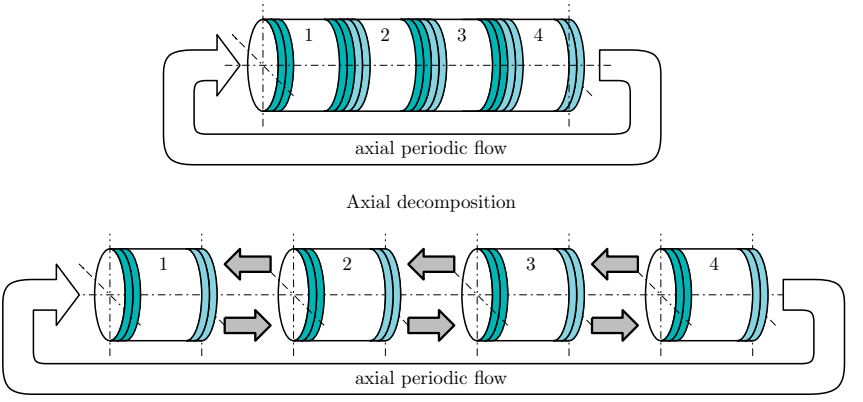

Figure 3.6: Axial decomposition into 4 axial parts

The integral in equation (3.33) can be analytically solved for the lower boundary T, written as

$$T = -\frac{A_c}{B_c} + \sqrt{\left(T_w + \frac{A_c}{B_c}\right)^2 - \frac{2}{B_c}\chi}. \tag{3.34}$$

Assuming dynamically and thermally fully developed flow basically requires the neglect of the axial variation of the averaged material properties due to the continuous heating of the fluid. Using an axially varying wall temperature would conflict with this requirement. Therefore, the axially averaged wall temperature $\langle T_w \rangle$ is used as upper boundary of equation (3.33), and further in (3.34), instead of the local value T_w. This ensures that the fluid property variation is restricted to the radial and azimuthal direction, so that the assumed axial periodicity of the flow variables u, v, w, π and χ, can consistently be applied. For the considered operating conditions, this simplification is only of minor quantitative importance. As will be shown in the discussion of the experiments carried out for validation of the DNS results, the axial increase of the wall temperature over the computationally considered pipe length is about $T_w|_{z=5D} - T_w|_{z=0} = 0.26\mathrm{K}$[2]. This is negligibly small as compared to the temperature difference between wall and bulk temperature of $T_w - T_m = 25.6\mathrm{K}$[2].

[2]Corresponding to measurement results of case $M20/8$, for detail see table 4.4 on page 66

3.2.7 Reference values

The present DNS solves the governing conservation equations in non-dimensional form as given in equation (2.97) - (2.101). All the reference values for the material properties are based on the wall conditions at the exit of the heated pipe, using

$$T_0 = T_w|_{z=L} \tag{3.35}$$

as reference temperature. This axial position corresponds to the end of the heated test section in the validation experiments. Figure 4.1 in the following chapter will show the exact position of this reference point.

3.2.8 Poisson equation

The solution of the Poisson equations (3.16) is responsible for the largest part of the computational expense in this DNS. For the here considered flow, the Poisson equation is written in cylindrical coordinates, as

$$\begin{aligned} &\frac{1}{r}\frac{\partial}{\partial r}\left(r\frac{\partial \pi^{n+1}}{\partial r}\right)+\frac{1}{r^2}\frac{\partial^2 \pi^{n+1}}{\partial \varphi^2}+\frac{\partial^2 \pi^{n+1}}{\partial z^2}= \\ &\frac{1}{\Delta t}\left[\frac{\partial \rho^{n+1}}{\partial t}-\left\{\frac{1}{r}\frac{\partial r\rho u}{\partial r}+\frac{1}{r}\frac{\partial \rho v}{\partial \varphi}+\frac{\partial \rho w}{\partial z}\right\}^{\star}\right] \end{aligned} \tag{3.36}$$

with the right hand being evaluated after the prediction step. This equation represents an three-dimensional elliptic problem, constituting a massive linear equation system. For the considered physical problem and the employed numerical discretisation, the azimutal and axial direction are homogeneous directions. This allows a "Fast Fourier Transformation" (FFT) in these directions. Using this method, only a 1-dimensional system, written as

$$\frac{1}{r}\frac{\partial}{\partial r}\left(r\frac{\partial \widehat{\pi}_{m,n}^{n+1}}{\partial r}\right)+(\lambda_{m,n})\pi_{m,n}^{n+1}=\widehat{RHS}, \tag{3.37}$$

has to be solved for each mode m and n of the Fourier transformed pressure $\widehat{\pi}_{m,n}(r)$. The parameter $\lambda_{m,n}$ stands for the "eigenvalue" and the maximum number of modes m and n corresponds to the number of cells in the homogeneous directions, j_{max} and k_{max}, respectively. Due to the 4^{th} order accurate spacial discretisation, $j_{max} \times k_{max}$ decoupled pentadiagonal linear systems have to be solved, using Gaussian elimination. In the last step, the solution has to be transformed back into physical space by an inverse FFT (iFFT).

One major issue regarding computational time arises from the axial domain decomposition used for parallel processing. While the FFT/iFFT in the azimuthal direction can be performed without any additional communication between computational nodes, some additional communication procedures are needed for applying the FFT/iFFT in axial direction.

4 EXPERIMENTS

The computational data produced by the DNS are validated against experimental data acquired on a specially designed pipe flow test facility. The obtained experimental data also represent a valuable database for further model validation. In this chapter, the experimental setup and the measurement procedure will be explained in detail.

4.1 Experimental setup

The aim of the experiments was, on the one hand, to generate a reliable database for the validation of the DNS results and, on the other hand, the evaluation of predictions from heat transfer models in flow regimes beyond the range amenable to DNS. Dynamically and thermally fully developed flow conditions needed to be realized in the experiments as well to deliver representative data for the conditions considered by the DNS. Special interest was devoted to Reynolds numbers covering the transition regime from laminar to turbulent flow. The constant wall heat flux boundary condition assumed in the computations was accomplished adopting a heating concept similar to the concept of Ghajar and Tam (1994). Figure 4.1 gives a schematic overview of the experimental loop with a detailed representation of the testsection. The loop essentially consists of a Coriolis mass flow meter, a heat exchanger in order to achieve thermally stationary flow conditions, an oil reservoir, a speed-controlled pump and the test-section. The test-section is made of stainless steel (1.4301) with an inner and outer diameter of $d_i = 12$ mm and $d_a = 15$ mm, respectively. The first part of the test-section is the "entrance section" with the length $L = 1.2$ m, representing 100 diameters, which is sufficiently long to ensure dynamically developed flow conditions at the begin of the "heated test-section". The uniform heat flux condition at the inner wall of the pipe was realized by electrically heating the pipe wall. The heat is generated by short circuiting the heated part of the test-section with an electrical transformer which provides high electrical current at low voltage. The length of the heated part of the test-section, being $L = 2$ m, was designed long enough to ensure thermally fully developed flow inside a large part near the exit of the section. Further downstream the fluid passes a well insulated "thermal equalization section", including a static mixer, where the temperature is supposed to reach a uniform value over the whole cross-section, representing the enthalpy flow equivalent outlet bulk temperature $T_{b,1}$. The inlet and outlet bulk temperatures ($T_{b,0}$ and $T_{b,1}$) as well as the wall temperature at the end of the heated test-section are measured using highly accurate resistance thermal probes (PT-100). Additionally, "Type T" thermocouples are mounted along selected axial position of the entire

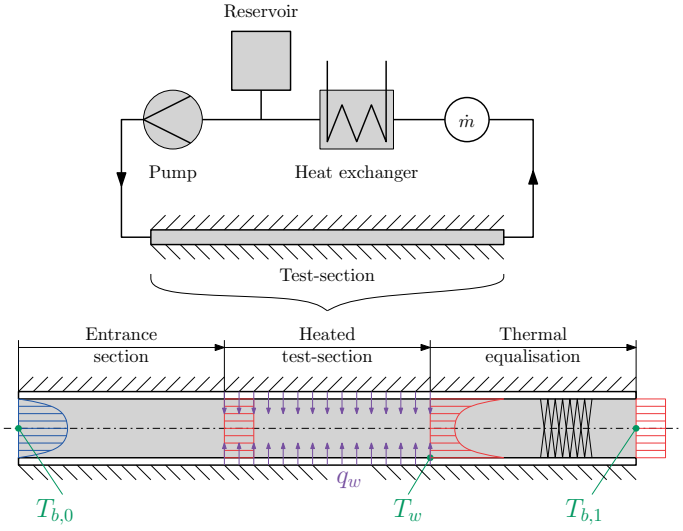

Figure 4.1: Experimental setup

"heated test-section" to measure the wall temperature gradient in flow direction. The whole test-section is thermally well isolated in order to avoid thermal losses.

To exclude any interference with the fully developed flow inside the pipe, exclusively the outer wall temperature is measured with the probes, which is further used to compute the inner wall temperature by solving a radial solid conduction equation. To avoid any influence of the electrical current used for heating on the temperature measurements, the temperature sensor is electrically isolated against the pipe surface by an additional layer of a Kapton tape. The actually applied setup can be seen in figure 4.2, including the thick outer thermal isolation against the ambience, made of glass wool with $\lambda_{iso} = 0.055\,\mathrm{W\,m^{-1}\,K^{-1}}$.

The computation of the inner wall temperature distinguishes two different radial layers, the heated pipe wall and the layer of the unheated Kapton tape. The radial heat transfer inside the heated pipe wall ($r_i \leqslant r \leqslant r_a$), which is made of stainless steel with a thermal conductivity $\lambda_p = 15\mathrm{W\,m^{-1}\,K^{-1}}$ is described by the following conduction equation

$$\lambda_p \frac{1}{r}\frac{\partial}{\partial r}\left(r\frac{\partial T}{\partial r}\right) + \dot{q}_{el} = 0 \tag{4.1}$$

where $\dot{q}_{el}$ is the volumetric heat source computed from the measured electrical current and

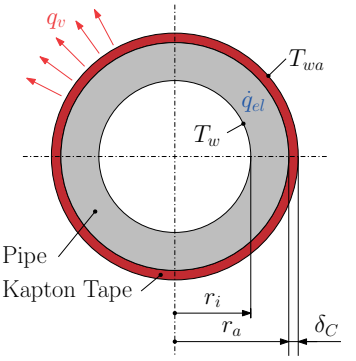

Figure 4.2: Temperature measurement setup

voltage output of the electrical transformer,

$$\dot{q}_{el} = \frac{P_{el}}{V_{HT}} = \frac{UI}{(d_a^2 - d_i^2)\pi/4L}. \tag{4.2}$$

Inside the unheated Kapton tape ($r_a \leqslant r \leqslant r_a + \delta_C$) the conduction equation reads

$$\lambda_C \frac{1}{r}\frac{\partial}{\partial r}\left(r\frac{\partial T}{\partial r}\right) = 0, \tag{4.3}$$

with the thickness being $\delta_C = 0.065$ mm and a thermal conductivity $\lambda_C = 0.16\,\mathrm{W\,m^{-1}\,K^{-1}}$. At the outer radial boundary, at $r = r_a + \delta_C$, an assumed heat loss is prescribed as $q_v = \partial T/\partial r$, and the temperature is set to the value measured by a sensor $T = T_{wa}$. Using these thermal boundary conditions, the solutions of equations (4.1) and (4.3) for the radial variations of the temperature read

- $r_i \leqslant r \leqslant r_a$

$$T_{pipe}(r) = T_{wa} + \frac{\dot{q}_{el}}{\lambda_p}\frac{r_a^2}{2}\left[\frac{1}{2} - \frac{1}{2}\left(\frac{r}{r_a}\right)^2 + \log\left(\frac{r}{r_a}\right)\right] - \frac{q_v}{\lambda_p}(r_a + \delta_C)\left[\frac{\lambda_p}{\lambda_C}\log\left(\frac{r_a}{r_a + \delta_C}\right) + \log\left(\frac{r}{r_a}\right)\right] \tag{4.4}$$

- $r_a \leqslant r \leqslant r_a + \delta_C$

$$T_C(r) = -\frac{q_v}{\lambda_C}(r_a + \delta_C)\log\left(\frac{r}{r_a + \delta_C}\right) + T_{wa} \tag{4.5}$$

The heat loss q_v is estimated from the thermal conductive heat transfer inside the thermal isolation layer, written as

$$q_v = \frac{1}{r_a \frac{1}{\lambda_{iso}} \log\left(\frac{r_{iso}}{r_a}\right)} \left(T_{iso} - T_{wa}\right). \tag{4.6}$$

The temperature difference occurring in (4.6) uses measured values for the outer pipe wall temperature T_{wa}, as well as for T_{iso}, which is measured with a probe at the outer surface of the isolation, $r = r_{iso}$. The pressure drop is measured using pressure probes located at two axially far distant positions within the heated testsection, in order to account for the variability of the fluid properties due to temperature increase. Based on the measured pressure drop, the corresponding wall shear stress can be computed as

$$\tau_w = \frac{\Delta p}{\Delta z} \frac{d_i}{4}, \tag{4.7}$$

and furthermore the skin-friction coefficient

$$c_f = \frac{\tau_w}{\rho_b \frac{\overline{w}_b^2}{2}}. \tag{4.8}$$

The Nusselt number is computed as

$$\mathrm{Nu} = \frac{\alpha d_i}{\lambda_b} = \frac{q_w d_i}{\lambda_w (T_w - T_{b,1})}, \tag{4.9}$$

where the wall heat flux q_w is computed based on the inlet and outlet bulk temperature as

$$q_w = \frac{\dot{m} c_{p,b} (T_{b,1} - T_{b,0})}{d_i \pi L_{heated}}. \tag{4.10}$$

This wall heat flux basically represents the amount of heat, which is produced by the electric volumetric heat source $\dot{q}_{el}$ and transferred per unit area into the fluid.
For the mean specific heat capacity $c_{p,b}$ the relation (2.112) is employed. An important distinction must be made regarding the reference quantities for the non-dimensional quantities. The subscript "b" denotes quantities computed with thermophysical fluid propertied based on the outlet bulk temperature, whereas subscript "w" denotes quantities computed based on the wall temperature.

4.1.1 Measurement error

For the measurement error of the skin-friction coefficient, the bulk velocity $\overline{w}_b$ can be estimated by expressing it in terms of the measured mass-flow rate $\dot{m}$ and the wall shear

stress in terms of the measured pressure drop according to (4.7), so that equation (4.8) can be rewritten as

$$c_f = \frac{\Delta p}{\Delta z}\frac{d_i^5 \pi^2 \rho_b}{32\dot{m}^2}. \tag{4.11}$$

The total error can be obtained from the error propagation

$$\frac{\Delta c_f}{c_f} = \frac{1}{c_f}\sqrt{\left(\frac{\partial c_f}{\partial \Delta p}\Delta(\Delta p)\right)^2 + \left(\frac{\partial c_f}{\partial \rho_b}\Delta\rho_b\right)^2 + \left(\frac{\partial c_f}{\partial \dot{m}}\Delta\dot{m}\right)^2} \tag{4.12}$$

$$= \sqrt{\left(\frac{\Delta(\Delta p)}{\Delta p}\right)^2 + \left(\frac{\Delta\rho_b}{\rho_b}\right)^2 + \left(2\frac{\Delta\dot{m}}{\dot{m}}\right)^2} \tag{4.13}$$

The relative error of the Nusselt number measurement is based on the error propagation determined from equation (4.9) in combination with equation (4.10), which yields

$$\mathrm{Nu} = \frac{\dot{m} c_{p,b}(T_{b,1} - T_{b,0})}{\lambda_b (T_w - T_{b,1})\pi L_{heated}}, \tag{4.14}$$

and the resulting total measurement error reads

$$\begin{aligned}\frac{\Delta \mathrm{Nu}}{\mathrm{Nu}} &= \frac{1}{\mathrm{Nu}}\sqrt{\begin{array}{l}\left(\frac{\partial \mathrm{Nu}}{\partial \dot{m}}\Delta\dot{m}\right)^2 + \left(\frac{\partial \mathrm{Nu}}{\partial c_{p,b}}\Delta c_{p,b}\right)^2 + \left(\frac{\partial \mathrm{Nu}}{\partial \lambda_b}\Delta\lambda_b\right)^2 + \\ \left(\frac{\partial \mathrm{Nu}}{\partial T_{b,1}}\Delta T_{b,1}\right)^2 + \left(\frac{\partial \mathrm{Nu}}{\partial T_{b,0}}\Delta T_{b,0}\right)^2 + \left(\frac{\partial \mathrm{Nu}}{\partial T_w}\Delta T_w\right)^2\end{array}} \\ &= \sqrt{\begin{array}{l}\left(\frac{\Delta\dot{m}}{\dot{m}}\right)^2 + \left(\frac{\Delta c_{p,b}}{c_{p,b}}\right)^2 + \left(\frac{\Delta\lambda_b}{\lambda_b}\right)^2 + \\ \left(\frac{\Delta T}{T_{b,0} - T_{b,1}}\right)^2 + \left(\frac{\Delta T (T_{b,0} - T_w)}{(T_{b,0} - T_{b,1})(T_{b,1} - T_w)}\right)^2 + \left(\frac{\Delta T}{T_{b,1} - T_w}\right)^2\end{array}}\end{aligned} \tag{4.15}$$

For the mass-flow rate and the pressure measurement sensors, the manufacturers specify a relative error, relative to the measured value, whereas for all other sensors an absolute error is specified, independent of the measured value. Table 4.1 shows the relative and absolute errors of all contributions to either error propagation equations (4.12) and (4.15).

Table 4.2 exemplarily shows the skin friction coefficient and the Nusselt number with their corresponding relative errors for a certain measurement case[2] presented at a later point.

[2] Corresponding to measurement results of case $M20/8$, for detail see table 4.4 on page 66

Table 4.1: Relative and absolute error for the error propagation of the skin-friction and Nusselt number measurement

Contribution	absolute error	Unit
$\Delta\dot{m}$	$0.20\text{E}-3\times\dot{m}$	$\mathrm{kg\,s^{-1}}$
ΔT	0.20	K
$\Delta(\Delta p)$	$0.35\text{E}-3\times\Delta p$	Pa
$\Delta\rho_b$	0.13	$\mathrm{kg\,m^{-3}}$
$\Delta c_{p,b}$	0.73	$\mathrm{J\,kg^{-1}\,K^{-1}}$
$\Delta\lambda_b$	$1.56\text{E}-5$	$\mathrm{W\,m^{-1}\,K^{-1}}$

4.2 Experimental results and validation

The validation of the experimental setup was carried out considering heated as well as unheated conditions. The latter was imposed to check the pressure measurements, performing measurements at various Reynolds numbers at constant temperatures in order to exclude any temperature effect of the fluid properties. The resulting skin-friction coefficients were then evaluated against the theoretical solution of c_f for the laminar flow regime, which reads

$$c_f^{lam} = \frac{16}{Re_b}, \tag{4.16}$$

and against the well validated empirical correlation of Konakov (1954)

$$c_f^{turb} = 0.25\,(1.8\log_{10}(Re_b) - 1.5)^{-2}, \tag{4.17}$$

for the turbulent flow regime.

Figure 4.3 compares the measurements against (4.16) and (4.17). Except for the laminar-turbulent transition region, where both above shown formulations are expectedly not applicable, the measurements agree very well.

The shown validation of the skin friction coefficient certainly just makes sense without heating because both of the equations (4.16) and (4.17) assume constant fluid properties.

Table 4.2: Skin friction coefficient and the Nusselt number with their corresponding relative errors

c_f	Δc_f	Nu	ΔNu
$\times 10^{-3}$	$\times 10^{-3}$	–	–
9.18	0.05	59	2

On the other hand, the radial temperature variation due to heating in combination with the fairly strong temperature dependence of the fluid properties may have a considerable effect on c_f. Therefore, the measurements for the Nusselt number, which are inherently associated with heated (or cooled) flow conditions, should only be validated against correlations that account for this dependency. Accordingly, measured Nusselt numbers were presently compared against the well established empirical Gnielinski (1995) correlation for the Nusselt number written as

$$\mathrm{Nu} = \frac{c_f/2\,\mathrm{Re}_b\mathrm{Pr}_b}{1+12.7\sqrt{c_f/2}\left(\mathrm{Pr}_b^{2/3}-1\right)}\left(\frac{\mathrm{Pr}_b}{\mathrm{Pr}_w}\right)^{0.11}. \tag{4.18}$$

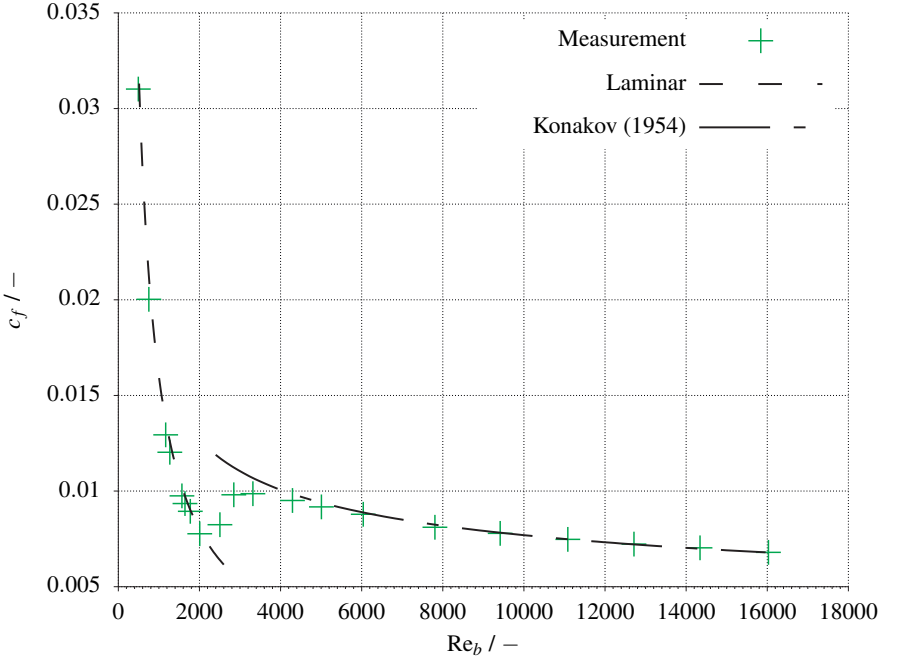

Figure 4.3: Skin-friction coefficients vs. bulk Reynolds number, isothermal flow

In principle this correlation was proposed for the range

$$0.1 \leqslant \mathrm{Pr}_b \leqslant 1000$$
$$10^4 \leqslant \mathrm{Re}_b \leqslant 10^6$$

which falls essentially into the fully turbulent regime. It is therefore consistently recommended to use the correlation of Konakov (1954), (4.17), for computing the skin friction coefficient c_f in (4.18). The last factor in equation (4.18) accounts for the temperature variation and the corresponding fluid property variation. There are only few Nusselt number measurements available for high Prandtl number fluids in the laminar-turbulent transition regime in literature and most of them are fairly old. Still, most of these measurements, e.g. by Morris and Whitman (1928), Sherwood (1932), which were also used by Gnielinski (1995) for validation, indicate an over-prediction of the Nusselt number from equation (4.18). Therefore, Gnielinski (1995) proposed an extended correlation for the transitional regime, $2300 \leq Re_b \leq 10^4$, introducing a linear interpolation between a laminar and a fully turbulent contribution, written as

$$\mathrm{Nu}_m = (1-\gamma)\mathrm{Nu}_{m,lam} + \gamma \mathrm{Nu}_{m,turb}. \tag{4.19}$$

The weighting parameter γ is defined as

$$\gamma = \frac{\mathrm{Re}_b - 2300}{10^4 - 2300}, \tag{4.20}$$

such that it varies within $0 \leqslant \gamma \leqslant 1$.

$\mathrm{Nu}_{m,L,lam}$ represents a laminar Nusselt number at $\mathrm{Re}_b = 2300$, which is determined by Gnielinski (2002) from

$$\mathrm{Nu}_{m,lam} = \left[3.66^3 + 0.7^3 + \left(1.615 \left(\mathrm{Re}_b \, \mathrm{Pr}_b \, \frac{d_i}{L} \right)^{1/3} \right)^3 \right]^{1/3} \tag{4.21}$$

$\mathrm{Nu}_{m,turb}$ denotes the fully turbulent contribution computed from equation (4.18) at $Re_b = 10^4$. Despite this extension proposed for the not fully turbulent low Reynolds number regime, the superposition (4.19) still under-predicts the Nusselt number when compared to the aforementioned measurements presented in literature for the transitional regime.

In the following all measurement results will be compared against the predictions of the Gnielinski correlation, and additionally, against data points from literature measured by Morris and Whitman (1928) and Sherwood (1932).

4.3 Measurement series

Table 4.3 gives an overview over the measurement cases, which were considered in this thesis and partly further used for the validation of the simulation results. As it can be seen from table 4.3, the individual series are distinguished by a certain roughly constant setting for the molecular Prandtl, while varying the Reynolds number. The molecular Prandtl number is based here on the wall conditions

$$\mathrm{Pr}_w = \frac{\nu_w \, \rho_w \, c_{p,w}}{\lambda_w}, \tag{4.22}$$

where the material properties are evaluated with the wall temperature T_w measured at the end of the heated test section (see figure 4.1). On the other hand, the bulk Reynolds number, which is defined as

$$\mathrm{Re}_b = \frac{D \, \overline{w}_b}{\nu_b}, \tag{4.23}$$

depends via the viscosity on the bulk temperature $T_{b,1}$, measured at the end of the thermal equalization section. The bulk velocity is determined from the massflow-rate, controlled by the pump.

As the higher molecular Prandtl numbers imply a higher molecular viscosity, the upper limit of the accessible range of Reynolds numbers is reduced for increasing Prandtl number. The increase in viscosity cannot be fully compensated by an increased mass flow rate due to the limited capacity of the pump.

In the following, the results of all five measurement series listed in table 4.3 are shown. At first, a table lists all important experimental parameters together with the measured skin-fiction coefficients and Nusselt numbers. Both transfer coefficients for momentum and heat, respectively are also shown as graphs dependent on the bulk Reynolds number.

Table 4.3: Measurement series

	Pr_w	Re_b range
M20	$21-25$	$4200-27000$
M30	$29-32$	$3700-20000$
M40	$33-39$	$7000-17000$
M50	$49-51$	$5200-13000$
M60	$56-61$	$5500-10000$

4.3.1 M20

Table 4.4: Parameters of measurement series M20

	T_{b_0}	T_{b_1}	T_w	$\dot{m}$	q_w	Re_b	Re_w	$\mathrm{Re}_{\tau,w}$	Pr_b	Pr_w	Nu	c_f
	K	K	K	$\mathrm{kg\,s^{-1}}$	$\mathrm{W\,m^{-2}}$	–	–	–	–	–	–	10^{-3}
1	445.85	447.75	454.25	0.332	22475	26592	28420	1544	26	25	334	5.90
2	445.25	447.75	456.15	0.280	25194	22461	24463	1366	26	24	290	6.23
3	445.05	448.15	458.15	0.233	25414	18789	20782	1170	26	24	245	6.34
4	444.15	448.15	460.75	0.176	25252	14195	16098	957	26	23	193	7.07
5	443.35	448.95	465.95	0.125	24559	10175	12002	748	26	22	140	7.77
6	443.05	450.35	472.05	0.094	24026	7772	9544	622	26	21	107	8.50
7	443.58	452.87	478.97	0.073	23548	6172	7835	536	25	21	89	8.78
8	438.25	446.85	472.45	0.054	15705	4275	5467	370	26	21	59	9.18

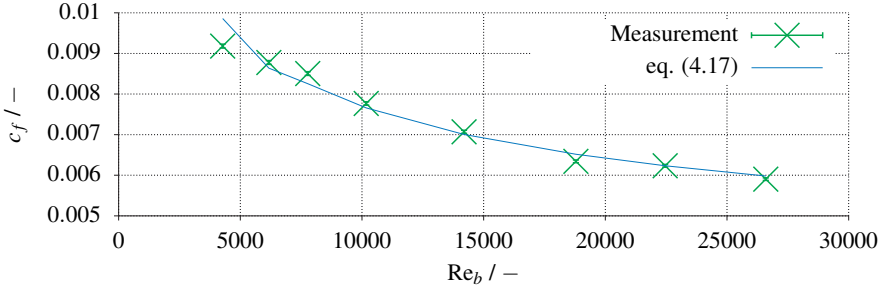

Figure 4.4: Skin-friction coefficient vs. bulk Reynolds number of measurement series M20

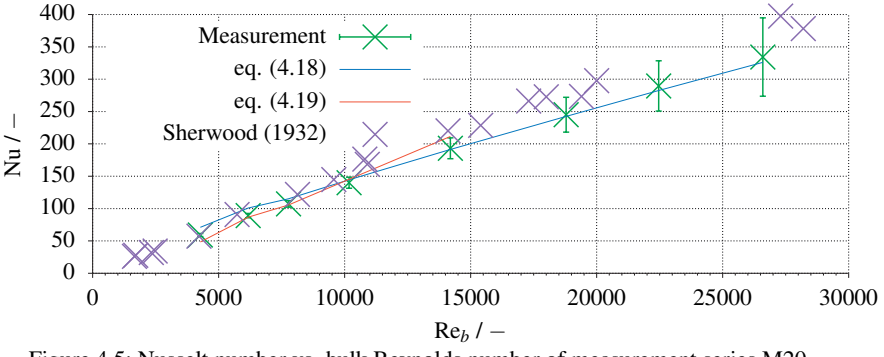

Figure 4.5: Nusselt number vs. bulk Reynolds number of measurement series M20

4.3.2 M30

Table 4.5: Parameters of measurement series M30

	T_{b_0}	T_{b_1}	T_w	$\dot{m}$	q_w	Re_b	Re_w	$\mathrm{Re}_{\tau,w}$	Pr_b	Pr_w	Nu	c_f
	K	K	K	$\mathrm{kg\,s^{-1}}$	$\mathrm{W\,m^{-2}}$	–	–	–	–	–	–	10^{-3}
1	419.95	421.75	429.05	0.337	21384	19511	21390	1217	34	32	279	6.47
2	419.85	421.95	430.35	0.288	21482	16721	18583	1068	34	31	242	6.61
3	419.75	422.35	432.35	0.234	21172	13650	15457	920	34	30	201	7.08
4	419.55	422.85	434.85	0.180	20192	10615	12303	756	34	30	159	7.56
5	416.65	420.45	434.75	0.149	19322	8459	10092	630	35	30	129	7.79
6	414.05	419.05	437.45	0.113	19151	6337	7947	508	35	29	199	8.18

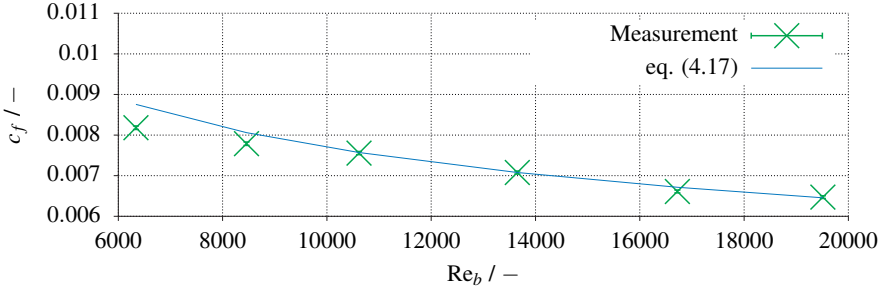

Figure 4.6: Skin-friction coefficient vs. bulk Reynolds number of measurement series M30

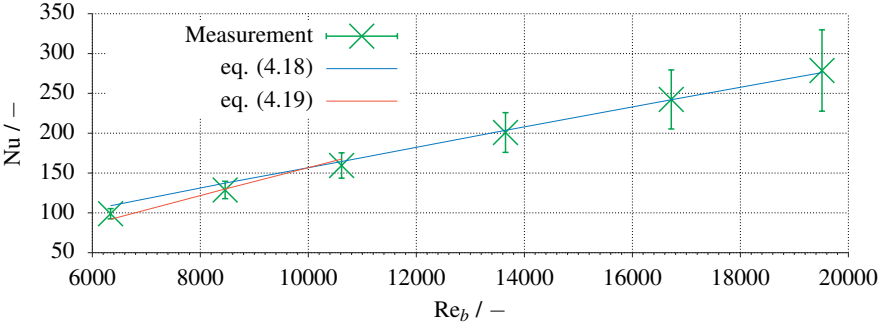

Figure 4.7: Nusselt number vs. bulk Reynolds number of measurement series M30

4.3.3 M40

Table 4.6: Parameters of measurement series M40

	T_{b_0}	T_{b_1}	T_w	$\dot{m}$	q_w	Re_b	Re_w	$\mathrm{Re}_{\tau,w}$	Pr_b	Pr_w	Nu	c_f
	K	K	K	$\mathrm{kg\,s^{-1}}$	$\mathrm{W\,m^{-2}}$	–	–	–	–	–	–	10^{-3}
1	404.45	405.75	411.85	0.340	15194	15559	16997	1001	42	39	236	6.93
2	404.25	405.85	413.35	0.289	16059	13259	14756	886	42	38	204	7.21
3	404.15	406.15	415.05	0.240	16079	11053	12557	759	42	37	170	7.30
4	404.05	406.75	417.85	0.189	16465	8802	10306	629	41	36	139	7.44
5	404.15	407.45	421.15	0.146	15886	6885	8321	547	41	35	110	8.63
6	403.35	407.45	424.05	0.121	16164	5689	7143	466	41	33	92	8.51

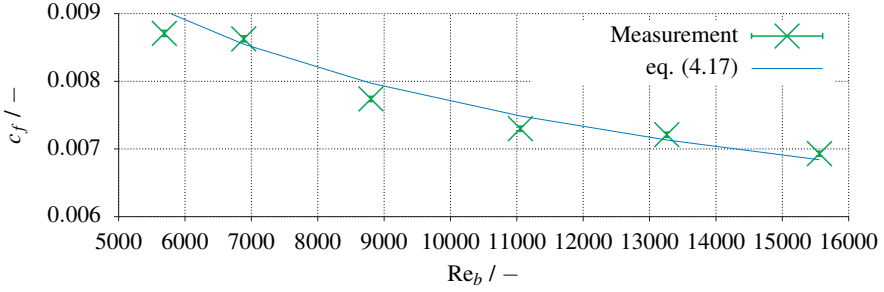

Figure 4.8: Skin-friction coefficient vs. bulk Reynolds number of measurement series M40

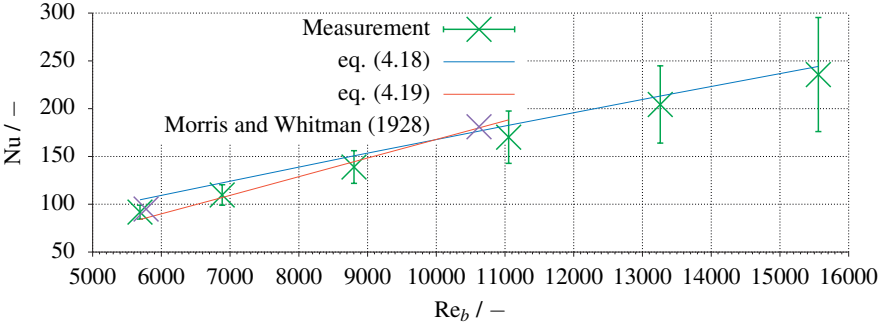

Figure 4.9: Nusselt number vs. bulk Reynolds number of measurement series M40

4.3.4 M50

Table 4.7: Parameters of measurement series M50

	T_{b_0}	T_{b_1}	T_w	$\dot{m}$	q_w	Re_b	Re_w	$\mathrm{Re}_{\tau,w}$	Pr_b	Pr_w	Nu	c_f
	K	K	K	$\mathrm{kg\,s^{-1}}$	$\mathrm{W\,m^{-2}}$	–	–	–	–	–	–	10^{-3}
1	385.05	386.34	393.68	0.340	15018	11159	12670	776	56	50	191	7.50
2	383.05	384.60	393.39	0.287	15459	9113	10626	667	58	50	164	7.88
3	381.85	383.79	394.25	0.235	14839	7353	8829	566	59	49	132	8.23
4	376.55	378.93	392.12	0.200	15610	5686	7218	476	64	51	110	8.69
5	371.45	374.81	394.34	0.144	15327	3773	5392	370	69	49	73	9.43
6	369.95	373.34	393.88	0.141	15083	3571	5218	360	71	50	68	9.50

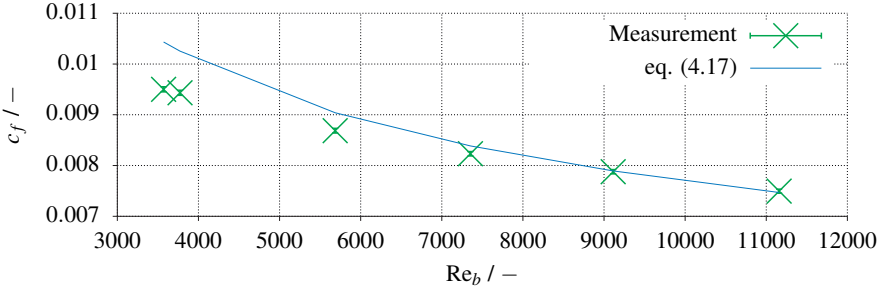

Figure 4.10: Skin-friction coefficient vs. bulk Reynolds number of measurement series M50

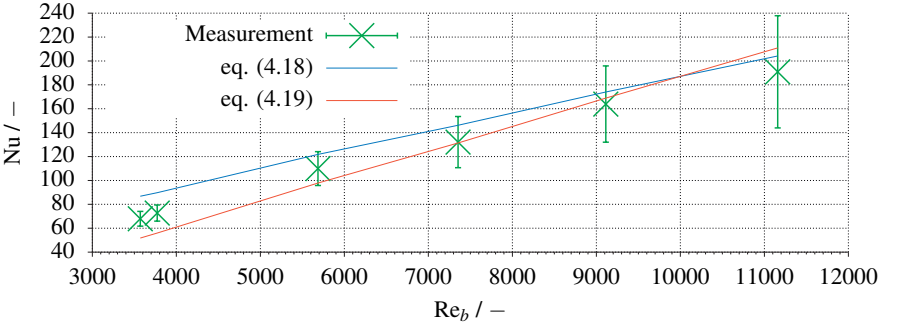

Figure 4.11: Nusselt number vs. bulk Reynolds number of measurement series M50

4.3.5 M60

Table 4.8: Parameters of measurement series M60

	T_{b_0}	T_{b_1}	T_w	$\dot{m}$	q_w	Re_b	Re_w	$\mathrm{Re}_{\tau,w}$	Pr_b	Pr_w	Nu	c_f
	K	K	K	$\mathrm{kg\,s^{-1}}$	$\mathrm{W\,m^{-2}}$	–	–	–	–	–	–	10^{-3}
1	370.05	386.35	393.65	0.335	18035	8189	9980	633	73	61	167	8.04
2	369.05	370.95	382.75	0.281	18106	6777	8547	554	74	60	142	8.40
3	366.95	369.25	383.05	0.248	18383	5769	7584	498	76	59	123	8.61
4	366.05	368.55	383.65	0.213	16930	4863	6576	437	77	59	103	8.84
5	365.45	368.30	386.02	0.176	15589	3995	5664	381	78	56	81	9.03

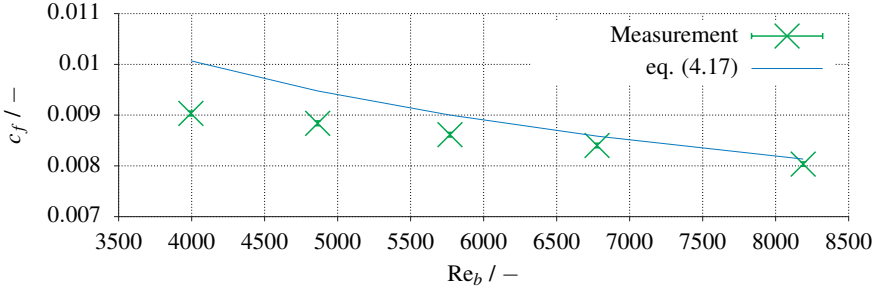

Figure 4.12: Skin-friction coefficient vs. bulk Reynolds number of measurement series M60

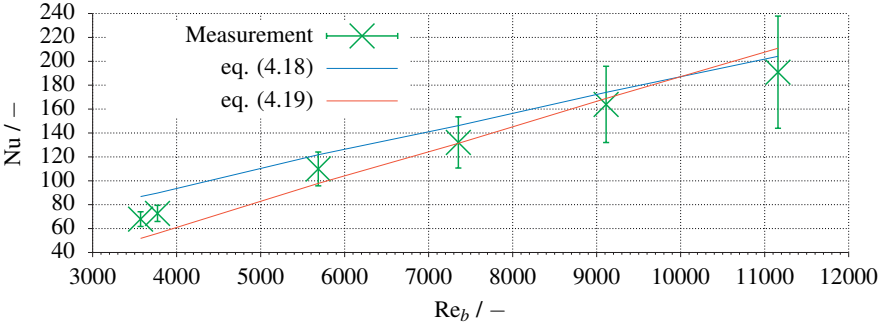

Figure 4.13: Nusselt number vs. bulk Reynolds number of measurement series M60

4.4 Discussion

Comparing the measured skin-friction coefficients to the Konakov (1954) correlation, as defined by equation (4.17), one can see that for low molecular Prandtl numbers the accordance is very good. With increasing Prandtl number the agreement gets worse, especially close to the laminar flow regime. Keeping in mind that the Konakov (1954) correlation was originally proposed for isothermal flow with constant fluid properties, the observed deviation in case of heating is still acceptable. Petukhov (1970) argued that due to the temperature difference between wall temperature and mean temperature, the reference temperature for the skin-friction as well as for the Nusselt number correlation needs to be adjusted. This adjustment should reflect the radial variation of the fluid properties, where the viscosity, due to its strong temperature dependency varies the most. Consequently, the bulk to wall viscosity ratio

$$K = \frac{\mu_b}{\mu_w} \tag{4.24}$$

is introduced to capture the effect of the variable properties. Figure 4.14 shows the variation of K dependent on the bulk Reynolds number for all measurement series. Due to the non-linear decrease of the viscosity with the temperature (see equation (2.114)), the ratio K is not only determined by the wall overtemperature, $T_w - T_b$, but also by the bulk temperature level T_b itself. This is exemplarily shown in figure 4.15 for the measurement cases M20/8 and M50/6, displaying the respective range of the radial viscosity variation.

The generally observed decrease of K with the bulk Reynolds number Re_b can be attributed to the increase of the Nusselt number for increasing Re_b. This increase in the Nusselt number is generally not compensated by a higher wall heat flux, so that the wall overtemperature, and hence, the span $\Delta\mu$ generally decreases, leading to a lower K. Accordingly,

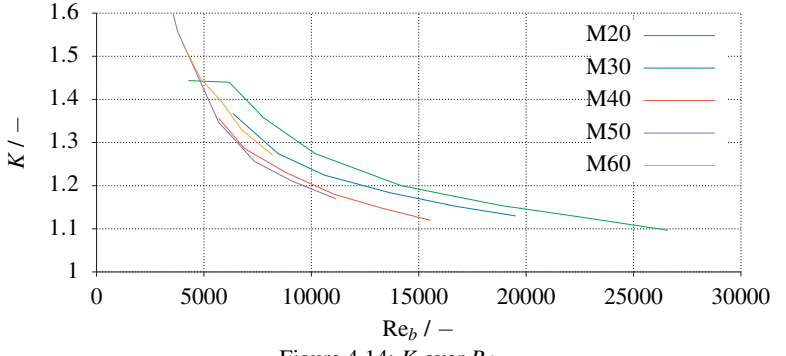

Figure 4.14: K over Re_b

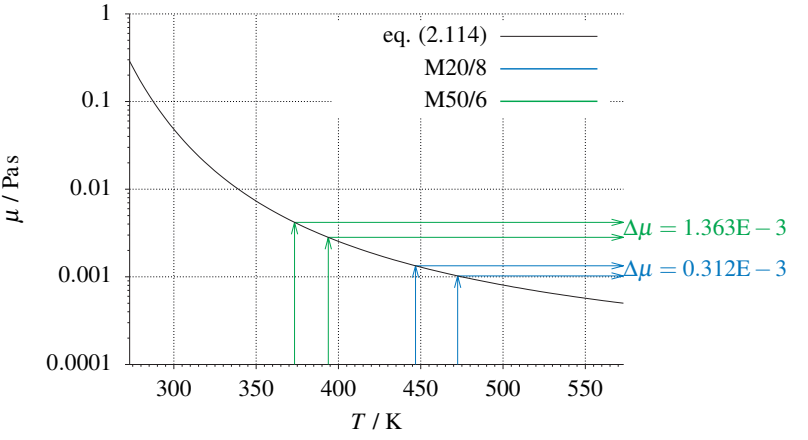

Figure 4.15: Temperature and viscosity ranges for the measurement cases M20/8 and M50/6

the highest K is observed for the measurement 6 of the M50 series, where in particular the overall fairly low temperature level results in a steep decrease in viscosity dependence on the temperature. The Nusselt number correlation of Gnielinski (1995) already uses the parameter K raised to some power in equation (4.18).

The validation of the present measurements against available data from previous measurements in literature of Morris and Whitman (1928) and Sherwood (1932) generally show good agreement. Comparing the present measurements with the Gnielinski (1995) Nusselt number correlation, it becomes evident that the linear superposition based Nusselt number correlation (4.19) tends to under-predict the heat transfer coefficient in the transition regime between laminar and turbulent flow. This under-prediction is also confirmed by a comparison against the measurements of Sherwood (1932). In the fully turbulent regime the measurements show a very good agreement with the correlation of Gnielinski (1995) (4.18), proposed for this regime. As already noted above, the fairly wide error margins in the measurements for the high Reynolds number are due the very low temperature difference between the wall and bulk temperature in these cases.

5 DNS ANALYSIS

This chapter is devoted to an in-depth analysis of the DNS data. At the beginning all simulation cases are listed together with the corresponding simulation meshes, which is followed by a discussion of the quality of the resolution. A major part of the chapter shall analyze the effect of real fluid behavior by comparing the DNS data of the constant fluid property simulations (DC) with the variable fluid property simulations (DV). Furthermore, the DNS data are compared with corresponding measurements, shown in section 4.3, in order to evaluate the simulation results.

For convenience, the discussion of the results does not always include a graphical presentation of all available data sets. These not included diagrams can be found in the appendix A.

5.1 DNS cases

The following tables show all computationally investigated cases, with their corresponding Reynolds number, Prandtl number, and the employed computational grid. Wall conditions are chosen as reference conditions for the friction velocity w_τ and friction temperature T_τ. Table 5.1 lists all cases with constant fluid properties and table 5.2 all cases with real temperature-dependent fluid properties.

Table 5.1: DNS simulations with constant fluid properties

	$\mathrm{Re}_{\tau,w}(\mathrm{Re}_b)$	Pr_w	Number of grid cells ($i_{max} \times j_{max} \times k_{max}$)
DC360/10	360(5275)	10	$256 \times 512 \times 1024$
DC360/20	360(5275)	20	$256 \times 512 \times 1024$
DC360/50	360(5275)	50	$256 \times 512 \times 1024$
DC500/10	500(7680)	10	$256 \times 512 \times 1024$
DC500/20	500(7680)	20	$256 \times 512 \times 1024$

For the constant fluid property cases, two Reynolds number $\mathrm{Re}_{\tau,w} = 360/500$ were considered in order to highlight the effect of the Reynolds number. The variation of the molecular Prandtl number from $\mathrm{Pr}_w = 10$ up to $\mathrm{Pr}_w = 50$ is intended to study the influence of an increasing thermal resistance near the wall.

Table 5.2: DNS simulation cases with real fluid properties

	$\mathrm{Re}_{\tau,w}(\mathrm{Re}_b)$	Pr_w	Number of grid cells ($i_{max} \times j_{max} \times k_{max}$)
DV370/21	370(4152)	21	$256 \times 512 \times 1024$
DV360/50	360(3557)	50	$256 \times 512 \times 1024$
DV520/20	519(6311)	20	$256 \times 512 \times 1024$

The input data for the real fluid cases are chosen so as to represent real measurement cases, as shown in section 4.3. In consistence with the cases for constant fluid properties, two different friction Reynolds numbers are considered associated with $\mathrm{Re}_{\tau,w} \approx 360/500$, to examine the influence of varying flow velocities. The measurement cases which actually correspond to the present DNS cases for variable fluid properties, are shown in table 5.3, including the reference quantities based on the experimental conditions.

Table 5.3: DNS simulation cases with real fluid properties and corresponding experimental cases

	Measurement case	$T_{ref} = T_w$	w_τ	T_τ
		K	$\mathrm{m\,s^{-1}}$	K
DV370/21	M20(8)	472.5	0.0419	0.1948
DV360/50	M50(6)	393.9	0.1053	0.0789
DV520/20	M20(7)	477.3	0.0564	0.2257

5.2 Resolution

All presently discussed simulations are done on a mesh with the same number of cells. Regardless of the input parameters shown in table 5.3, the radial cell size measured in wall units y^+, defined as

$$y^+ = \frac{y\, w_\tau}{\nu_w}, \tag{5.1}$$

was set to $\Delta y^+|_{wall} = 0.05$ and $\Delta y^+|_{center} = 0.4$, at the wall and the center, respectively, for all considered cases. Table 5.4 gives an overview over the minimum and maximum cell sizes for the individual directions, for the two most critical cases regarding Kolmogorov and Batchelor scale. These are the case with the highest Reynolds number and the case with the highest Prandtl number, DV520/20 and DV360/50, respectively.

The grid resolution was chosen in order to fulfill the DNS requirements for capturing suitably the smallest structures, measured by the Kolmogorov- and Batchelor- length scale,

Table 5.4: Mesh resolution for the two most critical cases

	Δr^+_{min}	Δr^+_{max}	$(r^+\Delta\varphi)_{max}$	Δz^+_{max}
DV360/50	0.05	1.375	2.207	1.756
DV520/20	0.05	2.180	3.187	2.536

defined in equations (2.17) and (2.18), respectively. Aside of the kinematic viscosity and the molecular Prandtl number, both length scales depend on the turbulent dissipation rate ϵ_{ii} of the turbulent kinetic energy $k = \overline{u_i'' u_i''}/2$, which can be obtained according to equation (2.31) based on the statistically averaged DNS velocity fluctuation, as

$$\epsilon^+_{ii} = -\overline{\tau'^+_{ik} \frac{\partial u_i''^+}{\partial x^*_k}}. \tag{5.2}$$

Figure 5.1 shows the radial profiles of the spatial resolution rescaled by these two length scales, for the most critical cases. Table 5.5 lists the occurring numerical minimum and maximum values.

Table 5.5: Minima and maxima of spatial resolution normalized with η and η_θ

	DV360/50	DV520/20
$\frac{\Delta r^+_{min}}{\eta}$	0.029	0.031
$\frac{\Delta r^+_{max}}{\eta}$	0.443	0.608
$\frac{(r^+\Delta\varphi)_{max}}{\eta}$	1.267	1.913
$\frac{\Delta z^+_{max}}{\eta}$	1.008	1.522
$\frac{\Delta r^+_{min}}{\eta_\theta}$	0.205	0.141
$\frac{\Delta r^+_{max}}{\eta_\theta}$	3.126	2.759
$\frac{(r^+\Delta\varphi)_{max}}{\eta_\theta}$	8.933	8.681
$\frac{\Delta z^+_{max}}{\eta_\theta}$	7.110	6.907

The chosen grid spacing appears as adequate to resolve the smallest near-wall turbulent structures. The radial variations shown in figure 5.1, make further evident that the spatial

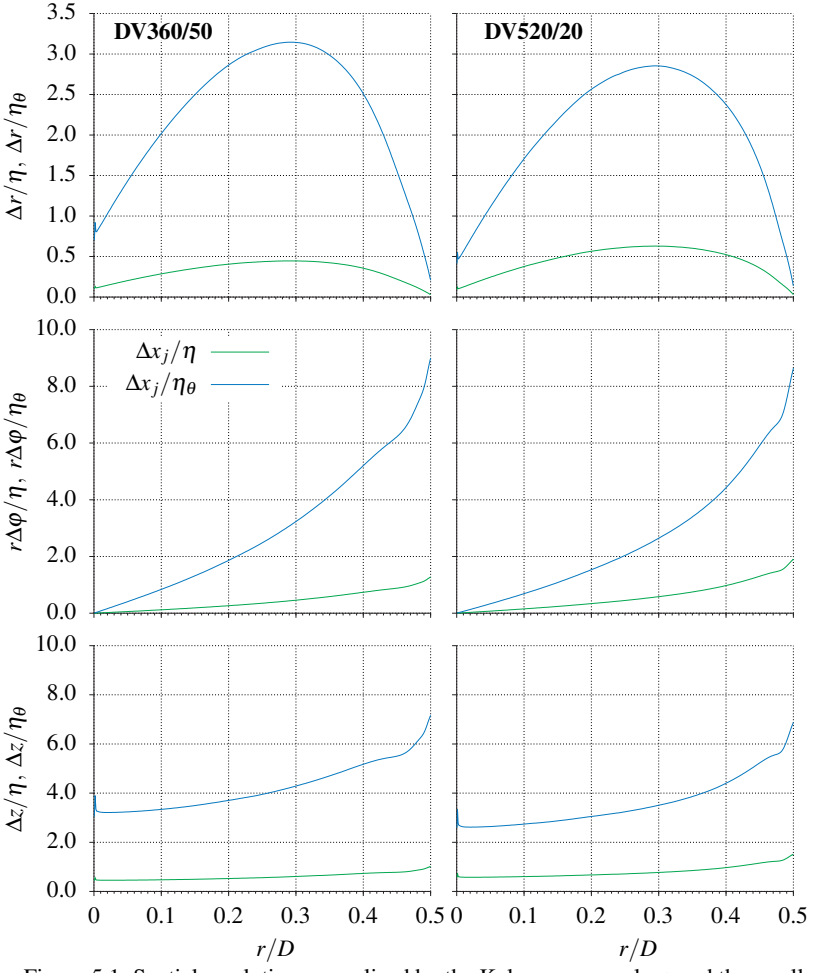

Figure 5.1: Spatial resolution normalized by the Kolmogorov scale η and the smallest turbulent thermal length scale η_θ

resolution for the dynamic and thermal structures remains sufficiently high over the whole cross-section. As such, the present resolution closely matches that of other recent DNS studies, such as of Zonta et al. (2012), Nemati et al. (2016) and Lee et al. (2013). The latter of these three applied a resolution, associated with $0.599 < \Delta y/\eta_\theta < 2.98$ in wall normal, $\Delta z/\eta_\theta = 7.91$ in span-wise and $\Delta x/\eta_\theta = 12.4$ in stream-wise direction, which is

well comparable to the present resolution.

5.3 First-order turbulence statistics

The here presented data is statistically averaged in space, along the two homogeneous directions, φ and z, as well as in time. For the latter, 30 flow-through times, defined as

$$t^*_{ftt} = \frac{L}{D\overline{w}^+_b}, \tag{5.3}$$

were employed as sampling period, once the solution was statistically converged. The statistical averages represent ensemble averages, as appearing in the Reynolds and Favre decompositions, shown in section 2.2.3. The Favre averages for the axial velocity and the enthalpy difference, discussed below, are in particular defined as

$$\widehat{w}^+ = \frac{\overline{\rho w^+}}{\overline{\rho}} \tag{5.4}$$

and

$$\widehat{\chi}^+ = \frac{\overline{\rho \chi^+}}{\overline{\rho}} \tag{5.5}$$

For the constant fluid property cases they are identical with the Reynolds averages $\overline{w}^+$ and $\overline{\chi}^+$, respectively.

In the presently considered flow associated with only minor density variations, the difference between the Reynolds and Favre averages are basically negligible. More importantly, turbulence models based on the Boussinesq eddy viscosity concept generally use Reynolds-averaged values. The reason for this is that this concept incorporates the turbulent stress tensor and a turbulent heat flux vector, as introduced in formulation (2.20) and (2.21) into the corresponding diffusive contribution, which involves only the gradients of Reynolds averaged quantities. Accordingly, all DNS data shown in the following are represented as Reynolds averages and the density fluctuation ρ' is assumed to be zero, which implies constant density independent of temperature fluctuation

$$\rho'\left(T'\right) \cong 0 \;\Rightarrow \rho = \overline{\rho} = \text{const.} \tag{5.6}$$

5.3.1 Velocity

In a first step, all obtained results need to be validated. Typically, this is done by comparing the DNS results to literature data. Especially, for the pipe flow at $\mathrm{Re}_{\tau,w} = 360$ there are various DNS data from previous isothermal studies available. On the other hand,

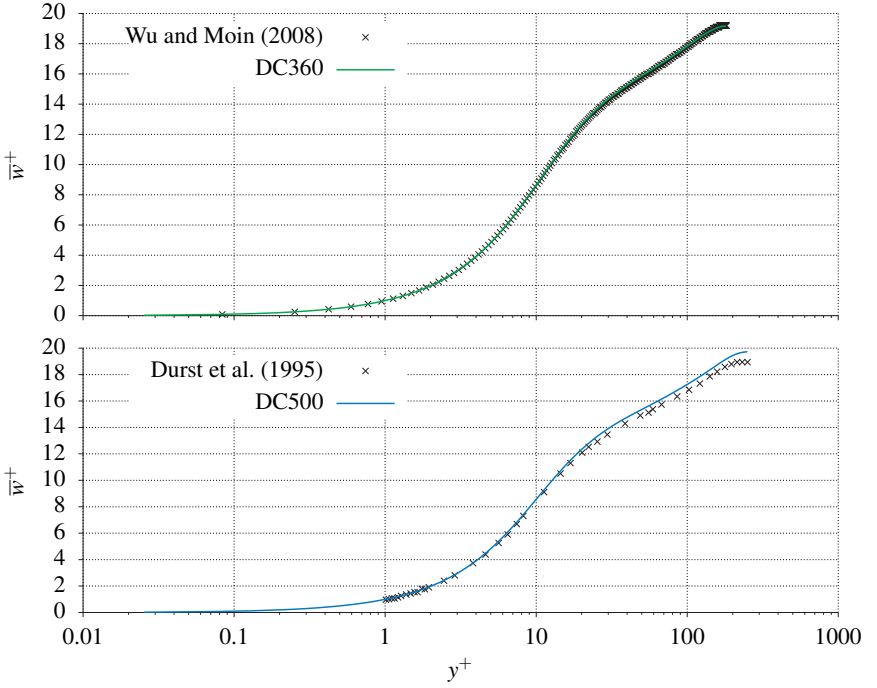

Figure 5.2: Comparison of the axial velocity to literature data

there exist only scarce validation data for high Prandtl number flows, especially including temperature-dependent fluid properties. For this reason, only the constant fluid properties cases are evaluated against literature data, while the DNS results for the variable fluid properties are validated against the in-house measurements presented in section 4. Concerning DNS data from literature, Wu and Moin (2008) published a highly resolved DNS of an isothermal pipe flow, providing accurate validation data for the case $\mathrm{Re}_{\tau,w} = 360$. The flow conditions of the second considered Reynolds number, $\mathrm{Re}_{\tau,w} = 500$, are covered by the experimental work done by Durst et al. (1995). Their LDA measurements consider an isothermal pipe flow case, at a moderate Reynolds number ($Re_b = 7442$), with an exceptional near-wall resolution.

The predicted axial variations for the average axial velocity are compared against the mentioned data from literature in figure 5.2. The agreement with the DNS data of Wu and Moin (2008) is excellent and only minor deviations are observed in the comparison of the

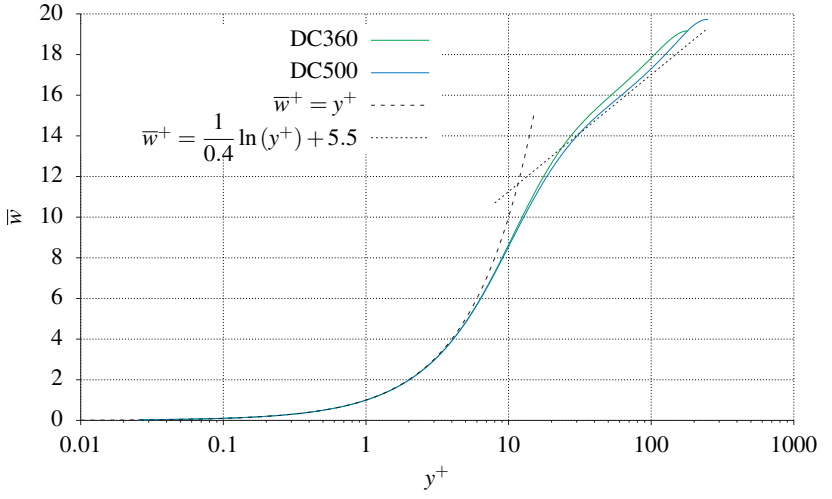

Figure 5.3: Axial velocity for the different Reynolds number of the DC cases

simulation data against the measurements. This confirms the accuracy of the simulation in predicting the first-order statistics of the velocity field.

It is noted that for the constant fluid property cases the conservation equations of momentum and heat are decoupled. The flow field therefore only depends on the Reynolds number, regardless of the considered Prandtl number. In contrast, in the variable fluid property simulations, the energy equation is coupled with the momentum transfer, through the temperature-dependent fluid properties, so that the velocity field depends both on Reynolds and Prandtl number.

As known from various previous studies, the presently considered turbulent pipe flow should be described very well by the universal wall laws. For this reason the axial velocity of cases DC360 and DC500 are compared to the universal wall laws in figure 5.3. The shown universal profiles read

$$\overline{w}^+ = y^+, \tag{5.7}$$

for the viscous sub-layer, and

$$\overline{w}^+ = \frac{1}{\kappa}\ln y^+ + \beta. \tag{5.8}$$

for the fully turbulent inertial sublayer, with the standard setting of $\kappa = 0.4$ and $\beta = 5.5$ suggested by Kays and Crawford (1980). Close to the wall, in the viscous sub-layer equation (5.7) reproduces the DNS results perfectly. Further remote from the wall, inside the

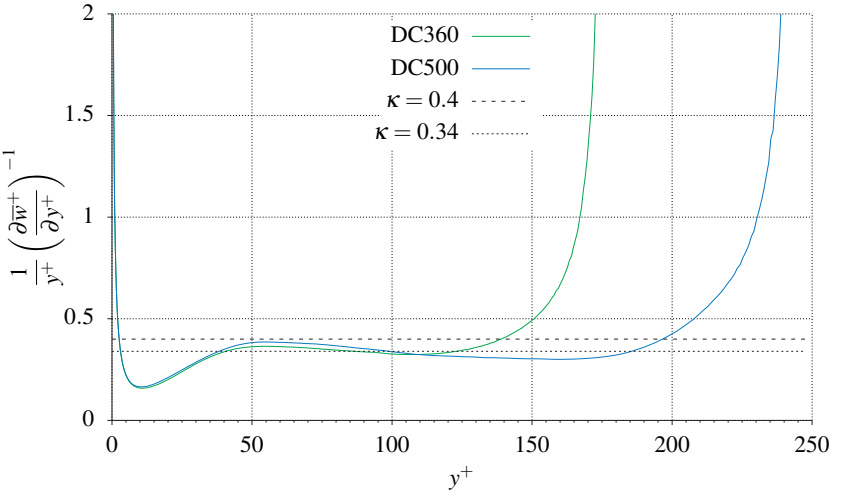

Figure 5.4: Variation of κ over the wall distance obtained by the the DNS results

inertial sub-layer, increasing deviations from the log-law can be perceived. However, with increasing Reynolds number, the deviations decrease. This tendency, which basically indicates a broadening of the inertial sub-layer with increasing Reynolds number and therefore widening the region, where the log-law is applicable, was already noted by Tennekes and Lumley (1972). DNS studies by Eggels et al. (1994) and Redjem-Saad et al. (2007) confirm this behavior. Additional confirmation gives the experimental study of Durst et al. (1998), which compares the axial velocity profiles of a fully developed turbulent plane channel flow for increasing Reynolds numbers.

The scope and the limits of the universal log-law (5.8) can be also measured by extracting the von Kármán constant from the DNS data. For this evaluation, equation (5.8) has to be derived with respect to y^+ and rearranged to isolate κ in terms of the expression

$$\kappa = \frac{1}{y^+}\left(\frac{\partial \overline{w}^+}{\partial y^+}\right)^{-1}. \tag{5.9}$$

Substituting the DNS data for the local axial velocity gradients into equation (5.9) results in the variations dependent on y^+ shown in figure 5.4.

It can be clearly seen that the standard setting $\kappa = 0.4$ suggested by Kays and Crawford (1980) differs from the DNS obtained plateau at $\kappa = 0.34$. This is due to the fairly low Reynolds numbers considered. This explanation is supported by the observed increase in

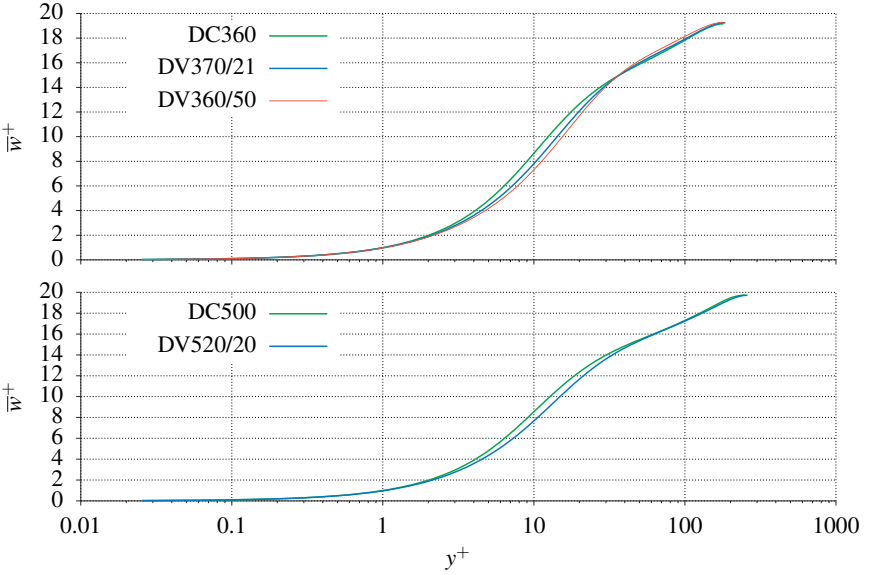

Figure 5.5: Variation of the axial velocities for the DC and the DV cases

the extracted value for the von Kármán constant inside the inertial sub-range for the case with the higher Reynolds number DC500 in figure 5.4.

In figure 5.5 the cases with temperature-dependent fluid properties are compared against the corresponding constant fluid property cases. The effect on the flow field due to fluid property variation is clearly seen here. At the wall, which represents the position of the reference state determining the reference quantities, the solution is expectedly the same for all cases. Inside the buffer layer, a substantial velocity decrease can be observed. For the case with the strongest variation of the fluid properties, seen from the highest value of T_τ in table 5.3, i.e., case DV360/50, a notable increase in velocity can be seen in the inertial sub-range.

5.3.2 Enthalpy and temperature

For the here considered high Prandtl number flows, no suitable literature data could be found for an evaluation of the thermal quantities predicted by the DNS. For this reason, table 5.6 compares the DNS results for the temperature difference of $T_w - \overline{T}_b$ against the corresponding data from the measurements described in section 4.

Table 5.6: Temperature difference comparison of the DNS results and the measurements

	$T_w - \overline{T}_b$	Discrepancy	
	K	K	%
DV370/21	26.02	0.42	1.64
M20(8)	25.60		
DV360/50	20.14	-0.36	-1.76
M50(6)	20.50		
DV520/20	26.97	0.89	3.38
M20(7)	26.09		

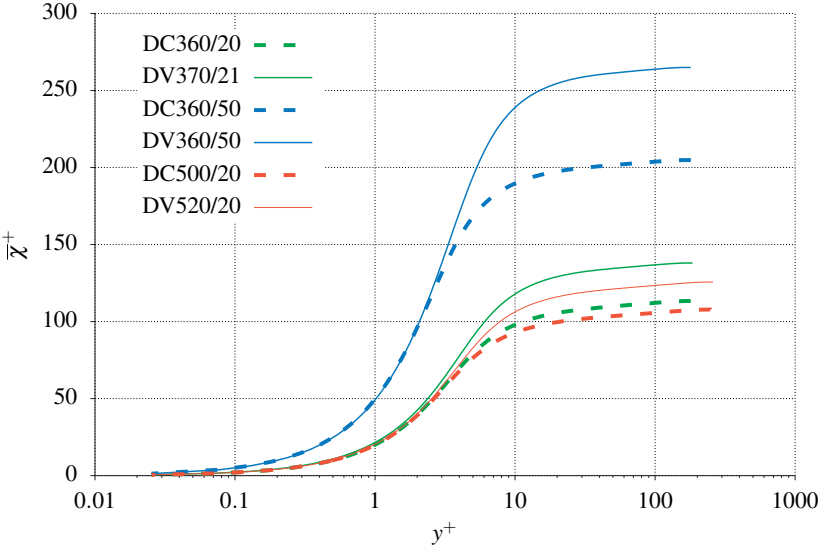

Figure 5.6: Variation of the enthalpy for the DC and the DV cases

The fairly small discrepancies shown in table 5.6 attests a high accuracy in the present DNS data. The fact, that the highest considered Reynolds number (case DV520/20) exhibits a by more than two times higher deviation than the other two cases, is also not very concerning. At a later point in this thesis, where comparing the Nusselt numbers, it will be seen that this deviation is still within the measurement error, which tends to be larger for increasing Reynolds numbers, as seen in section 4.3.

Figure 5.6 shows the DNS results (DV and DC cases) of the non-dimensional enthalpy $\overline{\chi}^+$ plotted over the wall distance y^+.

Owing to the constant specific heat capacity in the DC cases, the non-dimensional enthalpy χ^+ is identical with the non-dimensional temperature θ^+. The transition into almost straight lines heading towards the center indicates the formation of an inertial log-law sub-layer. Due to the effect of varying fluid properties, in particular the increase of the local viscosity towards the center, an considerable increase in the predicted level of the enthalpy in the inertial sub-layer is seen for all DV cases.

In order to highlight the increase in thermal resistance near the wall with increasing molecular Prandtl number, the data shown in figure 5.6 is plotted again in a double logarithmic axis scaling in figure 5.7

In general, with increasing Prandtl number the thermal resistance increases, which goes hand in hand with an increasing enthalpy gradient at the wall. This general trend is clearly visible for both the DC and the DV cases in figure 5.7. Regarding the DV cases, the wall value of the Prandtl number is imposed from the reference conditions, yet, due to the decreasing temperature towards the center, the local molecular Prandtl number increases. Therefore, the thermal resistance for the DV cases becomes higher than that for the DC cases in the core region.

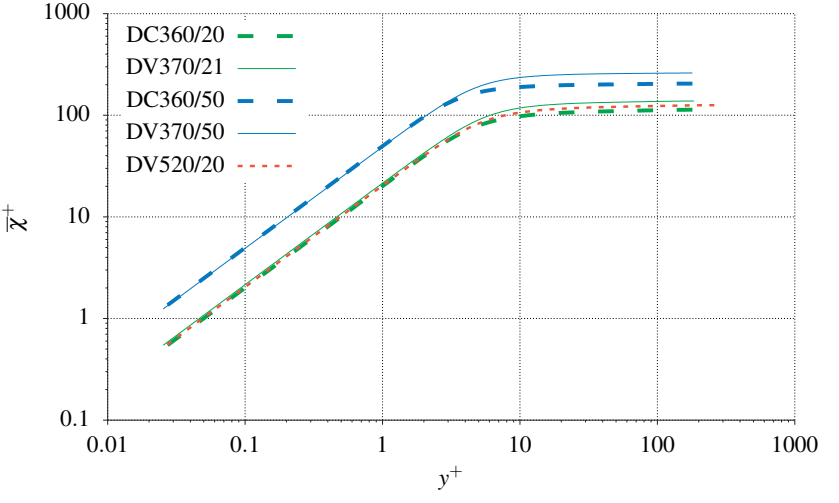

Figure 5.7: Variation of the enthalpy for the DC360 cases and all DV cases

The effect of the Reynolds number on the wall temperature gradient is evidently of minor importance, as seen from the red dotted line, representing a case with Prandtl number $\mathrm{Pr}_w \approx 20$ at a higher Reynolds number.

5.3.3 Averaged fluid properties

Using the temperature variation, which corresponds to the enthalpy variations shown in figure 5.6, the fluid properties can be evaluated and plotted over the wall distance. Figure 5.8 displays ρ^*, c_p^*, λ^* and μ^* for all considered DV cases.

As already indicated in the discussion for the dependence of material properties on the temperature in section 2.5, the radial variation of ρ^*, c_p^* and λ^* remains less than 5% for

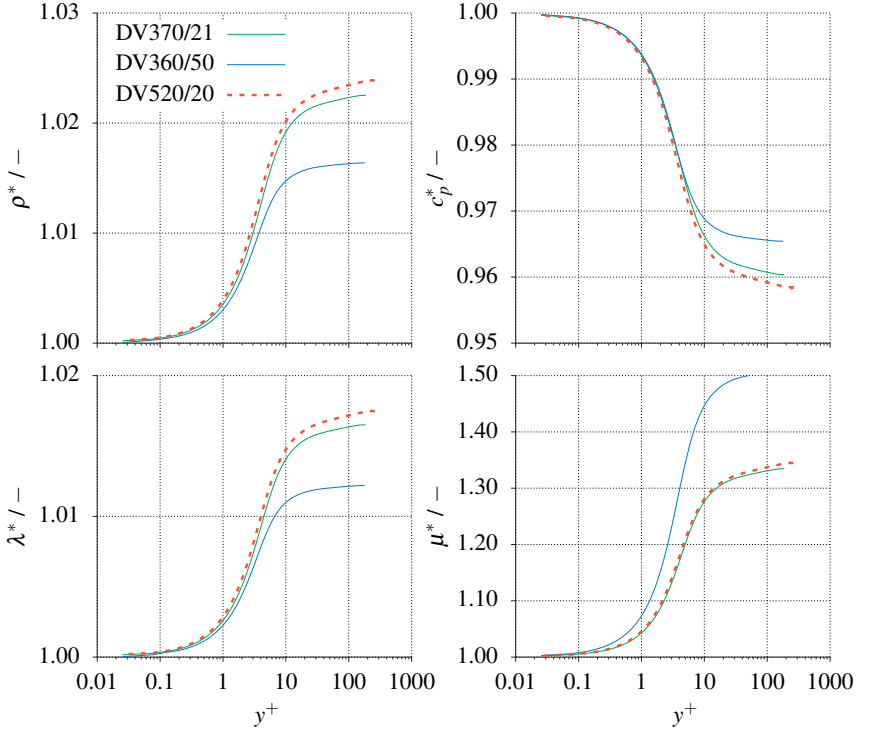

Figure 5.8: Variation of fluid properties vs. y^+

all cases, justifying the neglection of density fluctuations. In contrast, the viscosity varies up the almost 50%. Although the wall overtemperatures listed in table 5.6 show higher values of $T_w - \overline{T}_b$ for $\mathrm{Pr}_w = 20$, the corresponding DNS solution still exhibit less variation of viscosity than the case with $\mathrm{Pr}_w = 50$. This behavior is due to the slower decrease of the viscosity at higher temperature levels, which applies to the cases with $\mathrm{Pr}_w = 20$. This was already illustrated in figure 4.15, plotting the relevant viscosity ranges over the underlying temperature ranges. The influence of the Reynolds number variation is relatively low, which can be seen from the red-dotted line compared against the green line in figure 5.8.

The observed variations of the material properties, predominantly that of the viscosity, cause considerable variations in the radial distribution of the dimensionless parameters $\mathrm{Re}_{\tau,w}$ and Pr_w. Figure 5.9 shows their radial variation over the wall distance. For the constant fluid property cases, the prescribed wall values remain constant over the whole cross-section, whereas, for the DV cases, the Reynolds number decreases, and the Prandtl

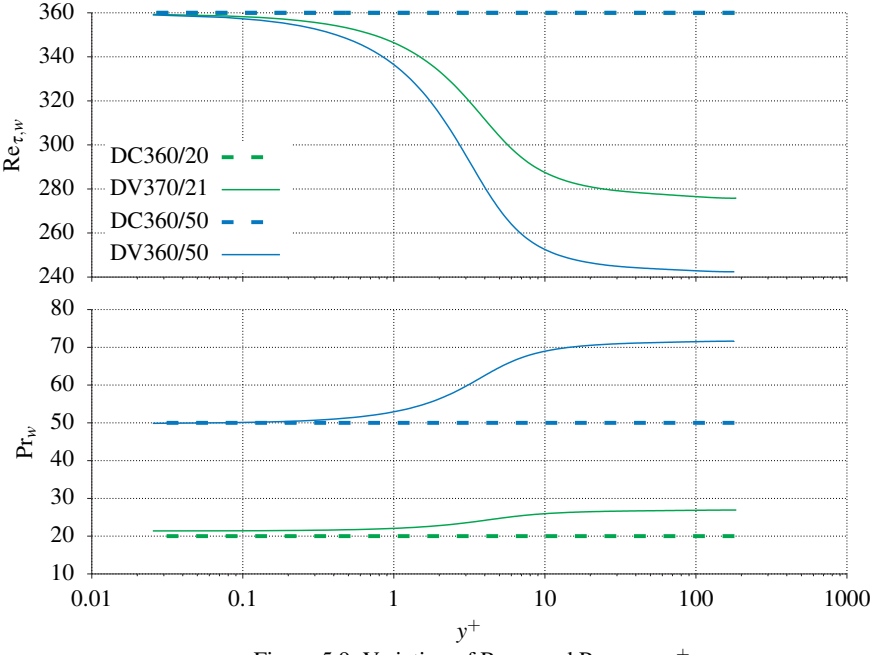

Figure 5.9: Variation of $\mathrm{Re}_{\tau,w}$ and Pr_w over y^+

number increases towards the center, which essentially reflects the variation of the viscosity shown in figure 5.8.

The shown radial variation of $\mathrm{Re}_{\tau,w}$ and Pr_w for the DV cases are useful to interpret the observed deviations in the velocity and enthalpy profiles from the corresponding DC cases. Especially the increasing Prandtl number with the associated increasing thermal resistance explains the higher level of the enthalpy, which is reached in the core region for the DV cases, as seen in figure 5.6. For a more detailed insight into the effect of the temperature-dependent real fluid properties on the momentum and heat transport, further analysis of the higher-order turbulence statistics is needed. This will be discussed in the following.

5.4 Higher-order turbulence statistics

This chapter will discuss the turbulent second-order moments obtained from the DNS data, examining in particular the differences observed for the variable fluid property cases in comparison to the constant property cases. The second-order moments and turbulence intensities are dependent on the radial position, $r = r_i$, and are computed as the statistical averages over the homogeneous directions (azimuthal j, axial k), and time t, generally written as

$$\overline{\varphi'\psi'}_i = \langle \left(\varphi_{ijk,t} - \overline{\varphi}_i\right) \left(\psi_{ijk,t} - \overline{\psi}_i\right) \rangle_{j,k,t} \tag{5.10}$$

and

$$\psi_{i,rms} = \langle {\psi'_{ijk,t}}^2 \rangle^{1/2}_{j,k,t} = \langle \left(\psi_{ijk,t} - \overline{\psi}_i\right)^2 \rangle^{1/2}_{j,k,t} \tag{5.11}$$

respectively.

5.4.1 Velocity fluctuations

Since no suitable data from literature is available to validate the DV cases, only the predictions from the DC cases shall be validated against previous DNS and experiments. Figure 5.10 compares the DNS results of the DC360 and DC500 against the corresponding data of Wu and Moin (2008) and Durst et al. (1995), respectively.

The agreement with both the simulation data and the experimental data is very good. Some deviations are seen for the case DC500. This is most probably due to the slightly higher Reynolds number ($\mathrm{Re}_b = 7680$) of the presently performed DNS compared to $\mathrm{Re}_b = 7442$, as considered in the experiments by Durst et al. (1995). Apart form that, the general shape of the profiles is predicted very well. Comparing the velocity fluctuations for the two different Reynolds numbers, it is remarkable that the axial turbulence intensity hardly depends on the Reynolds number. The peak of w^+_{rms} remains at same magnitude and position. For the intensities in the two other directions, the magnitude of the peak increases and shifts

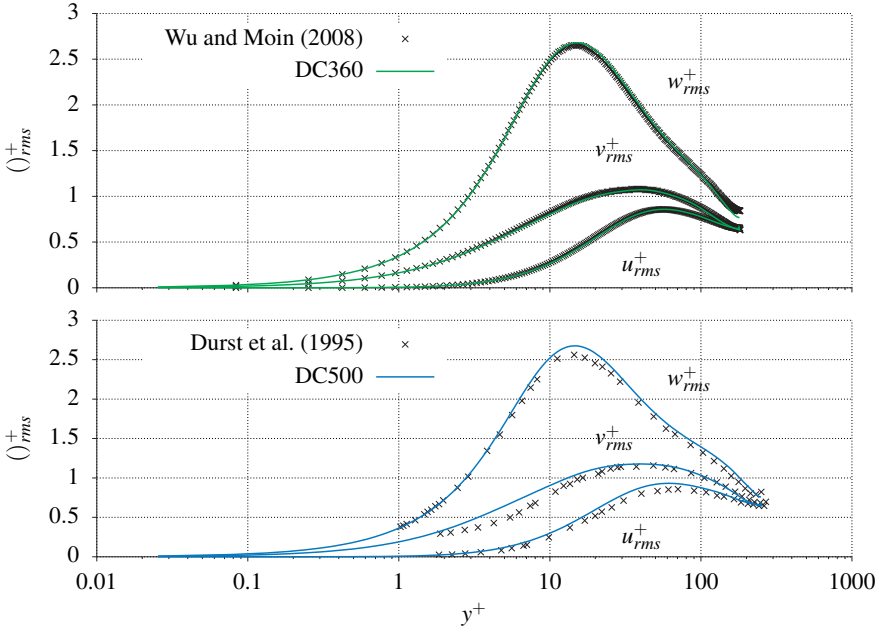

Figure 5.10: Comparison of u_{rms}, v_{rms} and w_{rms} of the DC360 and DC500 cases

towards the center of the pipe, for increasing Reynolds number. Durst et al. (1995) showed exactly this behavior in their LDA measurements.

In figure 5.11 the turbulence intensities of the DV cases are compared against the corresponding DC case. Since the tendencies for the different Reynolds numbers are practically identical, only the cases with $\mathrm{Re}_{\tau,w} = 360$ are shown and discussed in the following. The case with the higher Reynolds number can be found in the appendix A. The radial and azimuthal components of the rms-fluctuation for the DV cases generally decrease in magnitude, which is expected considering the decreasing Reynolds number, seen in figure 5.9. Following from the remarks in the validation against experiments above, it would have also been expected that the peak of the radial and azimuthal turbulence intensities would move towards the wall, as the Reynolds number decreases. However, the shift for all fluctuations goes into the opposite direction.

One way to address this issue is to consider that a reduction of the local Reynolds number basically implies an reduced normalized wall-distance relative to the definition $y^+ = yw_\tau/\nu_w$, based on the wall conditions where $\nu = \nu_w$. Representing the local flow condi-

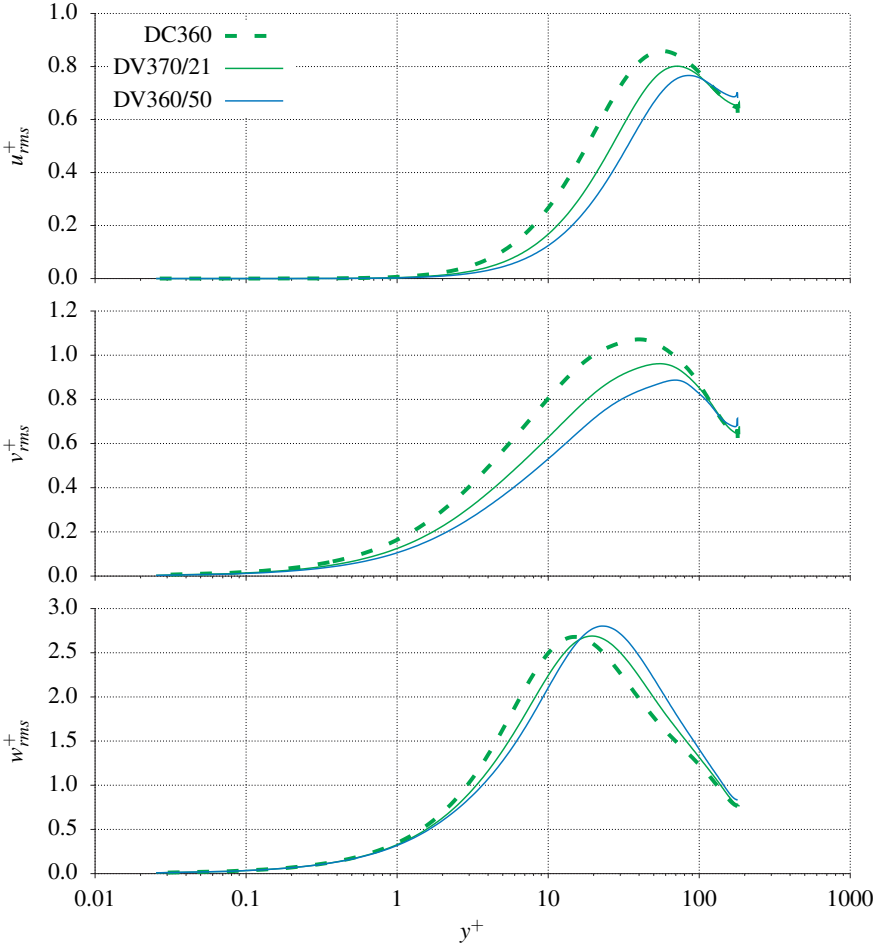

Figure 5.11: Variation of u^+_{rms}, v^+_{rms} and w^+_{rms} over the wall distance for the cases with $\mathrm{Re}_{\tau,w} = 360$

tions dependent on the localized wall distance $y^* = y w_\tau / \nu = y^+ \nu_w / \nu$, based on the local viscosity ν, would effectively shift all flow components towards the wall. However, it can be clearly seen that the variation of the fluid property not just causes a shift of the quantities towards the center of the pipe. It also causes a change in their magnitude, which cannot

be compensated by just rescaling the wall distance y^+. For this reason Patel et al. (2015) proposed a semi-local scaling for the velocity, which will be discussed in full detail later in this chapter.

5.4.2 Shear stress

In a fully turbulent, statistically stationary, axially symmetric pipe flow, the total shear stress, obtained as the component $\overline{\tau}_{13} = \tau_{tot}$ based on equation (2.22), consists of a laminar and a turbulent component, given as

$$\tau_{tot} = \underbrace{\overline{\mu}\frac{\partial \overline{w}}{\partial r}}_{\tau_{lam}} + \underbrace{\overline{\mu'\frac{\partial w'}{\partial r}}}_{\tau_{\mu}} \underbrace{-\rho\overline{u'w'}}_{\tau_{turb}} \cong (\overline{\mu} + \mu_T)\frac{\partial \overline{w}}{\partial r} \tag{5.12}$$

where the turbulent contribution is computed analogously to its viscous counterpart, applying the Boussinesq eddy viscosity concept

$$-\rho\overline{u'w'} = \mu_T \frac{\partial \overline{w}}{\partial r}. \tag{5.13}$$

Recast into wall coordinates, the total shear stress finally reads

$${\tau_{tot}}^+ = \frac{\tau_{tot}}{\tau_w} = -\overline{\mu}^* \left(1 + \frac{\mu_T}{\overline{\mu}}\right) \frac{\partial \overline{w}^+}{\partial y^+}. \tag{5.14}$$

The term τ_μ appears in (5.12) due to the fluctuation of the fluid properties, yet is of minor importance, and can therefore be neglected.

Figure 5.12 displays the total shear stress, as given by equation (5.12), together with the laminar and turbulent contributions, as well as the underlying shear rate. The insignificant contribution due to the variation of the fluid properties represented by τ_μ is not included.

As shown in section 2.4.3, in a statistically stationary fully developed turbulent pipe flow, the total shear stress varies always linearly with the wall distance, regardless of any variation of the fluid properties.

The laminar contribution τ^+_{lam}, shown in sub-figure (A) is increased in the buffer layer for the DV cases due to the increasing viscosity towards the center. Since the laminar shear stress depends on the viscosity as well as the shear rate, reading

$$\tau^+_{lam} = \overline{\mu}^* \frac{\partial \overline{w}^+}{\partial r^*}, \tag{5.15}$$

the variation of the latter, shown in sub-figure (B) has to be also considered in the interpretation of the magnitude of τ^+_{lam}. At the wall, which represents the reference point, all cases

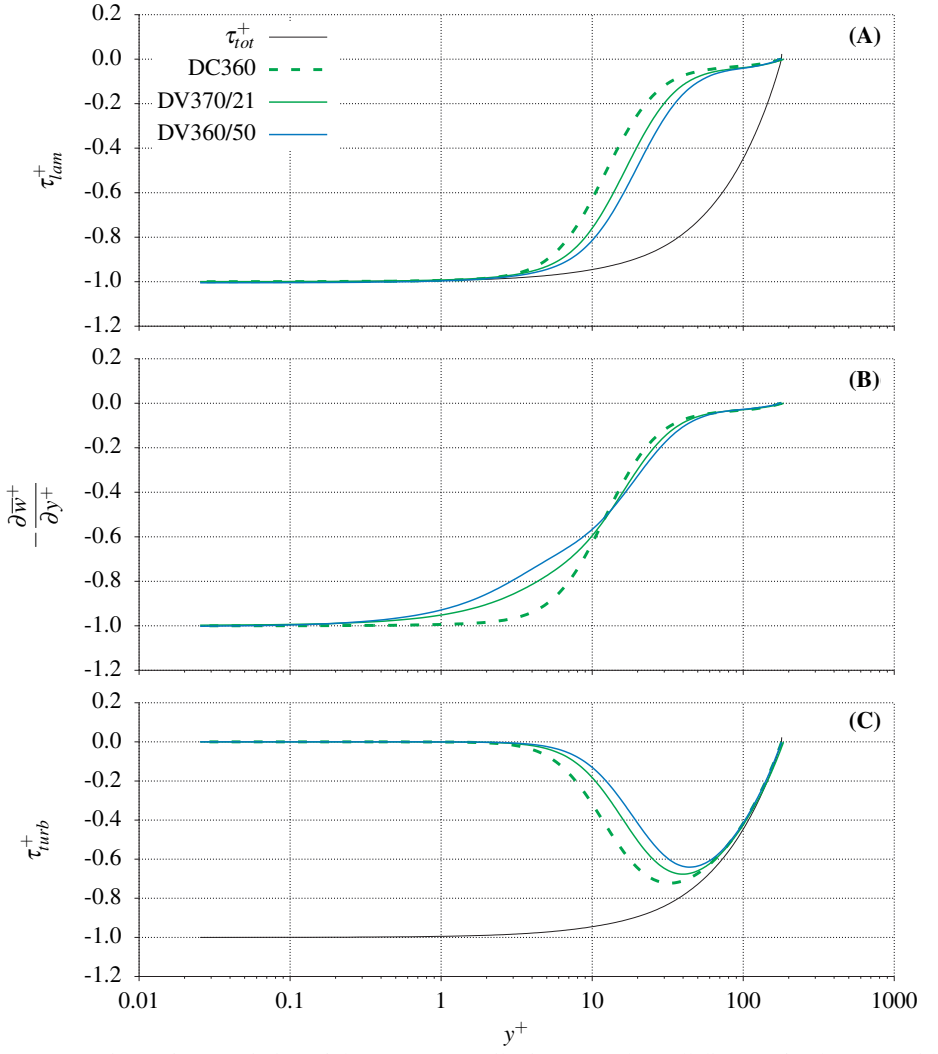

Figure 5.12: Variation of shear stress contributions over the wall distance for the cases with $\mathrm{Re}_{\tau,w} = 360$

have to show the same value as expected. Towards the center, the shear rate is significantly reduced for the DV cases. This decrease is evidently overcompensated by the substantial increase in viscosity, as shown in figure 5.8, resulting in a higher value of τ^+_{lam} for the DV cases. Close to the center, the shear rate of the DV cases exceeds that of the DC cases, so that both components in (5.15) show the same increasing tendency for the DV cases.

Sub-figure (C) shows the turbulent contribution to the total shear stress. Its behavior is complementary to that of τ^+_{lam}. Near the wall, the decreased shear rate, producing less intense turbulent mixing, combined with the increased viscosity, results in a reduction of turbulent shear stress, leading to a lower peak of τ^+_{turb}. In the following, the phenomena, which govern the budget of the turbulent and laminar stresses will be analyzed in detail.

Instantaneous turbulence coherent structures

The dynamics of turbulent coherent structures and their modification due to the influence of real fluid behavior are important for possible modeling purposes. Of special interest are bursting events, like sweep and ejection events, because alterations of these events have a major impact on the turbulent shear stress, and hence, the modeling of these. Wallace et al. (1972) proposed a quadrant analysis to identify fractional contributions to $\rho^* \overline{u'^+ w'^+}$. For this purpose, the fluxes were conditionally averaged, classifying them into four categories:

- Q1: $(-u'^+, +w'^+)$ are outward interactions, where streamwise motion moves from the wall to the center
- Q2: $(-u'^+, -w'^+)$ are ejection events, where counter-streamwise motion moves from the wall to the center
- Q3: $(+u'^+, -w'^+)$ are inward interactions, where counter-streamwise motion and hot fluid moves toward the wall
- Q4:$(+u'^+, +w'^+)$ are sweep events, where streamwise motion moves toward the wall

Ejection (Q2) and sweep (Q4) are gradient-type events, which means their motion is in favor of the mean streamwise velocity gradient, whereas Q1 and Q3 are counter gradient-type events.

Figure 5.13 shows the absolute fractional contributions to the turbulent shear stress. Ejection and sweep contribution make up for most part of the shear stress. Near the wall for all contributions, the variable fluid property case produces smaller values than the constant fluid property case, yet the reduction is larger for the sweep and ejection events, which have a positive contribution to the total value. The reason of this lower levels of turbulent velocity fluctuations, is the increased damping due to the increased viscosity for the

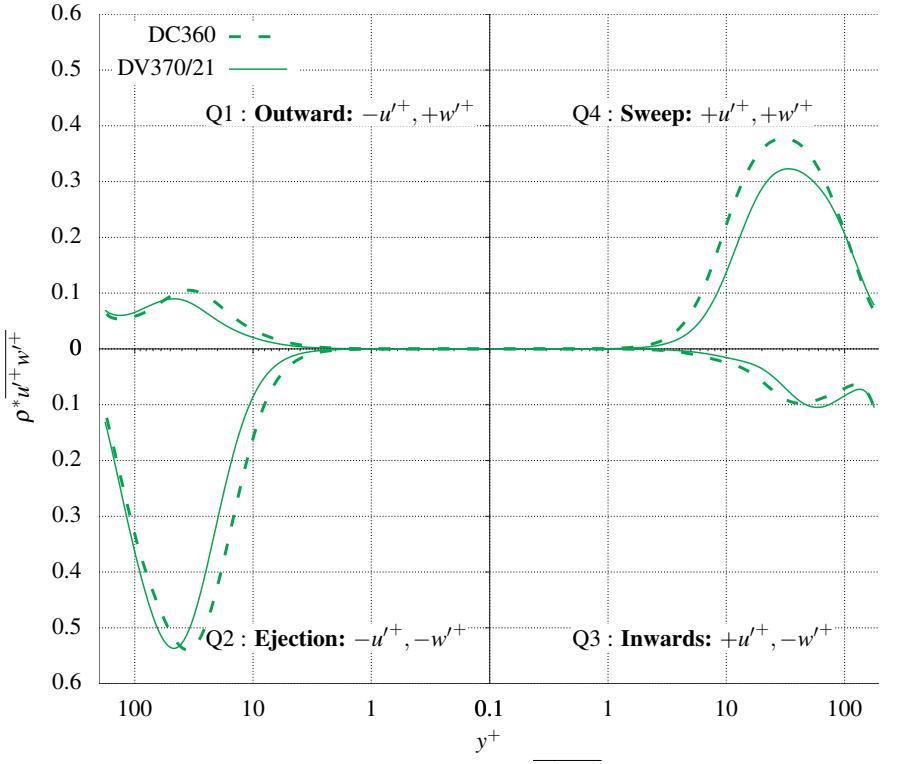

Figure 5.13: Fractional contributions to $\rho^* \overline{u'^+ w'^+}$ for DC360 and DV370/21

DV cases. Aside from the reduction in amplitude, a general shift towards the center in all quadrants is noticeable.

5.4.3 Turbulent kinetic energy

The turbulent kinetic energy per unit mass contained in the fluctuating velocity components represents a very important measure for total intensity of the turbulent motion. Based on the general definition shown in equation (2.13) the turbulent kinetic energy is computed from the previously shown turbulence intensities, as

$$k^+ = \frac{1}{2} \overline{u_i'^+ u_i'^+} = \frac{1}{2} \overline{u'^{+2} + v'^{+2} + w'^{+2}}. \tag{5.16}$$

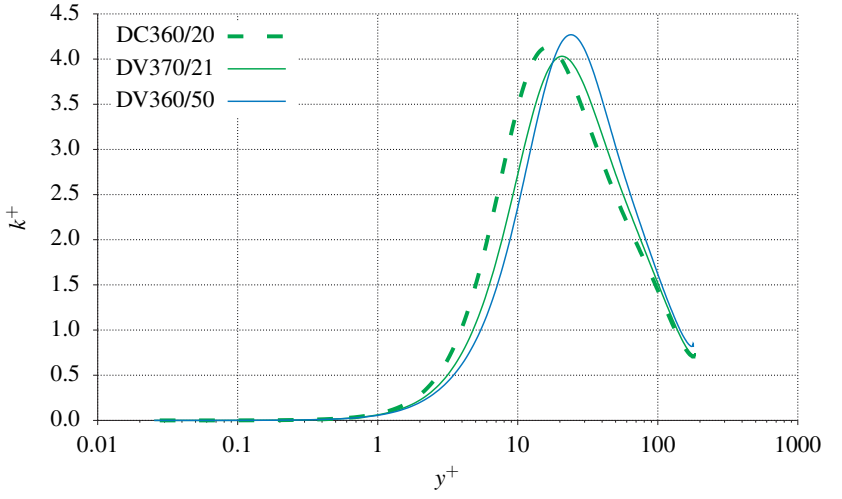

Figure 5.14: Variation of the turbulent kinetic energy over the wall distance for the $\mathrm{Re}_{\tau,w} = 360$ cases

Figure 5.14 displays the variation of k for the $\mathrm{Re}_{\tau,w} = 360$ cases. As expected, the turbulent kinetic energy for the variable fluid properties varies in consistence with the observations on the previously discussed components.

Turbulent kinetic energy budgets

The budget of the turbulent kinetic energy is determined by the individual sources, sinks, and transfer terms appearing in the Reynolds stress transport equations (2.24), contracted for the normal component, written as

$$\frac{1}{2}\frac{\partial \rho \overline{u_i' u_i'}}{\partial t} = \frac{\partial \rho k}{\partial t} = \underbrace{-\frac{1}{2}\frac{\partial \overline{u}_j\, \rho k}{\partial x_j}}_{C_k}$$
$$\underbrace{-\rho \overline{u_i' u_k'}\frac{\partial \overline{u}_i}{\partial x_k}}_{P_k} \underbrace{-\frac{1}{2}\frac{\partial \rho \overline{u_j' u_i' u_i'}}{\partial x_j}}_{T_k} \underbrace{-\frac{\partial \overline{p' u_i'}}{\partial x_i}}_{\Pi_k} + \underbrace{\frac{\partial \overline{\tau_{ij}' u_i'}}{\partial x_j}}_{D_k} \underbrace{-\overline{\tau_{ij}' \frac{\partial u_i'}{\partial x_j}}}_{\epsilon_k}. \tag{5.17}$$

As stated above in section 5.3, the density fluctuations are assumed to be zero, hence the contributions of Ψ_k and E_k vanish.

The following discussion examines in particular the case DV370/21 as representative for all DV cases, compared against its counterpart with constant material properties DC360/20. Figure 5.15 shows all contributions to the k budget, appearing on the rhs of equation (5.17). Near the wall all contributions are reduced for the DV case. Additionally, the viscous diffusion D_k and the turbulent diffusion T_k, are shifted towards the center due to the increasing viscosity. By far the greatest difference can be seen in the dissipation ϵ_k and production P_k. The dissipation is notably reduced up to a wall distance of $y^+ \approx 30$ and then remains approximately at the same value as for the DC cases. The production decreases inside the buffer layer around $y^+ \approx 10$, so that its peak is considerably shifted towards the center. By comparing the total alteration between the DC and the DV cases, it becomes evident that near the wall, the turbulent kinetic energy is reduced. However, due to the shift towards the wall, the contributions of D_k, T_k and P_k show higher values starting beyond $y^+ \approx 20$, resulting in a higher k, as seen in figure 5.14.

In order to further investigate the effect of the variable fluid properties on the budgets of

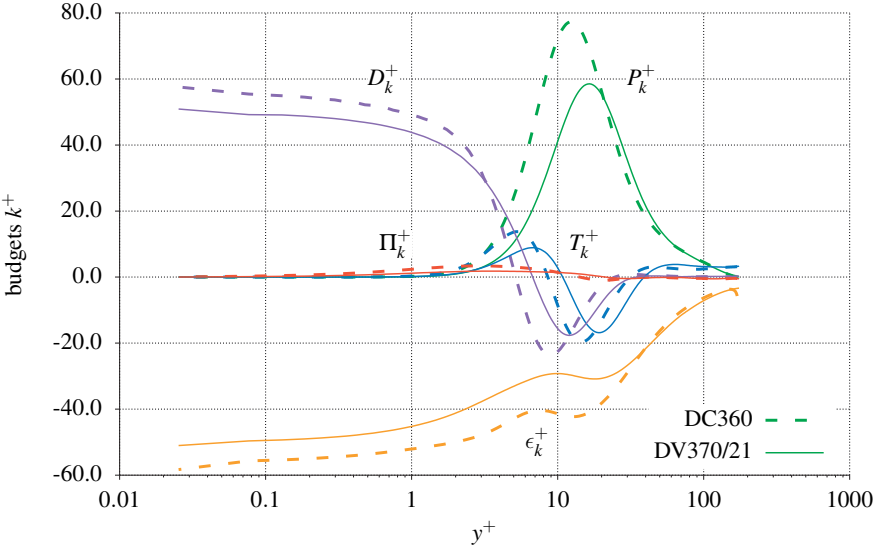

Figure 5.15: Variation of the turbulent kinetic energy budgets over the wall distance for the $\mathrm{Re}_{\tau,w} = 360$, $\mathrm{Pr}_w = 20$ cases

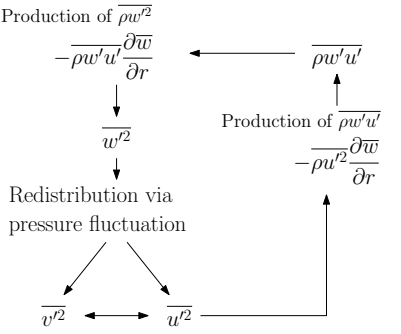

Figure 5.16: Loop of real fluid behavior impact on turbulent flow

the individual normal and turbulent stresses a concept proposed by Leschziner (2000) as "cycle of turbulence" will be employed. This schematic of the "cycle of turbulence" is shown in figure 5.16. Considering equation (2.24) for normal stresses $i = j = 1/2/3$ giving $\rho^* \overline{u'^{+2}}/\rho^* \overline{v'^{+2}}/\rho^* \overline{w'^{+2}}$ and assuming a fully turbulent, developed flow, it becomes evident that only the streamwise component contains a production term, while for the other directions the production term vanishes. The exact streamwise production rate reads

$$P_{zz}^{+} = -\rho^* \overline{w'^{+} u'^{+}} \frac{\partial \overline{w^{+}}}{\partial r^*}, \tag{5.18}$$

which contains the turbulent shear stress and the average shear rate, both already shown in figure 5.12. The fluctuation energy produced from P_{zz}^{+} is then redistributed primarily through the fluctuating pressure in the term ψ_{ij}^{+} (see Pope (2001)), which reads for the streamwise direction

$$\psi_{zz}^{+} = \overline{\pi'^* \frac{\partial w'^{+}}{\partial z^*}}. \tag{5.19}$$

Figure 5.17 plots the radial variation of all budget contributions to the axial velocity fluctuation. Starting from the wall, the increasing viscosity for the DV case causes a reduction of all contributions, which is consistent with the reduced rms-fluctuations observed in this region in figure 5.11. However, while the dissipation and the pressure diffusion/dilatation mainly undergo a reduction, the other contributions exhibit a shift towards the center as well. Due to this shift, it becomes evident that starting from $y^+ \approx 20$, the turbulent and viscous transport are intensified. The production term obviously shows the same tendencies as observed for the turbulent kinetic energy, exhibiting a slight increase beyond $y^+ \approx 30$. These two effects lead to an increase of the axial fluctuation in this region, as shown in figure 5.11. Furthermore, the pressure term is reduced over the whole radial

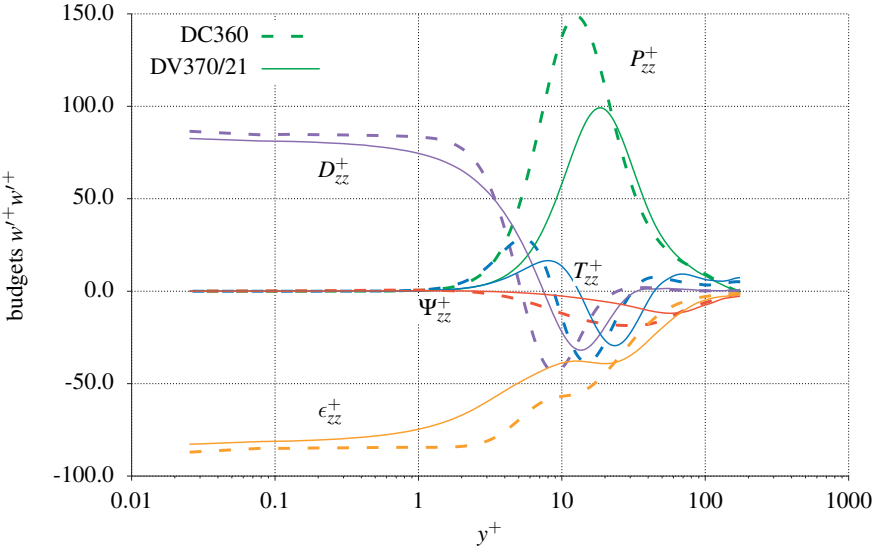

Figure 5.17: Variation of the turbulent statistics $\overline{w'^+w'^+}$ budgets over the wall distance for the $\mathrm{Re}_{\tau,w} = 360$, $\mathrm{Pr}_w = 20$ cases

domain, which essentially indicates an overall less intense redistribution of fluctuation energy. The reduced energy redistribution via pressure fluctuations together with the viscosity gradient counteract the homogenization of turbulence, steering the turbulence towards an anisotropic state, for the DV cases.

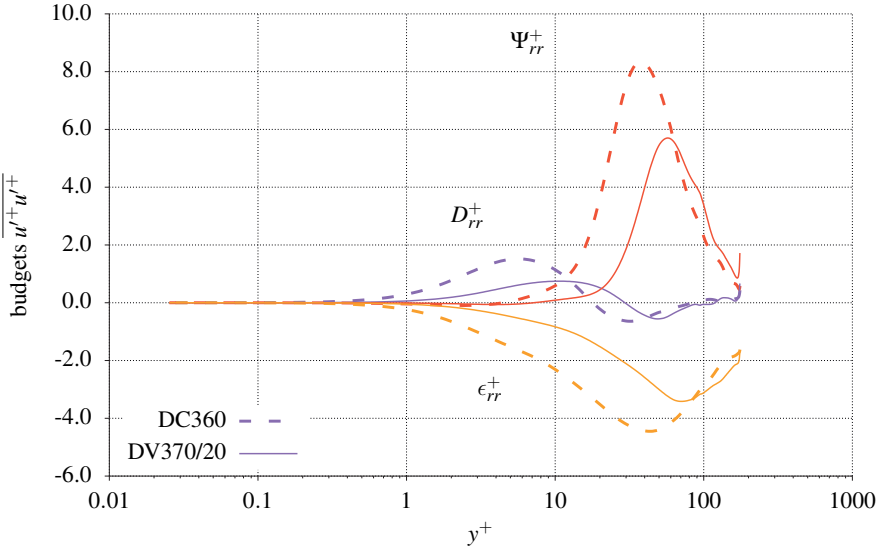

Figure 5.18: Variation of the turbulent budgets $\overline{u'^+u'^+}$ budgets over the wall distance for the $\mathrm{Re}_{\tau,w} = 360$, $\mathrm{Pr}_w = 20$ cases

In the budget for the radial velocity fluctuations, energy is not produced. Therefore, the budget of $\overline{u'^+u'^+}$ is mainly determined by the pressure fluctuation terms Ψ^+_{rr}, written as

$$\psi^+_{rr} = \overline{\pi'^* \frac{\partial u'^+}{\partial r^*}}, \tag{5.20}$$

which is counteracted by the dissipation term ϵ^+_{rr}, as seen in figure 5.18. The reduction in pressure redistribution term seen before in the budget of the axial fluctuations accordingly carries over to a reduced corresponding source term in the budgets of $\overline{u'^+u'^+}$. The dissipation, representing the major sink term in the $\overline{u'^+u'^+}$ budget, follows the pressure term reduction. Regarding the viscous transport term D^+_{rr}, its magnitude reduces and shifts towards the center, similar to the other contributions.

Figure 5.18 further indicates that the most pronounced reduction in the pressure redistribution term takes place at a wall distance of $y^+ \approx 20$. Yet, the reduction of the major sink term at this radial position ϵ^+_{rr} is less pronounced, resulting in a overall reduction of the u^+_{rms}. Figure 5.11 clearly confirms this by showing the higher differences between the

DC and DV cases at the wall distance of $y^+ \approx 20$. Further toward the center, both budget contributions, Ψ_{rr}^+ and ϵ_{rr}^+, exhibit a slight increase resulting in an unchanged u_{rms}^+ value.

Following from the turbulence cycle displayed in figure 5.16, a reduction of the normal radial stress $\rho^* \overline{u'^+ u'^+}$ component causes a reduction of the production term for the shear stress $\rho^* \overline{w'^+ u'^+}$, which reads

$$P_{rz}^+ = -\rho^* \overline{u'^{+2}} \frac{\partial \overline{w}^+}{\partial r^*}. \tag{5.21}$$

This also explains the reduced turbulent shear stress observed in figure 5.12.

As for the azimuthal normal stress components, described by equation (2.24), essentially the same statements as for its radial counterpart are applicable, which results in the similar shift and reduction in magnitude of the azimuthal component observed in figure 5.11.

5.4.4 Enthalpy fluctuations

Due to the lack of suitable validation data, the rms-enthalpy fluctuation of all presently considered high molecular Prandtl number cases could not be validated against literature data. Figure 5.19 compares therefore only internally the enthalpy rms-fluctuation of the variable fluid property cases against the constant fluid property cases.

In the upper sub-figure of figure 5.19, it can be seen by looking first only at the DC cases, that an increase in Prandtl number causes an increase in rms-fluctuation amplitude and a shift of the peak towards the wall. This typical behavior can be attributed to the increase in thermal resistance at higher Prandtl numbers. However, comparing the DV cases against the corresponding DC cases a partly different behavior is shown. Again, the magnitude of the peak increases for the higher Prandtl number, reaching higher levels than the DC cases, though. However, in contrast to the DC cases, the peaks are always shifted towards the center of the pipe. The observed increase of the peak rms value can be explained by the increase of the local Prandtl number with the wall distance leading to higher $\overline{\chi}^+$, as seen in figure 5.6, and the enthalpy fluctuations increase accordingly. A reasonable explanation for the shift into the opposite direction requires a closer examination of all underlying phenomena.

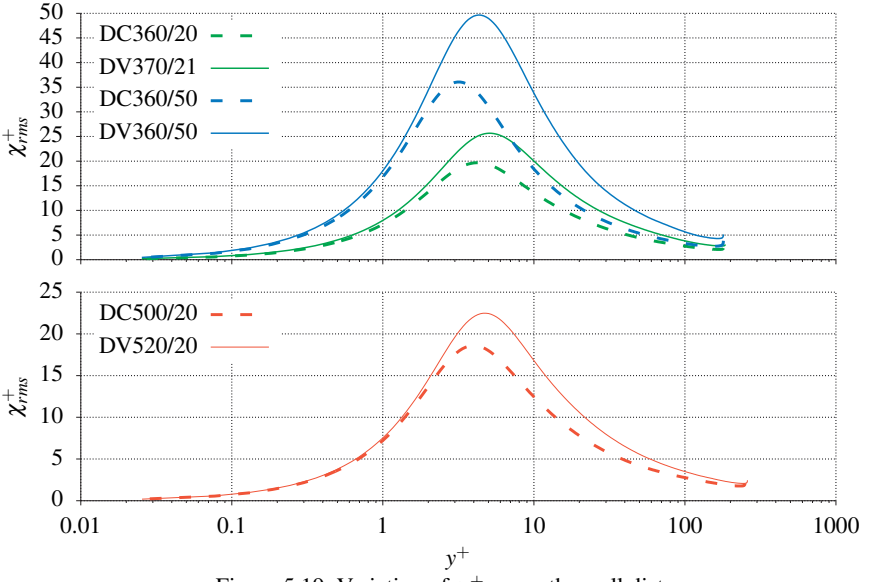

Figure 5.19: Variation of χ^+_{rms} over the wall distance

Budget of turbulent enthalpy fluctuation

Examining the reason for the differences in the turbulent thermal fluctuations exhibited by the DV cases compared to the DC cases, the turbulent budgets for the enthalpy fluctuation, presented in the conservation equation (2.35), are revisited at first. Concerning the effect of the material properties, it becomes evident that this equation is directly affected only by the variation of ρ^*, λ^* and c_p^*. Due to the fact that the variation of these properties is by far less than the variation of the viscosity, it can be assumed that the effect of the material properties enters the budgets rather indirectly through viscosity-dependent contributions. In the budgets given by equation (2.35) theses contributions are in particular the turbulent diffusion and production terms, written as

$$T_\chi^+ = -\frac{\partial \rho^* \overline{u'^+ \chi'^{+2}}}{\partial r^*} \tag{5.22}$$

and

$$P_\chi^+ = -\rho^* \overline{u'^+ \chi'^+} \frac{\partial \overline{\chi}^+}{\partial r^*} \tag{5.23}$$

respectively, both involving the viscosity-dependent fluctuation of the radial velocity u'^+. Considering the production term in figure 5.20, it seems, that the increase of the enthalpy

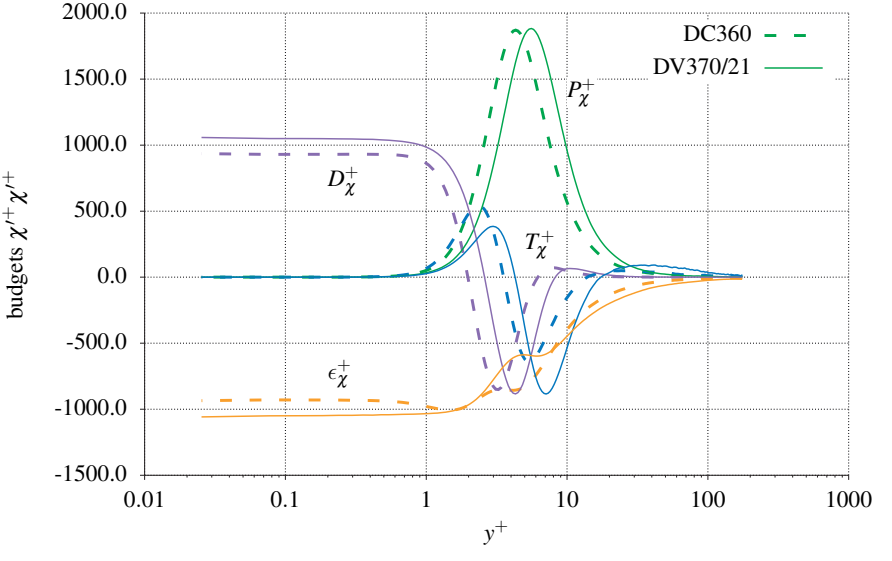

Figure 5.20: Radial variation of the turbulent statistics $\overline{\chi'^+ \chi'^+}$ budgets for the $\mathrm{Re}_{\tau,w} = 360$, $\mathrm{Pr}_w = 20$ cases

rms-fluctuation, see figure 5.19, compensates the viscosity induced notable decrease of the radial velocity rms-fluctuations. Both the turbulent and the molecular diffusion terms, T_χ^+ and D_χ^+, respectively, are shifted towards the center, as well, similar to P_χ^+. This finally leads to the shift of the peak of the χ^+-rms towards the center, as observed for the DV cases in figure 5.19.

5.4.5 Heat flux

Analogously to the shear stress, the total heat flux in a fully turbulent, statistically stationary, axially symmetric pipe flow consists of a laminar and a turbulent contribution given as

$$q_{tot} = \underbrace{-\overline{\lambda}\frac{\partial \overline{T}}{\partial r}}_{q_{lam}} \underbrace{-\overline{\lambda'\frac{\partial T'}{\partial r}}}_{q_\lambda} \underbrace{+\rho\overline{u'h'}}_{q_{turb}} \approx -\left(\rho\,\overline{a} + \overline{\rho}\,a_T\right)\frac{\partial \overline{h}}{\partial r}. \tag{5.24}$$

The contribution q_λ due to the fluctuations entering Fourier's law used for the conductive heat transfer is assumed as negligibly small. The turbulent convective contribution is computed analogously to its laminar counterpart, applying the Boussinesq eddy diffusivity concept

$$-\rho\overline{u'h'} = \rho a_T \frac{\partial \overline{h}}{\partial r}. \tag{5.25}$$

Rewritten in wall coordinates, the total heat flux finally reads

$${q_{tot}}^+ = \frac{q_{tot}}{q_w} = -\left(\frac{1}{\mathrm{Pr}_w}\frac{\overline{\lambda}^*}{\overline{c_p}^*} + \overline{\mu}^*\frac{\rho a_T}{\mu_T}\frac{\mu_T}{\mu}\right)\frac{\partial \overline{\chi}^+}{\partial y^+}. \tag{5.26}$$

Figure 5.21 shows the laminar and turbulent contributions of the heat flux together with the radial enthalpy gradient for the DC cases. With increasing Prandtl number the thermal resistance near the wall increases, which leads to an decreasing thickness of the diffusive sublayer. The increased thermal resistance as well as the thinning of the diffusive sublayer can be seen in sub-figure (A) from the shift of the laminar heat flux profile towards the wall and the strongly increased enthalpy gradient at the wall in sub-figure (B) as the Prandtl number becomes higher. Furthermore, this increased enthalpy gradient causes an intensified convective exchange of heat between the hot near-wall layer and the cooler bulk region. This essentially translates into an increased turbulent heat transfer, as seen in sub-figure (C) of figure 5.21 for the higher Prandtl numbers.

In consistence with the trend observed for the laminar component in sub-figure (A), the local increase of the complementary turbulent contribution, becoming dominant at the upper limit of the diffusive sublayer, is shifted towards the wall as well. This tendency effectively

raises the turbulent heat flux to a significant level very close to the wall, already at y^+ not far above unity, as seen in sub-figure (C).

Figure 5.22 compares the results for the DV cases with $\mathrm{Re}_{\tau,w} = 360$ and $\mathrm{Pr}_w = 20$ against the corresponding DC results. The total heat flux shown in subfigure (A) refers to the

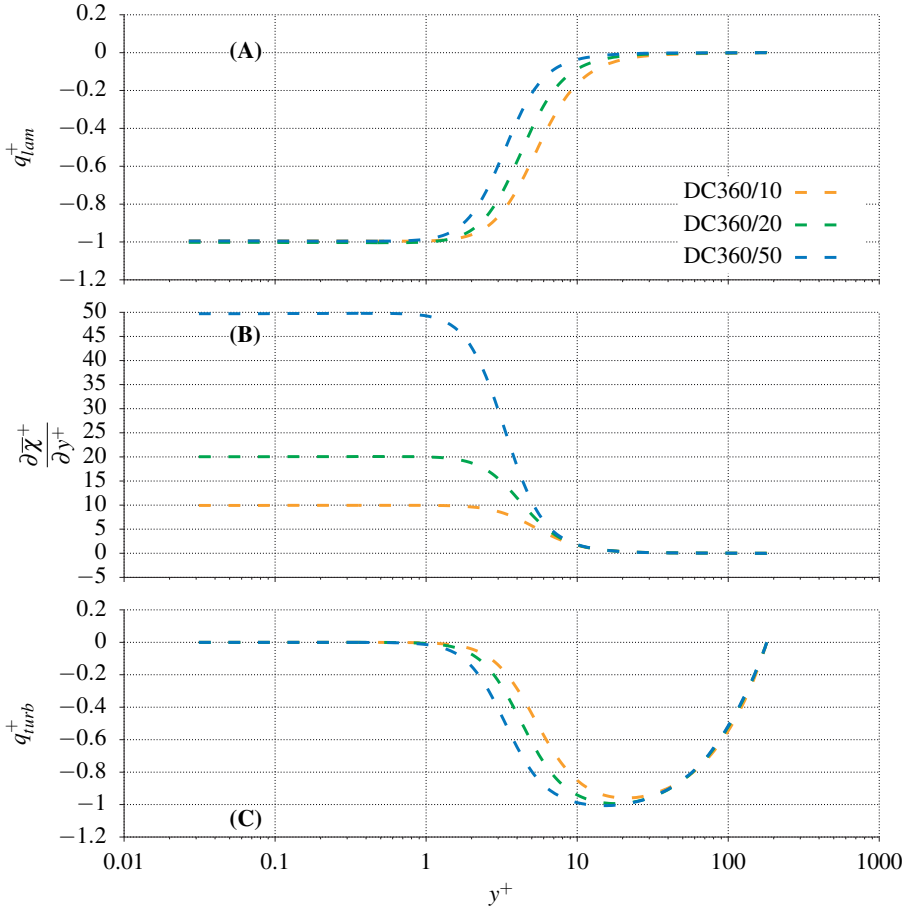

Figure 5.21: Variation of heat flux contributions over the wall distance for the DC cases

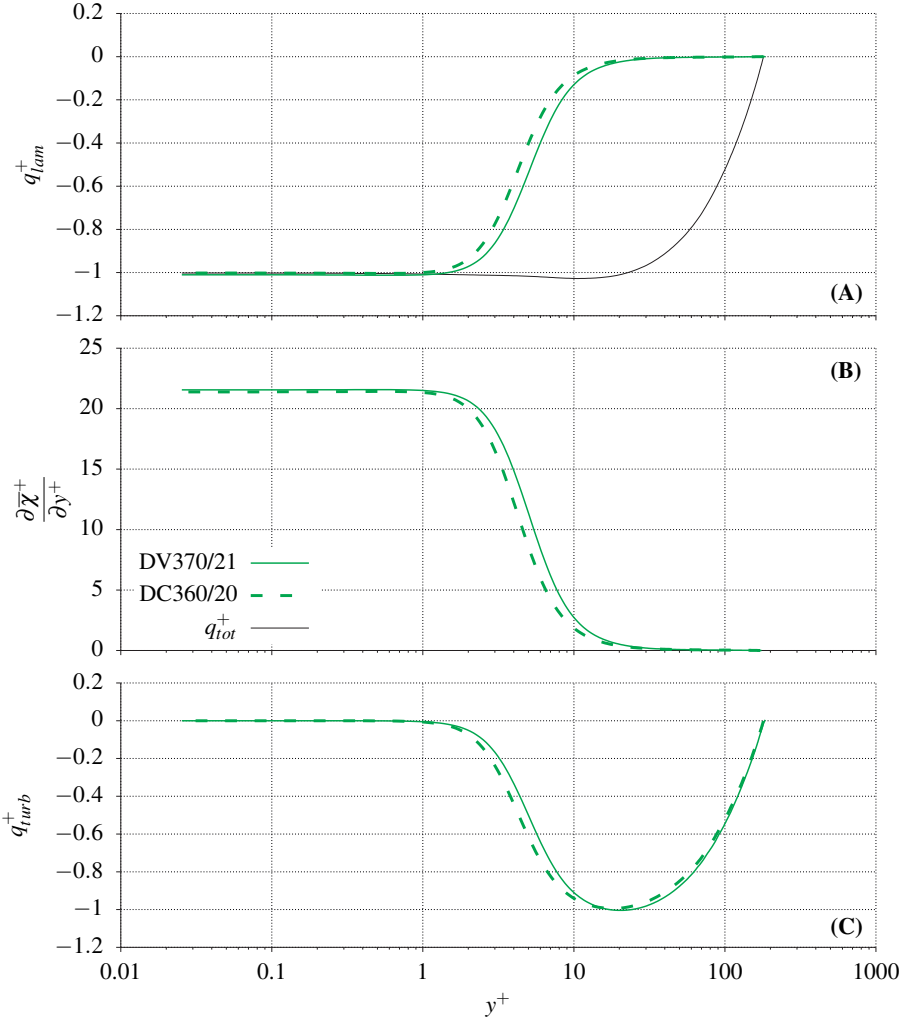

Figure 5.22: Variation of heat flux contributions over the wall distance for the cases with $\mathrm{Re}_{\tau,w} = 360$, $\mathrm{Pr}_w = 20$

results of the constant fluid property case (DC). As follows from equation (2.96), in a statistically stationary fully developed turbulent pipe flow the non-dimensional total heat flux reads

$$q_{tot}^{+} = \frac{1}{r^*} \int_{\tilde{r}^*=0}^{r^*} \tilde{r}\, \rho^* \overline{w}^{+}\, d\tilde{r}. \tag{5.27}$$

As seen from figure 5.5, the variation of the axial velocity $\overline{w}^{+}$ does not significantly differ for the DC and the DV case, except inside the buffer layer. Therefore, the variation of q_{tot}^{+} is hardly affected by the real fluid properties, so that the DC solution is well representative for the DV cases as well.

Sub-figure (A) of figure 5.22 compares the laminar contributions of the heat flux for the DC and DV case for $\mathrm{Re}_{\tau,w} = 360$. The increase in thermal resistance inside the diffusive sublayer due to the locally increasing Prandtl number is clearly indicated by the higher values of the laminar hear flux.

In accordance with the increasing local thermal resistance due to the increase in the Prandtl number with the distance from the wall, the near wall region associated with a high enthalpy gradient is extended for the DV cases, as seen from sub-figure (B).

Sub-figure (C) compares the turbulent contribution of the heat flux for the DC and the DV case. The shift of the DV profile to higher y^{+} reflects the thickened diffusive sublayer discussed above.

For a more detailed examination of the underlying transport phenomena, a quadrant analysis for the turbulent heat flux as well as an analysis of the turbulent budgets will be presented in the following.

Quadrant analysis

Similarly to the dynamic turbulent coherent structures the turbulent heat flux can be conditionally averaged and classified into four categories:

- Q1: $(-u'^{+}, +\chi'^{+})$ are outward interactions, where cold fluid moves from the wall to the center
- Q2: $(-u'^{+}, -\chi'^{+})$ are ejection events, where hot fluid moves from the wall to the center
- Q3: $(+u'^{+}, -\chi'^{+})$ are inward interactions, where hot fluid moves toward the wall
- Q4:$(+u'^{+}, +\chi'^{+})$ are sweep events, where cold fluid moves toward the wall

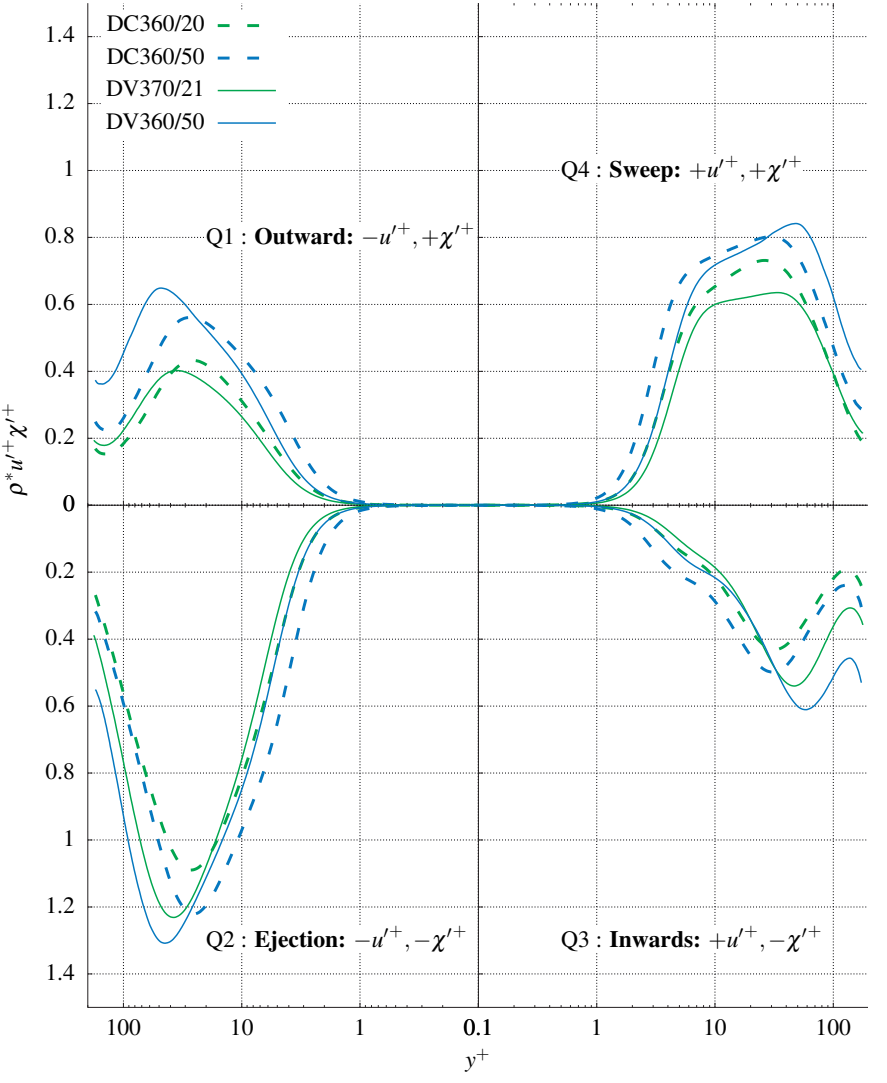

Figure 5.23: Fractional contribution $\rho^* \overline{u'^+ \chi'^+}$ for cases with $\mathrm{Re}_{\tau,w} = 360$

Similar tendencies are noticeable, when comparing the fractional contributions $\rho^* \overline{u'^+ \chi'^+}$ shown in figure 5.23 to the dynamic counterparts shown in figure 5.13. Again, the two major contributors to the turbulent heat flux are the ejection and sweep events. Both effects are associated with an enhanced heat transfer, because hot fluid moves away from the wall and cold fluid moves towards the wall. Yet, the difference in amplitude between these events and the outward/inward interaction is not as large as that observed for the turbulent shear stress. Considering the effect of the Prandtl number, the results keep a similar shape, yet up-scaled for increasing Prandtl number.

As a general feature of all presently shown DV cases, all fractional contributions are shifted closer to the center. This finally results in the already noted smaller turbulent heat flux as compared to the DC case. The tendency to a lower radial turbulent heat flux for the DV cases can be attributed to the fact that the radial velocity fluctuation is significantly reduced by the enhanced viscous damping due to the locally increasing viscosity. Nevertheless, the reduction observed for the turbulent heat flux in the DV cases is less pronounced than that observed for the turbulent shear stress, as shown in figure 5.12 and 5.22. The reduced convective turbulent mixing carried by the fluctuation u'^+ is apparently compensated to some extent by the increased intensity of the enthalpy fluctuations seen in figure 5.19 for the DV cases. Due to this compensating effect the turbulent heat even exceeds the value of the DC cases beyond $y^+ \approx 20$, as seen from figure 5.22 (C).

Turbulence budgets of the turbulent heat flux

A further insight into the interaction of the individual mechanism determining the turbulent heat flux is provided by the budgets, computed from equation (2.43) using the DNS data. The individual contributions are shown in figure 5.24 and 5.25 for the two considered Prandtl numbers with $\mathrm{Re}_{\tau,w} = 360$, respectively.

It can be observed, that all contributions for the DV cases exhibit a shift towards the center and a reduction in magnitude compared the corresponding DC components. This general tendency seems to be even enhanced with increasing molecular Prandtl number, seen in figure 5.25, which can be attributed to the increasing fluid property variation for the higher Prandtl number case. In order to further investigate the origin of the observed trends, the most relevant contributions of the turbulent heat flux will be examined in detail. The production term P_{qr}, generally defined in equation (2.45), actually reads

$$P_{qr}^+ = -\rho^* \overline{u'^+ u'^+} \frac{\partial \overline{\chi}^+}{\partial r^*}. \tag{5.28}$$

As such, it is strongly determined from the variation of the turbulent radial normal stress $\overline{u'^+ u'^+}$, which is considerably reduced in the region around $y^+ \approx 10$, as seen in figure 5.11.

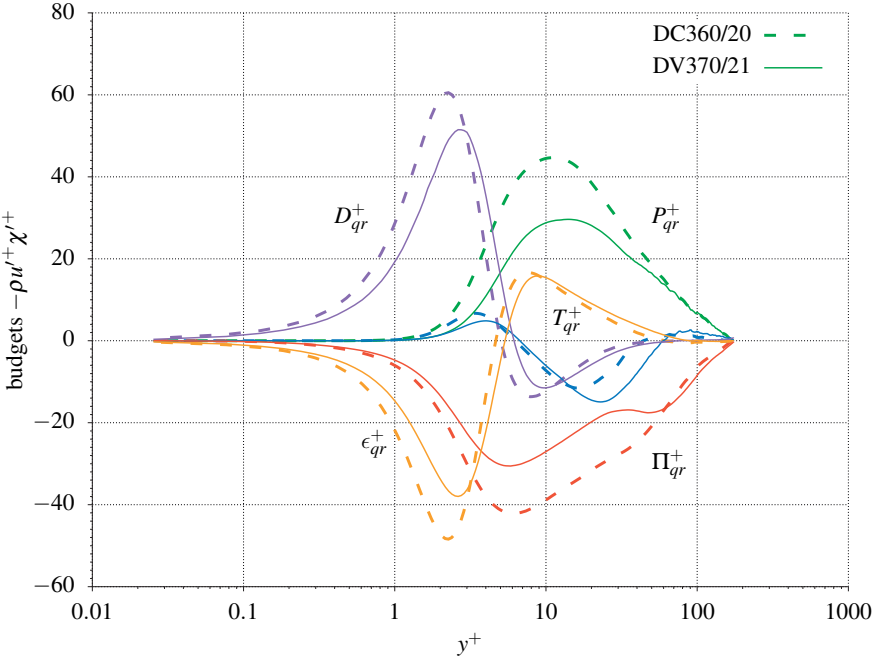

Figure 5.24: Variation of the turbulent heat flux budgets over the wall distance for the case $\mathrm{Re}_{\tau,w} = 360$, $\mathrm{Pr}_w = 20$

The present analysis of the budgets can also be incorporated into the schematic of the "cycle of turbulence", which was already shown in figure 5.16, by extending it with an additional enthalpy path, as sketched in figure 5.26. The starting point is the alteration of the radial turbulent stress $\overline{u'^+ u'^+}$ due to the real temperature-dependent fluid properties, which directly affects the production term P_{qr} of the turbulent heat flux. This resulting modified turbulent heat flux enters the production term P_χ for the turbulent $\overline{\chi'^+ \chi'^+}$ budgets which, in addition to the significant local Prandtl number variation, produces the observed significant differences in the variations of $\overline{\chi'^2}$ between the DC and the DV cases. The heat flux alterations further causes a variation of the temperature, which alters the fluid properties and thus the momentum transfer, closing the loop.

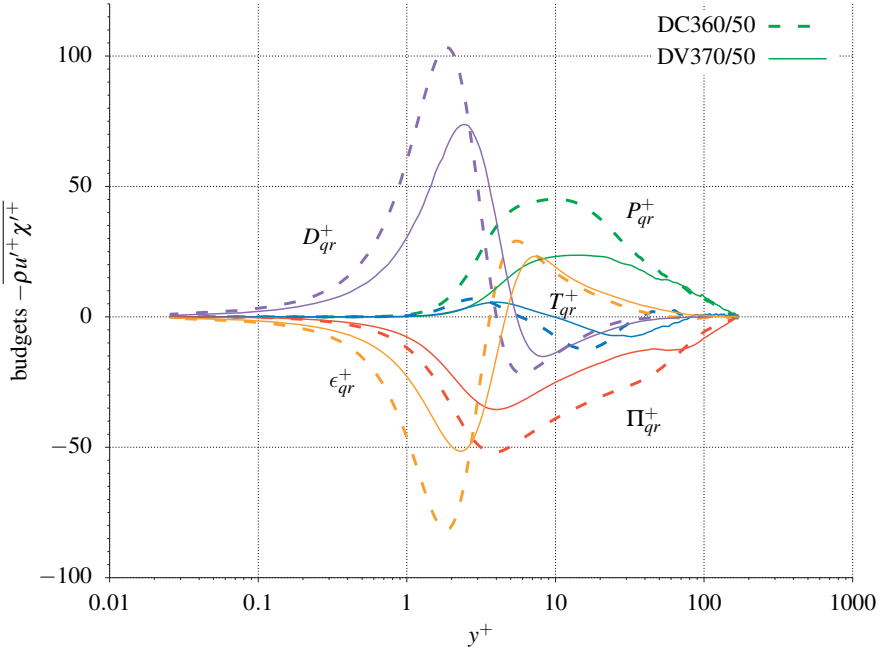

Figure 5.25: Variation of the turbulent heat flux budgets over the wall distance for the case $\mathrm{Re}_{\tau,w} = 360$, $\mathrm{Pr}_w = 50$

5.5 Turbulent transport coefficients

As shown in equations (5.12) and (5.24), the turbulent contributions of the shear stress and the heat flux are generally modeled based on the eddy viscosity ν_T and the eddy diffusivity a_T, respectively. Using the DNS results it is possible to determine these two transport coefficients, as dependent on the fully resolved fluctuating flow variables.

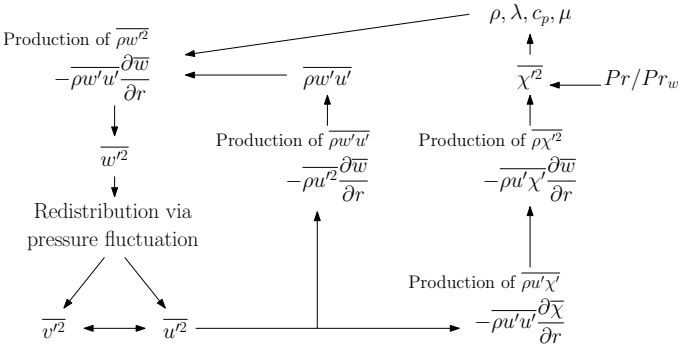

Figure 5.26: Extended "cycle of turbulence", including the effect of temperature-dependent material properties

5.5.1 Eddy viscosity

Following from equation (5.13), the eddy viscosity can be determined as

$$\frac{\mu_T}{\mu} = -\frac{\rho^* \overline{u^{+\prime} w^{+\prime}}}{\rho^* \frac{\partial \overline{w}^+}{\partial y^+}}, \tag{5.29}$$

based on DNS data. In addition, the near wall variation of the eddy viscosity can be obtained by analytical considerations. Very next to the wall the fluctuation velocity components can be assumed as Taylor series expansions of y^+. Enforced by continuity and no-slip wall conditions these expansions read

$$u^{+\prime} = c_u {y^+}^2 + ... \tag{5.30}$$

$$w^{+\prime} = b_w y^+ + ... \tag{5.31}$$

Along with the velocity gradient, being $d\overline{w}^+/dy^+ = 1$ for $y^+ \to 0$, this produces a ${y^+}^3$-dependence for the turbulent shear stress $\rho^* \overline{u'^+ w'^+}$ as well as for the eddy viscosity ratio.

Figure 5.27 plots the variation of the eddy viscosity ratio over the wall distance y^+, as extracted from the DNS data. It becomes evident that the near wall variation strictly follows the ${y^+}^3$-dependence for all cases. As already shown in figure 5.12, comparing the turbulent shear stress contribution for the DC to those for the DV cases, the increase in molecular viscosity with wall distance effectively dampens the turbulent fluctuations. Since the gradient of the average axial velocity $d\overline{w}^+/dy^+$ does not change in the near-wall region, the magnitude of the eddy-viscosity ratio is notably reduced, as seen from figure 5.27.

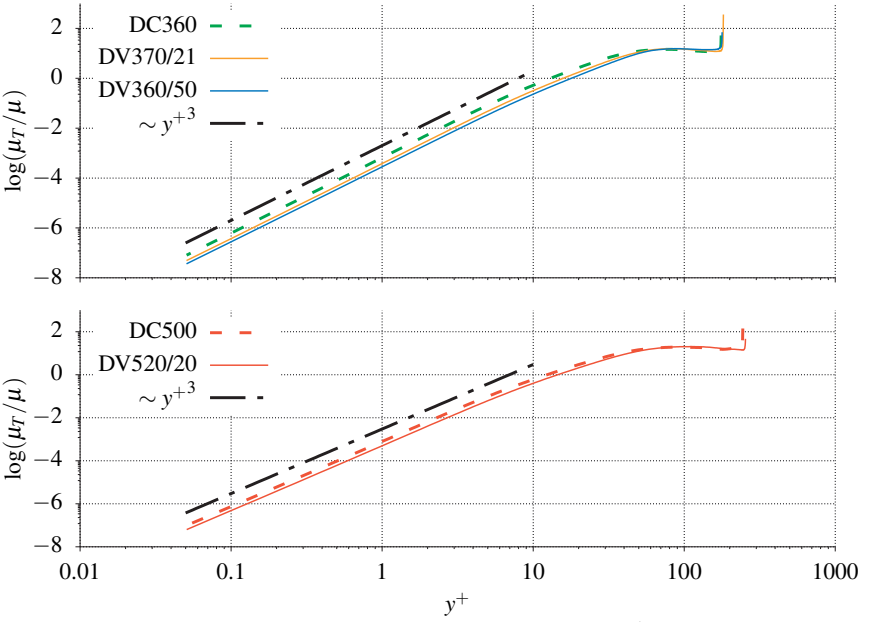

Figure 5.27: Eddy viscosity ratio vs. y^+

5.5.2 Eddy diffusivity

Analogously to the eddy viscosity, the eddy diffusivity can be determined incorporating the DNS results into equation (5.25), which yields

$$\frac{a_T}{\nu} = -\frac{\rho^* \overline{u'^+ \chi'^+}}{\rho^* \dfrac{\partial \overline{\chi}^+}{\partial y^+}}. \tag{5.32}$$

The same analytical consideration as for the eddy viscosity can be applied here, assuming a Taylor series expansions of y^+ the near wall variation of the enthalpy fluctuation, as

$$\chi^{+\prime} = b_\chi y^+ + \ldots \tag{5.33}$$

Together with the mean enthalpy gradient close to the wall being $d\overline{\chi}^+/dy^+ = \mathrm{Pr}_w$, this produces again a y^{+3}-dependence for the turbulent heat flux $\rho^* \overline{u'^+ \chi'^+}$, as well as for

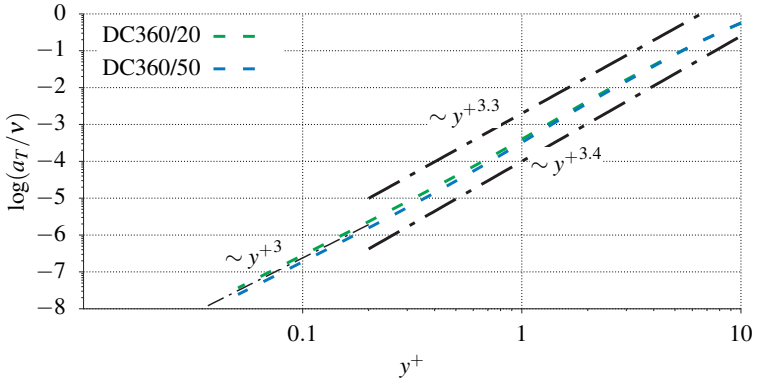

Figure 5.28: Eddy diffusivity ratio vs. y^+ for the DC cases with $\mathrm{Re}_{\tau,w} = 360$

the eddy diffusivity, which is strongly supported by various authors (see, e.g., Harriott and Hamilton (1965), Hubbard and Lightfoot (1966) and Sirkar and Hanratty (1969)). The near wall asymptotic variations obtained from the DNS results shown in figure 5.28 confirm this dependence for $y^+ \to 0$. Further away from the wall the exponential growth with y^+ becomes somewhat different, dependent on the molecular Prandtl number. This feature was also discussed by Irrenfried and Steiner (2017), where the variations of a_T/ν were compared against each other for different Prandtl numbers. For unity Prandtl number, the same y^{+n} with $n = 3$ dependency as for the eddy viscosity was observed while for increasing Prandtl number, the power n increased as well. This is also indicated here by the DC cases in figure 5.28. For the DC360/20 case, n needs to be increased to $n = 3.3$ and for the DC360/50 cases to $n = 3.4$.

The radial variation of the eddy diffusivity for the DV cases show the same asymptotic y^{+3}-dependence at the wall as the corresponding DC cases, as seen from figure 5.29. However, resulting from the differences in the turbulent heat flux, the y^+-dependence differs from the DC cases further away from the wall. It seems that the eddy diffusivity of the DV cases maintains the y^{+3}-dependence also beyond the diffusive sublayer.

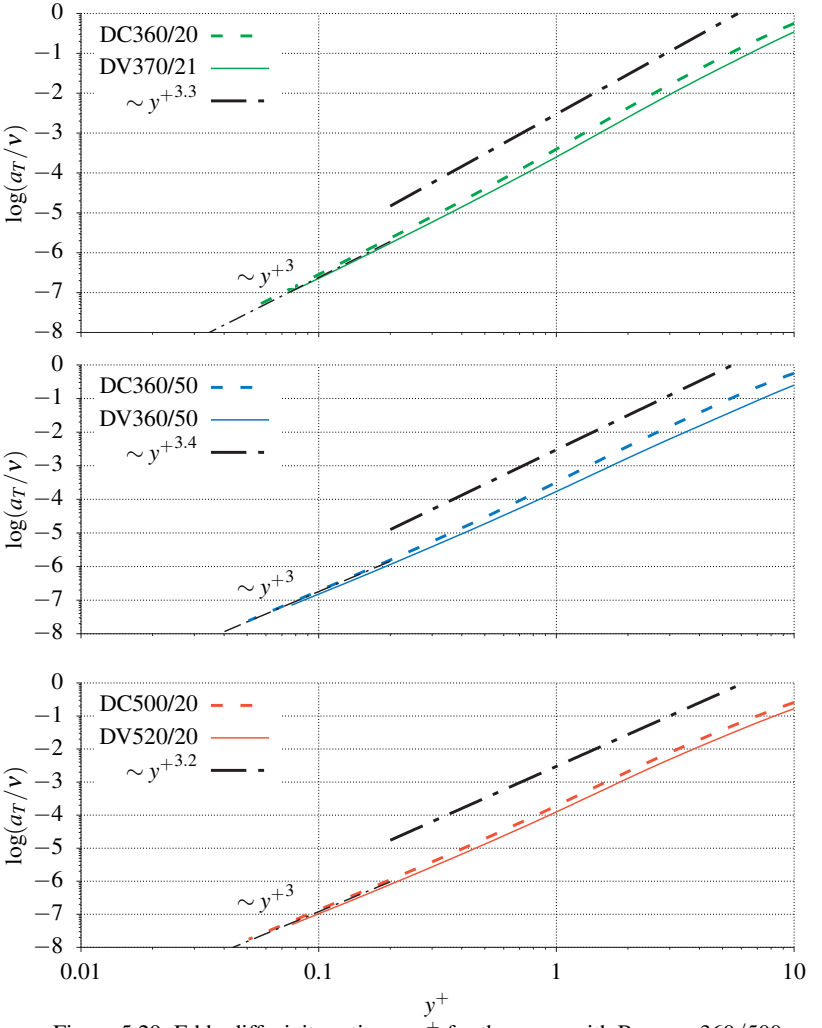

Figure 5.29: Eddy diffusivity ratio vs. y^+ for the cases with $\mathrm{Re}_{\tau,w} = 360/500$

5.5.3 Turbulent Prandtl number

The turbulent Prandtl number Pr_T can be interpreted as the turbulent equivalent of the molecular Prandtl number. It relates the eddy viscosity to the eddy diffusivity, as follows from its definition

$$\mathrm{Pr}_T = \frac{\nu_T}{a_T}. \tag{5.34}$$

Using DNS results it can be evaluated as

$$\mathrm{Pr}_T = \frac{\overline{u'^+ w'^+}}{\overline{u'^+ \chi'^+}} \frac{d\overline{\chi}^+/dy^+}{d\overline{w}^+/dy^+}. \tag{5.35}$$

Its radial variation for the DC data can be seen in figure 5.30. A commonly assumed value for the turbulent Prandtl number is $\mathrm{Pr}_{T,\infty} = 0.85$, which basically represents Pr_T in the limit $y^+ \to \infty$, and the DNS supports this assumption. Closer to the wall, inside the inertial sub-range, it remains around unity, independent of the molecular Prandtl number. Inside the viscous sub-range, $y^+ < 5$, a significant increase towards the wall can be observed for all cases. The wall asymptotic agrees with the previously shown analytical considerations, essentially resulting in

$$\lim_{y^+ \to 0} \mathrm{Pr}_T = \frac{b_w}{b_\chi} \mathrm{Pr}_w \to \text{const.} \tag{5.36}$$

These findings are consistent with the simulation results of Schwertfirm and Manhart (2007) as well as with the measurements of Hollingsworth et al. (1989). The magnitude of the asymptotically approached wall value is increased with increasing molecular Prandtl number. The steepening of the near wall gradient with increasing molecular Prandtl number is in accordance with the increase of the exponent n in the y^+-dependence of the eddy diffusivity seen in figure 5.28. The Reynolds number has evidently no notable effect on the variation of the turbulent Prandtl number. For the presently considered Reynolds numbers, the near wall behavior of Pr_T appears as decoupled from the momentum transfer.

Figure 5.31 compares the turbulent Prandtl number obtained for the DV cases to those obtained for the corresponding DC cases. It is evident that for all DV cases the asymptotically approached wall value is lower than for the DC cases. This reduction reflects the already discussed observation that the increase in the local viscosity with the wall distance leads to a stronger decrease in the turbulent shear stress than in the turbulent heat flux. The quantitatively different decrease in the turbulent fluxes translates into stronger reduction in the eddy viscosity than in the eddy diffusivity in the DV cases, as seen in figures 5.27 and 5.29, which explains the lower level of Pr_T near the wall observed for the DV cases. The radial variation of the fluid properties, furthermore also alter the turbulent Prandtl number remote from the wall. Inside the inertial sublayer, beyond $y^+ \approx 20$, the turbulent Prandtl number of the DV cases drops below the value of the DC cases. This deviation may be attributed by the increased turbulent heat flux due to the increases enthalpy fluctuations observed in this region for the DV cases (see figures 5.19, 5.22, and 5.23).

5.6 Skin-friction coefficient

For the validation of the predicted flow against experiments a comparison of the skin-friction coefficient is carried out. According to its definition already given in (4.8)

$$c_f = \frac{\tau_w}{\rho_b \frac{\overline{w}_b^2}{2}},$$

the skin-friction coefficient involves the wall shear stress and the bulk velocity. For the experimental reference value the latter is determined from the measured mass flow rate

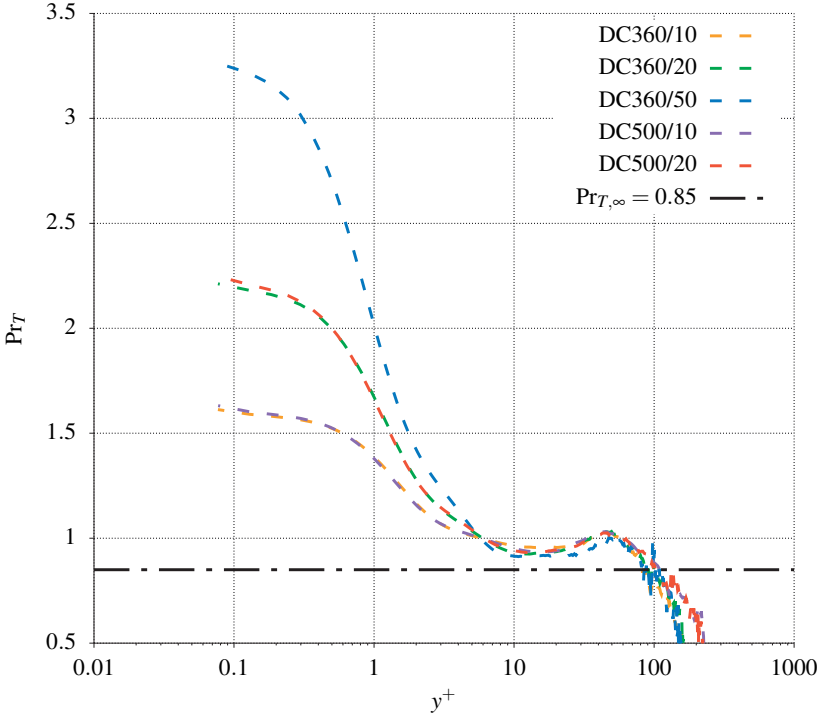

Figure 5.30: Turbulent Prandtl number vs. y^+

as

$$\overline{w}_b = \frac{\dot{m}}{\rho_b A}, \tag{5.37}$$

with A being the cross-sectional area of the pipe. The wall shear stress is experimentally determined from the measured axial pressure drop Δp substituted into (4.7).

The evaluation of c_f from the DNS results recalls the definition of the non-dimensional bulk velocity written as

$$\overline{w}_b^+ = \frac{8}{\rho_b^*} \int_{r^*=0}^{1/2} \rho^* \overline{w}^+ r^* \mathrm{d}r^*, \tag{5.38}$$

which directly yields the skin-friction coefficient as

$$c_f = 2\frac{\tau_w}{\rho_w}\frac{\rho_w}{\rho_b \overline{w}_b{}^2} = \frac{2}{\rho_b^* \overline{w}_b^{+2}}. \tag{5.39}$$

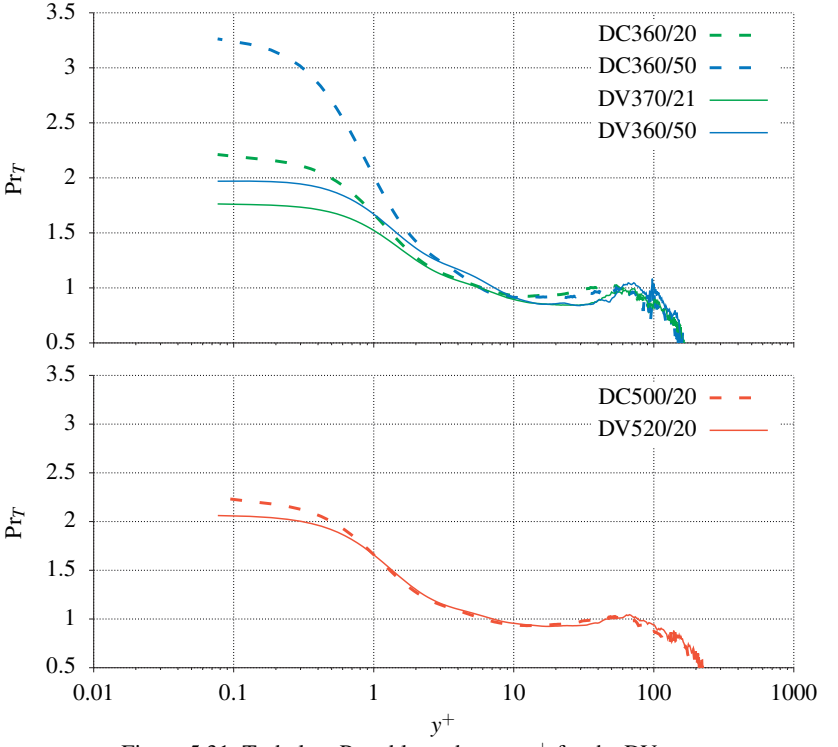

Figure 5.31: Turbulent Prandtl number vs. y^+ for the DV cases

Table 5.7: Skin-friction coefficient validation for the DV cases

	Re_b	c_f	error
	–	–	%
DC360	5275	0.00936	−0.2
Wu and Moin (2008)	5300	0.00938	
DC500	7680	0.00848	−6.1
Durst et al. (1995)	7442	0.00903	

Table 5.8: Skin-friction coefficient

#	c_f^M	c_f^{DC} (error in %)	c_f^{DV} (error in %)
	–	–	–
DV370/21	$0.0092 \pm 7 \times 10^{-5}$	0.009362 (1.7%)	0.00912 (0.9%)
DV360/50	$0.0095 \pm 7 \times 10^{-5}$		0.00943 (0.7%)
DV520/20	$0.0089 \pm 7 \times 10^{-5}$	0.008480 (−4.8%)	0.00854 (4.0%)

For the constant fluid property cases the c_f values predicted from the DNS are also validated against DNS results of Wu and Moin (2008) and experiments of Durst et al. (1995), as is shown in table 5.8. Table 5.8 compares the DNS predictions for both the DV and DC cases to the present own measurements discussed in section 4.

Comparing the different Prandtl number cases associated with the different DV cases, it can be generally stated that the higher the variation of the fluid properties, the higher is the discrepancy from the corresponding DC cases. Quantitatively the skin-friction coefficient still does not differ much from that of the DC case.

Comparing the DNS results to the measurements, a very good agreement with a maximum discrepancy of 4% can be seen. Due to the neglect of any material property variation, the DC cases expectedly show higher discrepancies. The observed good agreement proves a high reliability of the present DNS in predicting the radial velocity variation.

5.7 Nusselt number

The validation of the heat transfer is frequently done by comparing the predicted non-dimensional Nusselt number defined as

$$\mathrm{Nu}_w = \frac{\alpha D}{\lambda_w} = \frac{q_w D}{\lambda_w (T_w - T_b)} \tag{5.40}$$

against experimental values, as presently obtained from equation (4.9) with equation (4.10). It basically relates the convective heat transfer to the conductive heat transfer.

Recalling the definition of $\overline{\theta}$, introduced in (2.80), its non-dimensionalized bulk value reads

$$\overline{\theta}_b^+ = \frac{\overline{T}_w - T_b}{q_w} \rho_w c_{p,w} w_\tau \tag{5.41}$$

so that

$$\mathrm{Nu}_w = \frac{w_\tau}{\overline{\theta}_b^+} \frac{\rho_w c_{p,w} D}{\lambda_w} = \frac{\mathrm{Re}_{\tau,w} \mathrm{Pr}_w}{\overline{\theta}_b^+}. \tag{5.42}$$

The evaluation of Nu_w from the DNS results determines the enthalpy-equivalent bulk temperature as

$$\overline{\theta}_b^+ = \frac{1}{\dot{m}^*} \int_{r^*=0}^{1/2} \rho^* \overline{w}^+ \overline{\theta}^+ r^* \mathrm{d}r^*, \tag{5.43}$$

with the non-dimensionalized mass flow rate defined as

$$\dot{m}^* = \frac{\dot{m}}{\rho_w w_\tau D^2 \pi} = 2 \int_{r^*=0}^{1/2} \rho^* \overline{w}^+ r^* \mathrm{d}r^*. \tag{5.44}$$

Table 5.9 compares the DNS results for the DC and the DV cases to the own measurements for the corresponding experimental conditions. Unlike for the skin-friction coefficient, the discrepancy between the DC and the DV results is considerable. The DV results based on the real temperature-dependent fluid properties generally exhibit notably lower values, which is supported by the measurements.

The presently observed decrease of the Nusselt number due to real fluid behavior, was also addressed by Petukhov (1970) and is accounted for in the Nusselt number correlation of Gnielinski (2002) by the last Pr-dependent factor in equation (4.18).

The experimental data are in excellent agreement with the predictions of the DV cases, with a maximum error of around 3%. This further highlights the high reliability of the present DNS results, which proves this DNS data as an outstanding basis for further model evaluation and development.

Table 5.9: Nusselt number

#	Nu_w^M	Nu_w^{DC} (error in %)	Nu_w^{DV} (error in %)
	–	–	–
DV370/21	60.1 ± 2.9	65.29 (8.6%)	58.11 (3.3%)
DV360/50	68.7 ± 8.3	88.22 (28%)	68.66 (0.1%)
DV520/20	89.2 ± 4.4	94.24 (5.6%)	89.77 (0.7%)

5.8 Semi-local scaling

The radial variation of the material properties changes the results for the mean flow in a way, which at first glance, appears to exclude an universal description. Different scaling approaches have been still proposed to account for real fluid behavior and achieve a collapse of the rescaled flow quantities, independent of the material property variation. For non-hypersonic flows, van Driest (1951) proposed a scaling, written as

$$\mathrm{d}\overline{w}^{vD} = \sqrt{\frac{\overline{\rho}}{\rho_w}}\,\mathrm{d}\overline{w}^{+} \tag{5.45}$$

accounting for a variation of the density ρ with respect to the reference state, which is presently specified by the wall conditions. The transform (5.45), is supposed to describe compressible flow with universal laws, basically derived for constant density flow. Recently, it was shown by Sciacovelli et al. (2017) that the van Driest scaling collapses also results for high Mach numbers very well. Patel et al. (2016) extended this scaling approach introducing semi-local reference quantities, defined as $w_\tau^\bullet = \sqrt{\tau_w/\rho}$ and $\delta_m^\bullet = \overline{\mu}/(\rho w_\tau^\bullet)$, which depend on the local density ρ as well as the local molecular viscosity $\overline{\mu}$. Based on this scaling the semi-local Reynolds number is defined as

$$\mathrm{Re}_{\tau,w}^\bullet = \frac{D\,\rho\,w_\tau^\bullet}{\overline{\mu}} = \mathrm{Re}_{\tau,w}\,\frac{\sqrt{\overline{\rho}^*}}{\overline{\mu}^*} \tag{5.46}$$

and the semi-local molecular Prandtl number is defined as

$$\mathrm{Pr}^\bullet = \frac{\overline{\mu}\,\overline{c_p}}{\overline{\lambda}} = \mathrm{Pr}_w\,\frac{\overline{\mu}^*\,\overline{c_p}^*}{\overline{\lambda}^*}. \tag{5.47}$$

The reasoning behind this scaling approach is based on the observation of Patel et al. (2016), who showed that the rescaled viscous shear stress contributions, written as

$$\tau_{lam}^\bullet = -\frac{D}{\mathrm{Re}_{\tau,w}^\bullet}\,\frac{\mathrm{d}\overline{w}^{vD}}{\mathrm{d}y} \tag{5.48}$$

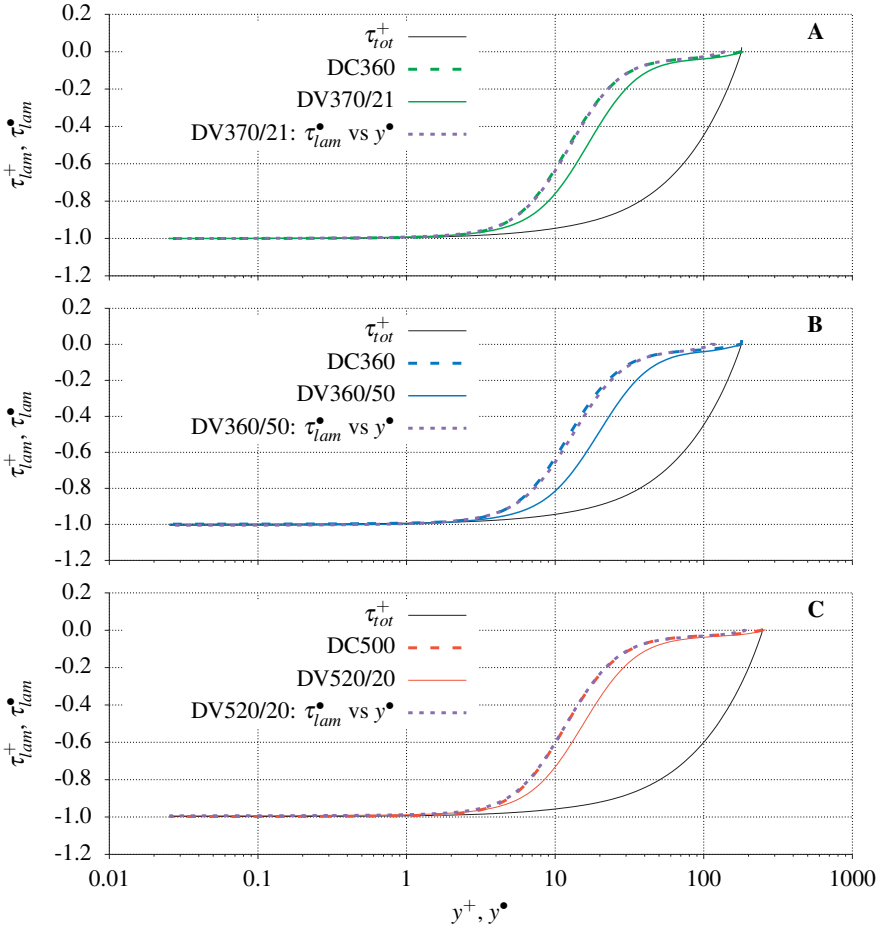

Figure 5.32: Variation of viscous shear stress contributions over the wall distance for the cases with $\mathrm{Re}_{\tau,w} = 360$ and 500, using the wall scaling $()^+$-units, and the semi-local scaling $()^\bullet$-units

collapse perfectly, when plotted over the semi-local wall distance

$$y^\bullet = \frac{y}{D}\,\mathrm{Re}^\bullet_{\tau,w}. \tag{5.49}$$

This collapse is also featured by present results displayed in figure 5.32, showing that the rescaled viscous shear stress contributions for the DV cases perfectly collapse with the corresponding DC contributions, if the wall distance is rescaled with the semi-local wall distance, as defined in formulation (5.49). Based on the observation

$$-\frac{D}{\mathrm{Re}^\bullet_{\tau,w}}\,\frac{\mathrm{d}\overline{w}^{vD}}{\mathrm{d}y} = \phi(y^\bullet) \tag{5.50}$$

Patel et al. (2016) derived the following relation for the rescaled velocity $\overline{w}^\bullet$ to $\overline{w}^{vD}$

$$\overline{w}^\bullet = \frac{\overline{w}}{w_\tau{}^\bullet} = -\int_0^{\overline{w}^{vD}} \left(1 + \frac{y^+}{\mathrm{Re}^\bullet_{\tau,w}}\,\frac{\mathrm{dRe}^\bullet_{\tau,w}}{\mathrm{d}y^+}\right) \mathrm{d}\overline{w}^{vD}. \tag{5.51}$$

Figure 5.33 compares the axial velocity of the DC case to the DV cases, rescaled according to the formulation (5.51). It can be seen that by applying this scaling, all velocity profiles collapse perfectly with that of the constant material property case for both shown molecular Prandtl numbers.

Regarding the scaling for the enthalpy, Patel et al. (2017) extended the scaling used of the shear stress to the diffusive heat flux, which implies for the gradient of the van Driest transformed temperature, defined by $\mathrm{d}\overline{\theta}^{vD} = \sqrt{\rho^*}\,\mathrm{d}\overline{\theta}^+$,

$$q^\bullet_{lam} = -\frac{D}{\mathrm{Re}^\bullet_{\tau,w}\mathrm{Pr}^\bullet}\,\frac{\mathrm{d}\overline{\theta}^{vD}}{\mathrm{d}y} = \phi(y^\bullet). \tag{5.52}$$

Figure 5.34 shows that, analogous to the viscouse shear stress, also the rescaled diffusive heat flux of the DV cases perfectly collapse with the corresponding DC cases, when plotted over the semi-local wall distance $y^\bullet$.

As proposed by Patel et al. (2017) for the temperature, based on equation (5.52), a relation analogous to (5.51) can be written for a rescaled enthalpy

$$\overline{\chi}^\bullet = \frac{\overline{\chi}}{\chi_\tau{}^\bullet} = -\int_0^{\overline{\theta}^{vD}} \left(1 + \frac{y^+}{\mathrm{Re}^\bullet_{\tau,w}}\,\frac{\mathrm{dRe}^\bullet_{\tau,w}}{\mathrm{d}y^+}\right) \mathrm{d}\overline{\theta}^{vD} \approx -\int_0^{y^\bullet} \frac{1-2y/D}{\rho a_T/\overline{\mu} + 1/\mathrm{Pr}^\bullet}\mathrm{d}y^\bullet, \tag{5.53}$$

involving the semi-local reference quantity $\chi^\bullet_\tau = q_w/(\rho\, w^\bullet_\tau)$. For the solution of $\overline{\chi}^\bullet$ dependent on $y^\bullet$ Patel et al. (2017) further suggested to separate the integrand on rhs of equation

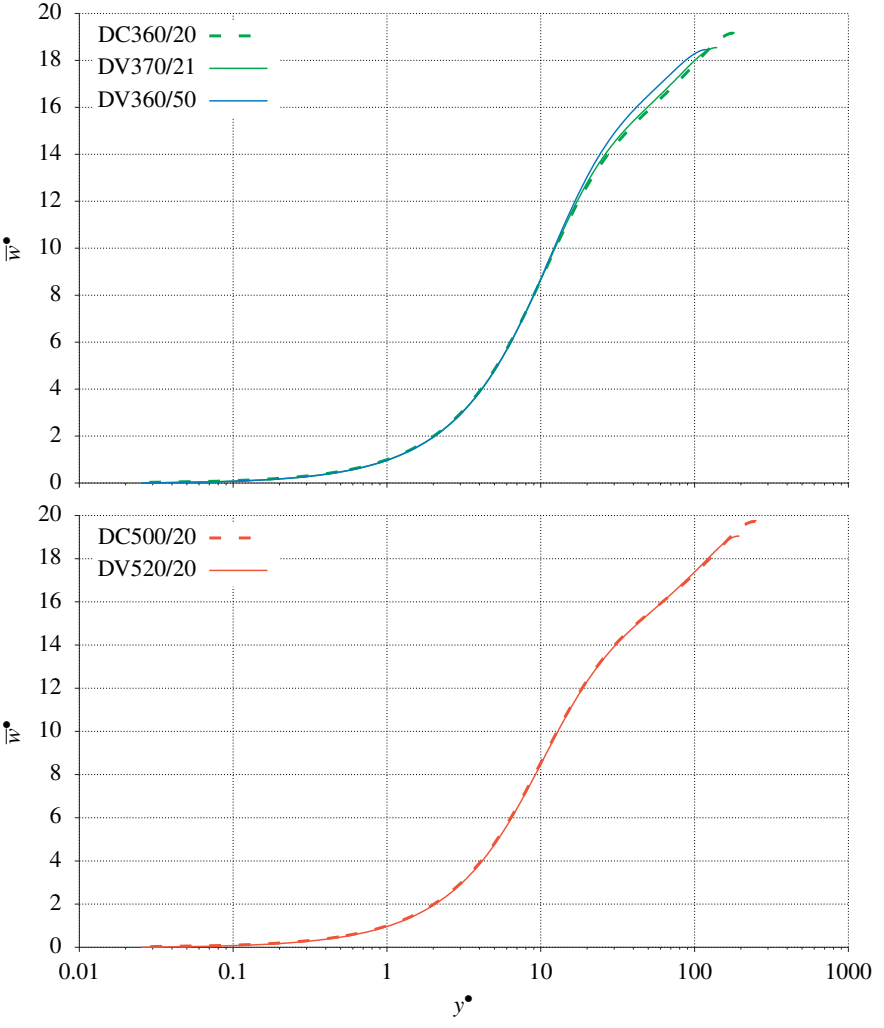

Figure 5.33: $\overline{w}^\bullet$ vs. $y^\bullet$ scaled according to relation (5.51) for the cases with $\mathrm{Re}_{\tau,w} = 360$ and 500

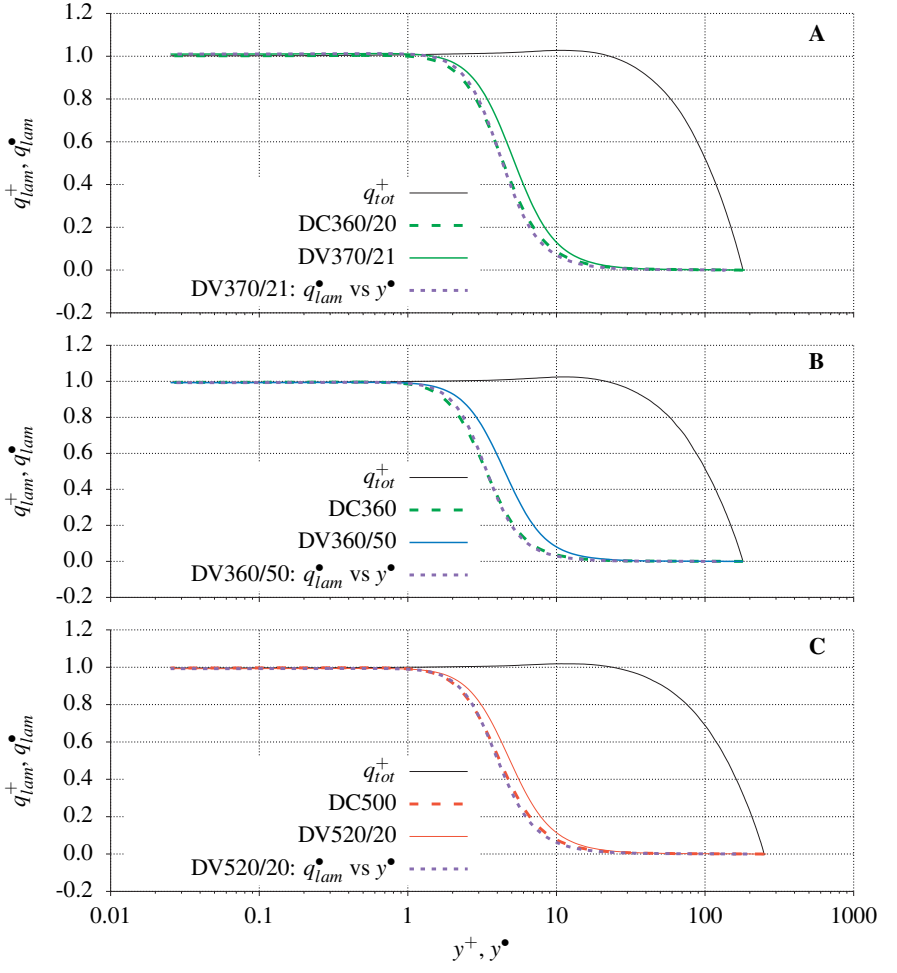

Figure 5.34: Variation of diffusive heat flux contributions over the wall distance for the cases with $\mathrm{Re}_{\tau,w} = 360$ and 500, using the wall scaling $()^+$-units, and the semi-local scaling $()^\bullet$-units

(5.53) into a contribution varying with the Reynolds number and a contribution accounting for the varying molecular Prandtl number. In consistence with the rescaled formulation for the total heat flux given by (5.26) we may accordingly write

$$\begin{aligned}\frac{\mathrm{d}\overline{\chi}^{\bullet}}{\mathrm{d}y^{\bullet}} &\approx -\frac{q^{+}_{tot}}{\rho a_T/\overline{\mu}+1/\mathrm{Pr}^{\bullet}} = \\ &= -\frac{q^{+}_{tot}}{\rho a_T/\overline{\mu}+1} + \frac{q^{+}_{tot}\left\{1-\left[1+\frac{1/\mathrm{Pr}^{\bullet}-1}{\rho a_T/\overline{\mu}+1}\right]^{-1}\right\}}{\rho a_T/\overline{\mu}+1}\end{aligned} \tag{5.54}$$

with

$$\overline{\chi}^{\bullet} = \overline{\chi}\frac{\rho\, w^{\bullet}_{\tau}}{q_w} = \overline{\chi}^{+}\,\rho^{*}\,\frac{w^{\bullet}_{\tau}}{w_{\tau}}. \tag{5.55}$$

Evidently, the latter contribution vanishes, if the Prandtl number is unity, hence it can be considered similar to a P-function, representing the thermal resistance of the diffusive sublayer. Instead of doing a series expansion for the Prandtl number dependent contribution, as shown in Patel et al. (2017), the term is computed directly here, by integrating the formulation (5.54) as

$$\overline{\chi}^{\bullet} = \underbrace{-\int_0^{y^{\bullet}} \frac{q^{+}_{tot}}{\rho a_T/\overline{\mu}+1}\mathrm{d}y^{\bullet}}_{\overline{\chi}^{\bullet}_{\mathcal{T}}} + \underbrace{\int_0^{y^{\bullet}} \frac{q^{+}_{tot}\left\{1-\left[1+\frac{1/\mathrm{Pr}^{\bullet}-1}{\rho a_T/\overline{\mu}+1}\right]^{-1}\right\}}{\rho a_T/\overline{\mu}+1}\mathrm{d}y^{\bullet}}_{\overline{\chi}^{\bullet}_{\mathcal{P}}}. \tag{5.56}$$

The results of this integration are shown in figure 5.35. Using this decomposition, the $\overline{\chi}^{\bullet}_{\mathcal{T}}$ contribution of all considered cases evidently collapse very well, while the $\overline{\chi}^{\bullet}_{\mathcal{P}}$ component accounts for the changes due to the actual different deviations of the molecular Prandtl number from unity.

The good collapse for the axial velocity as well as for the enthalpy contribution $\overline{\chi}^{\bullet}_{\mathcal{T}}$ indicate a suitable scaling for the first-order statistics, which is not necessarily restricted to low molecular Prandtl numbers near unity.

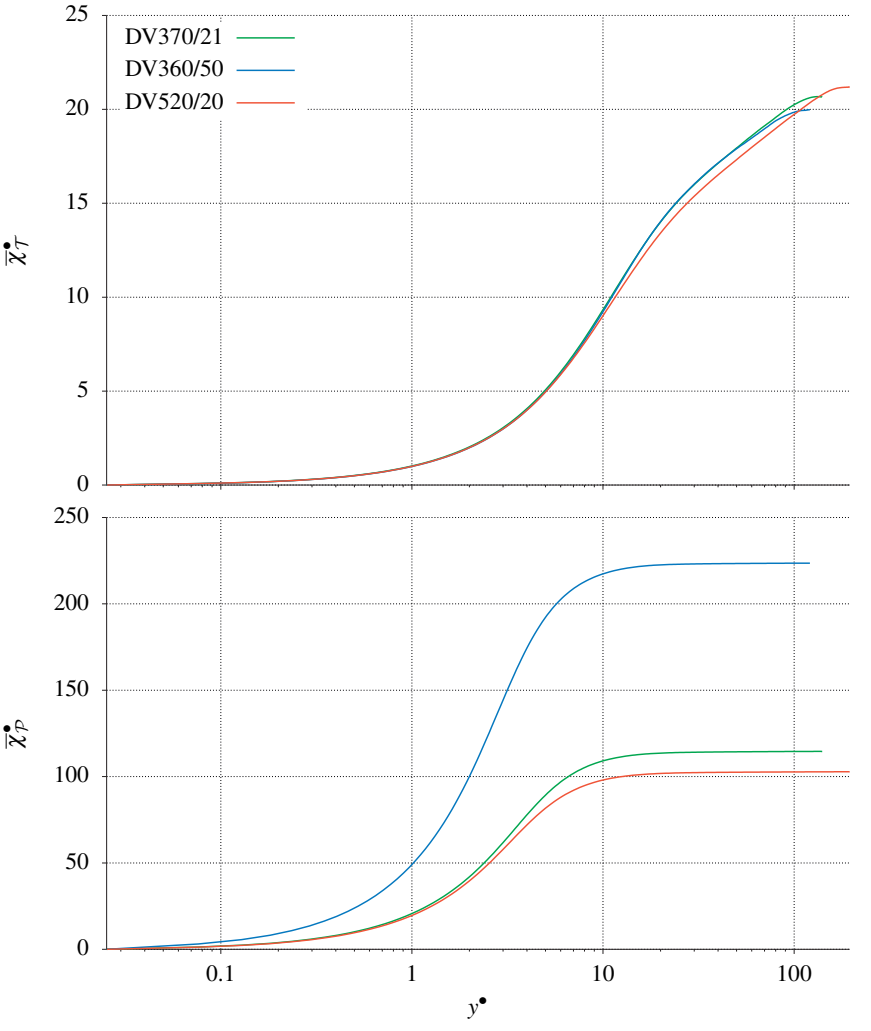

Figure 5.35: $\overline{\chi}^\bullet_T$ and $\overline{\chi}^\bullet_P$ vs. $y^\bullet$

6 NEAR WALL MODEL

In this chapter, some popular state-of-the-art models for the thermal boundary conditions in RANS type simulations are reviewed and compared against the previously shown DNS results. At the beginning the mathematically more elaborate P-function approach originally proposed by Spalding (1967) will be discussed and further developed. The second presently considered approach is the computationally simpler two-layer model.

6.1 P-function approach

The P-function approach was proposed for modeling the thermal boundary conditions in RANS-type simulations at high molecular Prandtl numbers. It represents a well established concept, which is basically derived by relating the total flux of momentum (equation (5.12)) to the total flux of heat (equation (5.24)). Using the non-dimensional representation shown in section 2.4.5, rewritten in wall units, these total fluxes read

$$\tau_{tot}{}^{+} = \frac{\tau_{tot}}{\tau_w} = -\overline{\mu}^{*}\left(1+\frac{\mu_T}{\mu}\right)\frac{\partial \overline{w}^{+}}{\partial y^{+}}, \tag{6.1}$$

$$q_{tot}^{+} = \frac{q_{tot}}{q_w} = -\overline{\mu}^{*}\left(\frac{1}{\mathrm{Pr}_w}\frac{\overline{a}^{*}}{\overline{\nu^{*}}}+\frac{1}{\mathrm{Pr}_T}\frac{\mu_T}{\mu}\right)\frac{\partial \overline{\chi}^{+}}{\partial y^{+}}. \tag{6.2}$$

Dividing (6.2) by (6.1) yields

$$d\overline{\chi}^{+} = \left[\frac{1+\frac{\mu_T}{\mu}}{\frac{1}{\mathrm{Pr}_w}\frac{\overline{a}^{*}}{\overline{\nu^{*}}}+\frac{1}{\mathrm{Pr}_T}\frac{\mu_T}{\mu}}\frac{q_{tot}^{+}}{\tau_{tot}^{+}}\right] d\overline{w}^{+}, \tag{6.3}$$

where the bracketed pre-factor can be interpreted as a total Prandtl number Pr_{tot}. The integration of this differential equation from $\overline{w}^{+}=0$ at the wall, up to some value obtained in the log-law region ($y^{+}>30$) associated with the velocity profile

$$\overline{w}^{+} = \frac{1}{\kappa}\log\left(y^{+}\right)+\beta.$$

finally gives

$$\overline{\chi}^{+} = \int_0^{\overline{w}^{+}} \mathrm{Pr}_{tot}\, d\overline{w}^{+} = \mathrm{Pr}_{T,\infty}\left(\overline{w}^{+}+P\right), \tag{6.4}$$

involving on rhs the bulk turbulent Prandtl number $\mathrm{Pr}_{T,\infty} = (\nu_T/a_T)_\infty$ in the limit of high $y^+ \gg 1$, and the P-function P

$$P = \int_0^\infty \left(\frac{\mathrm{Pr}_{tot}}{\mathrm{Pr}_{T,\infty}} - 1 \right) d\overline{w}^+ = \int_0^\infty \left(\frac{1 + \frac{\mu_T}{\mu}}{\frac{\mathrm{Pr}_{T,\infty}}{\mathrm{Pr}_w} \frac{\overline{a}^*}{\overline{\nu}^*} + \frac{\mathrm{Pr}_{T,\infty}}{\mathrm{Pr}_T} \frac{\mu_T}{\mu}} \frac{q^+_{tot}}{\tau^+_{tot}} - 1 \right) d\overline{w}^+ . \tag{6.5}$$

Considering the fact that the ratio $\mathrm{Pr}_{tot}/\mathrm{Pr}_{T,\infty}$ deviates from unity only beneath the inertial sub-range, the upper limit of the integral in the definition (6.5) has been extended from $\overline{w}^+$ to infinity, without changing the output value of the definite integral. Due to this independence of any upper limit, the P-function represents an universal integration constant in (6.4).

As seen from the definition (6.5), a reliable estimation of the P-function essentially depends on appropriate sub-models for the viscosity ratio μ_T/μ and the turbulent Prandtl number Pr_T in the proximity of the wall. The parameter $\mathrm{Pr}_{T,\infty}$ can be generally assumed to be close to unity, mostly set to $\mathrm{Pr}_{T,\infty} \approx 0.85$.

Various approaches for the computational modeling of turbulent near-wall transfer of momentum and heat can be found in literature, which model the P-function directly, or would deliver equivalent expressions extracted from their model formulations (see, e.g., von Kármán (1939), Hofmann (1940), Spalding (1967), Jayatilleke (1969), Kader and Yaglom (1972), Malin (1987)). Among these, the P-function models of Spalding (1967) and Jayatilleke (1969) have become most popular representatives, especially, when considering molecular Prandtl numbers considerably larger than unity.

Since the integrand of the P-function in (6.5) has essentially support only inside the thermal diffusive sub-layer δ_{th}, which is thinner than the viscous sub-layer δ_m for molecular Prandtl numbers $\mathrm{Pr}_w > 1$, Spalding (1967) argued that the viscosity ratio, defined as

$$\frac{\mu_T}{\mu} = \frac{\rho^*}{\overline{\mu}^*} \ell_m^{+2} \left| \frac{\partial \overline{w}^+}{\partial y^+} \right| , \tag{6.6}$$

can be approximated using a series expansion of the mixing-length ansatz of Van Driest (1956), which is defined as

$$\ell_m^+ = \kappa y^+ \left(1 - \exp\left(-y^+/A^+ \right) \right) , \tag{6.7}$$

in the limit of vanishingly small y^+. Assuming accordingly the near-wall asymptotic behavior inside the viscous sub-layer for the velocity being $\overline{w}^+ = y^+$, this approximation reads

$$\frac{\mu_T}{\mu} \approx \frac{\kappa^2}{A^{+2}} \overline{w}^{+4} . \tag{6.8}$$

As for the turbulent Prandtl number, Spalding (1967) simply assumed the constant bulk value, $\mathrm{Pr}_T = \nu_T/a_T = \mathrm{Pr}_{T,\infty} = \text{const.}$, throughout the whole range of y^+. Applying this uniform value for Pr_T, the approximation (6.8), and further assuming the total flux ratio to be constant and unity over the whole cross-section,

$$\frac{q^+_{tot}}{\tau^+_{tot}} = 1, \tag{6.9}$$

equation (6.5) can be solved analytically to yield

$$P = \left(\frac{\mathrm{Pr}_w}{\mathrm{Pr}_T} - 1\right)\left(\frac{\mathrm{Pr}_T}{\mathrm{Pr}_w}\right)^{\frac{1}{4}} \frac{\pi/4}{\sin(\pi/4)}\left(\frac{A^+}{\kappa}\right)^{\frac{1}{2}}. \tag{6.10}$$

Based on a best fit to a very comprehensive set of experimental data Jayatilleke (1969) later proposed

$$P = 9.24\left[\left(\frac{\mathrm{Pr}_w}{\mathrm{Pr}_T}\right)^{\frac{3}{4}} - 1\right]\left[1 + 0.28\exp\left(-0.007\frac{\mathrm{Pr}_w}{\mathrm{Pr}_T}\right)\right], \tag{6.11}$$

which essentially modifies Spalding's analytically derived expression (6.10) in the lower Prandtl number range near unity, while it still approaches the same asymptotic limit for $\mathrm{Pr}_w \to \infty$.

Both shown P-function approaches assume constant fluid properties. Therefore, the enthalpy profiles predicted by (6.4) using there P-functions are consistently compared against the results of the constant fluid property DNS (DC) cases in figure 6.1. For the model parameters in the P-functions of equations (6.10) and (6.11), a standard setting proposed by Kays and Crawford (1980) was prescribed, using $\kappa = 0.4$, $\beta = 5.5$, $A^+ = 26$ and $\mathrm{Pr}_T = 0.85$. The empirically based correlation of Jayatilleke (1969) shows very good agreement with the DNS data, while the prediction of the analytically based correlation of Spalding (1967) shows worse agreement with increasing molecular Prandtl number. These discrepancies are mainly due to the simplifying assumptions made in the derivation of equation (6.10), which are

- near-wall approximation of the eddy viscosity μ_T/μ
- assumption of unity turbulent flux ratio q^+_{tot}/τ^+_{tot}
- assumption of a constant turbulent Prandtl number Pr_T

In general, an analytically based P-function would be preferred over an empirical one due to the more universal character. For this reason, the presently proposed P-function model basically relies on the same analytical concept as applied by Spalding, while eliminating the shortcomings mentioned above and extending it further to varying fluid properties as well.

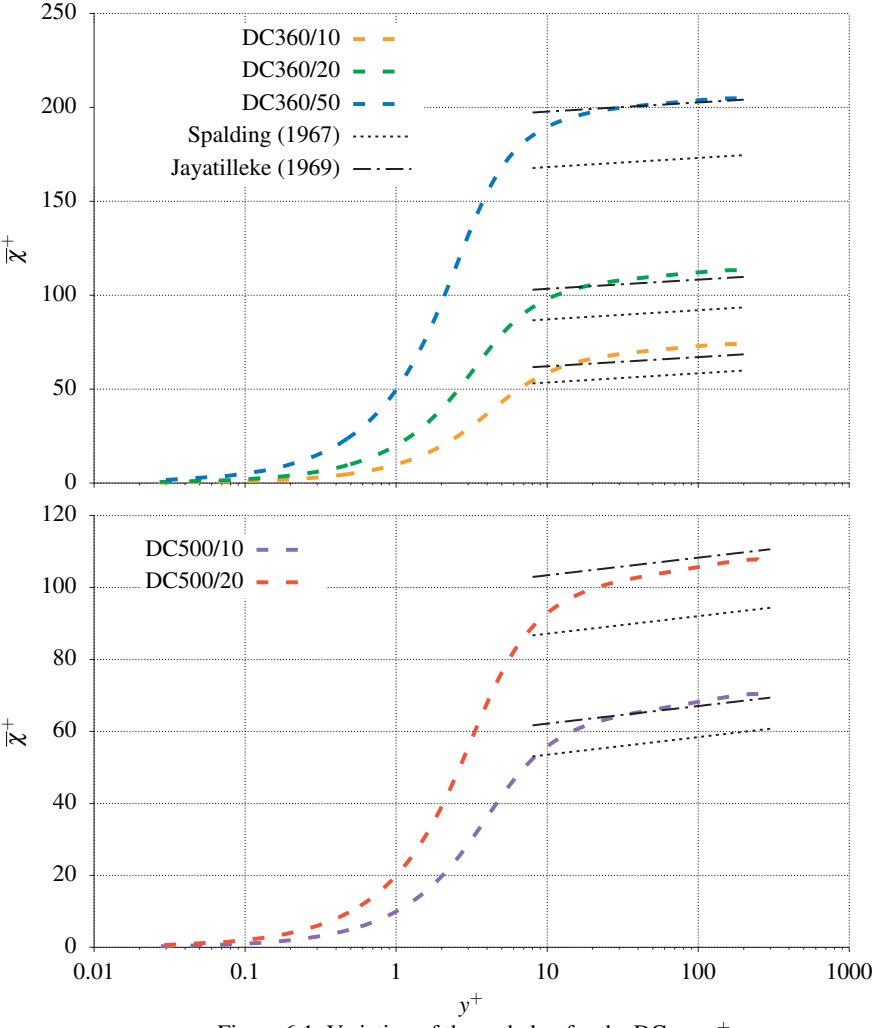

Figure 6.1: Variation of the enthalpy for the DC vs. y^+

6.1.1 Modeling of the eddy viscosity

The present approach prescribes the full van Driest equation for the mixing length rather than the near-wall approximation (6.7) applied by Spalding (1967). This extension notably improves the description of the eddy viscosity, especially in the buffer layer. However, it still predicts a wrong near-wall asymptotics. The eddy viscosity of either approaches, using the full van Driest formulation or its near wall approximation of Spalding (1967) asymptotically varies as y^{+4} next to the wall, whereas analytical considerations as well as the DNS results shown in figure 5.27 require a y^{+3}-dependency. The present approach enforces the correct near wall asymptotic, by adopting a modification of the van Driest mixing length ansatz proposed by Grifoll and Giralt (2000). This modification assumes the damping coefficient (A_m^+) in the van Driest formulation as dependent on y^+ , written as

$$A_m^+ = A_0 \left[1 - \exp\left(-y^+/C\right)\right]^{0.5}, \tag{6.12}$$

with the model parameter C defined as

$$C = \frac{bA_0^2}{\kappa^2}. \tag{6.13}$$

Substituting the modified damping parameter A_m^+ into the mixing length formulation (6.7) yields for the eddy viscosity ratio

$$\frac{\mu_T}{\mu} = \frac{\rho^*}{\overline{\mu^*}} \ell_m (A_m^+)^2 \left|\frac{d\overline{w}^+}{dy^+}\right| = \frac{\rho^*}{\overline{\mu^*}} \left[\kappa y^+ \left(1 - \exp\left(-\frac{y^+}{A_m^+(y^+)}\right)\right)\right]^2 \left|\frac{d\overline{w}^+}{dy^+}\right|. \tag{6.14}$$

The resulting near wall asymptotic behavior of this eddy viscosity formulation for $y^+ \to 0$ can be shown by expanding formulation (6.14) in terms of a series expansion around $y^+ = 0$, which yields

$$\frac{\mu_T}{\mu} = b{y^+}^3 - \frac{b^{3/2}}{\kappa} {y^+}^{7/2} + \mathcal{O}(4), \tag{6.15}$$

predicting the analytically proven correct ${y^+}^3$-dependence near the wall.

The present model for the viscosity ratio evidently involves three parameters, κ, A_0 and b. Van Driest (1956) originally proposed $A_0 = 26$, while Grifoll and Giralt (2000) obtained a better agreement with measurements by increasing this parameter. The best agreement with the present DNS results is observed prescribing a value of $A_0 = 33$. Regarding b, Kays (1994) proposed the setting $b = 0.001$, based on DNS results for a fully turbulent flat plate boundary layer flow, and they considered b as a universal constant for turbulent flows. On the other hand, the present DNS data in the transition regime suggest lower values dependent on the Reynolds number. In the present setting, A_0 is always assumed as constant being $A_0 = 33$, while the other two model parameters, the von Kármán constant κ,

Table 6.1: Setting of κ and b

	κ	b
DC360	0.34	0.0006
DC500	0.36	0.0008

and b were adjusted dependent on the flow Reynolds number. Table (6.1) lists the chosen values of κ and b for the DC cases based on the DNS results.

Figures 6.2 and 6.3 show the DNS based eddy viscosity ratios extracted from DNS com-

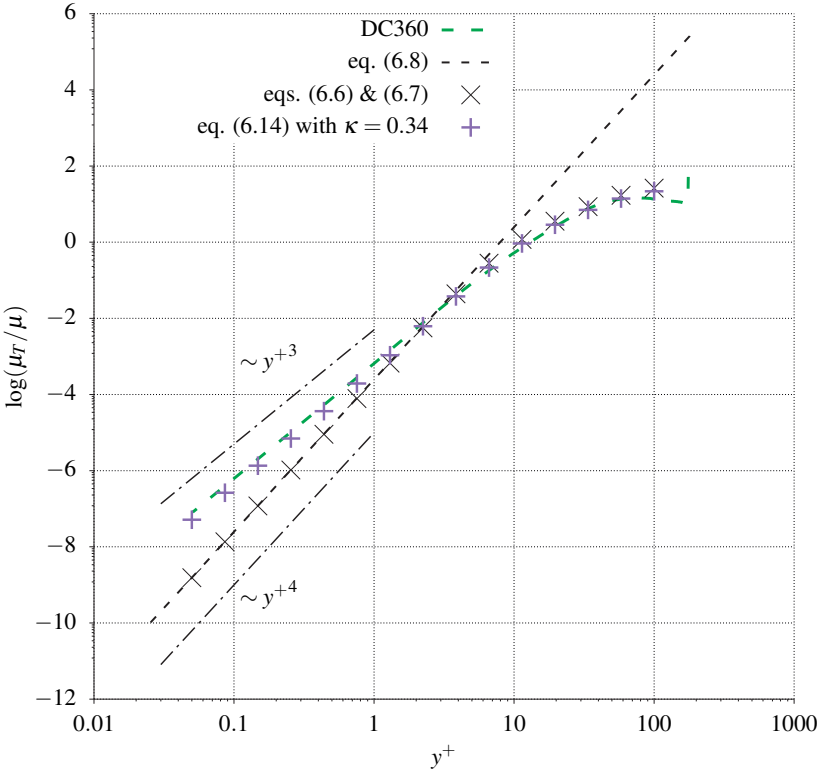

Figure 6.2: Eddy viscosity ratio vs. y^+ for the case with $\mathrm{Re}_{\tau,w} = 360$

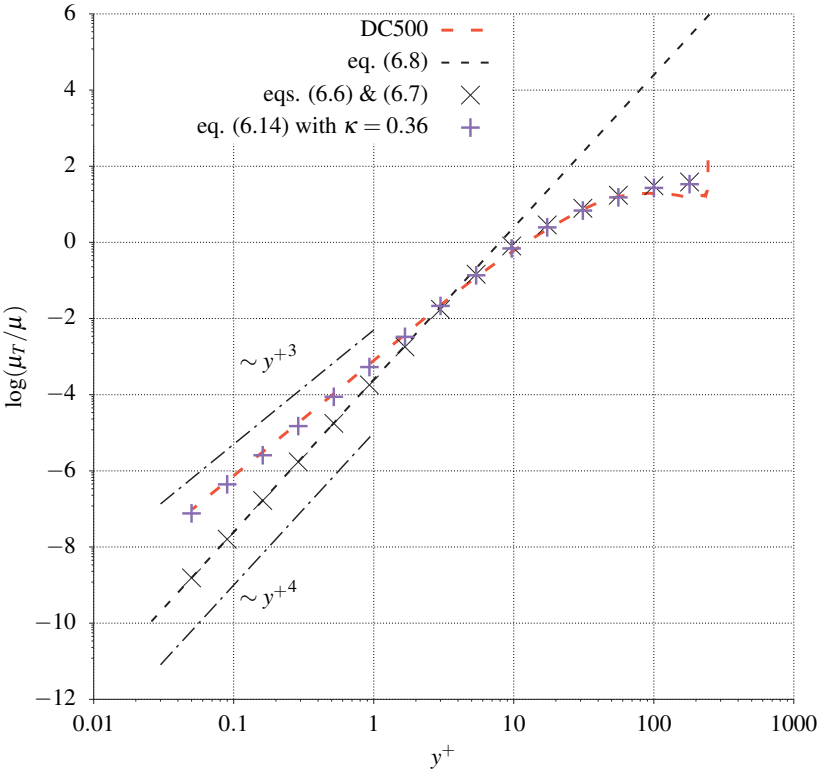

Figure 6.3: Eddy viscosity ratio vs. y^+ for the case with $\mathrm{Re}_{\tau,w} = 500$

pared against the model predictions. In this first step of model development and validation, the fluid properties are still assumed to be constant, implying $\rho^* = 1$ and $\overline{\mu}^* = 1$. The near-wall approximation of the eddy viscosity computed with the van Driest mixing length proposed by Spalding (1967) using the standard setting of $\kappa = 0.4$ and $A^+ = 26$ generally shows the worst agreement. The best agreement with the DNS data over the whole computational domain is shown by the eddy viscosity predicted by equation (6.14). The observed very good agreement of the viscosity ratio predicted by the present approach translates into a reliable prediction of the axial velocity $\overline{w}^+$ dependent on the wall coordinate y^+. The velocity profile is obtained by incorporating the formulation (6.6) into expression for

the total shear stress (6.1), yielding

$$\frac{d\overline{w}^+}{dy^+} = -\frac{2\frac{\tau_{tot}^+}{\overline{\mu}^*}}{1+\sqrt{1-4\,\ell_m^{+2}\tau_{tot}^+\frac{\rho^*}{\overline{\mu}^{*2}}}}. \tag{6.16}$$

The total shear stress τ_{tot}^+ varies linearly with the wall coordinate, as shown in equation (2.94) and the mixing length is evaluated based on (6.14). The formulation for the axial velocity gradient (6.16) is important for two reasons. On the one hand, it is used to express the integrand in the P-function (6.5) in terms of wall distance y^+ instead of velocity $\overline{w}^+$. On the other hand, as follows from the formulation for the temperature (6.4), the predicted axial velocity determines directly the prediction of the temperature. The good agreement of the predicted axial velocity with the DNS data is shown in figure 6.4.

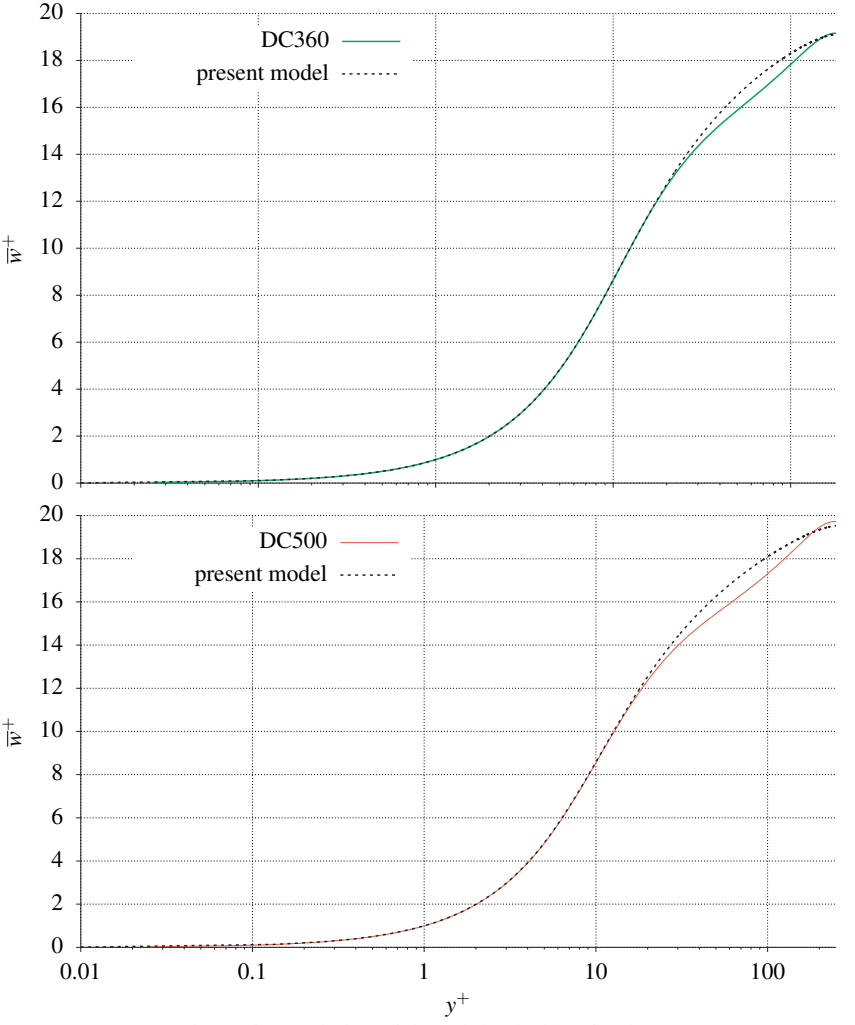

Figure 6.4: Variation of the axial velocities for the DC cases

6.1.2 Analytical determination of the total flux ratio

Assuming hydraulically and thermally fully developed flow with constant wall heat flux, equations (2.94) and (2.96) can be used to compute the radial variation of the total shear stress for the total heat flux, respectively. Rewritten in non-dimensional representation, these fluxes read

$$\tau_{tot}^{+} = -1 + 2\frac{y^{+}}{\mathrm{Re}_{\tau,w}} \tag{6.17}$$

and

$$q_{tot}^{+} = -\frac{1 - \dfrac{1}{\dot{m}^{*}}\dfrac{1}{\mathrm{Re}_{\tau,w}}\displaystyle\int_{0}^{y^{+}} \rho^{*}\overline{w}^{+}\left(1 - 2\frac{\tilde{y}^{+}}{\mathrm{Re}_{\tau,w}}\right)\mathrm{d}\tilde{y}^{+}}{1 - 2\dfrac{y^{+}}{\mathrm{Re}_{\tau,w}}}, \tag{6.18}$$

where the radial coordinate has been consistently replaced by the wall coordinate y^{+} defined as

$$y^{+} = \left(\frac{1}{2} - r^{*}\right)\mathrm{Re}_{\tau,w}. \tag{6.19}$$

The axial velocity occurring in equation (6.18) is computed from the integration of equa-

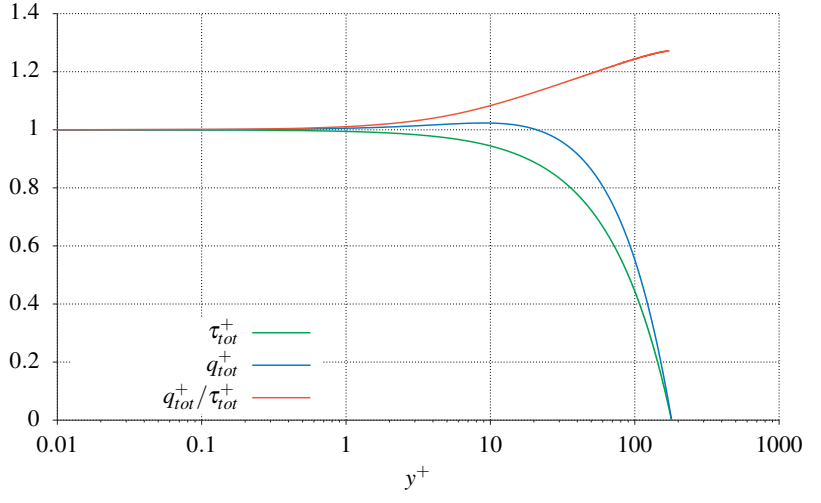

Figure 6.5: Total shear stress and heat flux vs. y^{+} for case DC360/20

tion (6.16). Figure 6.5 plots the analytically obtained solution for the total shear stress and the total heat flux. It can be seen that the total heat flux considerably exceeds the total shear shear stress over the whole radial domain. Therefore, the flux ratio q^+_{tot}/τ^+_{tot} deviates markedly from unity. Including this variation into the P-function, as specified in (6.5), the under-prediction of the original approach of Spalding (1967), who applies the commonly used assumption of unity flux ratio, can be reduced.

6.1.3 Modeling of the turbulent Prandtl number

In literature several models for predicting the turbulent Prandtl number have been proposed. However, none of these approaches can be regarded as superior over the others, which is particularly due to the lack of reliable experimental data for validation.

Some of the existing models, capable of representing the previously shown DNS data will be discussed and validated against the DNS results in the following. In general, these models can be classified into two categories:

- Purely empirical
- Experimentally adapted analytical models (semi-empirical)

Purely empirical

Graeber (1970) performed heat transfer measurements on different geometries for a variety of $\mathrm{Re}_{\tau,w}$ and Pr_w. Based on the measured Nusselt numbers he derived a rather simple correlation for the turbulent Prandtl number. In this correlation the radial variation of the turbulent Prandtl number was completely neglected, and only the molecular Prandtl number is used as model parameter. The empirical correlation reads

$$\mathrm{Pr}_T = 0.91 + 0.13\,\mathrm{Pr}_w^{0.545}, \tag{6.20}$$

and a comparison against DNS data is shown in figure 6.6.

This simple model is evidently capable to account for the increasing asymptotic wall level for increasing molecular Prandtl number as seen in the DNS data, still with under-predictions though. In turn, the insensitivity to the radial position leads to strong over-predictions in the core region.

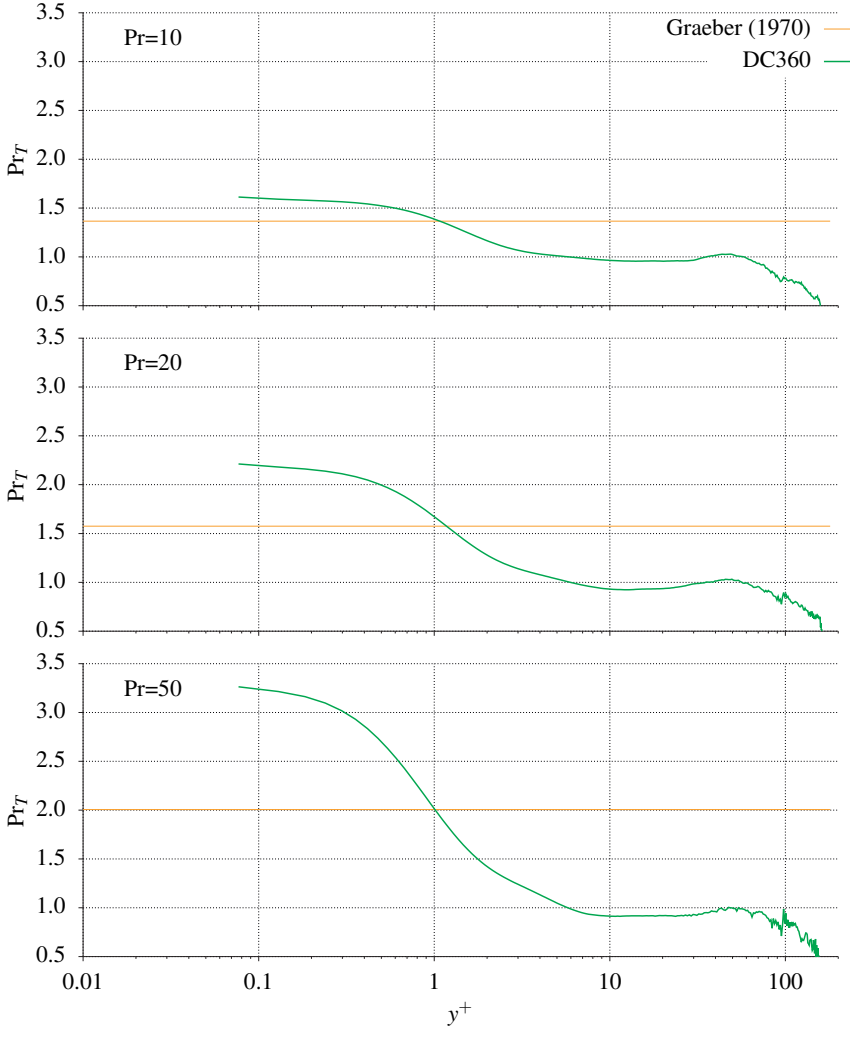

Figure 6.6: Empirical turbulent Prandtl number model compared against the DNS results for case DC360

Experimentally adapted analytical models

Cebeci (1973) proposed a semi-empirical model, where the Van Driest (1956) mixing length ansatz for the momentum is extended to the thermal mixing length. The formulation for the turbulent Prandtl number accordingly reads,

$$\mathrm{Pr}_T = \frac{k_m\left[1-\exp\left(-y^+/A^+\right)\right]}{k_h\left[1-\exp\left(-y^+/B^+\right)\right]}. \tag{6.21}$$

The four model parameters appearing in (6.21) are determined dependent on the Reynolds number, which is defined as

$$\mathrm{Re}_{\delta_2} = \frac{\overline{w}_c\delta_2}{\nu}, \tag{6.22}$$

based on the momentum-thickness δ_2. The empirically obtained functional dependencies read

$$\begin{aligned}
k_m &= 0.40 + \frac{0.19}{1+0.49(\mathrm{Re}_{\delta_2}/1000)^2}\\
k_h &= 0.44 + \frac{0.22}{1+0.42(\mathrm{Re}_{\delta_2}/1000)^2}\\
A^+ &= 26 + \frac{14}{1+(\mathrm{Re}_{\delta_2}/1000)^2}\\
B^+ &= 35 + \frac{25}{1+0.55(\mathrm{Re}_{\delta_2}/1000)^2}.
\end{aligned}$$

For the considered pipe flow the momentum thickness required for Re_{δ_2} is computed from

$$\delta_2 = \int_0^{D/2} \frac{\overline{w}}{\overline{w}_c}\left(1-\frac{\overline{w}}{\overline{w}_c}\right) dr, \tag{6.23}$$

where $\overline{w}_c$ denotes the Reynolds-averaged axial velocity at the center of the pipe. The here evidently unconsidered dependence on the molecular Prandtl was later introduced into the model by Na and Habib (1973). They proposed an empirically based logarithmic relationship between the parameters B^+ and Pr_w written as

$$B^+ = \sum_{i=1}^{5} C_i(\log_{10}\mathrm{Pr}_w)^{i-1} \tag{6.24}$$

with the model constants

$$C_1 = 34.96,\ C_2 = 28.79,\ C_3 = 33.95,\ C_4 = 6.33,\ C_5 = -1.19$$

while they prescribed a standard constant setting for the remaining parameters:

$$k_m = 0.40,\ k_h = 0.44,\ A^+ = 26.$$

Figure 6.7 compares the DNS results of the different molecular Prandtl number cases for $\mathrm{Re}_{\tau,w} = 360$ with the model predictions based on equation (6.21). The model of Cebeci (1973) as well as the extension proposed by Na and Habib (1973) evidently account for the increase towards the wall. However, the magnitude of the asymptotically approached wall level observed in the DNS results is strongly under-predicted for increasing molecular Prandtl number.

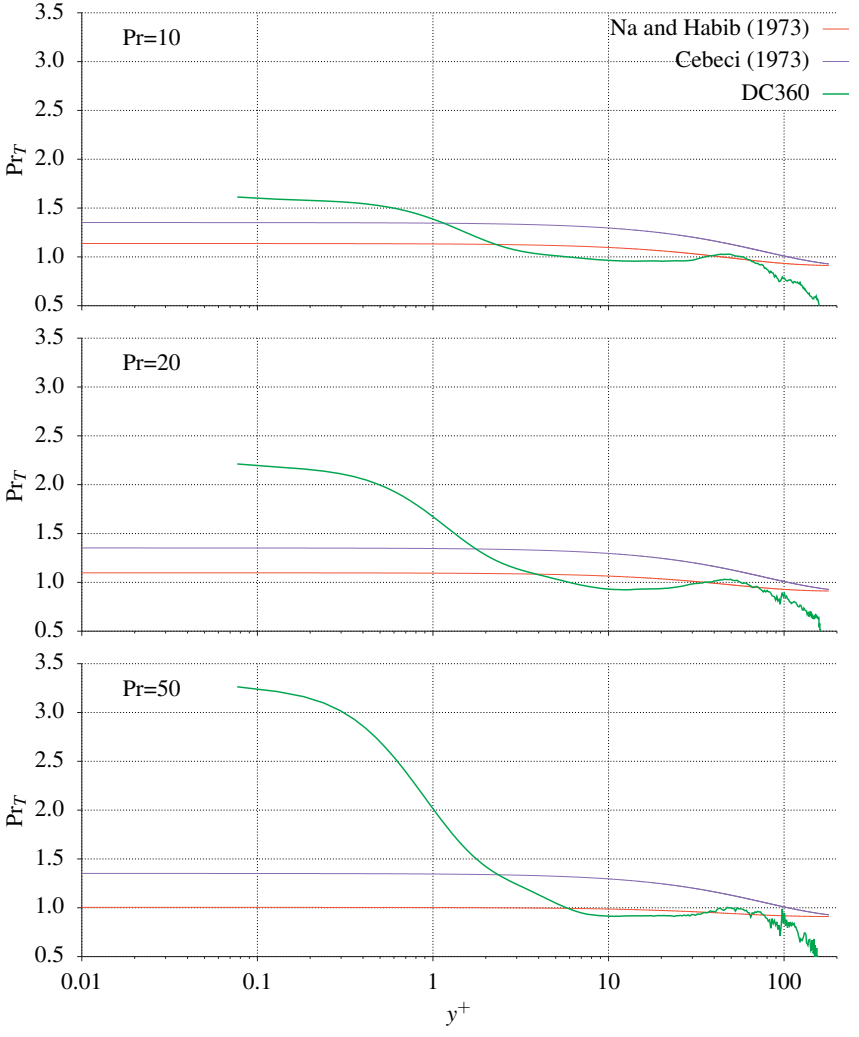

Figure 6.7: Turbulent Prandtl number predictions compared against the DNS results for case DC360

Based on a simplified description of the relevant transfer mechanisms of momentum and heat from a turbulent eddy, Jenkins (1951) proposed an analytical formulation for the turbulent Prandtl number. The principle idea of this approach is that a turbulent eddy loses heat at a different rate than it loses momentum, assuming simple conduction for the thermal heat loss and viscous shear for the momentum loss. The downside of the formulation derived therefrom is that it inherently predicts a uniformly constant $Pr_T = 1$ for unity molecular Prandtl number, and it offers hardly any possibilities for model adjustment. For this reason, Kays and Crawford (1980) extended this approach by the idea that the transfer of momentum is also strongly driven by the action of the turbulent pressure forces rather than by viscous forces. This implies, that the eddies transfer momentum mainly in a non-diffusive way, differently from their diffusive transfer of heat. Their further advanced approach allows for model adjustment introducing a model parameter C_T. Its value was chosen based on experimental data, taken from measurements by Blackwell et al. (1972) for air in a turbulent boundary layer with adverse pressure gradient. The formulation for the turbulent Prandtl number proposed by Kays and Crawford (1980) reads

$$\mathrm{Pr}_T = \left(\frac{0.5}{\mathrm{Pr}_{T\,\infty}} + C_T \mathrm{Pe}_T \sqrt{\frac{1}{\mathrm{Pr}_{T,\infty}}} - (C_T \mathrm{Pe}_T)^2 \left[1 - \exp\left(-\frac{\mathrm{Pr}_{T,\infty}^{-1/2}}{C_T \mathrm{Pe}_T} \right) \right] \right)^{-1},$$

with the model coefficient $C_T = 0.2$, and Pe_T being the turbulent Peclet number defined as

$$\mathrm{Pe}_T = \frac{\mu_T}{\mu} \mathrm{Pr}_w. \tag{6.25}$$

Figure 6.8 compares the predictions of this model against DNS data. The model, by definition approaches the prescribed bulk turbulent Prandtl number $\mathrm{Pr}_{T,\infty}$ in the limit $y^+ \to \infty$. Furthermore, the near wall increase observed in measurements, e.g. Blackwell et al. (1972) and Hollingsworth et al. (1989), as well as in the present DNS results for increasing Prandtl number, is featured by the model. However, it predicts always the same value $\mathrm{Pr}_T = 2\,\mathrm{Pr}_{T,\infty}$ at the wall, regardless of the Prandtl number, which is in much contrast to the DNS results. Aside from this deficit, the model is still capable of prescribing qualitatively the increase of Pr_T towards the wall starting from a wall distance around $y^+ = 5$. For this reason, this model was chosen as a well suited candidate for further improvement to finally produce a better agreement with the DNS results.

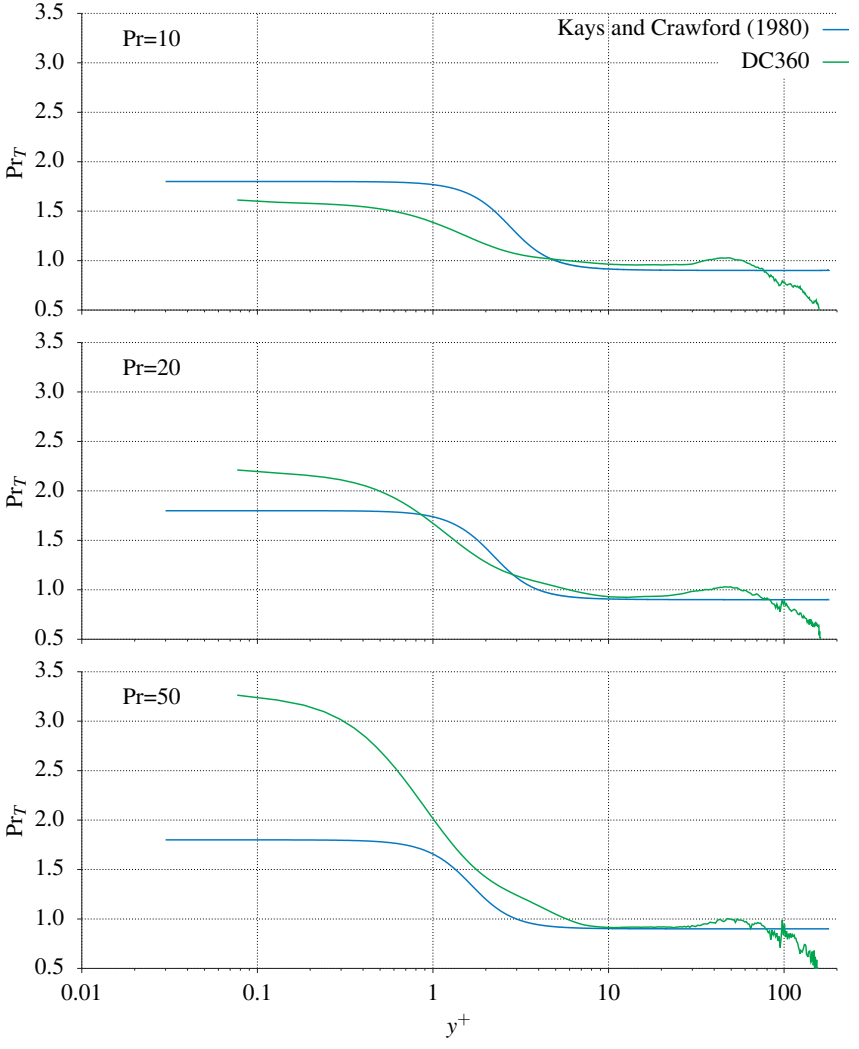

Figure 6.8: Turbulent Prandtl number model of Kays and Crawford (1980) compared against the DNS results for case DC360

Modification of turbulent Prandtl number model

As discussed in section 5.5.3, the magnitude of the asymptotic wall value of the turbulent Prandtl number for the DC cases depends predominately on the molecular Prandtl number and not on the Reynolds number. For this reason, an additional model parameter γ is introduced into equation (6.25), which determines the near wall asymptotics. The inverse of this parameter represents the asymptotically approached wall value of Pr_T dependent on the molecular Prandtl number. Based on a best-fit to DNS data, as shown in figure 6.9, it is defined as

$$\gamma = \frac{1}{\mathrm{Pr}_{T,\infty} + \mathrm{Pr}_w^{0.7}/6}. \tag{6.26}$$

The formulation of the turbulent Prandtl number originally proposed by Kays and Crawford (1980) is accordingly modified to

$$\mathrm{Pr}_T = \left(\gamma + C_T \mathrm{Pe}_T \sqrt{2\left(\frac{1}{\mathrm{Pr}_{T,\infty}} - \gamma\right)} - (C_T \mathrm{Pe}_T)^2 \left[1 - \exp\left(-\frac{1}{C_T \mathrm{Pe}_T} \sqrt{2\left(\frac{1}{\mathrm{Pr}_{T,\infty}} - \gamma\right)} \right) \right] \right)^{-1}, \tag{6.27}$$

The coefficient C_T is set to $C_T = 1.5$. A comparison between the DNS results and the present model can be seen in figure 6.10. The modified formulation evidently reproduces the near-wall asymptotics observed the DNS-results very well, while it predicts the same asymptotic behavior for $y^+ \to \infty$ as the original approach of Kays and Crawford (1980).

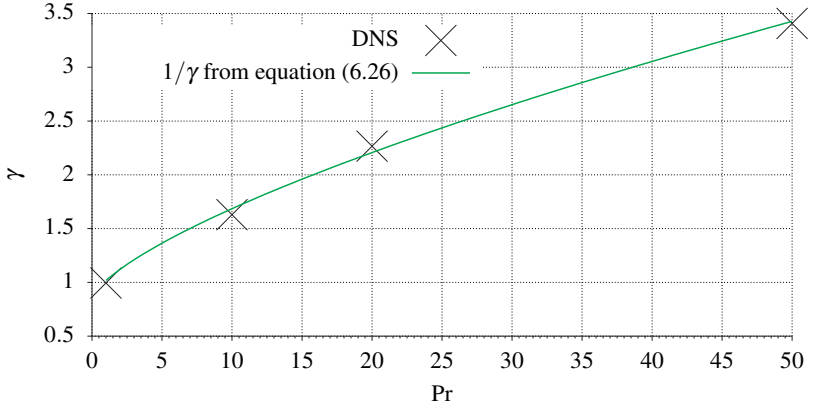

Figure 6.9: Best-fit of the model parameter γ to DNS data for the case DC360

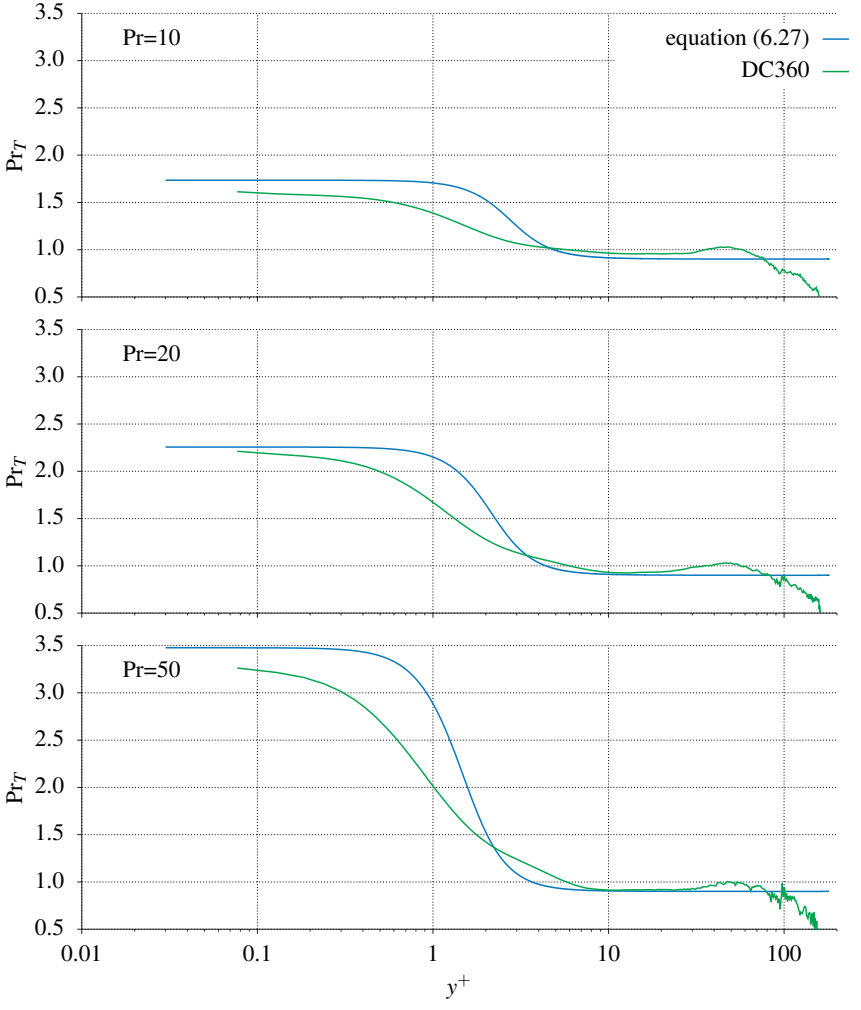

Figure 6.10: Turbulent Prandtl number predicted by modified Kays and Crawford (1980) model using equation (6.27) compared against the DNS results for case DC360

6.1.4 Model validation against DNS for constant fluid properties

Including the presently proposed sub-models for describing the viscosity ratio, the total flux ratio and the turbulent Prandtl number into the formulation for the P-function, defined in (6.5), brings the results of this definite integral very close to the corresponding DNS data. This is exemplary shown in figure 6.11 for the case DC360/20. The model parameters used for all DC cases are listed in table 6.2. The here observed good agreement of the P-function with the corresponding DNS-results further translates into very accurate predictions for the temperature as seen in figure 6.12.

.

Table 6.2: Model parameters for DC cases

Case	κ	A_0	b	$\mathrm{Pr}_{T,\infty}$
DC360/10-50	0.34	33	0.0006	0.85
DC500/10-20	0.36	33	0.0008	0.85

In comparison to the analytical model of Spalding (1967) and its semi-empirical extension of Jayatilleke (1969) the present model offers major improvements with regards to accuracy and applicability.

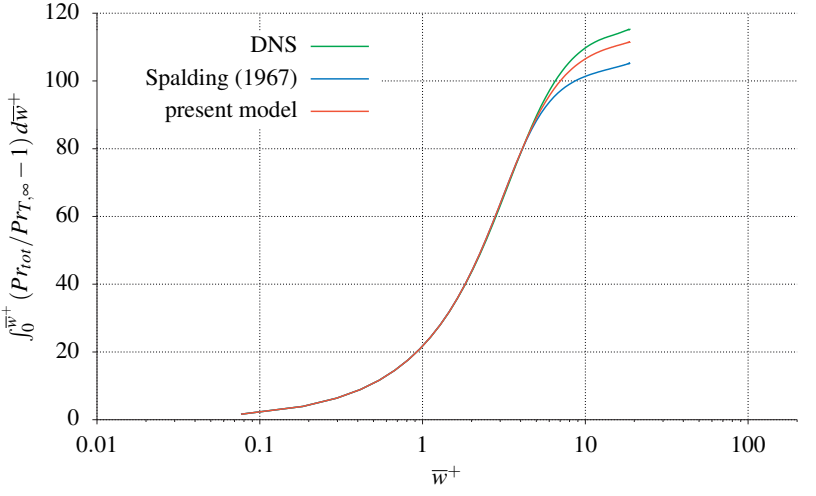

Figure 6.11: Variation of the integral of the P-function with the upper limit $\overline{w}^+$ for case DC360/20

Due to the reliable description of the P-function, the integral of (6.4) can be solved up to an arbitrary y^+ value. Therefore, the whole y^+ domain can be covered, from the diffusive sub-layer up to the inertial sub-range, whereas the classical P-function approach is limited to the inertial sub-range. As such, being not restricted to a certain range of y^+, the present approach provides highly convenient and accurate thermal boundary conditions for RANS with molecular Prandtl numbers well beyond unity. The observed accuracy over the whole y^+-range is also reflected by the global characteristic parameters for the momentum transfer, the skin friction coefficient, computed as

$$c_f = \frac{2}{\overline{w}_b^{+2}}, \tag{6.28}$$

dependent on the bulk velocity defined in equation (5.6). The Nusselt number, which represents an analogous global characteristic parameter for the heat transfer, is computed as

$$\mathrm{Nu}_w = \frac{\mathrm{Re}_{\tau,w}\mathrm{Pr}_w}{\overline{\theta}_b^+}. \tag{6.29}$$

As shown in table 6.3 the predicted skin friction coefficient and Nusselt numbers agree very well with the corresponding DNS results. This indicates, that the bulk velocity $\overline{w}_b^+$ and temperature $\overline{\theta}_b^+$ are predicted very accurately.

Table 6.3: Skin-friction and Nusselt number for the DC cases

Case	c_f^{DNS}	c_f^{model}		Nu^{DNS}	Nu^{model}	
	10^{-3}	10^{-3}	%	–	–	%
DC360/10	9.68	8.88	−4.76	51.40	53.65	4.19
DC360/20	9.68	8.88	−4.76	65.95	67.80	2.73
DC360/50	9.68	8.88	−4.76	89.69	90.86	1.28
DC500/10	8.70	7.97	−7.00	74.89	76.49	2.10
DC500/20	8.70	7.97	−7.00	96.03	97.57	1.57

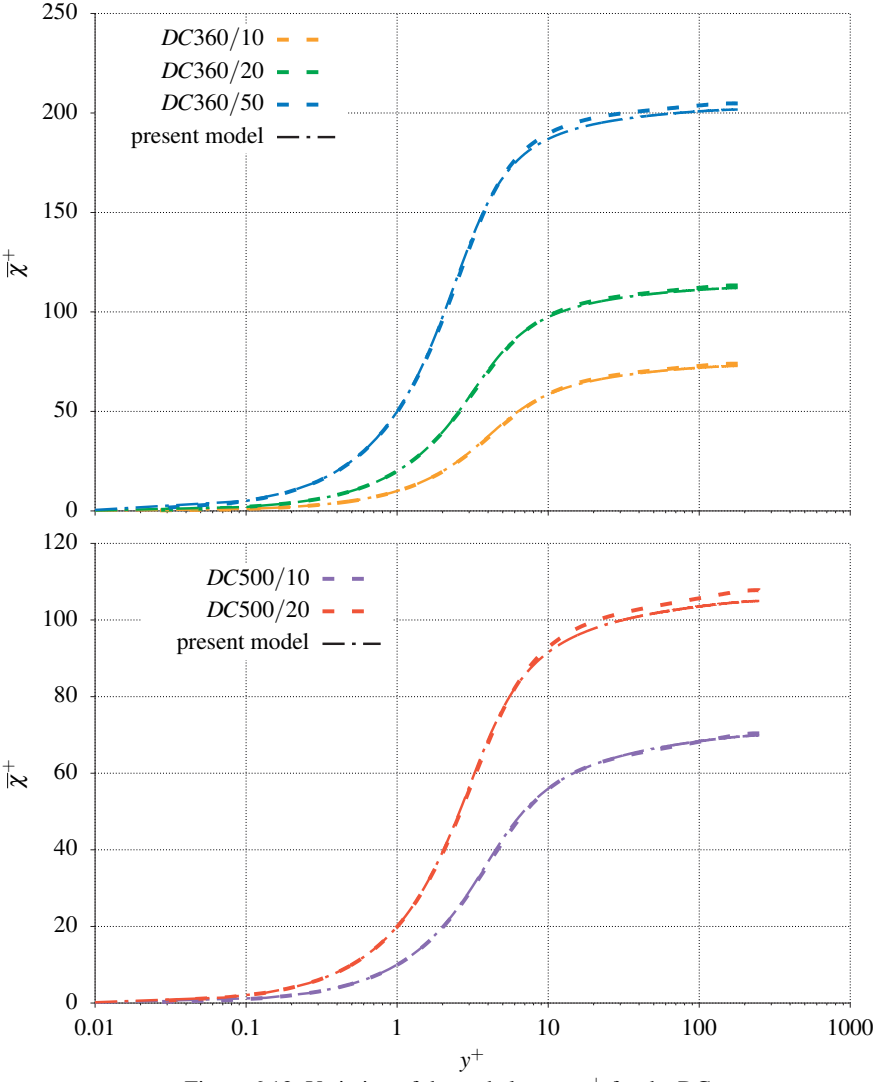

Figure 6.12: Variation of the enthalpy vs. y^+ for the DC cases

6.1.5 Extension to temperature-dependent fluid properties

The approach for the real fluid property cases is essentially the same as for the constant fluid properties, however extended by additional iterative loops in order to account for the variation of the fluid properties. The iteratively recomputed radial temperature variation is used to update the variation of the material properties (section 2.5) which are used in the successive loop for computing the new velocity and temperature field based on equations (6.16) and (6.4), respectively. Additionally, the formulations for the mixing length (6.14) and the turbulent Prandtl number (6.27), were somewhat modified to capture in particular the most significant effect of the temperature-dependent viscosity.

The actually applied modifications will be discussed below.

Modified mixing length formulation

The presently introduced modification starts from revisiting the original concept of the van Driest mixing length, which is based on the second problem of Stokes (1851). This generic flow problem considers the motion of a fluid above an infinite horizontal plate. The plate performs a harmonic horizontal oscillation prescribed by the plate velocity u being

$$u(y=0,t) = u_0 \cos(\omega t). \tag{6.30}$$

For this problem the conservation equations of momentum (2.2) reduce to

$$\frac{\partial u}{\partial t} = \frac{\partial}{\partial y}\left[\nu \frac{\partial u}{\partial y}\right]. \tag{6.31}$$

Using (6.30) as no-slip moving wall boundary condition the solution of (6.31) reads

$$u = u_0 \, e^{-\frac{y}{\sqrt{2}y_s}} \cos\left(\omega t - \frac{y\omega}{\sqrt{2}u_s}\right) \tag{6.32}$$

with the length and velocity scales

$$y_s = \frac{\mu_w}{u_s \rho} \tag{6.33}$$

and

$$u_s = \left(\frac{\mu_w \omega}{\rho}\right)^{1/2}, \tag{6.34}$$

respectively.

Assuming the frame of reference as moving with the oscillating plate, which means a switching to a configuration with a fixed horizontal wall covered by an oscillating fluid,

basically the same solution like (6.32) can be applied, which basically represents a velocity bandwidth u_{BW} determined by the envelope of (6.32) as

$$u_{BW} = \pm u - u_0 \exp\left(-\frac{y}{\sqrt{2}y_s}\right). \tag{6.35}$$

The corresponding local amplitude of the velocity can be accordingly written as

$$u_{BW} \sim u' = u'_0\left(1 - e^{-m\,y}\right) \tag{6.36}$$

with

$$m = \frac{u_s \rho}{\mu_w \sqrt{2}}. \tag{6.37}$$

Figure 6.13 exemplarily shows instantaneous non-dimensional velocity profiles u/u_0 plotted versus y/y_s, based on a numerical solution of equation (6.31). In order to highlights the impact of the viscosity, a viscosity variation similar to the variation for the case DV360/50 (figure 5.8), shown in figure 6.13 is substituted into equation (6.31) which is then numerically solved for $u(t,y)$. It can be seen, that the envelope of equation (6.38) underpredicts the numerical solution, yet by including the bulk viscosity into the formulation of m, as

$$m = \frac{u_s \rho}{\sqrt{2}\mu_b}, \tag{6.38}$$

the agreement with the numerical results can be improved.

Considering the velocity amplitude as turbulent fluctuation (indicated in figure 6.13 with u'), the local turbulent shear stress can be written as

$$-\rho\overline{u'w'} = -\rho\overline{u'_0 w'_0}\left(1 - e^{-m\,y}\right)^2 \tag{6.39}$$

with $-\rho\overline{u'_0 w'_0}$ being the turbulent shear stress in the initial sub-range, which is independent of the viscosity, and is modeled according to Prandtl's mixing length theory as

$$\overline{u'_0 w'_0} = \ell_0^2 \left(\frac{\partial u}{\partial y}\right)^2 \tag{6.40}$$

with

$$\ell_0 = \kappa y. \tag{6.41}$$

The damping coefficient defined in (6.38) is rewritten as

$$m = \frac{w_\tau \rho}{A^+ \mu_b}. \tag{6.42}$$

The definition (6.42) involves the wall friction velocity w_τ as relevant velocity scale and the model parameter A^+, similar to the original Van Driest formulation. On the other

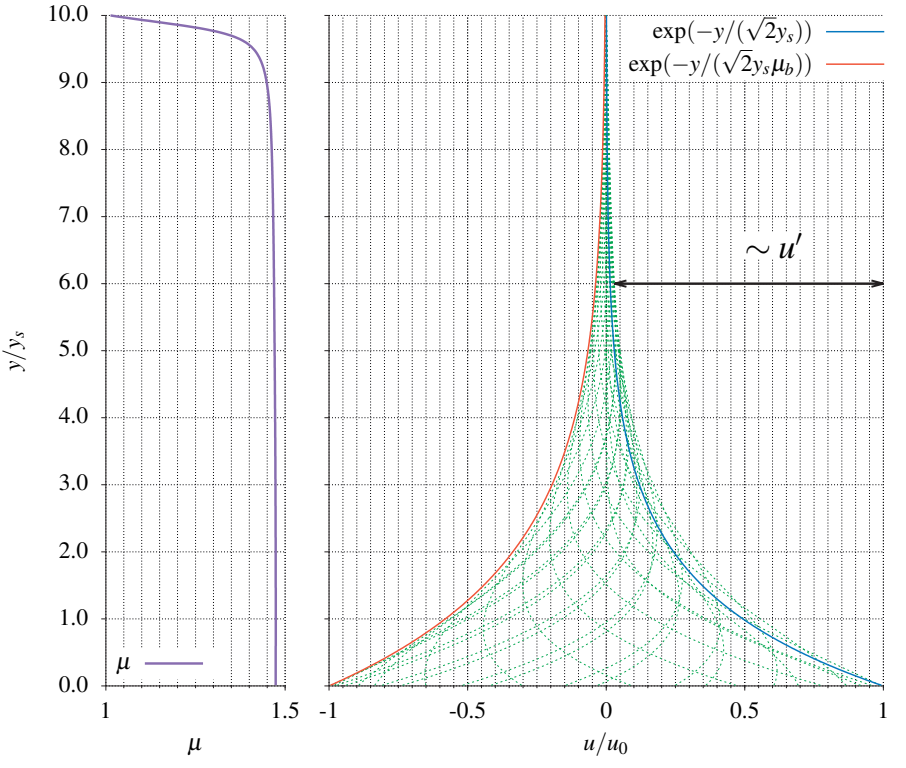

Figure 6.13: Stokes second problem

hand, accounting for the effect of the temperature dependent material properties, the cross-sectional averaged viscosity μ_b is used as relevant value for the viscous damping. Thus, rewriting the mixing length as

$$\ell^+_{m,v} = \kappa y^+ \left[1 - \exp\left(-\frac{y^+}{A^+\overline{\mu}^*_b}\right)\right] \tag{6.43}$$

allows for capturing the increased viscous damping due to the increase of the temperature-dependent viscosity with distance to the wall. Incorporating this modified mixing length formulation (6.43) into the eddy viscosity formulation (6.14) and expanding it in terms of

the wall distance around $y^+ = 0$, yields

$$\frac{\mu_T}{\mu} = \frac{b}{\overline{\mu_b^*}^2} y^{+3} - \frac{b^{3/2}}{\kappa \overline{\mu_b^*}^3} y^{+7/2} + \mathcal{O}(4). \tag{6.44}$$

Consequently, the prefactor of the leading order term on the right-hand side of (6.44) is reduced to

$$\tilde{b} = \frac{b}{\overline{\mu_b^*}^2}, \tag{6.45}$$

so that the near wall asymptotic viscosity ratio becomes

$$\frac{\mu_T}{\mu} = \tilde{b} y^{+3}. \tag{6.46}$$

Figure 6.14 plots the DNS based eddy viscosity of the cases DV370/21 and DV520/20 together with the eddy viscosity predicted from the modified mixing length formulation. It can be seen that the presently applied modification to the mixing length yields a very good agreement with the DNS data over the whole near wall region.

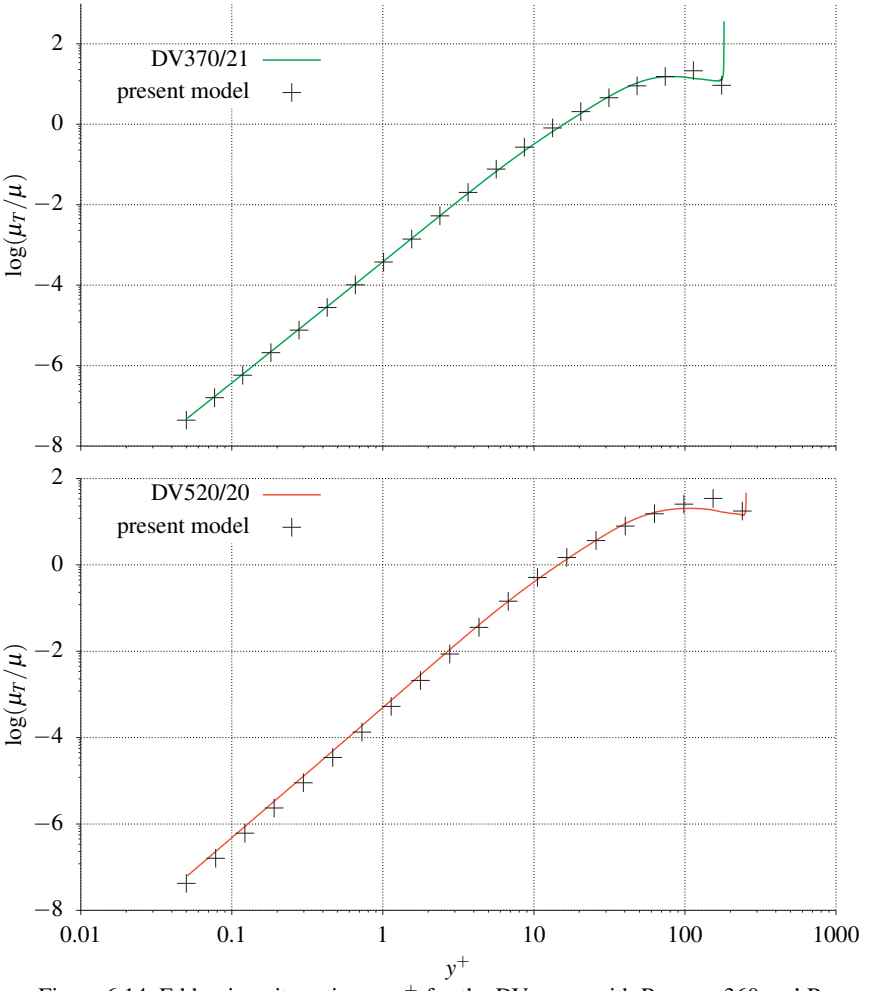

Figure 6.14: Eddy viscosity ratio vs. y^+ for the DV cases with $\mathrm{Re}_{\tau,w} = 360$ and $\mathrm{Re}_{\tau,w} = 500$ and for $\mathrm{Pr}_w = 20$

Modified turbulent Prandtl number formulation

As shown in figure 5.31, the variable fluid properties also alter the radial variation of the turbulent Prandtl number. Especially, the magnitude of the asymptotic wall value decreases notably. The temperature-dependent variation of the material properties already enters the model formulation (6.27) through the local viscosity ratio as part of the turbulent Peclet number, $\mathrm{Pe}_T = \frac{\mu_T}{\mu}\mathrm{Pr}_w$. For reflecting correctly the observed trend in the near wall asymptotics, as noted above, the model parameter γ defined in equation (6.26) is further modified with the relative bulk viscosity μ_b^* to

$$\gamma = \frac{\mu_b^*}{\mathrm{Pr}_{T,\infty} + \mathrm{Pr}_w^{0.7}/6}. \tag{6.47}$$

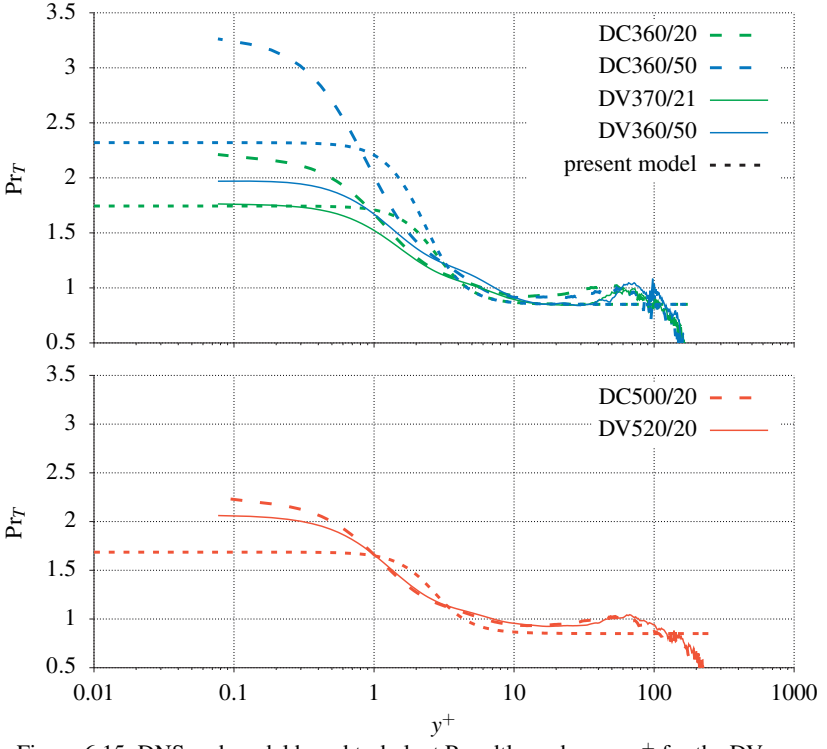

Figure 6.15: DNS and model based turbulent Prandtl number vs. y^+ for the DV cases

Table 6.4: Skin-friction and Nusselt number for the DV cases

Case	c_f^{DNS}	c_f^{model}		Nu^{DNS}	Nu^{model}	
	10^{-3}	10^{-3}	%	–	–	%
DV370/21	9.12	9.04	−0.9	58.11	59.72	2.8
DV360/50	9.43	9.69	2.8	68.66	67.63	−1.5
DV520/20	8.54	8.10	−5.5	90.68	84.50	−6.8

Predicted velocity and enthalpy for the DV cases

Figures 6.16 and 6.17 compare the predictions of the present model for the velocity and enthalpy variation to the corresponding DNS results, including all previously shown modifications and adaptions into the submodels for μ_T/μ and Pr_T.

It can be seen, that the deviations of the predicted velocity and enthalpy variations from the DNS results are very small for all considered cases. The present model evidently predicts very well the whole range from the diffusive near wall sublayer up the inertial sub-range also for the DV cases. Consistently, the predicted skin-friction coefficients and Nusselt numbers, shown in table 6.4, are very close to the DNS data for all here considered cases.

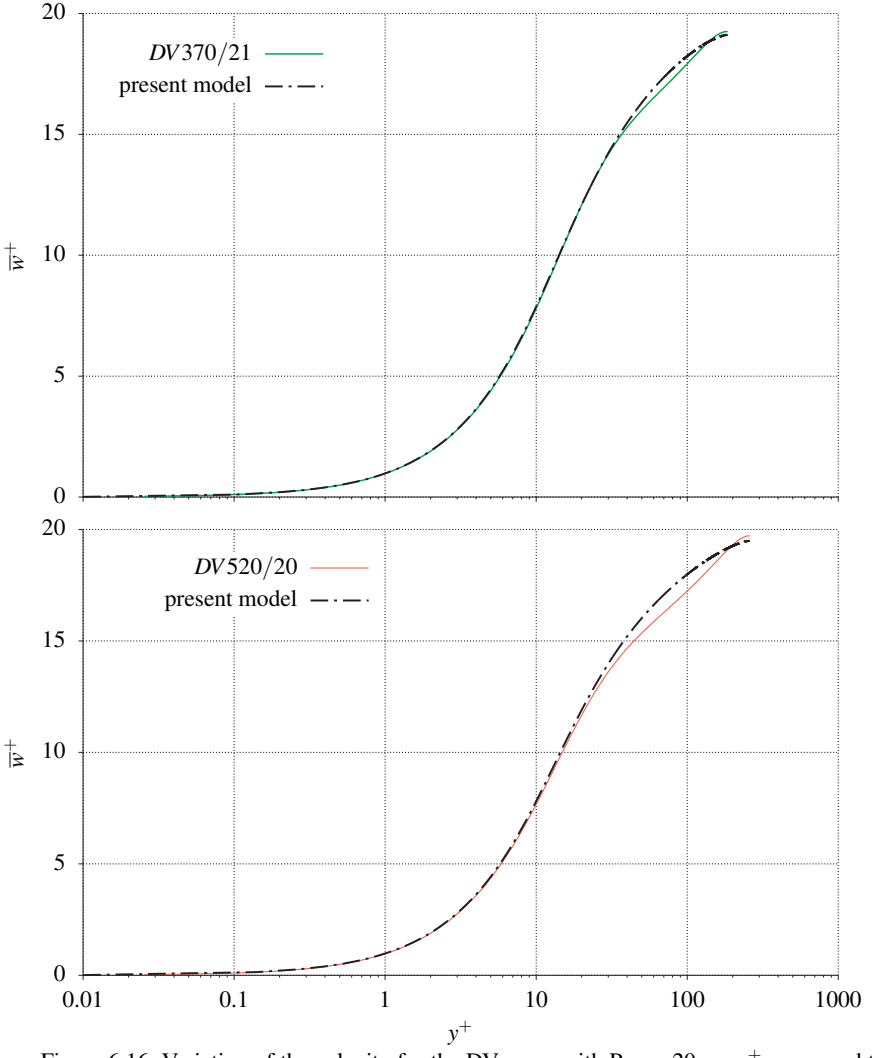

Figure 6.16: Variation of the velocity for the DV cases with $\mathrm{Pr}_w = 20$ vs. y^+ compared to the present model

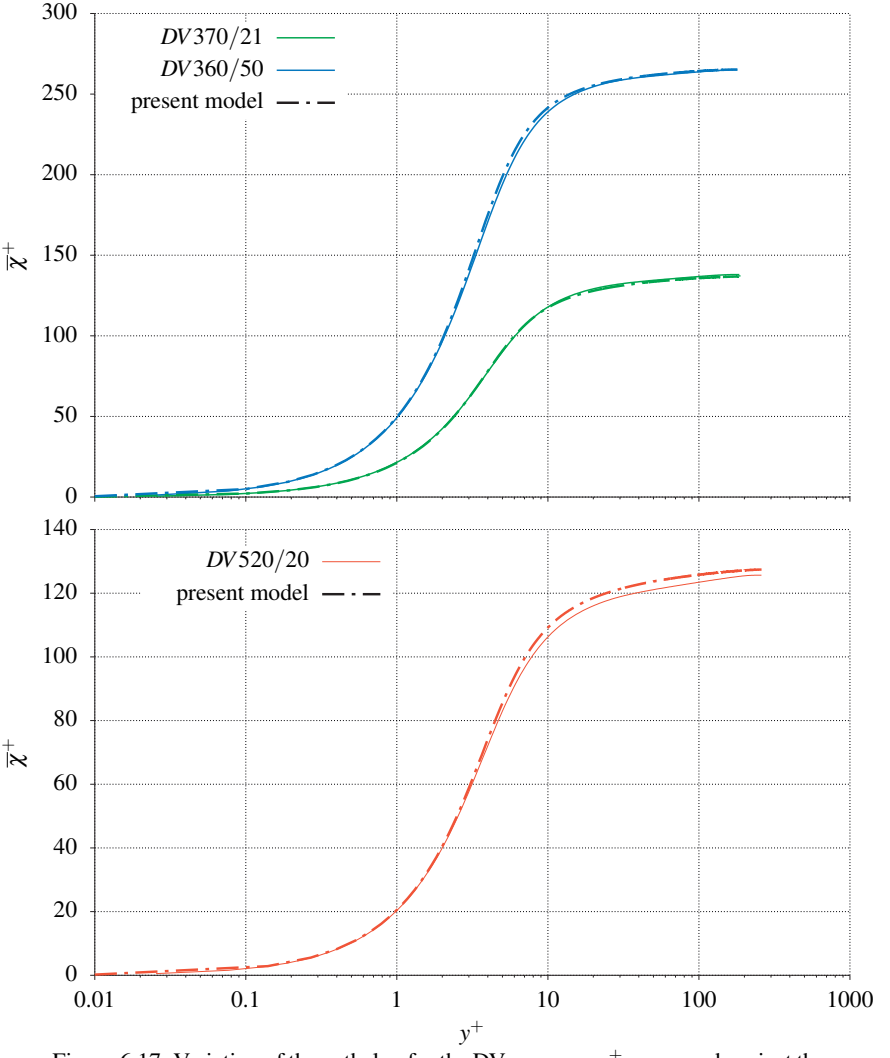

Figure 6.17: Variation of the enthalpy for the DV cases vs. y^+ compared against the present model

6.1.6 Model validation against experiments

For further assessing the scope and the limits of the present model also for flow conditions not amenable to DNS, the model predictions are compared against experimental data, obtained from the own measurements described in chapter 4 and from literature.

Comparison against own measurements

The measurements described in chapter 4 do not provide any information about the radial variation of the axial velocity or the enthalpy. Therefore, the validation of the model is based here on a comparison against the available data, being the measured skin-friction coefficient and Nusselt number. Most high Reynolds number data with $\mathrm{Re}_b > 10^4$ could be acquired in the measurement series M20, associated with $\mathrm{Pr}_w = 20$ to 25. The measured and predicted data for these particular conditions are quantitatively shown in table 6.5. A comprehensive visual validation is further given in figures 6.18 to 6.27, comparing the model predictions against the data of all measurement series M20 to M60 associated with increasing levels of molecular Prandtl numbers, as specified in chapter 4. The two model parameters, κ and b, which markedly determine the viscosity ratio μ_T/μ have been set to $\kappa = 0.4$ and $b = 0.001$, respectively, as suggested by Kays (1994) for the fully turbulent cases. For cases corresponding to the laminar-turbulent transition regime, associated with $\mathrm{Re}_b > 10^4$, the parameters are reduced according to table 6.2.

Table 6.5: Validation cases from the measurement-series M20 and predictions of the present model

	Re_b	$\mathrm{Re}_{\tau,w}$	Pr_w	Nu^{exp}	Nu^{model}	error	c_f^{exp}	c_f^{model}	error
	–	–	–	–	–	%	10^{-3}	10^{-3}	%
M20/1	26592	1544	25	334	329	-1.6	5.90	5.85	-0.9
M20/2	22461	1366	24	290	286	-1.4	6.23	6.07	-2.6
M20/3	18789	1170	24	245	241	-1.6	6.34	6.38	0.6
M20/4	14195	957	23	193	193	-0.2	7.07	6.84	-3.3
M20/5	10175	748	22	140	146	4.0	7.77	7.51	-3.3

The discrepancy between model predictions and experimental data is evidently very small over the whole Reynolds number range. The agreements is generally better with increasing Reynolds number.

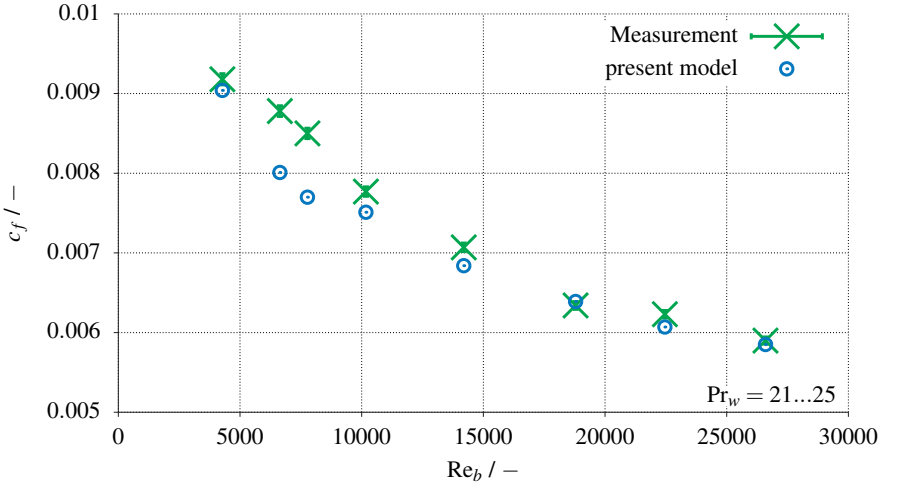

Figure 6.18: Skin-friction coefficient vs. bulk Reynolds number of measurement series M20 compared to the present model

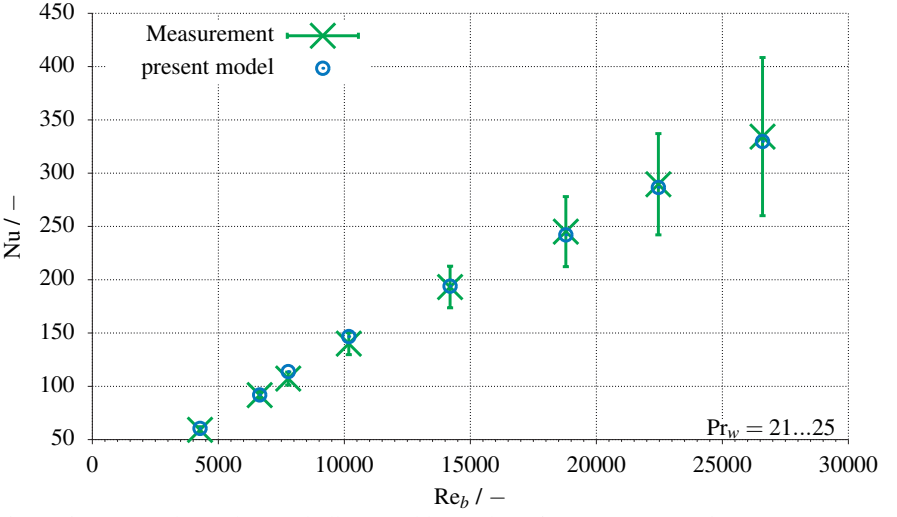

Figure 6.19: Nusselt number vs. bulk Reynolds number of measurement series M20 compared to the present model

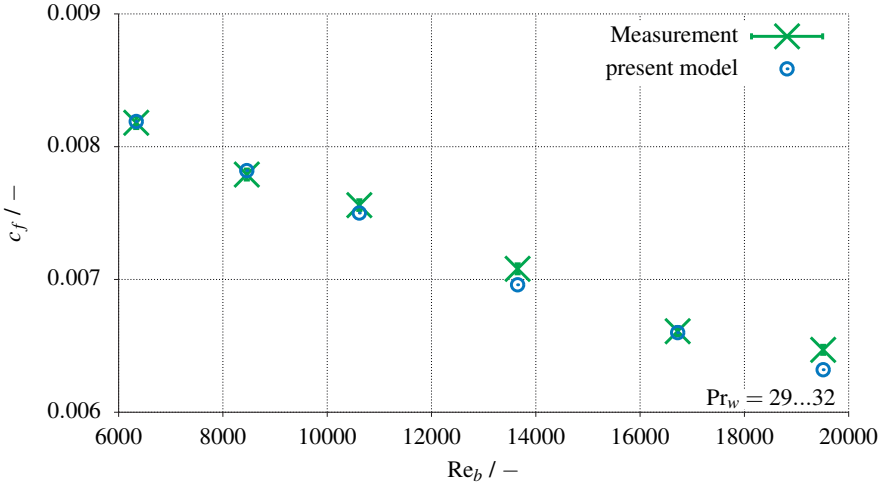

Figure 6.20: Skin-friction coefficient vs. bulk Reynolds number of measurement series M30 compared to the present model

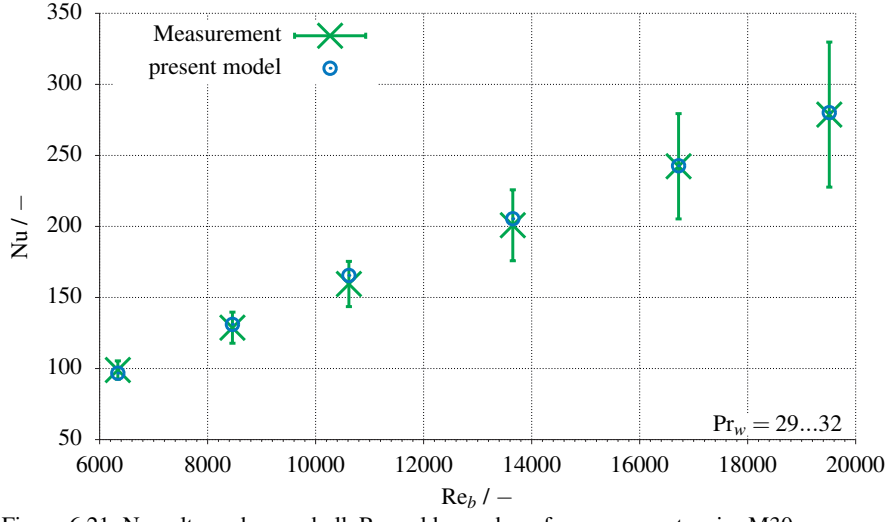

Figure 6.21: Nusselt number vs. bulk Reynolds number of measurement series M30 compared to the present model

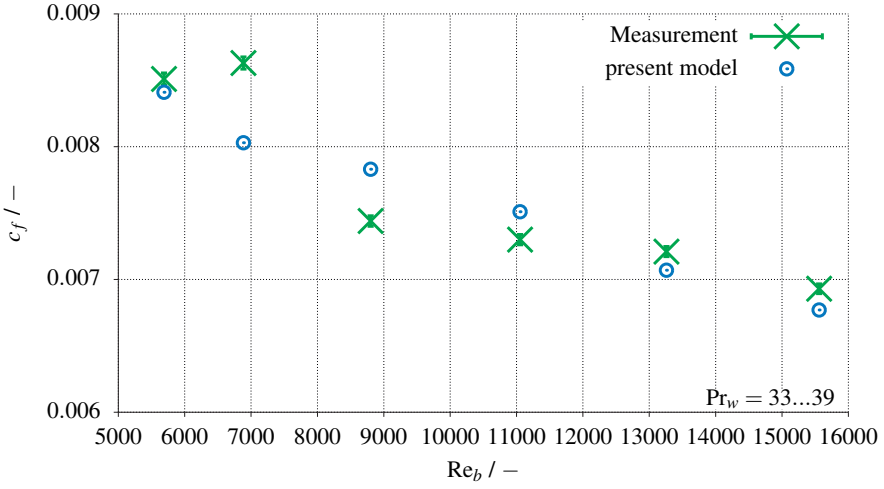

Figure 6.22: Skin-friction coefficient vs. bulk Reynolds number of measurement series M40 compared to the present model

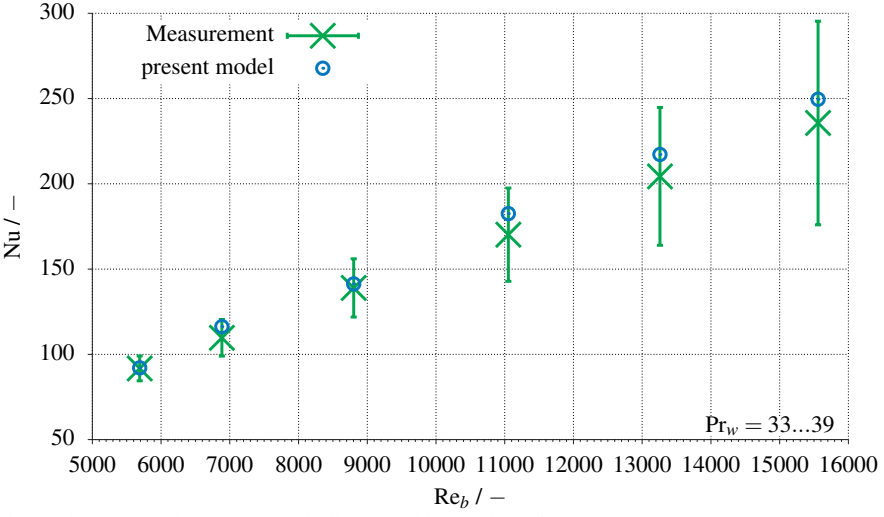

Figure 6.23: Nusselt number vs. bulk Reynolds number of measurement series M40 compared to the present model

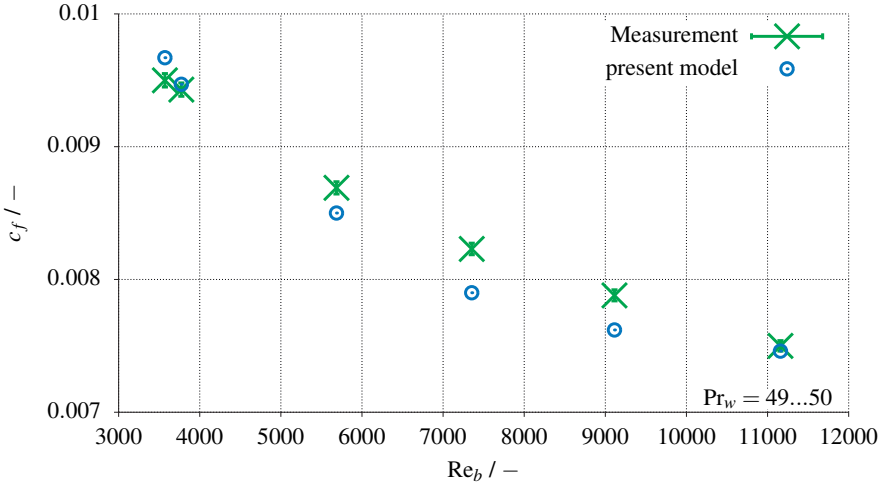

Figure 6.24: Skin-friction coefficient vs. bulk Reynolds number of measurement series M50 compared to the present model

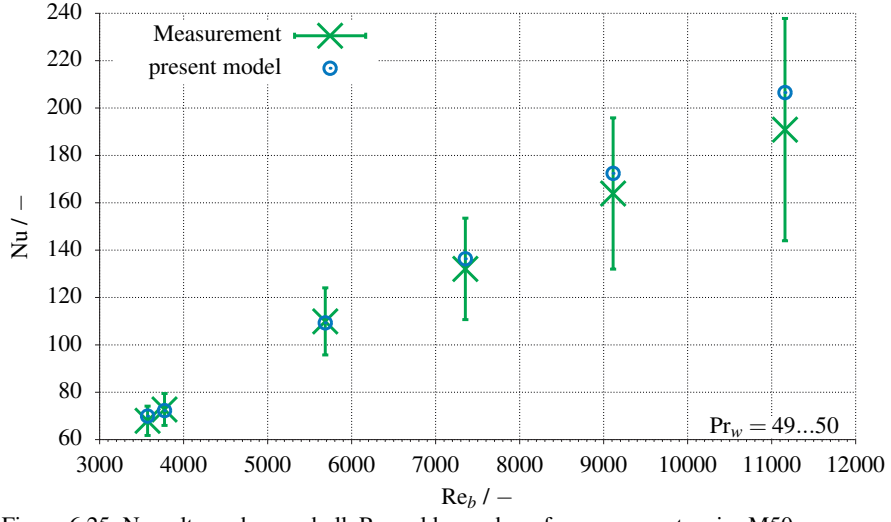

Figure 6.25: Nusselt number vs. bulk Reynolds number of measurement series M50 compared to the present model

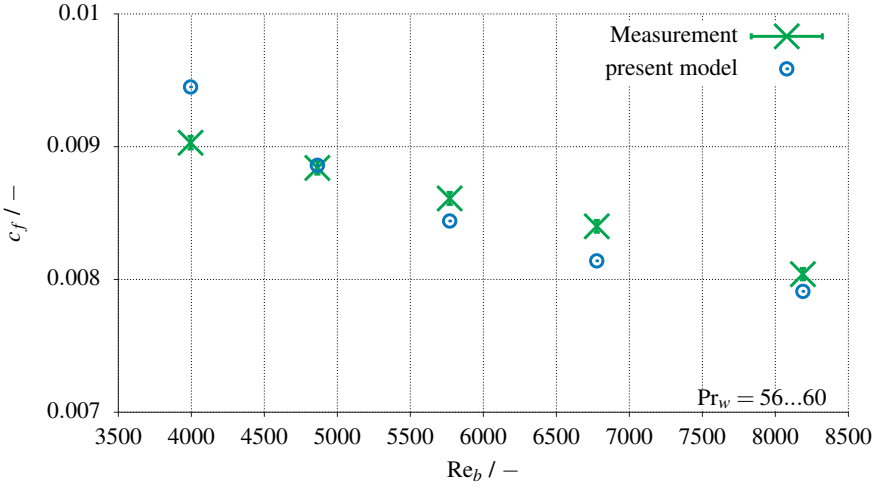

Figure 6.26: Skin-friction coefficient vs. bulk Reynolds number of measurement series M60 compared to the present model

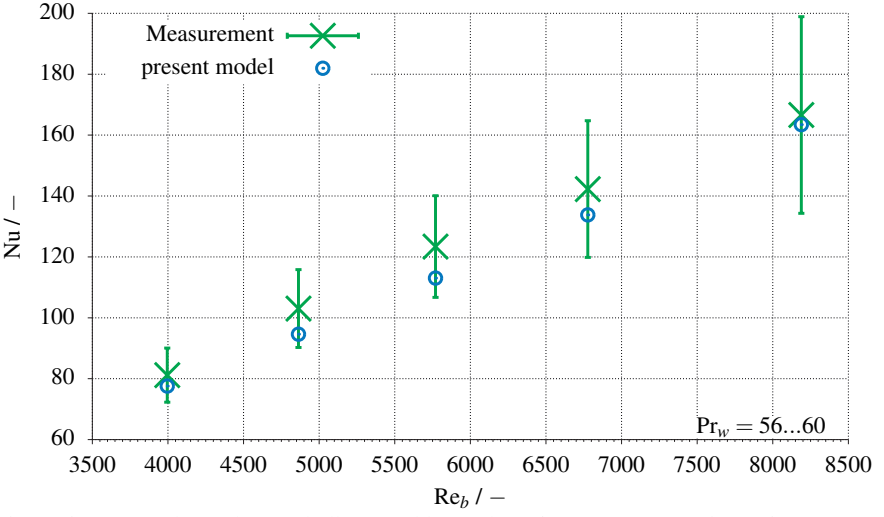

Figure 6.27: Nusselt number vs. bulk Reynolds number of measurement series M60 compared to the present model

Comparison against experimental data from literature

Due to the difficulties in measuring accurately the near wall variation of the enthalpy, reliable experimental data for the enthalpy or temperature variation are very rare, especially for turbulent heated pipe flow with high molecular Prandtl numbers. Hollingsworth et al. (1989) published near wall temperature measurements, yet in a fully turbulent boundary layer of a open channel flow. The momentum thickness based Reynolds number, characterizing this particular flow situation, is defined as

$$\mathrm{Re}_{\delta_2} = \frac{\overline{w}_\infty \delta_2}{\nu_b}, \tag{6.48}$$

with the momentum thickness given as

$$\delta_2 = \int_0^\infty \frac{\overline{w}}{\overline{w}_\infty}\left(1 - \frac{\overline{w}}{\overline{w}_\infty}\right) dy.$$

Hollingsworth et al. (1989) considered a rather high flow rate corresponding to $\mathrm{Re}_{\delta 2} \approx 1400$. The considered fluid was water with a boundary layer averaged Prandtl number of $\mathrm{Pr}_b = 5.9$ and an associated temperature variation inside the boundary layer of $T_w - T_\infty = 4\mathrm{K}$. In order to ensure comparable flow conditions with the present pipe configuration, all free-stream quantities, denoted with "∞" were set to the centerline quantities. The friction Reynolds number $\mathrm{Re}_{\tau,w}$ was equivalently assumed as $\mathrm{Re}_{\tau,w} = 2100$, which provides the same momentum thickness based Reynolds number as in the experiments of Hollingsworth et al. (1989), essentially resulting in a comparable skin-friction coefficient. Since the here considered flow conditions are fully turbulent, the same setting for the parameters κ and b was used as in the comparison against own high Reynolds number data, being $\kappa = 0.4$ and $b = 0.001$. The resulting model predictions for the velocity and temperature are plotted in figures 6.28 and 6.29, respectively.

It can be clearly seen that, the velocity is somewhat over-predicted, especially in the inertial sub-range. The discrepancy is minor, though. As for the temperature variation, the agreement between model and measurement data is very good. The model under-predicts the temperature in the inertial sub-range. However, considering the fact that the reference measurements are fairly old and were obtained with thermocouples, the shown discrepancy may partly also be attributed to considerable measurement errors.

Summing up, it can be stated, that both the comparison against own measurements and available literature data further proves the present model as a reliable approach for predicting the dynamic and thermal near wall conditions at Reynolds numbers and Prandtl numbers beyond the limits of DNS.

6.2 Two-layer approach

The idea of dividing the near wall velocity variation sharply into a laminar layer near the wall and a turbulent core region was originally proposed by Prandtl (1910) and Taylor (1916). This idea was later further extended by von Kármán et al. (1930), leading to the wall laws, as given by equations (5.7) and (5.8). The two-layer approach is still very popular for prescribing near wall boundary conditions in RANS. Hereby, the sharp transition between the two layers is often smoothened using a blending function (see Kader (1981)). In the following, the assumptions and simplifications commonly made for the two-layer approach are reviewed and verified against the DNS results. Based on this validation, a suitable two-layer model formulation shall be developed, which can also predict real flow conditions with temperature-dependent fluid properties with acceptable accuracy. For the computation of the velocity we recall the equations for the total shear stress, already presented in equation (6.1)

$$\tau_{tot}{}^{+} = \underbrace{-\overline{\mu}^{*}\frac{\partial \overline{w}^{+}}{\partial y^{+}}}_{\tau_{lam}{}^{+}} \underbrace{-\overline{\mu}^{*}\frac{\mu_T}{\mu}\frac{\partial \overline{w}^{+}}{\partial y^{+}}}_{\tau_{turb}{}^{+}},$$

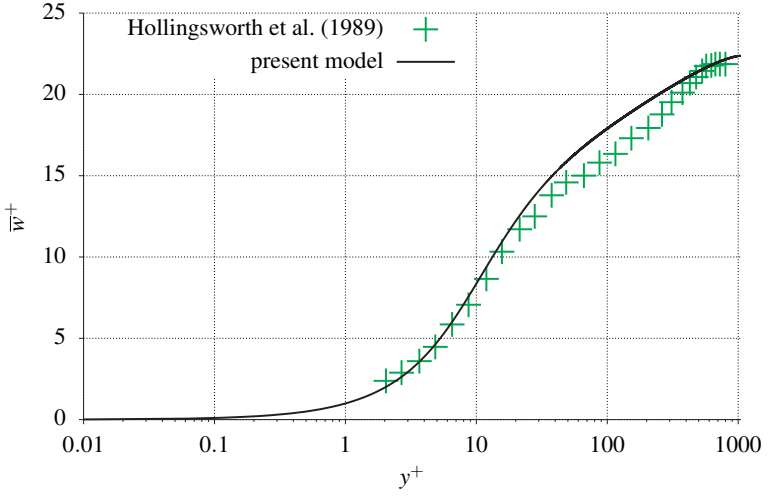

Figure 6.28: Predicted velocity variation $\overline{w}^{+}$ compared against measurements of Hollingsworth et al. (1989)

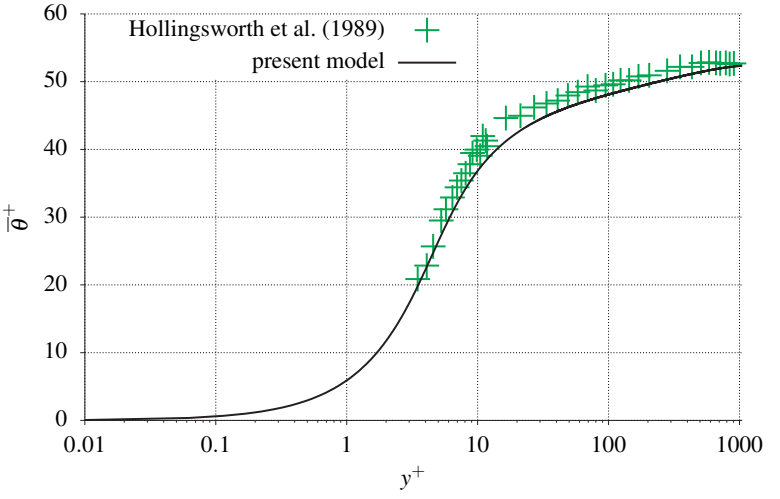

Figure 6.29: Predicted temperature variation compared against measurements of Hollingsworth et al. (1989)

and rearrange it to

$$\overline{w}^+ = -\int_0^{y^+} \frac{{\tau_{tot}}^+}{\overline{\mu}^* + \overline{\mu}^* \dfrac{\mu_T}{\mu}} dy^+. \tag{6.49}$$

Introducing a wall distance $y^+_{c,m}$ representing the boundary between the viscous sublayer and inertial sub-range, the integral (6.49) can be split into two parts. In the first part close to the wall, $0 < y^+ < y^+_{c,m}$, the viscous shear stress is the dominant contribution and the turbulent contribution can be neglected. In the second part, $y^+ > y^+_{c,m}$, the turbulent shear stress is dominant, hence the laminar diffusive contribution can be neglected. The integration of (6.49) is accordingly decomposed into

$$\overline{w}^+ = \begin{cases} -\displaystyle\int_0^{y^+} \frac{{\tau_{tot}}^+}{\overline{\mu}^*} dy^+ & \text{for } y^+ \le y^+_{c,m} \\ -\displaystyle\int_0^{y^+_{c,m}} \frac{{\tau_{tot}}^+}{\overline{\mu}^*} dy^+ - \int_{y^+_{c,m}}^{y^+} \frac{{\tau_{tot}}^+}{\overline{\mu}^* \dfrac{\mu_T}{\mu}} dy^+ & \text{for } y^+ > y^+_{c,m} \end{cases}. \tag{6.50}$$

providing the solution for the respective layers. The applied distinction between the two layers allows for a couple of simplifications. The presently applied simplifications are discussed in the following.

- Near wall variation of the total shear stress:

  Revisiting the analytic solution for the total shear stress, as given by equation (2.94), it can be seen, that τ_{tot}^+ is very close to minus unity in the near wall region, which is represented here by the interval $0 < y^+ < y_{c,m}^+$. This motivates the assumption of a constant total shear stress. Although, being applicable only very close to the wall, this assumption is extended to the fully turbulent region represented by the second integral in (6.50) for $y^+ > y_{c,m}^+$, as it is commonly done in most two-layer approaches.

- Eddy viscosity formulation

  Instead of employing the full eddy viscosity formulation, based on equation (6.14), including the velocity gradient evaluated according to formulation (6.16), which would yield

$$\frac{\mu_T}{\mu} = \frac{\rho^*}{\overline{\mu}^*} \ell_m^{+2} \left| \frac{2\frac{\tau_{tot}^+}{\overline{\mu}^*}}{1+\sqrt{1+4\,\ell_m^{+2}\tau_{tot}^+\frac{\rho^*}{\overline{\mu}^{*2}}}} \right|, \tag{6.51}$$

  Spalding (1961) suggests rather the prescription of the asymptotic limit (6.51) for $y^+ \to \infty$. It is argued, that the eddy viscosity appears in the second integral, covering rather high wall distances, where $\ell_m^+ = \ell_m^+|_{y^+\to\infty} >> 1$, so that equation (6.51) can be simplified to

$$\left.\frac{\mu_T}{\mu}\right|_{y^+\to\infty} \approx \frac{\sqrt{\rho^*}}{\overline{\mu}^*}\,\ell_m^+|_{y^+\to\infty} = \frac{\sqrt{\rho^*}}{\overline{\mu}^*}\,\kappa y^+. \tag{6.52}$$

- Near wall variation of the fluid properties

  As already extensively discussed above, the radial variation of the fluid properties mainly takes place very close to the wall (see figure 5.8). For this reason, the fluid property variation is accounted for in the near wall region, associated with $y^+ \le y_{c,m}^+$. Using the simplification (6.52) the second integral for $y^+ > y_{c,m}^+$ only involves the density, as the viscosity $\overline{\mu}^*$ cancels out. Since the variation of the density is generally very small in the considered temperature range, it can be neglected , assuming $\rho^* = 1$.

Applying the simplifications described above to equation (6.50) the two-layer velocity wall variation can be computed as

$$\overline{w}^+ = \begin{cases} \displaystyle\int_0^{y^+} \frac{1}{\overline{\mu}^*} dy^+ & \text{for } y^+ \leq y^+_{c,m} \\ \underbrace{\displaystyle\int_0^{y^+_{c,m}} \frac{1}{\overline{\mu}^*} dy^+ - \frac{1}{\kappa}\log\left(y^+_{c,m}\right)}_{\beta_m} + \frac{1}{\kappa}\log\left(y^+\right) & \text{for } y^+ > y^+_{c,m} \end{cases} \tag{6.53}$$

Von Karman (1939) proposed an extension of this two-layer approach for computing the temperature variation. Accordingly, the two-layer approach will be applied here for determining the enthalpy variation near the wall. Analogous to the previous derivation of the equation for the velocity, the total heat flux shown in equation (6.2) is split into a laminar and a turbulent contribution, which reads

$$q^+_{tot} = -\underbrace{\frac{\overline{\lambda}^*}{\overline{c_p}^*}\frac{1}{\mathrm{Pr}_w}\frac{\partial \overline{\chi}^+}{\partial y^+}}_{{q_{lam}}^+} - \underbrace{\overline{\mu}^*\frac{1}{\mathrm{Pr}_T}\frac{\mu_T}{\mu}\frac{\partial \overline{\chi}^+}{\partial y^+}}_{{q_{turb}}^+}. \tag{6.54}$$

This equation can be further rearranged and integrated in terms of the wall distance, yielding

$$\overline{\chi}^+ = -\int_0^{y^+} \frac{q^+_{tot}}{\dfrac{\overline{\lambda}^*}{\overline{c_p}^*}\dfrac{1}{\mathrm{Pr}_w} + \overline{\mu}^*\dfrac{1}{\mathrm{Pr}_T}\dfrac{\mu_T}{\mu}} dy^+. \tag{6.55}$$

Introducing a wall distance $y^+_{c,th}$ representing the boundary between the diffusive sublayer and the fully turbulent region, the integral can be split in the same manner as equation (6.50) into two parts, resulting in

$$\overline{\chi}^+ = \begin{cases} -\mathrm{Pr}_w \displaystyle\int_0^{y^+} \frac{q^+_{tot}\overline{c_p}^*}{\overline{\lambda}^*} dy^+ & \text{for } y^+ \leq y^+_{c,th} \qquad (6.56) \\ -\mathrm{Pr}_w \displaystyle\int_0^{y^+_{c,th}} \frac{q^+_{tot}\overline{c_p}^*}{\overline{\lambda}^*} dy^+ - \int_{y^+_{c,th}}^{y^+} \frac{q^+_{tot}\mathrm{Pr}_T}{\overline{\mu}^*\dfrac{\mu_T}{\mu}} dy^+ & \text{for } y^+ > y^+_{c,th}\,. \qquad (6.57) \end{cases}$$

The evaluation of these integrals is based on similar assumptions as applied for the computation of the velocity variation:

- Near wall variation of the total heat flux

  Based on the analytic solution for the total heat flux, as given by equation (2.96), the integrand in the integrals covering the region $y^+ < y_{c,th}$ in equation (6.56) can be reduced to solely a variation of the fluid properties. Similar to the total shear stress, also the total heat flux is assumed as constant minus unity inside the entire considered y^+-region covered by both layers.

- Eddy diffusivity formulation

  The eddy diffusivity, appearing in the second integral of the layer associated with $y^+ > y^+_{c,th}$ in integral (6.57) is determined from the eddy viscosity and the turbulent Prandtl number, as

$$\frac{a_t}{\mu} = \frac{\mu_T}{\mu}\,\frac{1}{\mathrm{Pr}_T}. \tag{6.58}$$

  The eddy viscosity is consistently obtained from the simplified (6.52), whereas the turbulent Prandtl number is prescribed as

$$\frac{1}{\mathrm{Pr}_T} = \frac{\rho\, a_T}{\mu_T} = \frac{1}{\mathrm{Pr}_{T,\infty}}\left[1 - \exp\left(-\frac{y^+}{A^+}\right)\right], \tag{6.59}$$

  involving a van Driest-type damping term to reflected the more pronounced decrease in ρa_T in comparison to μ_T inside the diffusive sublayer, as indicated by the increase of Pr_T near the wall (see figures 5.30 and 5.31).

The resulting two-layer based solution is then obtained upon introduction of the mentioned simplifications into equation (6.56) and (6.57), as

$$\overline{\chi}^+ = \begin{cases} \mathrm{Pr}_w \displaystyle\int_0^{y^+} \frac{\overline{c_p}^*}{\overline{\lambda}^*} dy^+ & \text{for } y^+ \le y^+_{c,th} \\ \mathrm{Pr}_w \displaystyle\int_0^{y^+_{c,th}} \frac{\overline{c_p}^*}{\overline{\lambda}^*} dy^+ + \mathrm{Pr}_{T,\infty} \int_{y^+_{c,th}}^{y^+} \frac{1}{\kappa y^+ \left[1 - \exp\left(-y^+/A^+\right)\right]} dy^+ & \text{for } y^+ > y^+_{c,th} \end{cases}. \tag{6.60}$$

One major challenge of the two-layer approach lies with the definition of a suitable formulation for determining the effective thickness of the viscous and diffusive sublayers in terms of the distances $y^+_{c,m}$ and $y^+_{c,th}$, respectively.

Table 6.6: Model-coefficients $y^+_{c,m}$

α_c^m	27.625
γ_c^m	−0.137
δ_c^m	1.047

Table 6.7: Model-coefficients $y^+_{c,th}$

β_c^{th}	−0.304
δ_c^{th}	−0.294

We assume following functional dependencies

$$y^+_{c,m} = f\left(\mathrm{Re}_{\tau,w}, \mu(T)\right) \tag{6.61}$$

$$\frac{y^+_{c,th}}{y^+_{c,m}} = f\left(\mathrm{Pr}_w, \mu(T)\right) \tag{6.62}$$

which shall be rewritten as the power laws

$$y^+_{c,m} = \alpha_c^m \, \mathrm{Re}_{\tau,w}^{\gamma_c^m} \, (\mu_b^*)^{\delta_c^m} \tag{6.63}$$

$$y^+_{c,th} = y^+_{c,m} \, \mathrm{Pr}_w^{\beta_c^{th}} \, (\mu_b^*)^{\delta_c^{th}} \tag{6.64}$$

dependent on the model parameters α_c^m, β_c^{th}, γ_c^m, δ_c^m and δ_c^{th}. These parameters are obtained from a best fit of the skin-friction coefficients and the Nusselt numbers predicted by the model equations (6.53) and (6.60) against the corresponding DNS results. The resulting coefficients are listed in tables 6.6 and 6.7. The quality of the best-fitted power laws is demonstrated in figures 6.30 and 6.31, comparing the DNS based values $y^{+\ DNS}_{c,m}$ and $y^{+\ DNS}_{c,th}$ against the predictions from (6.63) and (6.64), including the correlation coefficient R^2. The values for $y^{+\ DNS}_{c,m}$ and $y^{+\ DNS}_{c,th}$ are determined by equating the predictions for c_f and Nu_w, obtained from the model formulations (6.53) and (6.60) with the corresponding predictions of the DNS.

The effective thickness of viscous sublayer $y^+_{c,m}$ weakly decreases with the increase of wall friction Reynolds number $Re_{\tau,w}$, as it was expected. The possible influence of the temperature-dependent viscosity is reflected by the positive correlation with μ_b^*. This positive correlation effectively reproduces the thickening of the viscous sublayer observed in figure 5.12 for the DV cases.

The effective thickness of the diffusive sublayer obtained from (6.64) decreases relative to $y^+_{c,m}$ with increasing molecular Prandtl numbers, as it is supposed to be. For the cases with temperature-dependent viscosity this trend is also supported by the negative correlation with μ_b^*, as $\delta_c^{th} < 0$. However, this decreasing tendency for increasing μ_b^* is overcompensated by the increase of the thickness of the viscous sublayer, as $\left(\delta_c^m + \delta_c^{th}\right) > 0$. This on the first glance counter-intuitive behavior, because the increase of the local Prandtl number should suggest the opposite trend, effectively reproduces the thickening of the diffusive sublayer observed for the DV cases as compared to the DC cases, as seen in figure 5.22.

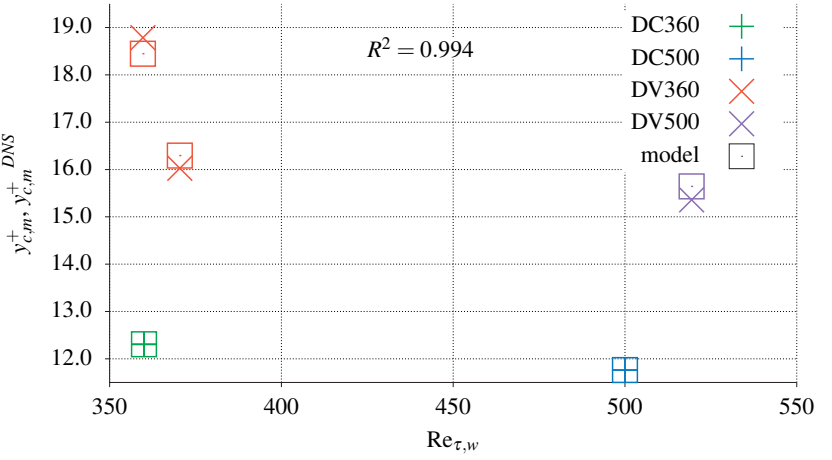

Figure 6.30: DNS based $y^+_{c,m}$ values compared to corresponding fit for the DC and DV cases

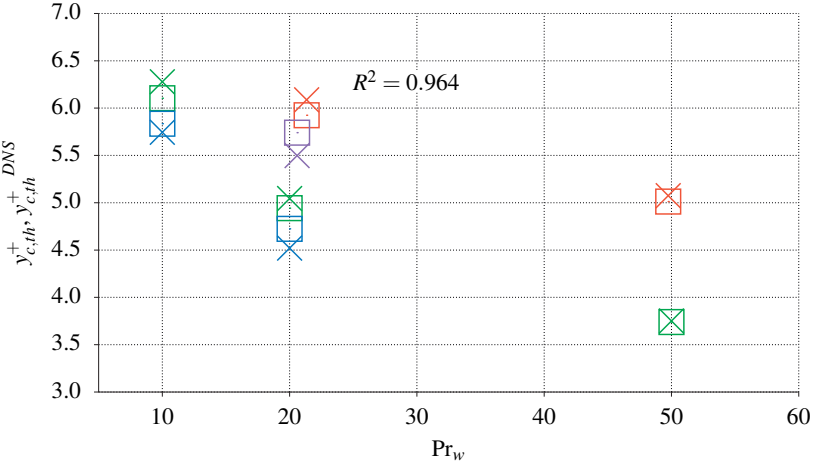

Figure 6.31: DNS based $y^+_{c,th}$ values compared to corresponding fit for the DC and DV cases

Assuming constant material properties and uniform turbulent Prandtl number $\mathrm{Pr}_T \approx \mathrm{Pr}_{T,\infty}$, it can be further shown that the dependence on the molecular Prandtl number implied by (6.64) is in good match with previously proposed alternative descriptions of the fully turbulent region, as found in literature. Setting $\mathrm{Pr}_T = \mathrm{Pr}_{T,\infty}$, equation (6.60) can be analytically integrated for $y^+ > y^+_{c,th}$ yielding

$$\overline{\chi}^+ = \frac{\mathrm{Pr}_{T,\infty}}{\kappa}\log\left(y^+\right) + \underbrace{\mathrm{Pr}_w\, y^+_{c,th} - \frac{\mathrm{Pr}_{T,\infty}}{\kappa}\log\left(y^+_{c,th}\right)}_{\beta_\chi} \tag{6.65}$$

Equation (6.65) resembles the thermal log-law, as commonly applied in the fully turbulent region, with the parameter β_χ being dependent on the molecular Prandtl number only. Substituting $y^+_{c,th}$, as defined by the correlation (6.64), into (6.65), the parameter β_χ can be computed exhibiting the following dependence on the molecular Prandtl number

$$\beta_\chi \propto \mathrm{Pr}_w^{0.696}. \tag{6.66}$$

This dependence is very close to the analytical consideration of Levich (1962), indicating a $\mathrm{Pr}_w^{2/3}$ dependence of β_χ, and results of Kader and Yaglom (1972), who obtained the same dependence by fitting experimental data.

Applying the present correlations for the effective sublayer thickness $y^+_{c,m}$ and $y^+_{c,th}$, the velocity and the enthalpy variation can be determined by numerically solving the equations (6.53) and (6.60). A standard setting is used for the other parameters, in particular, $\kappa = 0.4$, $A^+ = 26$ and $\mathrm{Pr}_{T,\infty} = 0.85$.

Table 6.8: Predicted skin-friction coefficients compared against DNS data for the DC cases.

Case	c_f^{DNS}	c_f^{model}	
	$-$	$-$	$\%$
DC360	$9.30e-03$	$9.22e-03$	-0.95
DC500	$8.53e-03$	$8.61e-03$	0.92

Figures 6.32 and 6.33 show a comparison of the predicted velocity and enthalpy profiles against the DNS data for the DC cases. A comparison of the corresponding skin-friction coefficients and Nusselt numbers is given in table 6.8 and table 6.9, respectively. The most obvious difference to the previously shown predictions of the P-function based model is that the two-layer model does not produce a smooth profile. The kink at the boundary between the two layers, located at $y^+_{c,m}$ and $y^+_{c,th}$ is clearly visible. Despite this conceptual shortcoming, the discrepancy between the DNS based skin friction coefficient and Nusselt

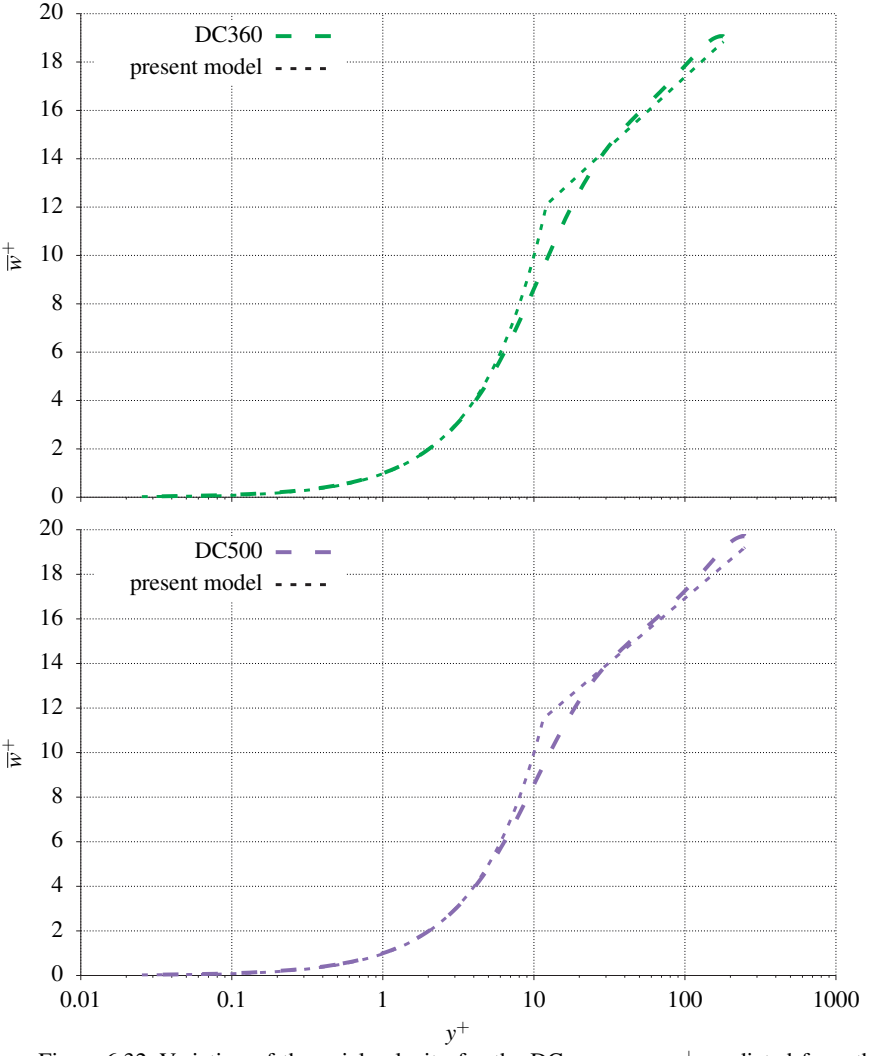

Figure 6.32: Variation of the axial velocity for the DC cases vs. y^+ predicted from the two-layer model

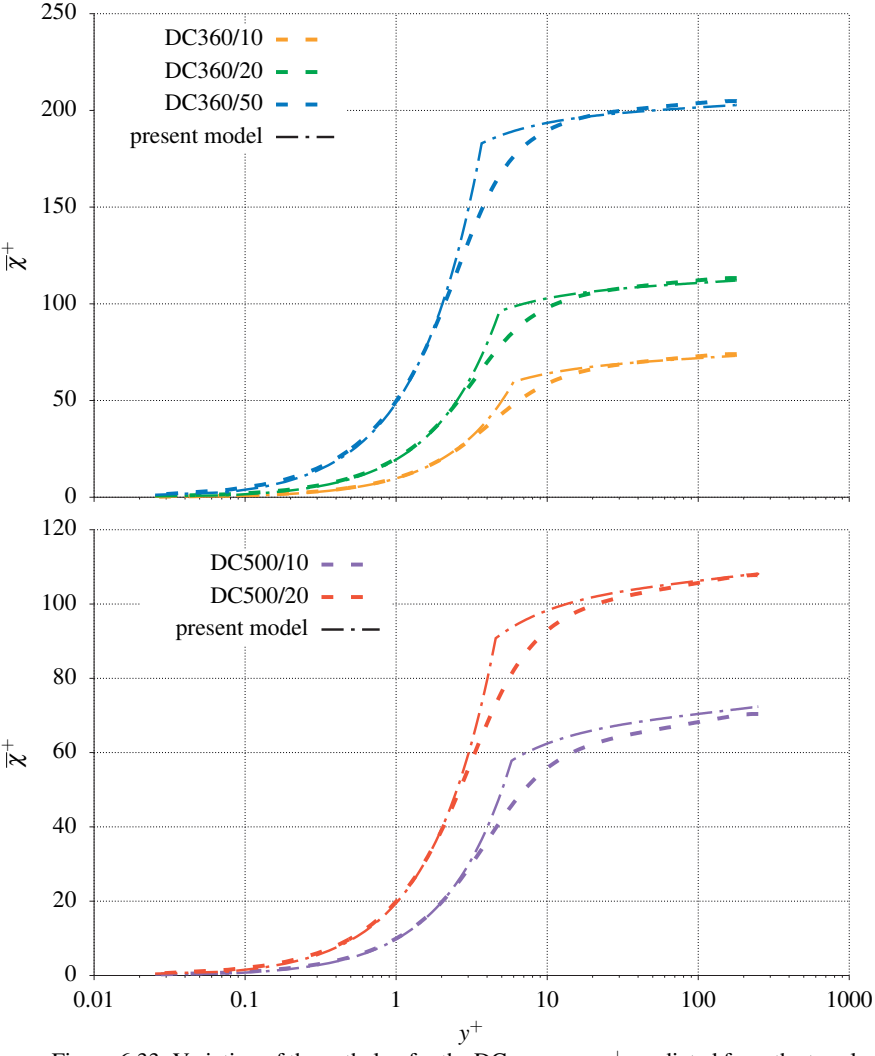

Figure 6.33: Variation of the enthalpy for the DC cases vs. y^+ predicted from the two-layer model

Table 6.9: Predicted Nusselt numbers computed against DNS data for the DC cases.

Case	Nu^{DNS}	Nu^{model}	
	–	–	%
DC360/10	51.40	52.37	1.86
DC360/20	65.95	66.46	0.77
DC360/50	89.69	88.96	−0.82
DC500/10	74.88	73.63	−1.69
DC500/20	96.03	94.41	−1.72

number and the model predictions is still within an acceptable range, particularly in view of the very simple model formulations.

Furthermore, as seen from the radial variations in figures 6.32 and 6.33, the two-layer model predicts the conditions inside the fully turbulent layer pretty well. Since RANS typically impose the wall boundary conditions inside this range, the two-layer model appears as a good candidate for providing suitable dynamic and thermal boundary conditions in RANS-type simulations.

In the cases with variable fluid properties, basically the same iterative procedure as used in the P-function approach for computing the temperature-dependent thermo-physical properties is employed. The resulting radial variations of the velocity and enthalpy can be seen in figures 6.34 and 6.35, respectively. Table 6.10 and table 6.11 compare the predicted skin-friction coefficients and Nusselt numbers against the DNS results, respectively.

Table 6.10: Predicted skin-friction coefficients compared against DNS data for the DV cases.

Case	c_f^{DNS}	c_f^{model}	
	–	–	%
DV370/21	$9.12e-03$	$9.13e-03$	0.1
DV360/50	$9.43e-03$	$9.56e-03$	1.3
DV520/20	$8.54e-03$	$8.42e-03$	−1.4

Again the most pronounced discrepancies are observed near the kinks of the two-layer profiles. On the other hand, the conditions inside the fully turbulent layer are still predicted reasonably well. This translates again into the fairly well predicted wall friction coefficients and Nusselt numbers shown in tables 6.10 and 6.11, respectively.

In summary, it can be stated that despite the strong simplifications leading to a rather simple model formulation, the obtained predictions are generally in good agreement with

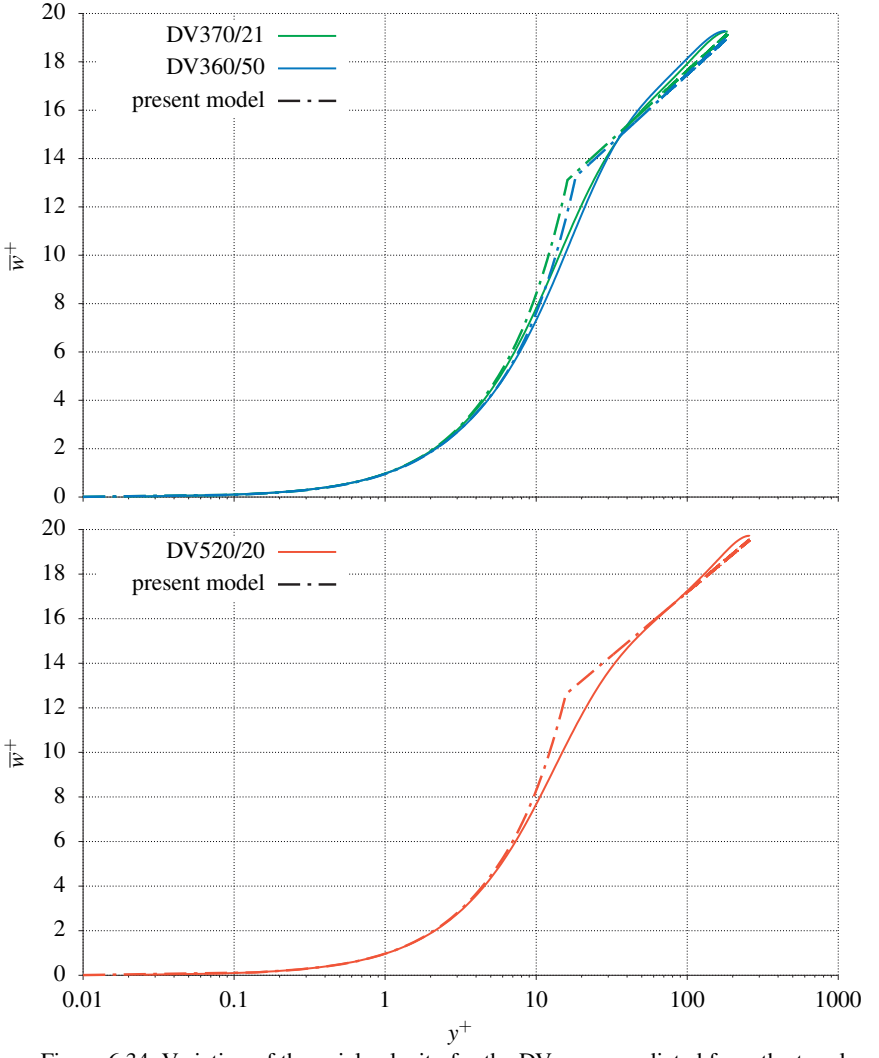

Figure 6.34: Variation of the axial velocity for the DV cases predicted from the two-layer model

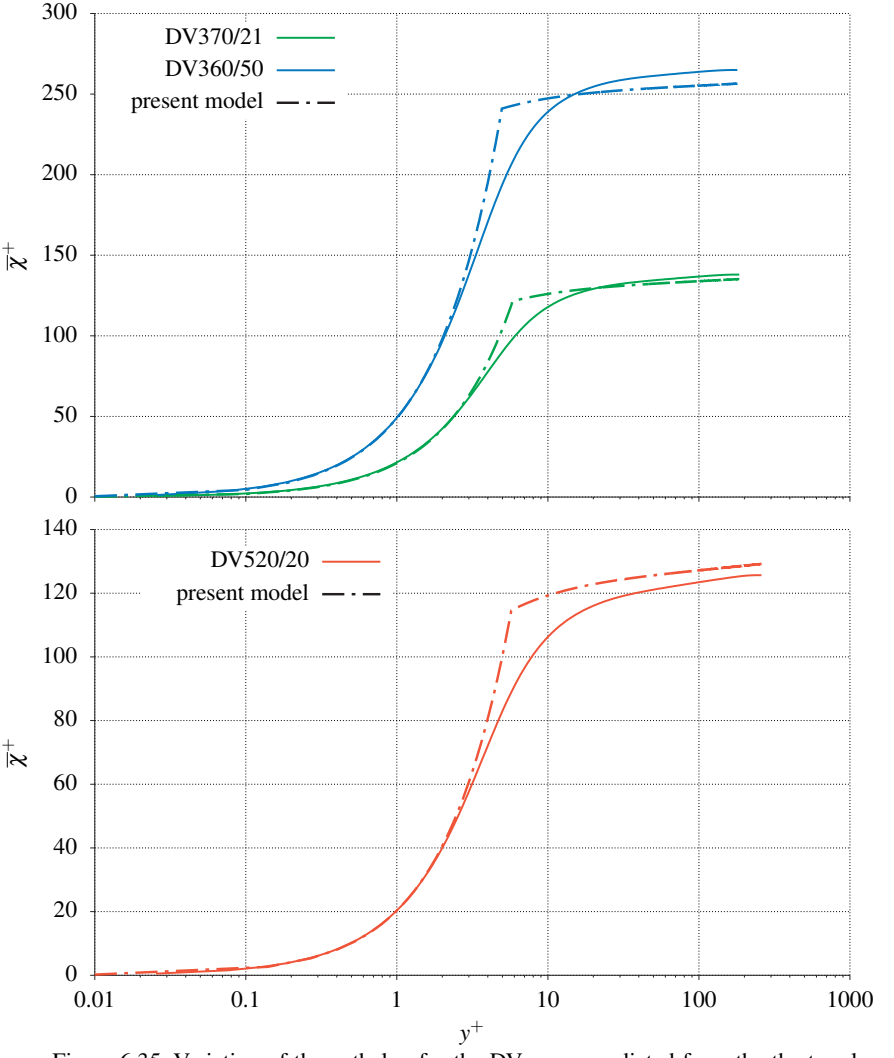

Figure 6.35: Variation of the enthalpy for the DV cases predicted from the the two-layer model

Table 6.11: Predicted Nusselt numbers compared against DNS data for the DV cases.

Case	Nu^{DNS}	Nu^{model}	
	–	–	%
DV370/21	58.11	60.71	4.5
DV360/50	68.66	71.43	4.0
DV520/20	90.68	85.07	−6.2

the DNS data for the constant as well as the variable fluid property cases. Such a good agreement is also seen in the figures (6.36) - (6.45), where the predictions of the present two-layer model for the skin friction coefficient and the Nusselt number are compared against all own experimental data acquired in the measurement series M20 to M60, shown in chapter 4. This comparison extends the validation of the model to a high Reynolds and Prandtl number range not amenable to DNS.

M20

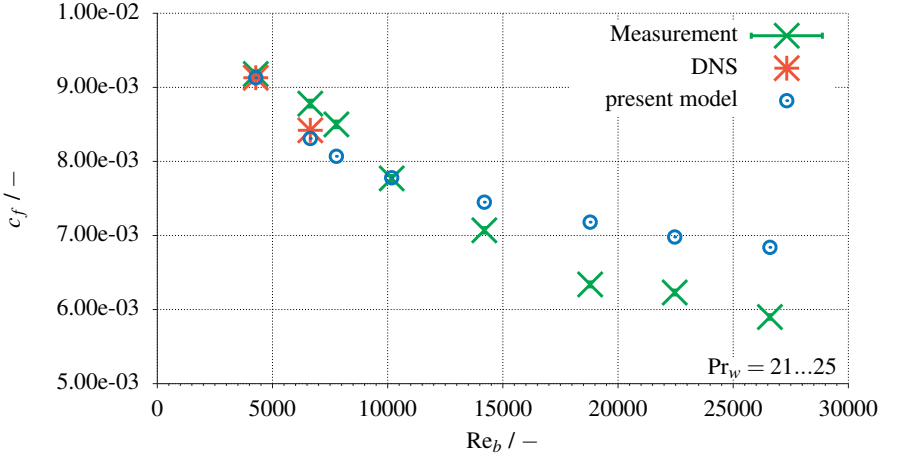

Figure 6.36: Skin friction coefficient vs. bulk Reynolds number of measurement series M20 compared to the present two-layer model

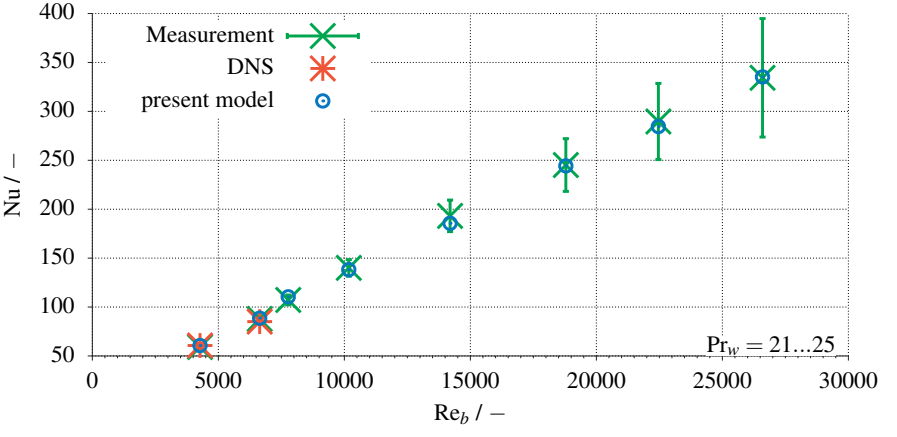

Figure 6.37: Nusselt number vs. bulk Reynolds number of measurement series M20 compared to the present two-layer model

M30

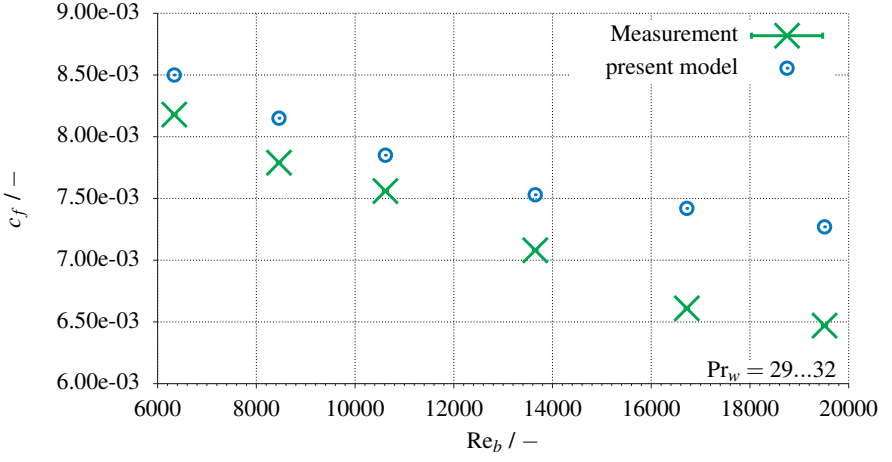

Figure 6.38: Skin friction coefficient vs. bulk Reynolds number of measurement series M30 compared to the present two-layer model

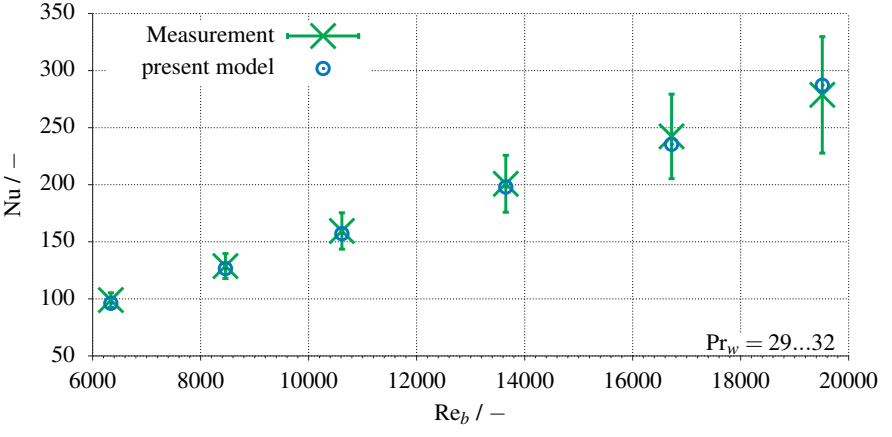

Figure 6.39: Nusselt number vs. bulk Reynolds number of measurement series M30 compared to the present two-layer model

M40

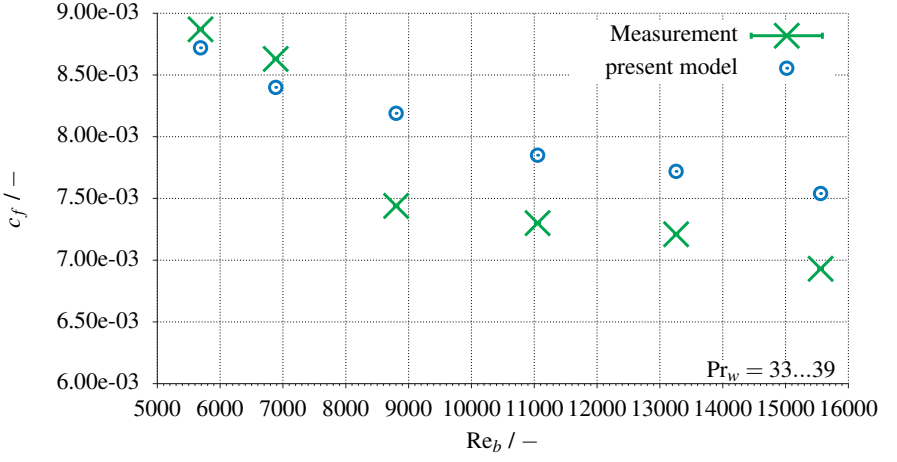

Figure 6.40: Skin friction coefficient vs. bulk Reynolds number of measurement series M40 compared to the present two-layer model

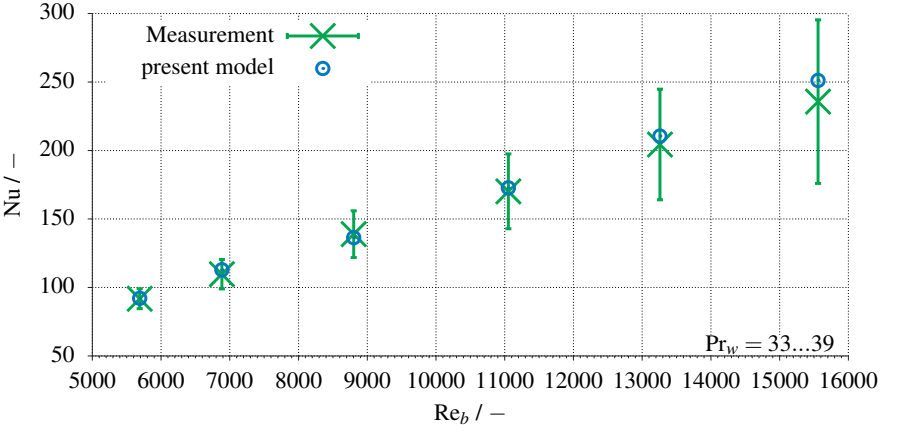

Figure 6.41: Nusselt number vs. bulk Reynolds number of measurement series M30 compared to the present two-layer model

M50

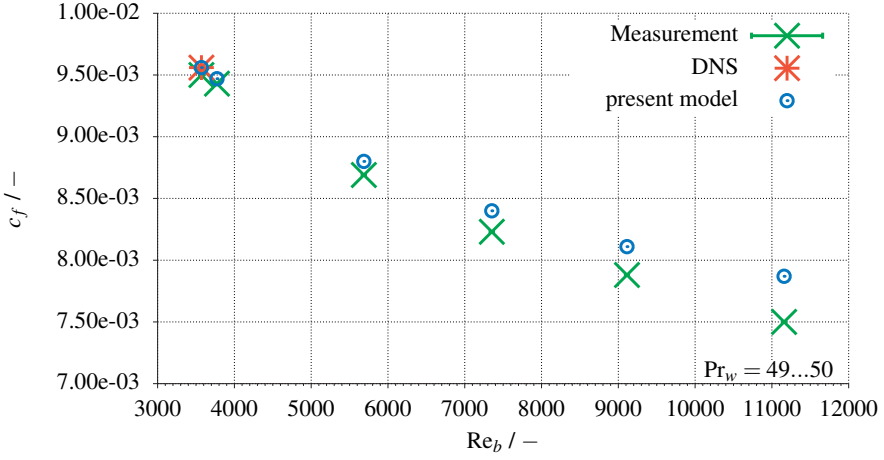

Figure 6.42: Skin friction coefficient vs. bulk Reynolds number of measurement series M50 compared to the present two-layer model

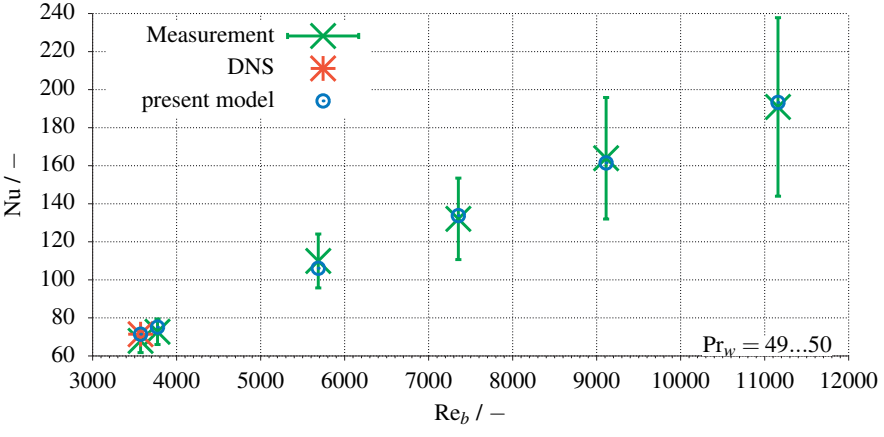

Figure 6.43: Nusselt number vs. bulk Reynolds number of measurement series M50 compared to the present two-layer model

M60

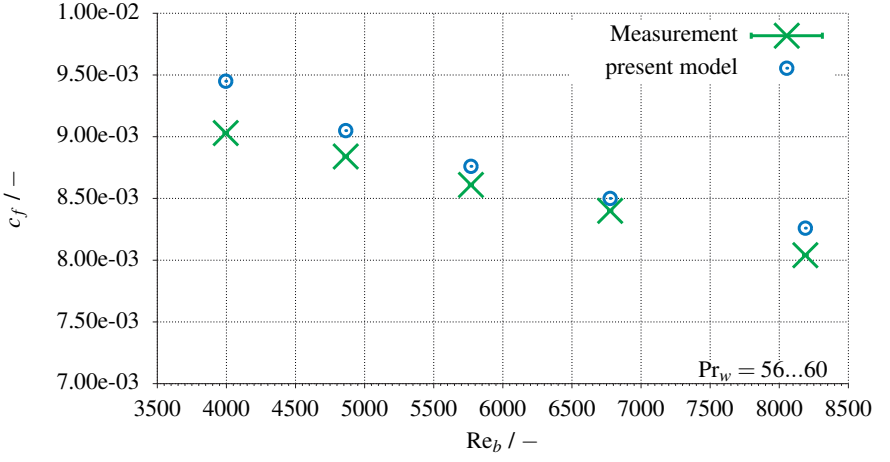

Figure 6.44: Skin friction coefficient vs. bulk Reynolds number of measurement series M60 compared to the present two-layer model

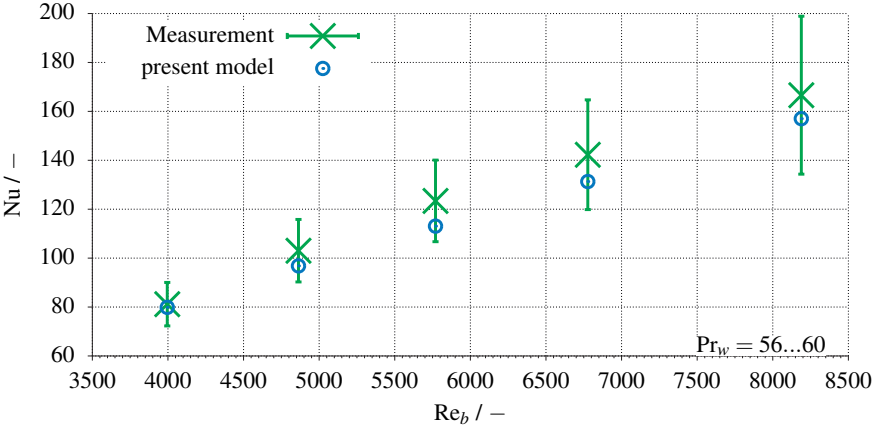

Figure 6.45: Nusselt number vs. bulk Reynolds number of measurement series M60 compared to the present two-layer model

6.2.1 Blending between the laminar and the turbulent layer

Including the van Driest-type damping into the modeled variation of the turbulent Prandtl number (6.56) effectively reduces the over-prediction of the enthalpy around the sharp transition from the diffusive sublayer to the fully turbulent layer. Nonetheless, a notable deviation from the DNS data still remains in the transition region. Considering the field of application in RANS, an accurately predicted enthalpy in the thermal boundary condition is essential for reliable results. The observed over-prediction of the two-layer model in the buffer region due to the sharp transition between the two layers would certainly cause inaccuracies when applied as thermal boundary condition in RANS. For this reason, Kader (1981) proposed a blending between the two thermal layers. Later on, this idea was adopted for computing the velocity by Popovac and Hanjalic (2007), which improved the velocity prediction in the buffer region of momentum flux. The blending based approach essentially starts from the two-layer solution for the velocity and enthalpy, as already presented in formulations (6.53) and (6.60), with the additional simplification $\mathrm{Pr}_T \approx \mathrm{Pr}_{T,\infty}$, which read

$$\overline{w}^+ = \begin{cases} \displaystyle\int_0^{y^+} \frac{1}{\overline{\mu}^*} dy^+ & \text{for } y^+ \leq y^+_{c,m} \\ \dfrac{1}{\kappa}\log\left(y^+\right) + \beta_m & \text{for } y^+ > y^+_{c,m} \end{cases} \tag{6.67}$$

and

$$\overline{\chi}^+ = \begin{cases} \mathrm{Pr}_w \displaystyle\int_0^{y^+} \frac{\overline{c_p}^*}{\overline{\lambda}^*} dy^+ & \text{for } y^+ \leq y^+_{c,th} \\ \dfrac{\mathrm{Pr}_{T,\infty}}{\kappa}\log\left(y^+\right) + \beta_\chi & \text{for } y^+ > y^+_{c,th} \end{cases}, \tag{6.68}$$

respectively. A popular standard setting is used here for the von Kármán constant $\kappa = 0.40$. For determining the parameter β_χ, a variety of different formulations can be found in literature, which are exclusively proposed for constant fluid properties. Table 6.12 gives an overview of the most popular formulations.

Table 6.12: Overview over the most popular formulations for the parameter β_χ

Jayatilleke (1969)	$\mathrm{Pr}_{T,\infty}\left(\beta_m + P\right)$ P based on formulation (6.11)
Kader and Yaglom (1972)	$12.5\,\mathrm{Pr}_w^{2/3} + 2.12\,\log\left(\mathrm{Pr}_w\right) - 1.5$
Kader (1981)	$\left(3.85\,\mathrm{Pr}_w^{1/3} - 1.3\right)^2 + 2.12\,\log\left(\mathrm{Pr}_w\right)$
Petukhov et al. (1988)	$12.7\,\mathrm{Pr}_w^{2/3} - 6.7$

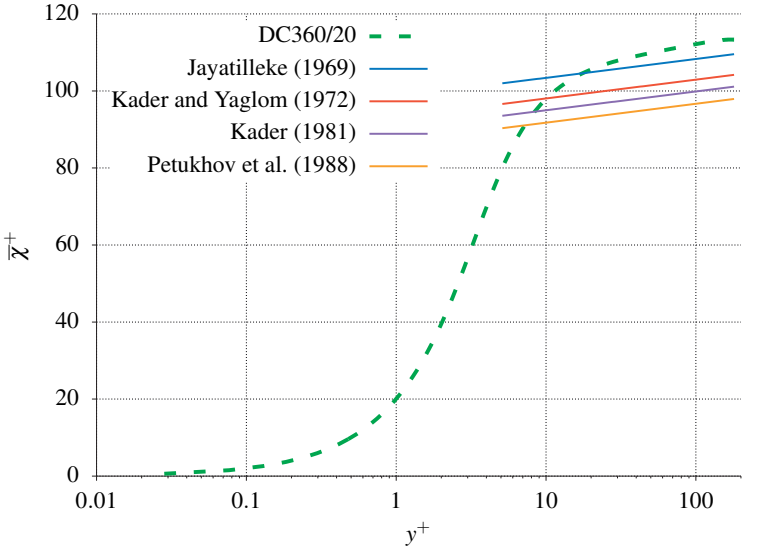

Figure 6.46: Comparison of the two-layer thermal wall law based on different β_χ formulations

Figure 6.46 compares the DNS data for the case DC360/20 to the enthalpy predicted from (6.68) applying the β_χ formulations presented in table 6.12. The effective thicknesses of the viscous and diffusive sublayers are again determined from the correlations (6.63) and (6.64), respectively. It is clearly visible that the β_χ formulation based on the P-function of Jayatilleke (1969) produces by far the best agreement with the DNS data. However, as already noted, the sharp transition from the diffusive to the fully turbulent layer, located at the wall distance of $y^+_{c,th}$, inherently produces a non-physical kink in the predicted radial variation. In an attempt to enforce a physically more plausible smooth transition, Kader (1981) proposed a blending between the two layers, represented by a single equation, covering the whole near wall domain. This formulation reads

$$\overline{\chi}^+ = \mathrm{Pr}_w\, y^+ \, \exp\left(-\Gamma_\chi\right) + \left(\frac{\mathrm{Pr}_{T,\infty}}{\kappa}\, \log\left(y^+\right) + \beta_\chi\right) \exp\left(-\frac{1}{\Gamma_\chi}\right), \tag{6.69}$$

with a blending function defined as

$$\Gamma_\chi = \frac{0.01\, \left(\mathrm{Pr}_w\, y^+\right)^4}{1 + 5\, \mathrm{Pr}_w^3\, y^+}. \tag{6.70}$$

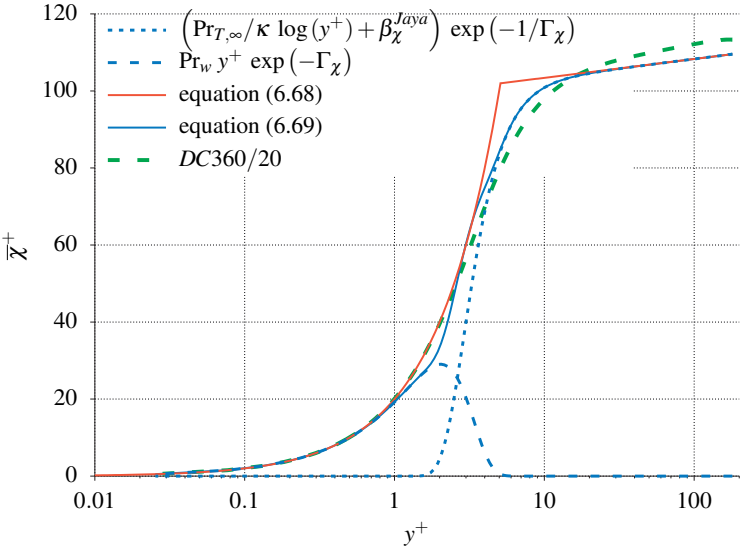

Figure 6.47: Comparison between the DNS data and the thermal wall model based on equation (6.68) and (6.69)

Introducing the S-shaped blending function defined by equation (6.70) results in a smooth transition between the two layers. This is shown in figure 6.47, comparing the DNS data to the predictions of equation (6.69) including the blended laminar and turbulent contributions.

In comparison to the edged profile obtained from the model with a sharp transition the blending evidently produces significantly better results in the buffer region. At the lower end of the buffer region, the blended radial variation still exhibits some notable deviation, which is caused by the presently used formulation for the blending function as defined in equation (6.70).

Instead of using one of the expressions listed in table 6.12, the parameter β_χ can be alternatively determined based on equation (6.65), where it appears as

$$\beta_\chi = \mathrm{Pr}_w \int_0^{y^+_{c,th}} \frac{\overline{c_p}^*}{\overline{\lambda}^*} dy^+ - \frac{\mathrm{Pr}_{T,\infty}}{\kappa} \log(y^+_{c,th}), \tag{6.71}$$

Table 6.13: Model-coefficients $y^+_{c,m}$

$\tilde{\alpha}_c^m$	24.076
$\tilde{\gamma}_c^m$	−0.109
$\tilde{\delta}_c^m$	0.100

Table 6.14: Model-coefficients $y^+_{c,th}$

$\tilde{\beta}_c^{\,th}$	−0.306
$\tilde{\delta}_c^{\,th}$	0.496

dependent on the effective sublayer thickness $y^+_{c,th}$. The effective thickness of the diffusive sublayer is modeled again using the power-law correlations (6.63) and (6.64), however, with adjusted coefficients, to conform better with the blending function based formulation (6.69). The adjusted values were obtained by a best fit of the skin friction coefficient and the Nusselt number, predicted from the blending function based model to the DNS data, and are listed in tables 6.13 and 6.14. Substituting directly the so modified correlations (6.63) and (6.64) for determining $y^+_{c,th}$ into equation (6.71) yields the expression

$$\begin{aligned}\beta_\chi =& \mathrm{Pr}_w \int_0^{y^+_{c,th}} \frac{\overline{c_p}^*}{\overline{\lambda}^*} dy^+ \\ &- \frac{\mathrm{Pr}_{T,\infty}}{\kappa}\left(\log\left(\tilde{\alpha}_c^m\right) + \tilde{\gamma}_c^m \log\left(\mathrm{Re}_{\tau,w}\right) + \left(\tilde{\delta}_c^m + \tilde{\delta}_c^{\,th}\right) \log\left(\mu_b^*\right) + \beta_c^{\,th} \log\left(\mathrm{Pr}_w\right)\right).\end{aligned} \tag{6.72}$$

where the similarities and differences to the alternative formulations, presented in table 6.12, become very obvious. It can be seen that a similar dependence on the molecular Prandtl number arises. Additionally, the formulation (6.72) shows a dependence on the Reynolds number $\mathrm{Re}_{\tau,w}$, and on account of the spacial variation of the fluid properties a contribution based on μ_b^* appears as well.

Popovac and Hanjalic (2007) applied the blending function based approach to the computation of the velocity profile. This yields for the velocity variation the following expression

$$\overline{w}^+ = y^+ \exp\left(-\Gamma\right) + \left(\frac{1}{\kappa}\log\left(y^+\right) + \beta_m\right) \exp\left(-\frac{1}{\Gamma}\right). \tag{6.73}$$

The blending function is defined here as

$$\Gamma = \frac{0.01\ \left(y^+\right)^4}{1 + 5\, y^+}, \tag{6.74}$$

which corresponds to the expression for Γ_χ given by (6.70) with $\mathrm{Pr}_w = 1$.

The parameter β_m, based on equation (6.53) reads

$$\beta_m = \int_0^{y^+_{c,m}} \frac{1}{\overline{\mu}^*} dy^+ - \frac{1}{\kappa}\log\left(y^+_{c,m}\right), \tag{6.75}$$

which can be supplied with the correlations for the effective momentum thickness (6.63), yielding

$$\beta_m = \int_0^{y^+_{c,m}} \frac{1}{\overline{\mu}^*} dy^+ + \\ - \frac{1}{\kappa} \left(\log(\tilde{\alpha}_c^m) + \tilde{\gamma}_c^m \log(\mathrm{Re}_{\tau,w}) + \tilde{\delta}_c^m \log(\mu_b^*) \right). \tag{6.76}$$

To assess the scope of the present blending function based model for velocity and enthalpy, the model predictions of the formulations (6.73) and (6.69) are validated against the DNS data. Two different submodels for β_χ are considered, the first is the presently proposed model formulation (6.72), the second is based on the P-function approach of Jayatilleke (1969) as shown in table 6.12, which represents a very popular approach in commercial CFD. A standard setting $\kappa = 0.4$ and $\beta_m = 5.5$ suggested by Kays and Crawford (1980) is prescribed in the Jayatilleke (1969) P-function approach. Figures 6.48 and 6.49 compare the radial axial velocity variation against the DNS data of the DC and DV cases, respectively. Figures 6.50 and 6.51 compare the radial variation of the enthalpy against the DNS data of the DC and the DV cases, respectively.

Due to the alternative setting for the parameter β_m based on equation (6.76) and the incorporation of the fluid property variation, the model predictions for the velocity are very good.

Regarding the enthalpy, the model based on the parameter β_χ using the P-function of Jayatilleke (1969) produces an excellent agreement with the DNS results, yet with somewhat stronger deviations with increasing Reynolds numbers. It is important to state that the P-function is determined here with the bulk Prandtl number. Using the wall values instead would lead to significantly lower predictions for $\overline{\chi}^+$ in the inner region. The present blending function based model using (6.72) shows some discrepancies for the highest considered Prandtl number, yet besides this, the agreement with the DNS is still quite good. Furthermore, a slight edge near the lower limit of the buffer region is clearly visible for all cases, which in turn reduces the discrepancy in the upper part of the buffer layer.

For validating the model accuracy in the regime of higher Reynolds and Prandtl numbers, representing fully turbulent flow conditions, the predicted wall friction coefficients and Nusselt numbers are compared against all the experimental data obtained in the measurement series M20 through M60, as discussed in chapter 4. This comparison is shown in the figures 6.52-6.61.

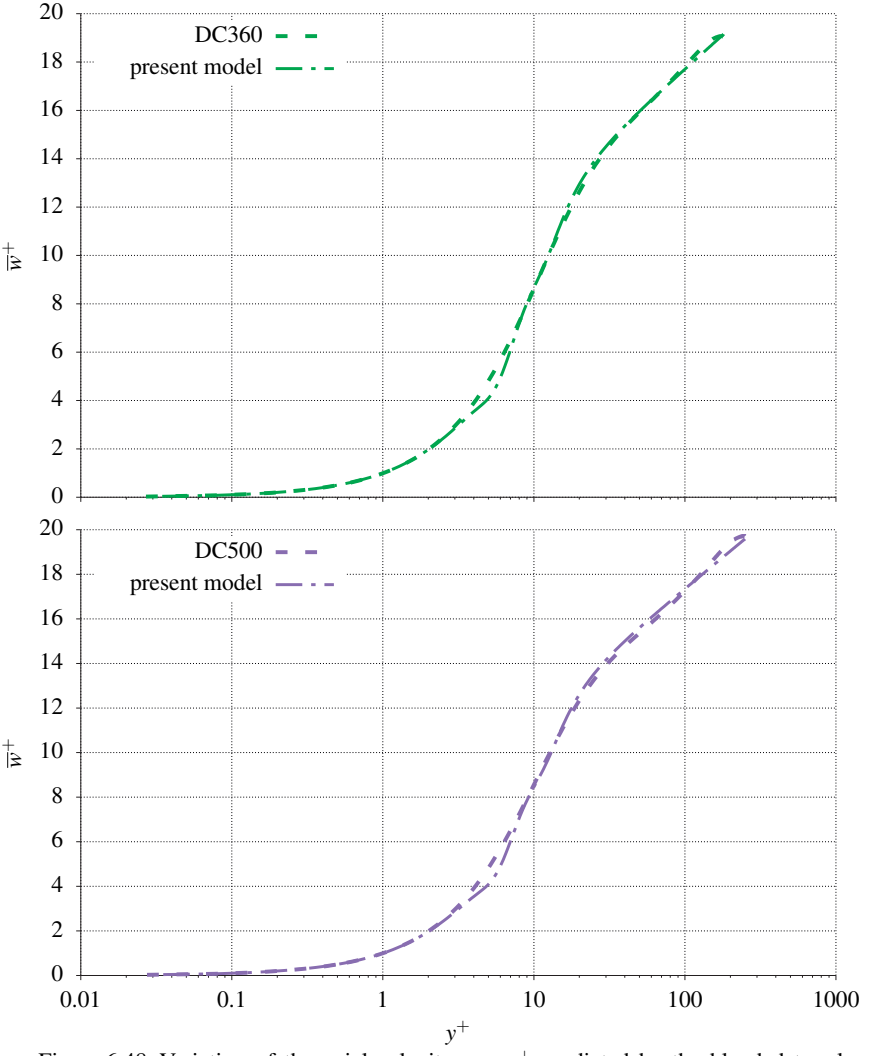

Figure 6.48: Variation of the axial velocity vs. y^+ predicted by the blended two-layer model compared against DNS data for the DC cases

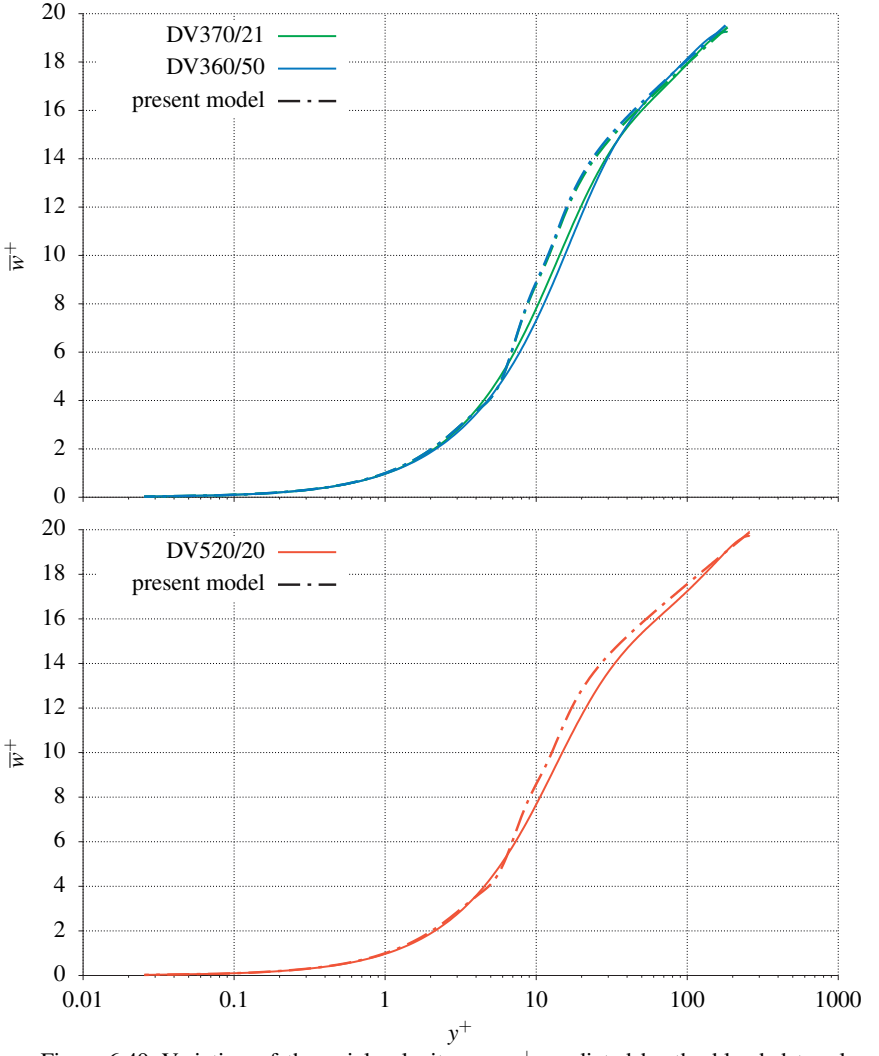

Figure 6.49: Variation of the axial velocity vs. y^+ predicted by the blended two-layer model compared against DNS data for the DV cases

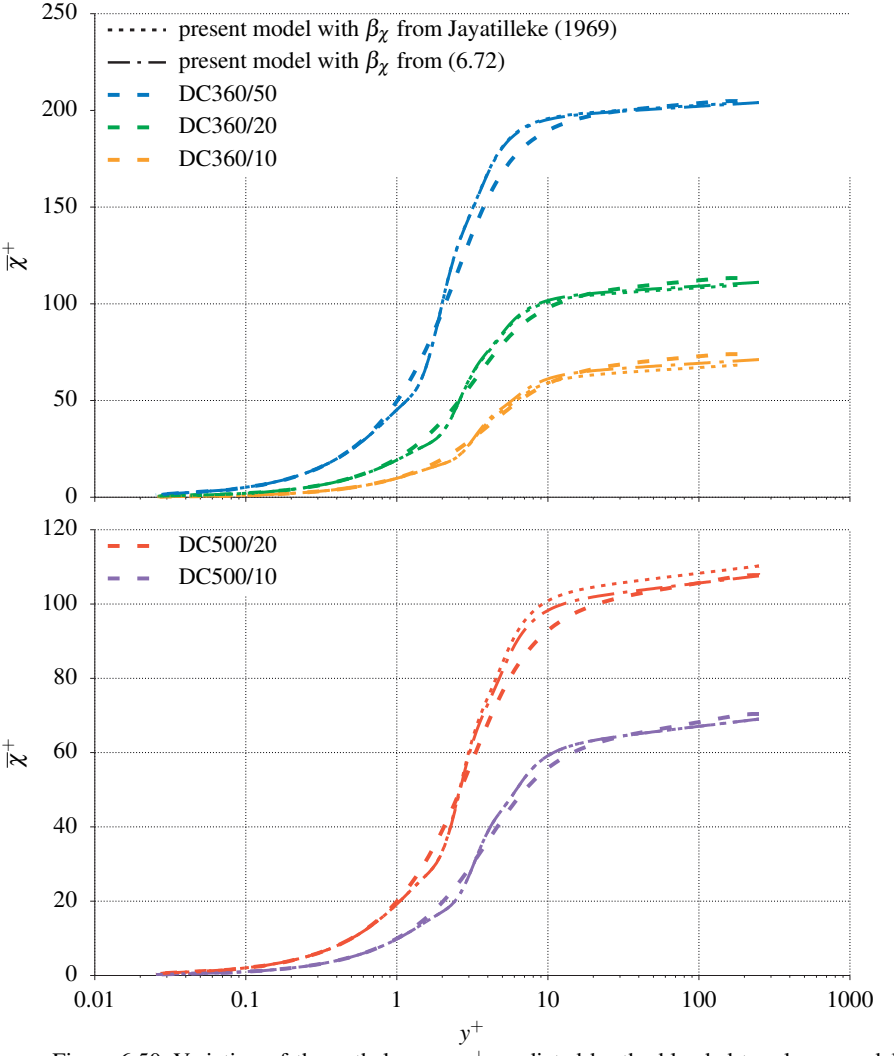

Figure 6.50: Variation of the enthalpy vs. y^+ predicted by the blended two-layer model compared against DNS data for the DC cases

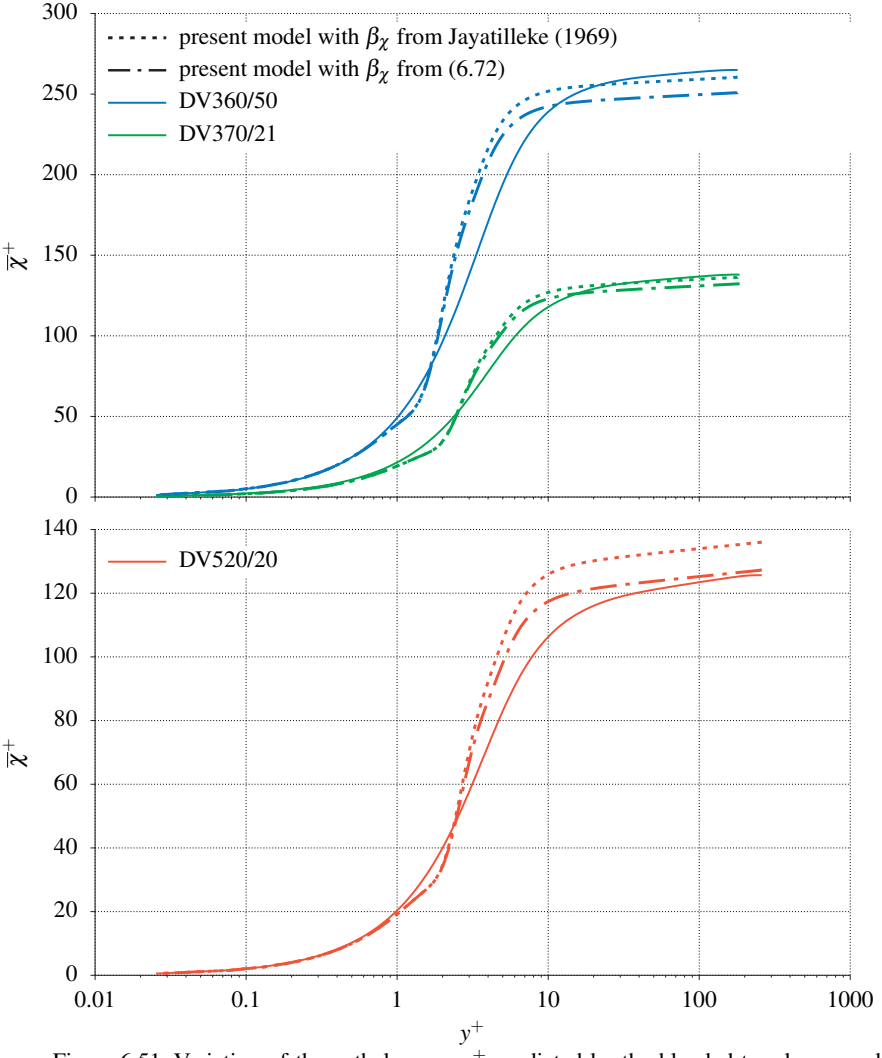

Figure 6.51: Variation of the enthalpy vs. y^+ predicted by the blended two-layer model compared against DNS data for the DV cases

M20

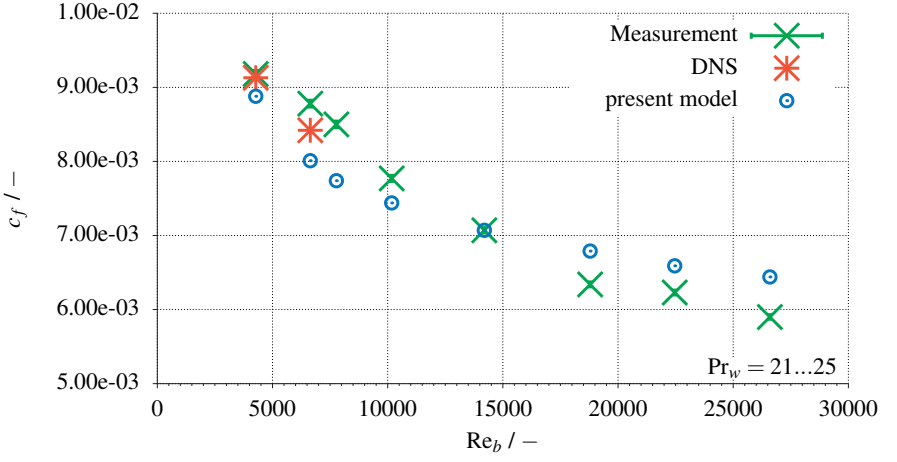

Figure 6.52: Friction coefficient vs. bulk Reynolds number of measurement series M20 compared to the present blended two-layer model

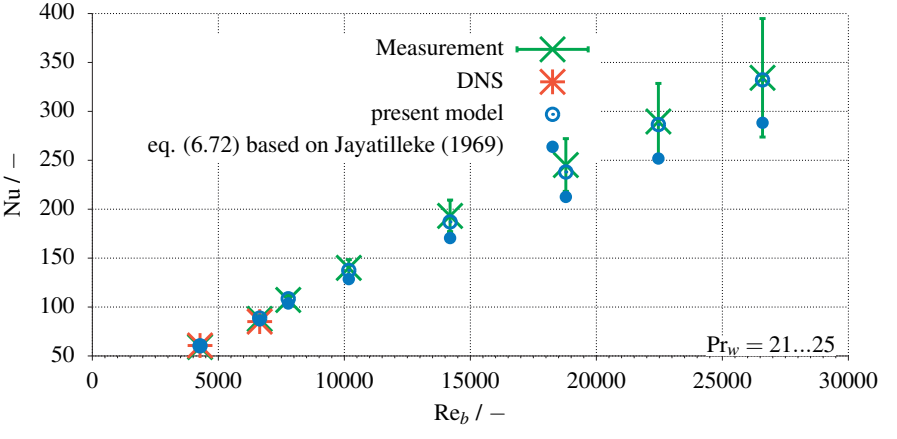

Figure 6.53: Nusselt number vs. bulk Reynolds number of measurement series M20 compared to the present blended two-layer model

M30

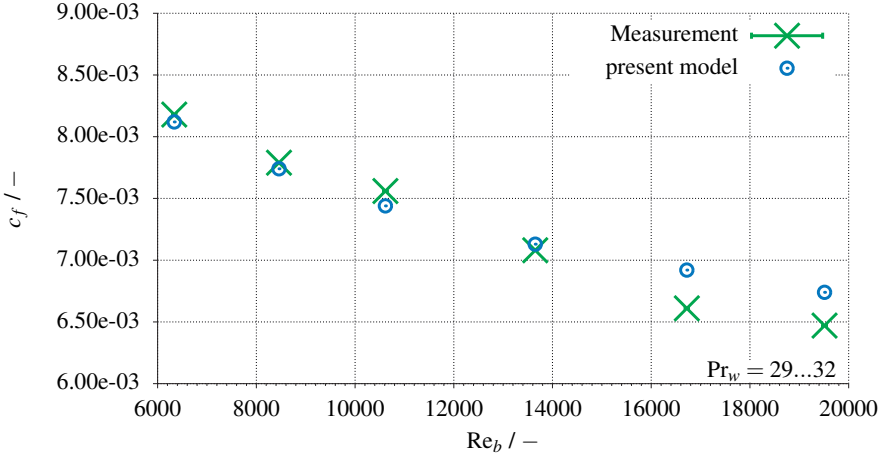

Figure 6.54: Friction coefficient vs. bulk Reynolds number of measurement series M30 compared to the present blended two-layer model

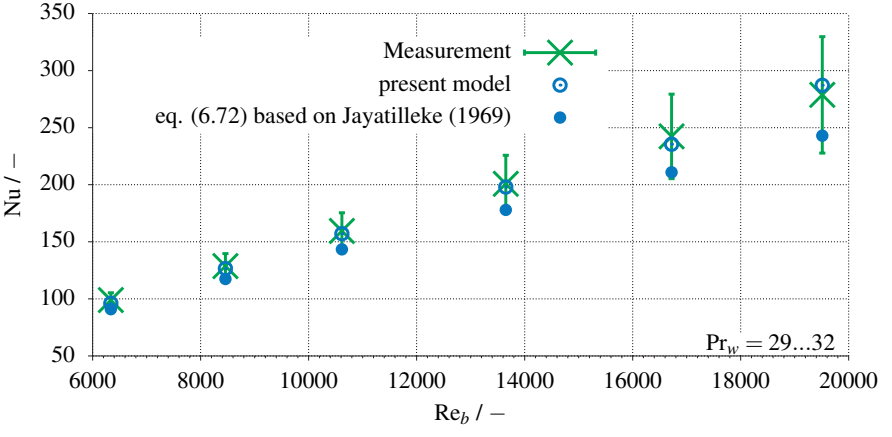

Figure 6.55: Nusselt number vs. bulk Reynolds number of measurement series M30 compared to the present blended two-layer model

M40

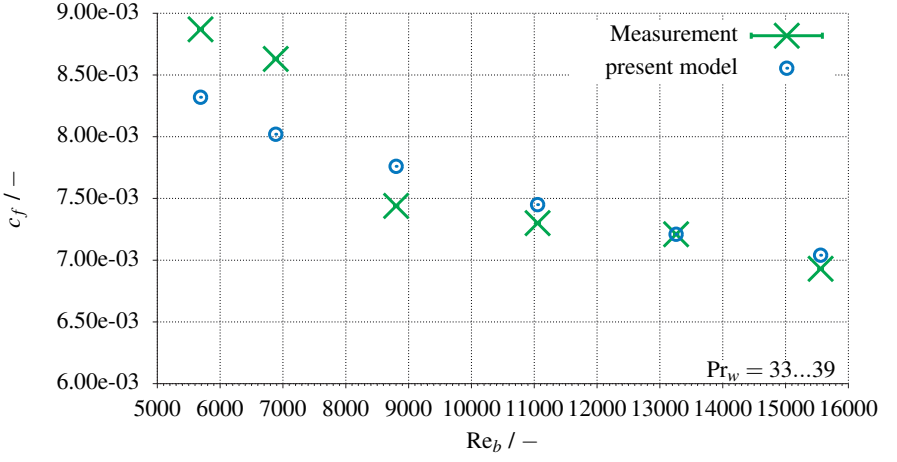

Figure 6.56: Friction coefficient vs. bulk Reynolds number of measurement series M40 compared to the present blended two-layer model

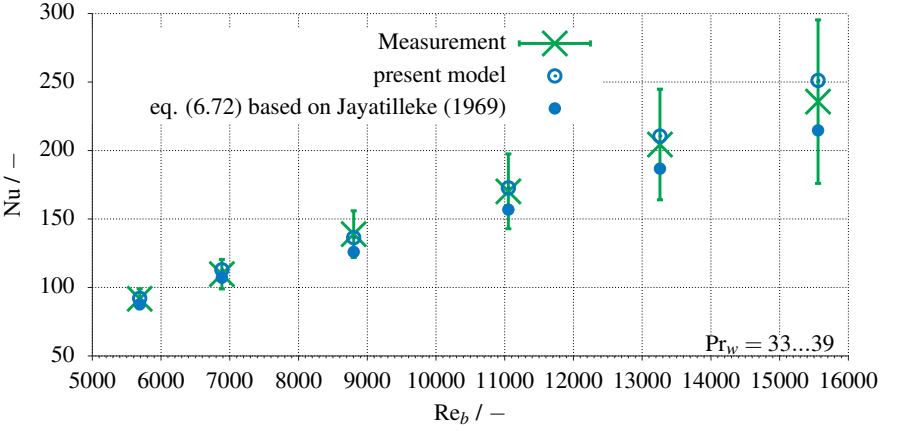

Figure 6.57: Nusselt number vs. bulk Reynolds number of measurement series M40 compared to the present blended two-layer model

M50

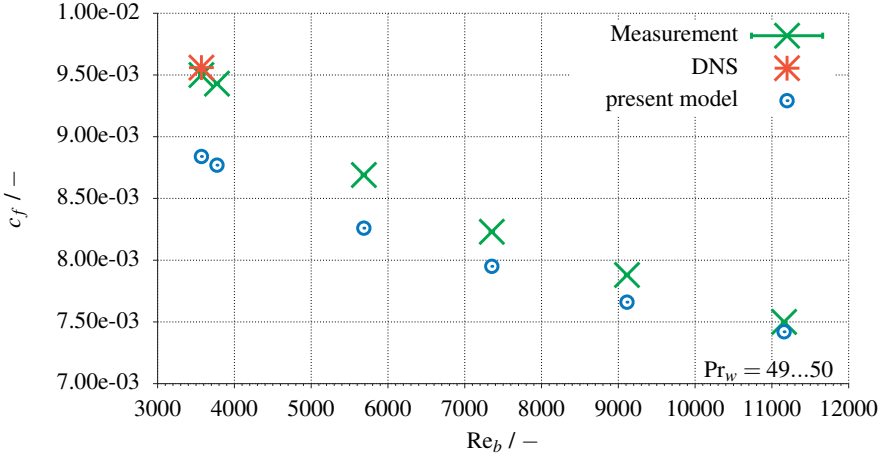

Figure 6.58: Friction coefficient vs. bulk Reynolds number of measurement series M50 compared to the present blended two-layer model

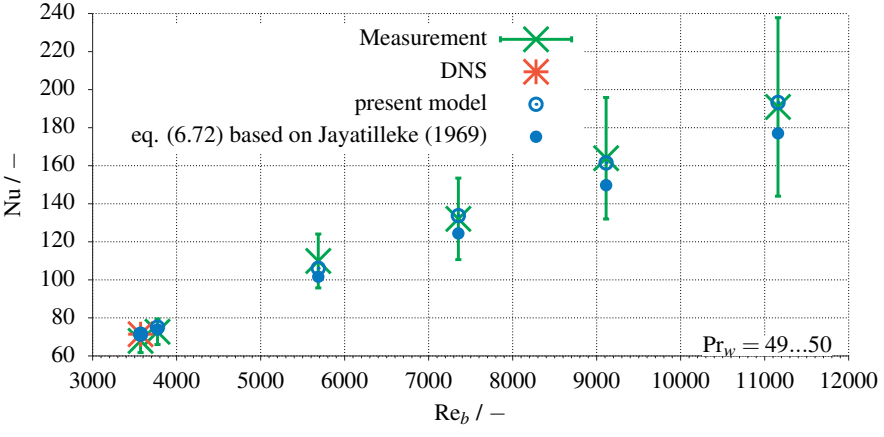

Figure 6.59: Nusselt number vs. bulk Reynolds number of measurement series M50 compared to the present blended two-layer model

M60

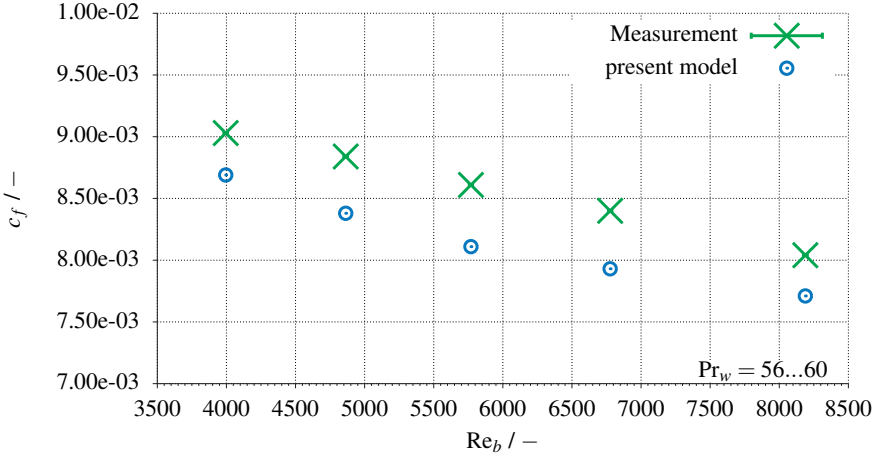

Figure 6.60: Friction coefficient vs. bulk Reynolds number of measurement series M60 compared to the present blended two-layer model

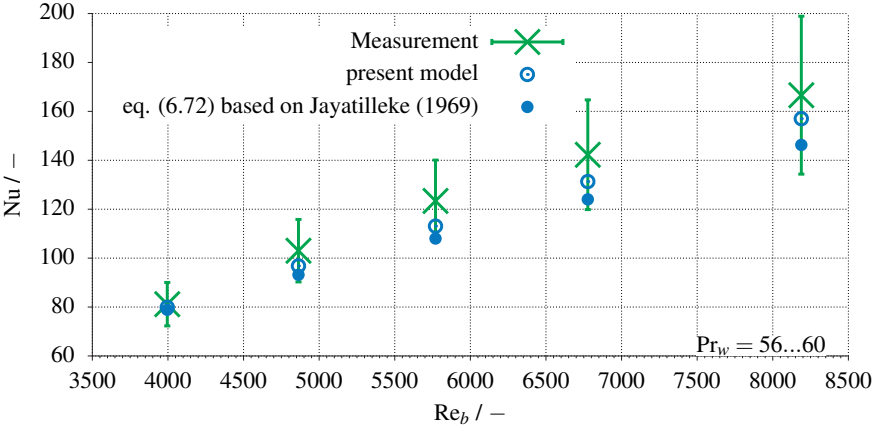

Figure 6.61: Nusselt number vs. bulk Reynolds number of measurement series M60 compared to the present blended two-layer model

The comprehensive comparison against all measured data unveils that the present blended two-layer model supplied with β_χ from Jayatilleke (1969) tends to increasingly underpredict the Nusselt number for increasing Reynolds number. In contrast, the present model supplied with β_χ from (6.72) is capable of producing a good agreement with the measured Nusselt numbers over the whole Reynolds number range.

6.2.2 Fully analytical computation of the Nusselt number

Assuming constant material properties and $\mathrm{Pr}_T \approx \mathrm{Pr}_{T,\infty}$ for $y^+ > y^+_{c,th}$, reduces the two-layer formulations given by (6.67) and (6.68), yielding to the following most simplified representations

$$\overline{w}^+ = \begin{cases} y^+ & \text{for } y^+ \leq y^+_{c,m} \\ \dfrac{1}{\kappa}\log\left(y^+\right) + \beta_m & \text{for } y^+ > y^+_{c,m} \end{cases} \tag{6.77}$$

and

$$\overline{\chi}^+ = \begin{cases} \mathrm{Pr}_w\, y^+ & \text{for } y^+ \leq y^+_{c,th} \\ \dfrac{\mathrm{Pr}_{T,\infty}}{\kappa}\log\left(y^+\right) + \beta_\chi & \text{for } y^+ > y^+_{c,th} \end{cases}, \tag{6.78}$$

respectively. The obtained simplified formulation offers the attractive possibility of deriving an analytical expression for the Nusselt number. The effective thickness of the diffusive sublayer is again modeled using the power-law correlations (6.63) and (6.64) with the coefficients shown in table 6.13 and 6.14.

In consistence with equation (5.42), the Nusselt number can be generally computed as

$$\mathrm{Nu} = \frac{\mathrm{Re}_{\tau,w}\,\mathrm{Pr}_w\, c^*_{p,b}}{\overline{\chi}^+_b} \tag{6.79}$$

dependent of the bulk enthalpy computed as,

$$\overline{\chi}^+_b = \frac{2}{\dot{m}^*}\int_{y^+=0}^{\mathrm{Re}_{\tau,w}/2} \rho^*\,\overline{w}^+\,\overline{\chi}^+\left(\frac{1}{2} - \frac{y^+}{\mathrm{Re}_{\tau,w}}\right)\mathrm{d}y^+, \tag{6.80}$$

with the mass flow rate obtained from

$$\dot{m}^* = 2\int_{y^+=0}^{\mathrm{Re}_{\tau,w}/2} \rho^*\,\overline{w}^+\left(\frac{1}{2} - \frac{y^+}{\mathrm{Re}_{\tau,w}}\right)\mathrm{d}y^+. \tag{6.81}$$

An analytical computation of the bulk enthalpy for predicting the Nusselt number was similarly proposed by Kader and Yaglom (1972). Yet, they assumed that the Reynolds and Prandtl number are high enough to provide a sufficiently thin diffusive sublayer thickness for neglecting its contribution to the bulk enthalpy completely. Accordingly, they used the enthalpy formulation for the turbulent sublayer ($y^+ > y^+_{c,th}$) for the whole radial domain down to the wall. In contrast, the present approach does not adopt this simplification, while considering rigorously the contribution from the diffusive sublayer as well. This

means that the mass flux is computed as the sum of the two definite integrals, Im_{lam} and Im_{turb}, connected at the boundary of the two sub-layers $y^+ = y^+_{c,m}$. For the bulk enthalpy, three definite sub-integrals, $Im\chi_{lam}$, $Im\chi_{int}$ and $Im\chi_{turb}$ have to be distinguished in order to combine correctly the locally applying functions for the velocity and enthalpy. The three sub-integrals are connected at $y^+ = y^+_{c,th}$ and $y^+ = y^+_{c,th}$, as highlighted in figure 6.62.

Splitting the radial domain into these sub-integrals, the Nusselt number can be computed as

$$\mathrm{Nu} = \mathrm{Re}_{\tau,w}\,\mathrm{Pr}_w\,c^*_{p,b}\frac{Im_{lam}+Im_{turb}}{Im\chi_{lam}+Im\chi_{int}+Im\chi_{turb}}, \tag{6.82}$$

with the analytical expressions of the sub-integrals given in equations (6.83) - (6.87).

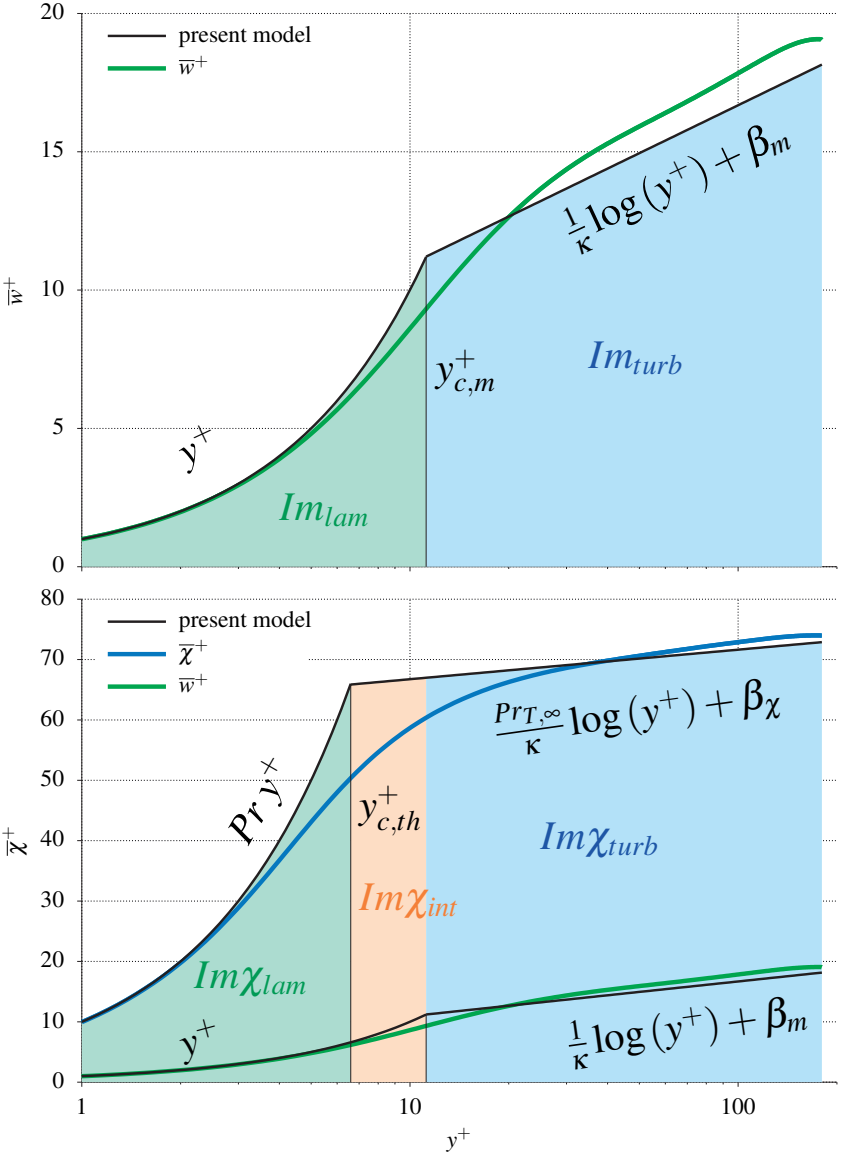

Figure 6.62: Different regimes for the analytical integration for the the mass flux and the bulk enthalpy

$$Im_{lam} = {y^+_{c,m}}^2 \left(\frac{1}{2} - \frac{2y^+_{c,m}}{3\mathrm{Re}_{\tau,w}} \right) \tag{6.83}$$

$$Im_{turb} = \frac{\mathrm{Re}^2_{\tau,w}\left(\kappa(-y^+_{c,m}) + 2(\kappa y^+_{c,m} - 1) + \frac{1}{2}\right) + \mathrm{Re}^2_{\tau,w}\left(\log\left(\frac{\mathrm{Re}_{\tau,w}}{2}\right) - \log(y^+_{c,m})\right) + 4\mathrm{Re}_{\tau,w} y^+_{c,m}(1 - \kappa y^+_{c,m}) + 4{y^+_{c,m}}^2\left(\kappa y^+_{c,m} - \frac{1}{2}\right)}{4\kappa \mathrm{Re}_{\tau,w}} \tag{6.84}$$

$$Im\chi_{lam} = \frac{\mathrm{Pr}\,{y^+_{c,th}}^3\left(\frac{\mathrm{Re}_{\tau,w}}{3} - \frac{y^+_{c,th}}{2}\right)}{\mathrm{Re}_{\tau,w}} \tag{6.85}$$

$$Im\chi_{int} = -2\frac{\begin{array}{r}\kappa\mathrm{Pr}_w y^+_{c,th}\left(-\frac{\mathrm{Re}_{\tau,w}{y^+_{c,m}}^2}{4} + \frac{\mathrm{Re}_{\tau,w}{y^+_{c,th}}^2}{4} + \frac{{y^+_{c,m}}^3}{3} - \frac{{y^+_{c,th}}^3}{3}\right) + \mathrm{Pr}_{T,\infty}\left(\frac{\mathrm{Re}_{\tau,w}{y^+_{c,m}}^2}{8} - \frac{\mathrm{Re}_{\tau,w}{y^+_{c,th}}^2}{8} - \frac{{y^+_{c,m}}^3}{9} + \frac{{y^+_{c,th}}^3}{9}\right) + \\ \mathrm{Pr}_{T,\infty}{y^+_{c,m}}^2\left(\left(\frac{\mathrm{Re}_{\tau,w}}{4} - \frac{y^+_{c,m}}{3}\right)\log(y^+_{c,th}) + \left(\frac{y^+_{c,m}}{3} - \frac{\mathrm{Re}_{\tau,w}}{4}\right)\log(y^+_{c,m})\right)\end{array}}{\kappa\mathrm{Re}_{\tau,w}} \tag{6.86}$$

$$Im\chi_{turb} = \frac{\begin{array}{r}\kappa\left(-\frac{3\mathrm{Re}^2_{\tau,w}}{2} + 4\mathrm{Re}_{\tau,w}y^+_{c,m} - 2{y^+_{c,m}}^2\right)(\mathrm{Pr}_w y^+_{c,th} + \mathrm{Pr}_{T,\infty}y^+_{c,m}) + \\ \log(y^+_{c,m})\left(\kappa(-\mathrm{Pr}_w)\mathrm{Re}^2_{\tau,w}y^+_{c,th} + \mathrm{Pr}_{T,\infty}\left(\frac{3\mathrm{Re}^2_{\tau,w}}{2} + 4\mathrm{Re}_{\tau,w}y^+_{c,m}(1 - \kappa y^+_{c,m}) + 4{y^+_{c,m}}^2\left(\kappa y^+_{c,m} - \frac{1}{2}\right)\right) + \mathrm{Pr}_{T,\infty}\mathrm{Re}^2_{\tau,w}(\log(y^+_{c,th}) + \log(2))\right) + \\ \mathrm{Re}^2_{\tau,w}\log(\mathrm{Re}_{\tau,w})(\kappa\mathrm{Pr}_w y^+_{c,th} + \mathrm{Pr}_{T,\infty}(\kappa(-y^+_{c,m}) + 2(\kappa y^+_{c,m} - 2) + 1) + \mathrm{Pr}_{T,\infty}(-\log(y^+_{c,m}) - \log(y^+_{c,th}) - 2\log(2))) + \\ \mathrm{Re}^2_{\tau,w}\log(2)(\kappa(-\mathrm{Pr}_w)y^+_{c,th} + \mathrm{Pr}_{T,\infty}(3 - \kappa y^+_{c,m}) + \mathrm{Pr}_{T,\infty}\log(y^+_{c,th})) + \kappa^2\mathrm{Pr}_w y^+_{c,m}y^+_{c,th}\left(\mathrm{Re}^2_{\tau,w} - 4\mathrm{Re}_{\tau,w}y^+_{c,m} + 4{y^+_{c,m}}^2\right) + \\ \mathrm{Pr}_{T,\infty}\log(y^+_{c,th})\left(\mathrm{Re}^2_{\tau,w}\left(\kappa y^+_{c,m} + 2(1 - \kappa y^+_{c,m}) - \frac{1}{2}\right) + 4\mathrm{Re}_{\tau,w}y^+_{c,m}(\kappa y^+_{c,m} - 1) + 4{y^+_{c,m}}^2\left(\frac{1}{2} - \kappa y^+_{c,m}\right)\right) + \\ \mathrm{Pr}_{T,\infty}\left(\frac{7\mathrm{Re}^2_{\tau,w}}{2} - 8\mathrm{Re}_{\tau,w}y^+_{c,m} + 2{y^+_{c,m}}^2\right) + \mathrm{Pr}_{T,\infty}\mathrm{Re}^2_{\tau,w}\log^2(\mathrm{Re}_{\tau,w}) + \mathrm{Pr}_{T,\infty}\mathrm{Re}^2_{\tau,w}\log^2(2)\end{array}}{4\kappa^2\mathrm{Re}_{\tau,w}} \tag{6.87}$$

For the von Kármán constant and the turbulent Prandtl number a standard setting is applied, reading $\kappa = 0.4$ and $\mathrm{Pr}_{T,\infty} = 0.85$. For the parameters β_m and β_χ, the presently proposed model formulations (6.72) and (6.76) are used, respectively, incorporating the effective boundary thicknesses, $y^+_{c,m}$ and $y^+_{c,th}$ from equations (6.63) and (6.64), respectively, together with the coefficients listed in tables 6.13 and 6.14.

Figures 6.63-6.67 compare the experimentally obtained Nusselt numbers for the measurement series M20-M60 to the present model. It can be clearly seen that the whole Reynolds number range, from the intermediate range between laminar and turbulent flow, up to the fully turbulent regime is well predicted. Furthermore, also the effect of the Prandtl number variation is well captured, although the discrepancy increases slightly with increasing molecular Prandtl numbers. In order to assess the full scope of the present fully analytic two-layer model, further experimental data, exceeding the shown Prandtl number range, would be certainly needed.

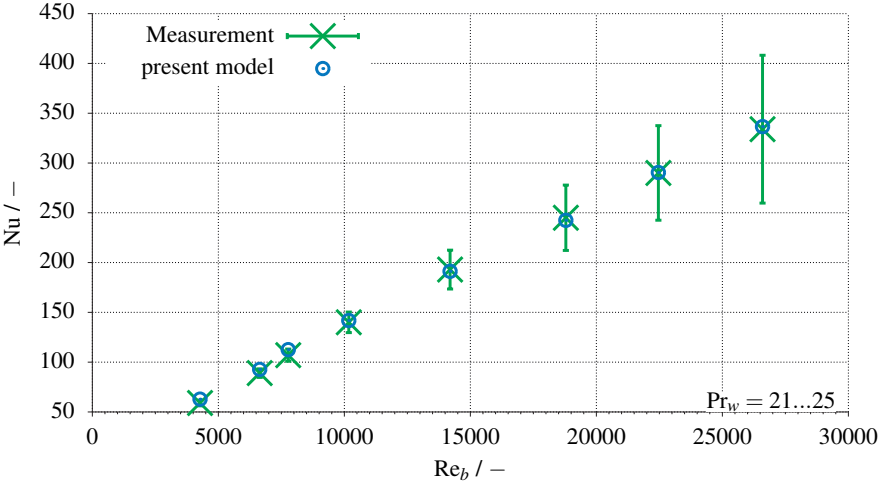

Figure 6.63: Nusselt number vs. bulk Reynolds number of measurement series M20 compared to the fully analytical two-layer model

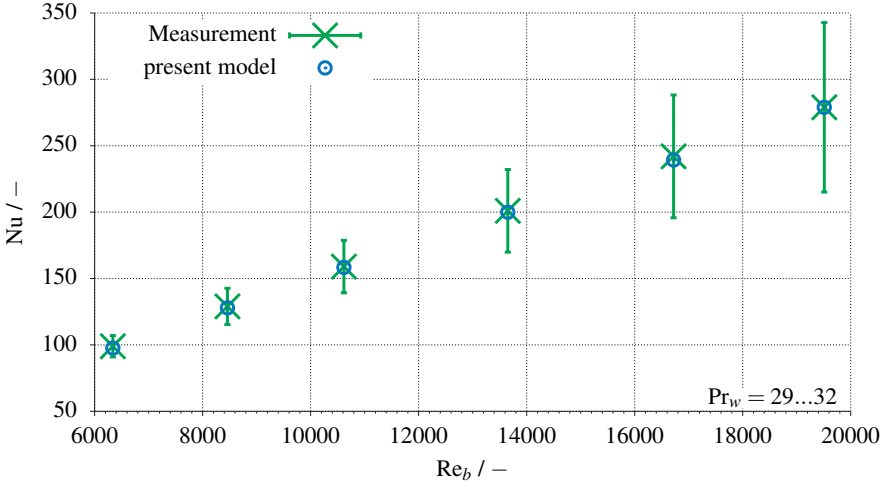

Figure 6.64: Nusselt number vs. bulk Reynolds number of measurement series M30 compared to the fully analytical two-layer model

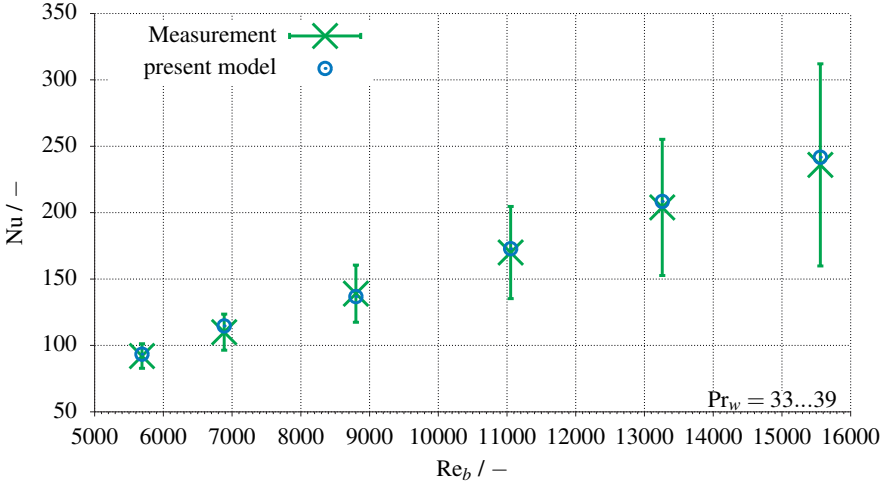

Figure 6.65: Nusselt number vs. bulk Reynolds number of measurement series M40 compared to the fully analytical two-layer model

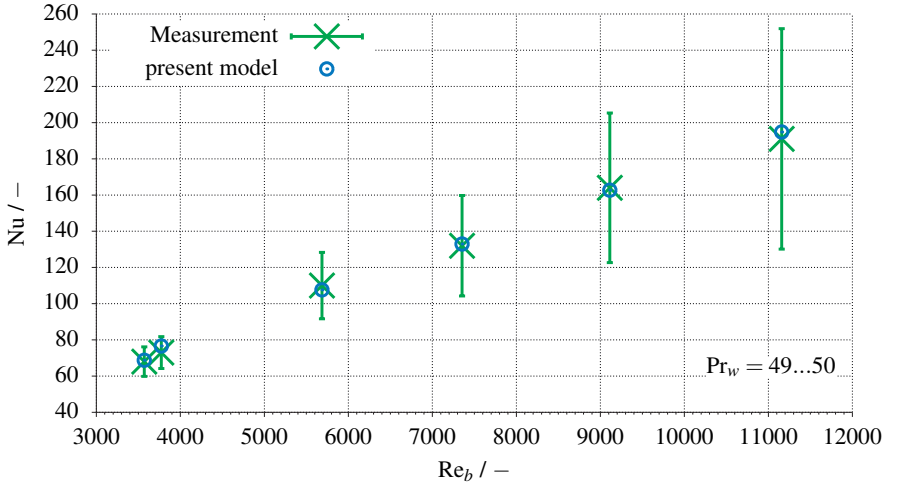

Figure 6.66: Nusselt number vs. bulk Reynolds number of measurement series M50 compared to the fully analytical two-layer model

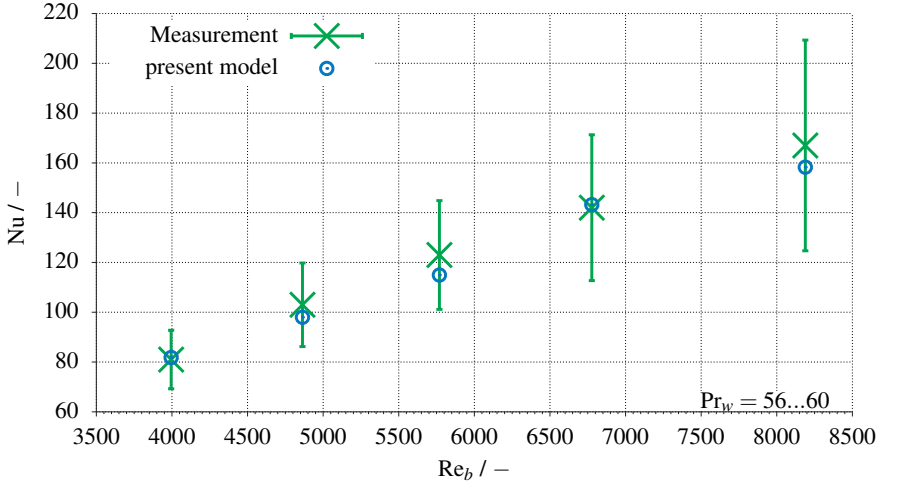

Figure 6.67: Nusselt number vs. bulk Reynolds number of measurement series M60 compared to the fully analytical two-layer model

7 CONCLUSIONS

The present work performed Direct Numerical Simulations (DNS) of turbulent heated pipe flows at high molecular Prandtl numbers examining the effect of real fluid properties. Due to the scarcity of adequate reference data, heat transfer measurements on the same configuration were performed as well providing data for validation of the computational results.

An especially for this purpose designed test-bench was build, capable of performing heat transfer measurements on a set-up well comparable to the DNS cases assuming real fluid properties. Special interest was on the intermediate regime between laminar and turbulent flow. Besides this fairly low Reynolds number regime considered for validation of the DNS results, the experiments also covered fully turbulent conditions with high Reynolds numbers. All measurements were validated against the popular Nusselt number correlation of Gnielinski (2002) and some available but rather old measurements from literature. The measurements agree very well with the correlation of Gnielinski (2002) in the fully turbulent regime, whereas for low Reynolds numbers the correlation tends to under-predict the heat transfer coefficient. This finding is also supported by the comparison against the mentioned fairly old measurements of Morris and Whitman (1928) and Sherwood (1932).

Two types of DNS have been basically carried out in this work, considering constant fluid properties and real temperature-dependent fluid properties, assuming the same operating fluid as used in the experiments. All simulations were carried out on a very fine simulation mesh, comparable to recent DNS studies from literature. The comparison between the DNS results for the skin-friction coefficient and Nusselt number against the corresponding measurements showed a very good agreement, which proves the high accuracy of the simulations.

All alterations in the flow and thermal field due to the real fluid behavior were analyzed in much detail by a comparison of the DNS results against those for the corresponding constant fluid property cases. As one of the major findings this analysis showed that, although the DV cases are associated with a higher bulk molecular Prandtl number due to the increasing viscosity towards the colder center, the effective thickness of diffusive sublayer still thickens. This effectively decreases the heat transfer rate. The turbulent budgets, demonstrated that the observed thickening of the diffusive sublayer could be mainly attributed to a reduced radial turbulent transport of momentum. Furthermore, the DNS data provided very insightful findings regarding the turbulent transport coefficients, as commonly employed in RANS modeling. Special interest was here on the turbulent Prandtl number. The typical asymptotic increase of Pr_T towards the wall, which has been frequently reported in literature, when considering molecular Prandtl numbers higher than

unity and imposing zero temperature fluctuations at the wall, was clearly confirmed by the present DNS results. On the other hand, this already existing knowledge could be extended by a further insight into the influence of the real fluid properties on the magnitude of the asymptotically approached near wall value of Pr_T, which was considerably decreased for the considered conditions in the DV cases. Finally, it was shown that the semi-local scaling proposed by Patel et al. (2016) for the shear stress and a modified version of the semi-local scaling later presented by Patel et al. (2017) for the diffusive heat flux produces a very good collapse of the velocity and enthalpy variations for the considered real fluid property cases with those obtained for the constant fluid properties.

The knowledge obtained from the rich DNS data base was further applied in the validation and further development of two commonly used RANS boundary condition approaches. The first revisited approach is the mathematically rather elaborate P-function approach based on analytical considerations of Spalding (1967). The underlying assumption originally made in this approach were reviewed and modified based on the DNS findings. The predictions of this thermal wall model could be most significantly improved by modifying the eddy viscosity, the ratio of the total shear stress and heat flux, and the turbulent Prandtl number. For the eddy viscosity, the typically used Van Driest (1956) mixing length ansatz, prescribing an incorrect near wall asymptotic, was replaced by the modified mixing length ansatz of Grifoll and Giralt (2000), providing the analytically proven correct near wall variation of the eddy viscosity. Accounting for the effect of the fluid property variation, the mixing length formulation was additionally adjusted by including a viscosity dependence. The influence of the temperature-dependent fluid properties was also included into the sub-model for the turbulent Prandtl number. Instead of neglecting the near wall variation assuming this parameter simply as constant, various different model proposals found in literature were reviewed and compared against the DNS data. Among these, the experimentally adapted analytical model by Kays and Crawford (1980) was selected as a well-suited candidate for further development. The original model was already capable of prescribing the near wall increase of Pr_T, so that model extensions essentially incorporated the missing molecular Prandtl number dependence as well as the influence of the real fluid properties. The predictions of the presently proposed extended analytical P-function model generally showed a very good agreement with the DNS results for both the constant and the real fluid property cases. As a further attractive feature, the present approach is capable of describing the enthalpy variation over the whole radial domain, spanning from the diffusive sublayer to the inertial subrange, while the popular alternative P-function model of Jayatilleke (1969) covers only the latter subrange. The improvements are also highlighted by comparing the DNS based skin-friction coefficients and Nusselt numbers against the model predictions. Both the agreement with the constant and the real fluid cases are excellent. The second considered candidate for specifying dynamic and thermal boundary conditions is a classical two-layer approach. The original idea was proposed by Spalding (1961) for the near wall velocity variation and basically divides the flow field into two sublayers, the diffusion dominated near wall layer and the fully turbulent inertial inner layer.

The same approach was applied here for the enthalpy variation. The advantage of this splitting into two layers lies in its computational simplicity resulting from certain model assumptions. A suitable submodel for the boundary between the diffusive and the inertial sublayer (y_c^+) is still needed, while the turbulent Prandtl number model can be dispensed setting it simply constant to $Pr_{T,\infty}$. An additional advantage of the presented two-layer approach is that it allows for a fully analytical formulation for the Nusselt number, which produced a very good agreement with the own measurements over the whole considered range of Reynolds and Prandtl numbers.

Besides the DNS based modifications, which have been introduced for model parametrization and calibration, both of the presently proposed concepts for providing reliable thermal boundary conditions have a strong analytical foundation. This analytical description of the underlying transport mechanisms makes them clearly preferable over empirically based models, due to their universal character and good scalability over wide ranges of Reynolds and Prandtl numbers.

Appendices

A FIGURES

Here are all figures, which were not shown in the previous.

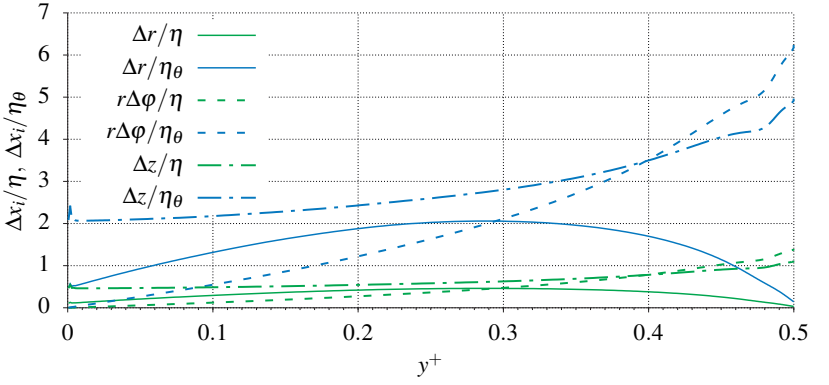

Figure A.1: Spatial resolution normalized by the Kolmogorov scale η and the smallest turbulent thermal scale η_θ for the case $DC360/50$

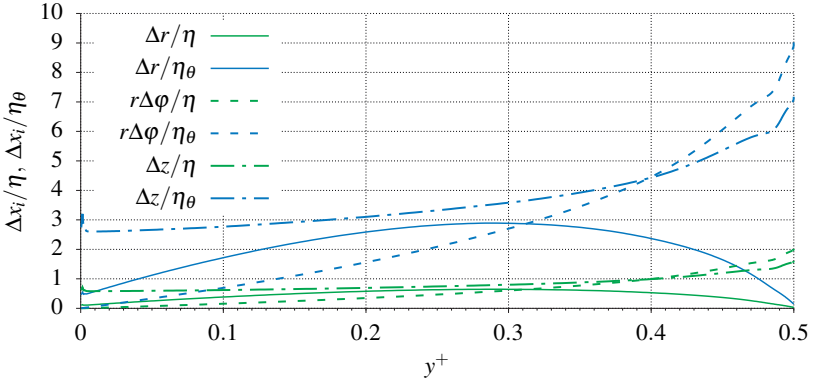

Figure A.2: Spatial resolution normalized by the Kolmogorov scale η and the smallest turbulent thermal scale η_θ for the case $DC500/20$

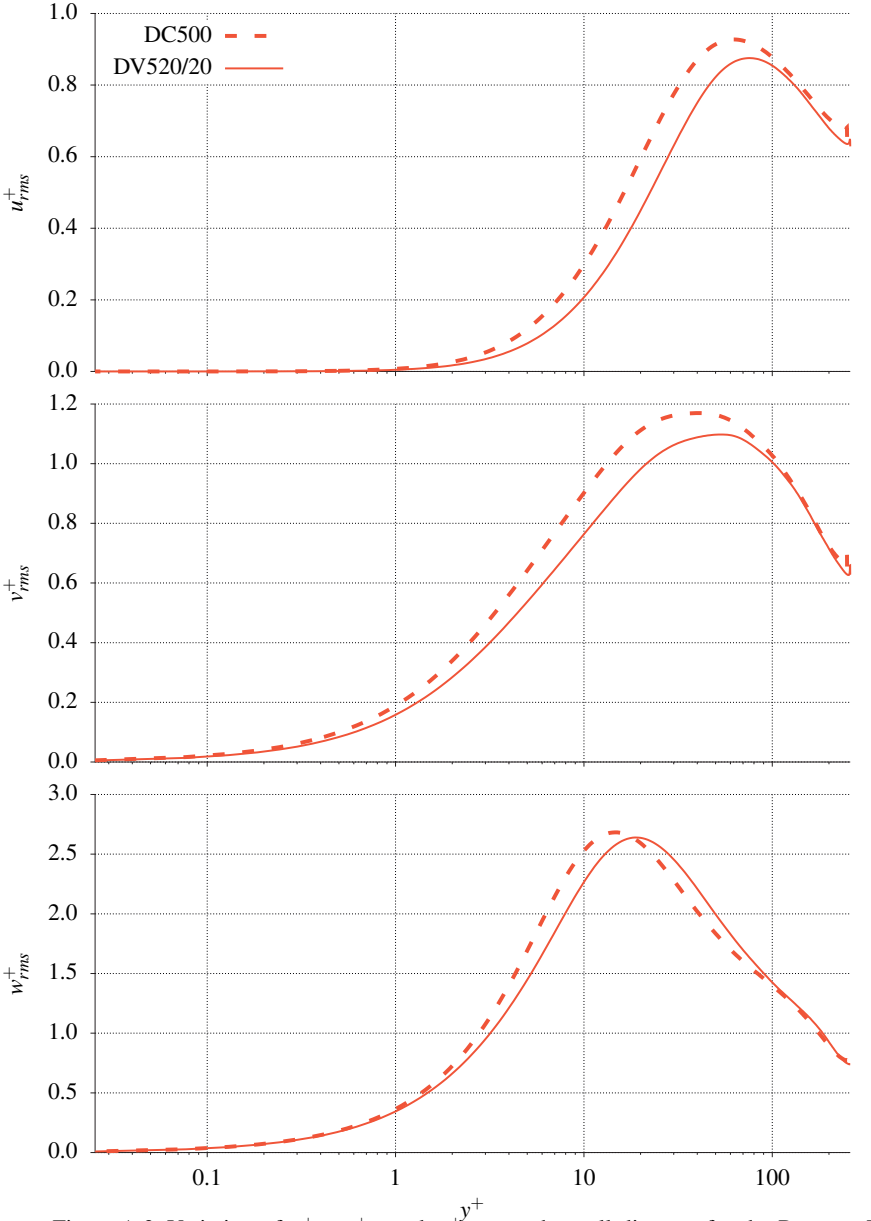

Figure A.3: Variation of u^+_{rms}, v^+_{rms} and w^+_{rms} over the wall distance for the $\mathrm{Re}_{\tau,w} = 500$ cases

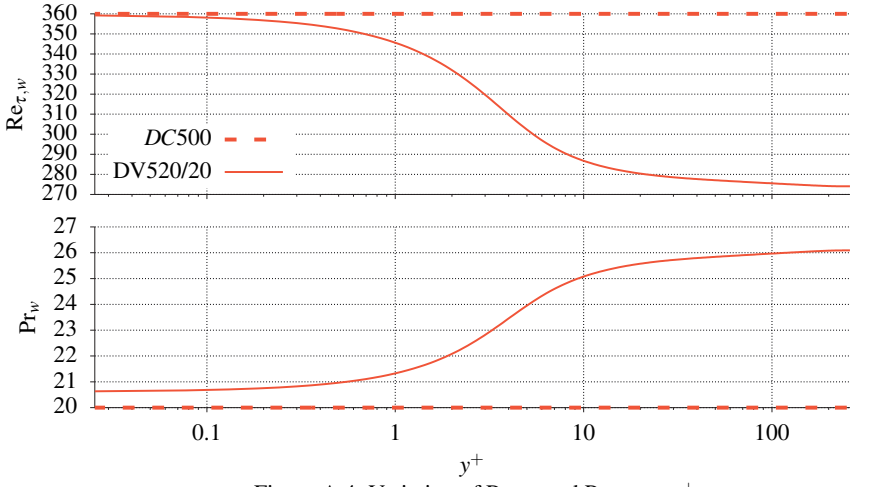

Figure A.4: Variation of $\mathrm{Re}_{\tau,w}$ and Pr_w over y^+

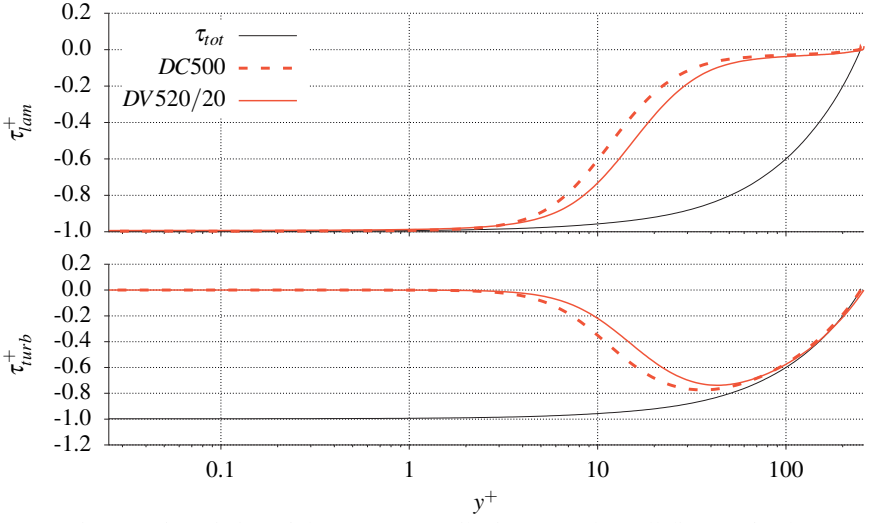

Figure A.5: Variation of shear stress contributions over the wall distance for the cases with $\mathrm{Re}_{\tau,w} = 500$

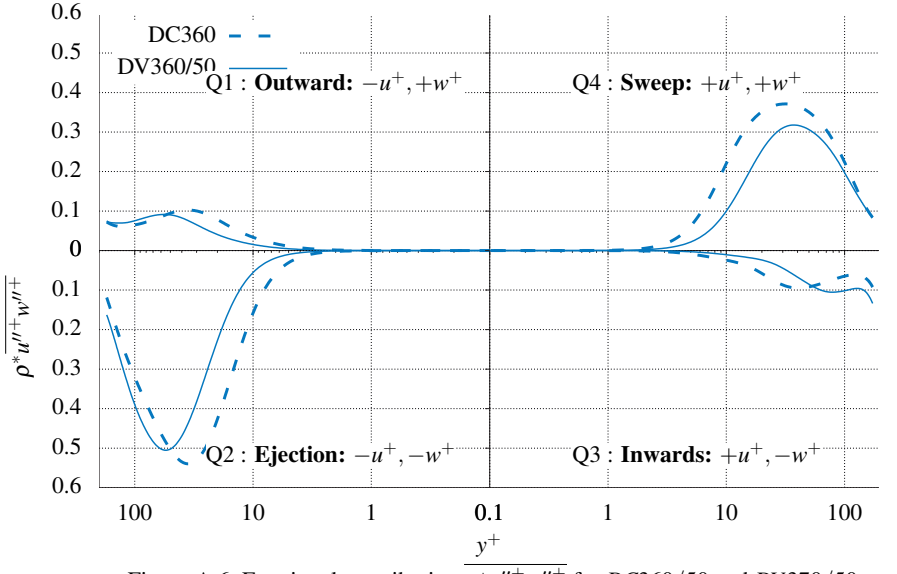

Figure A.6: Fractional contribution $\overline{\rho^* u''^+ w''^+}$ for $DC360/50$ and $DV370/50$

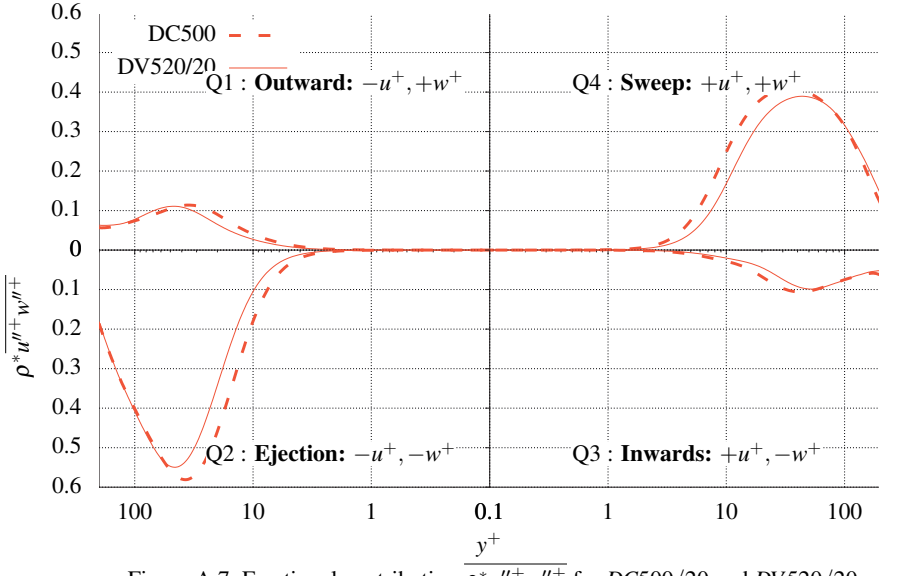

Figure A.7: Fractional contribution $\overline{\rho^* u''^+ w''^+}$ for $DC500/20$ and $DV520/20$

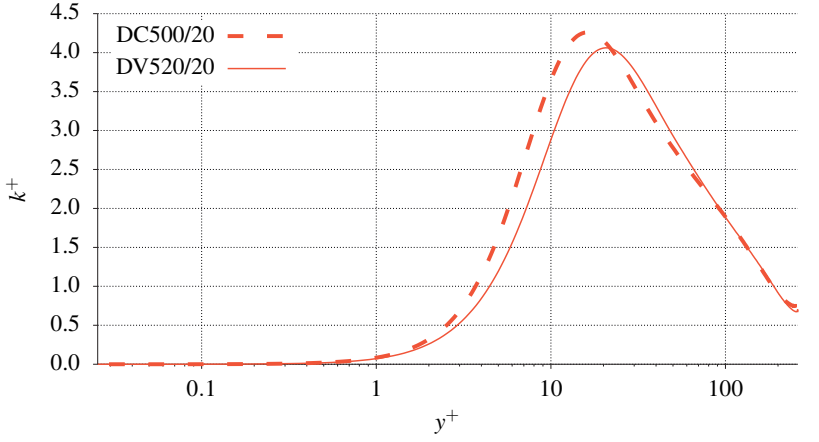

Figure A.8: Variation of the turbulent kinetic energy over the wall distance for the $\mathrm{Re}_{\tau,w} = 500$ cases

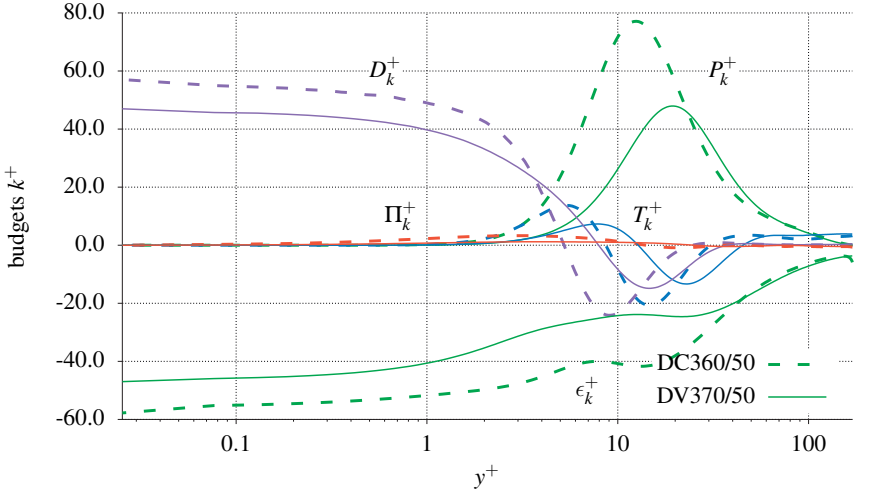

Figure A.9: Variation of the turbulent kinetic energy budgets over the wall distance for the $\mathrm{Re}_{\tau,w} = 360$, $\mathrm{Pr}_w = 50$ cases

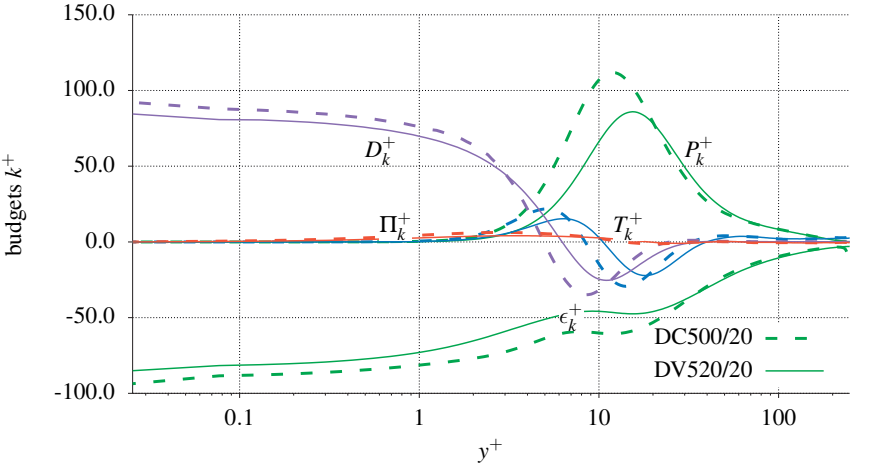

Figure A.10: Variation of the turbulent kinetic energy budgets over the wall distance for the $\mathrm{Re}_{\tau,w} = 500$, $\mathrm{Pr}_w = 20$ cases

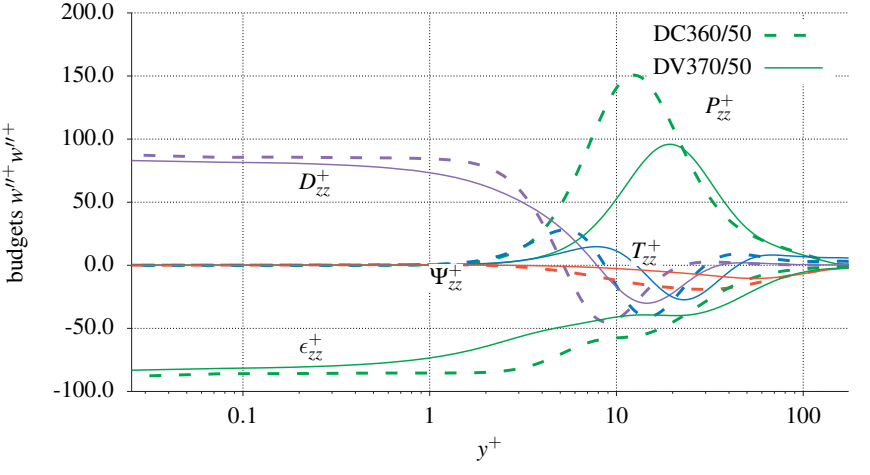

Figure A.11: Variation of the turbulent statistics $\overline{w''^+w''^+}$ budgets over the wall distance for the $\mathrm{Re}_{\tau,w} = 360$, $\mathrm{Pr}_w = 50$ cases

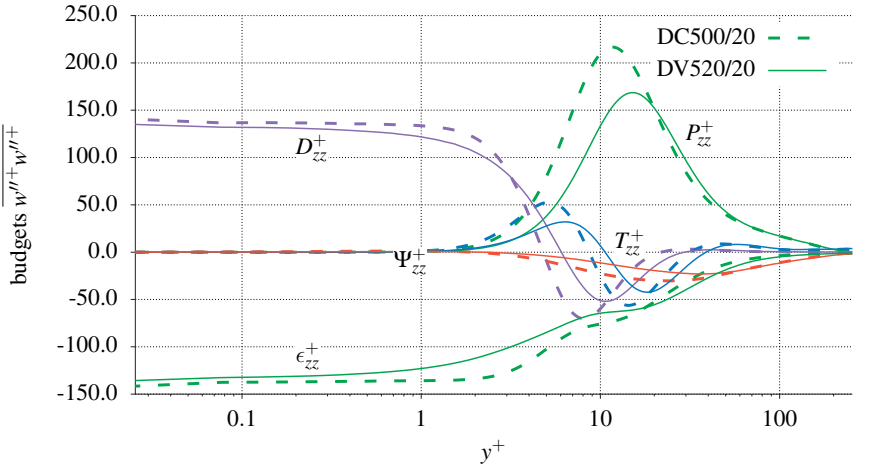

Figure A.12: Variation of the turbulent statistics $\overline{w''^+w''^+}$ budgets over the wall distance for the $\mathrm{Re}_{\tau,w} = 500$, $\mathrm{Pr}_w = 20$ cases

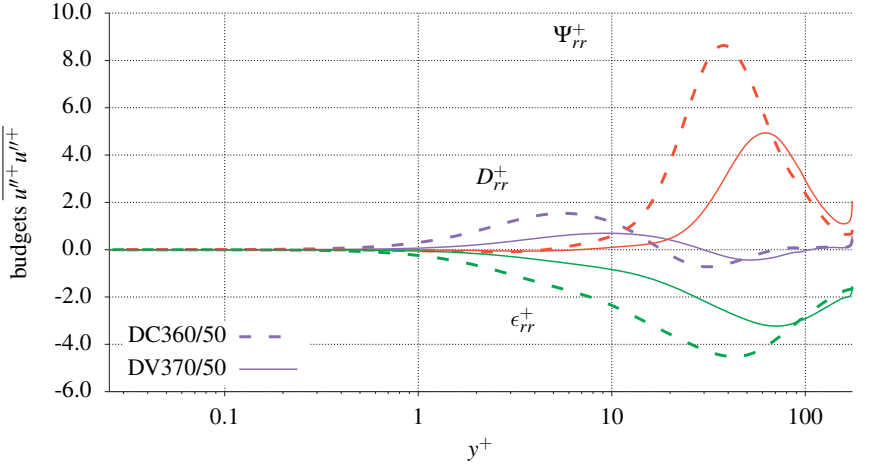

Figure A.13: Variation of the turbulent statistics $\overline{u''^+u''^+}$ budgets over the wall distance for the $\mathrm{Re}_{\tau,w} = 360$, $\mathrm{Pr}_w = 50$ cases

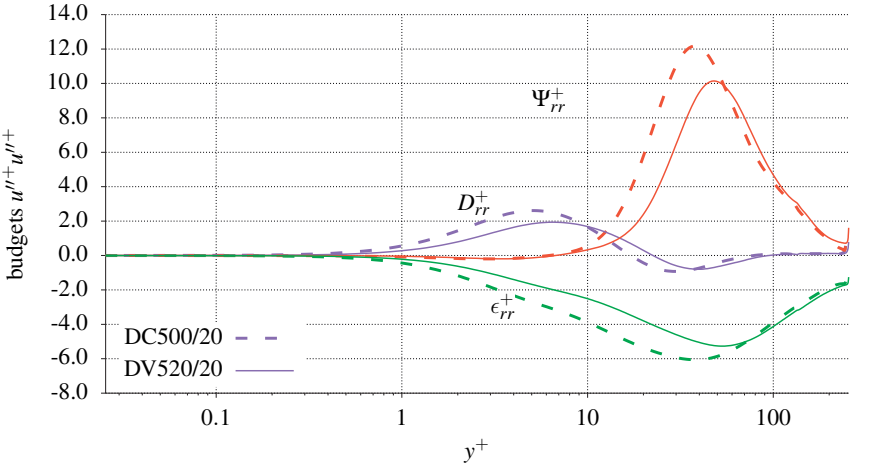

Figure A.14: Variation of the turbulent statistics $\overline{u''^+u''^+}$ budgets over the wall distance for the $\mathrm{Re}_{\tau,w} = 500$, $\mathrm{Pr}_w = 20$ cases

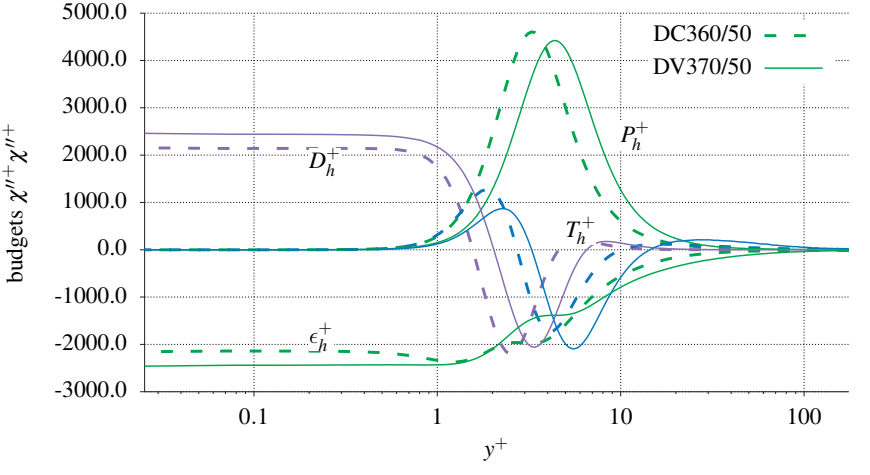

Figure A.15: Radial variation of the turbulent statistics $\overline{\chi''^+\chi''^+}$ budgets for the $\mathrm{Re}_{\tau,w} = 360$, $\mathrm{Pr}_w = 50$ cases

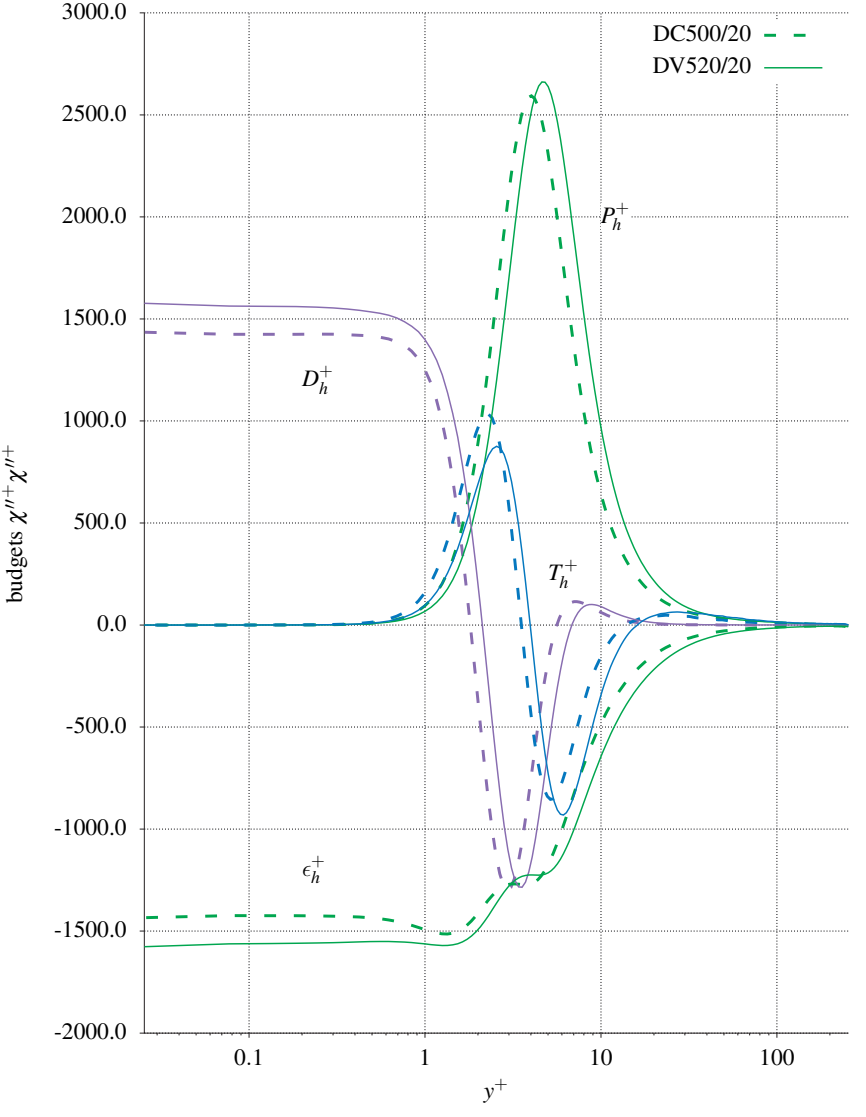

Figure A.16: Radial variation of the turbulent statistics $\overline{\chi''^+\chi''^+}$ budgets for the $\mathrm{Re}_{\tau,w} = 500$, $\mathrm{Pr}_w = 20$ cases

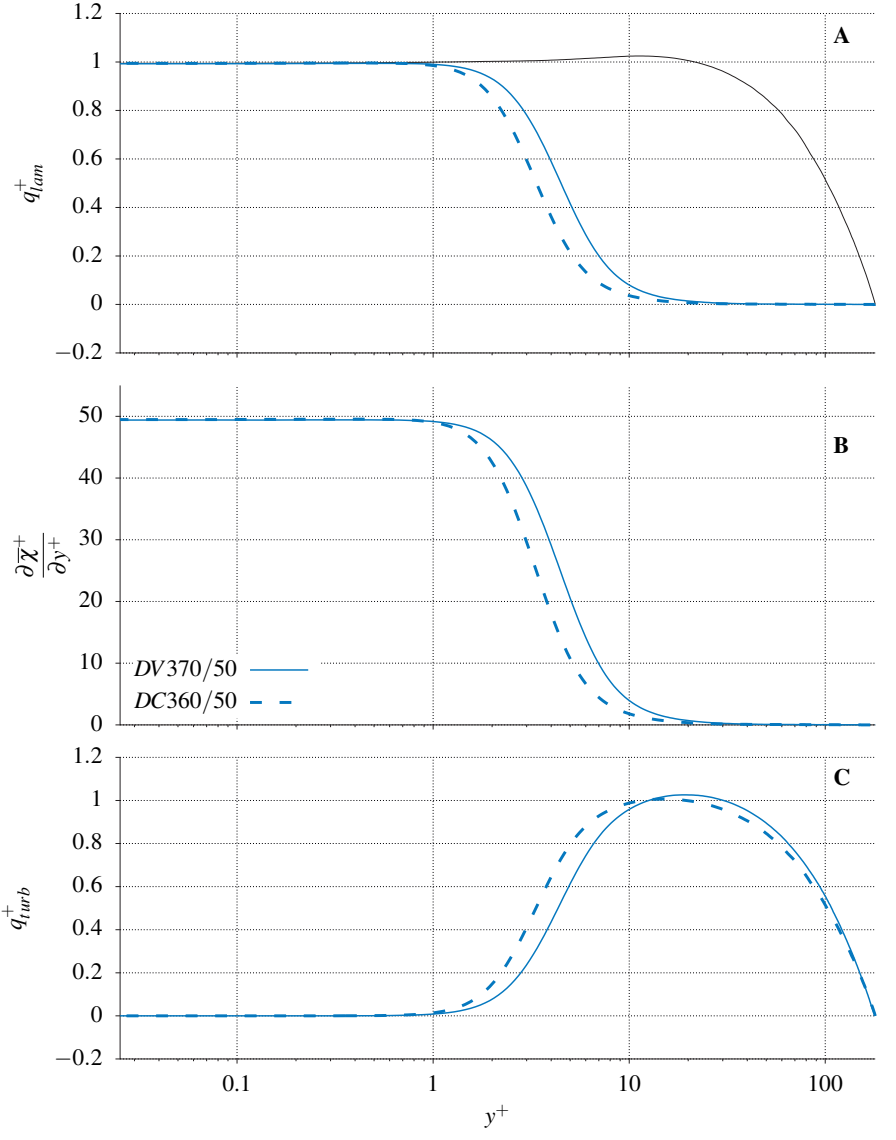

Figure A.17: Variation of heat flux contributions over the wall distance for the cases with $\mathrm{Re}_{\tau,w} = 360$, $\mathrm{Pr}_w = 50$

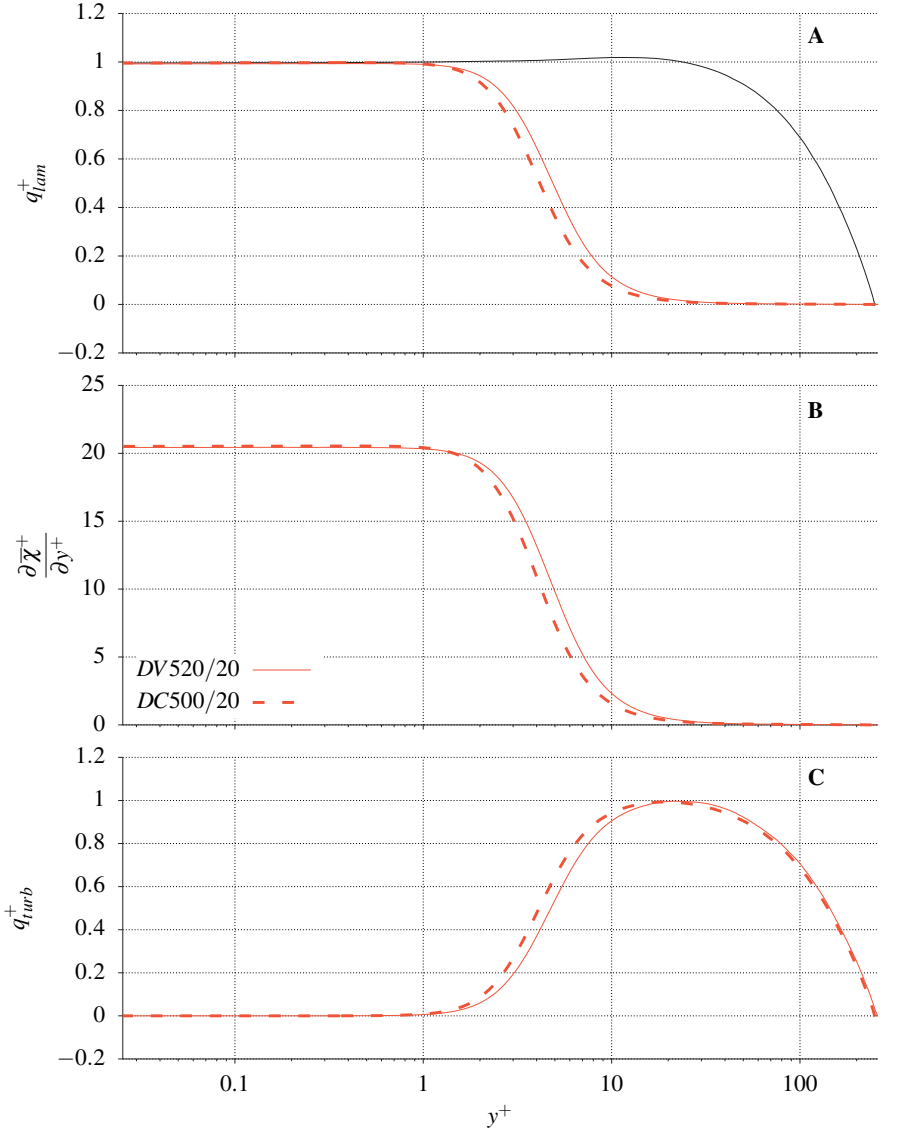

Figure A.18: Variation of heat flux contributions over the wall distance for the cases with $\mathrm{Re}_{\tau,w} = 500$, $\mathrm{Pr}_w = 20$

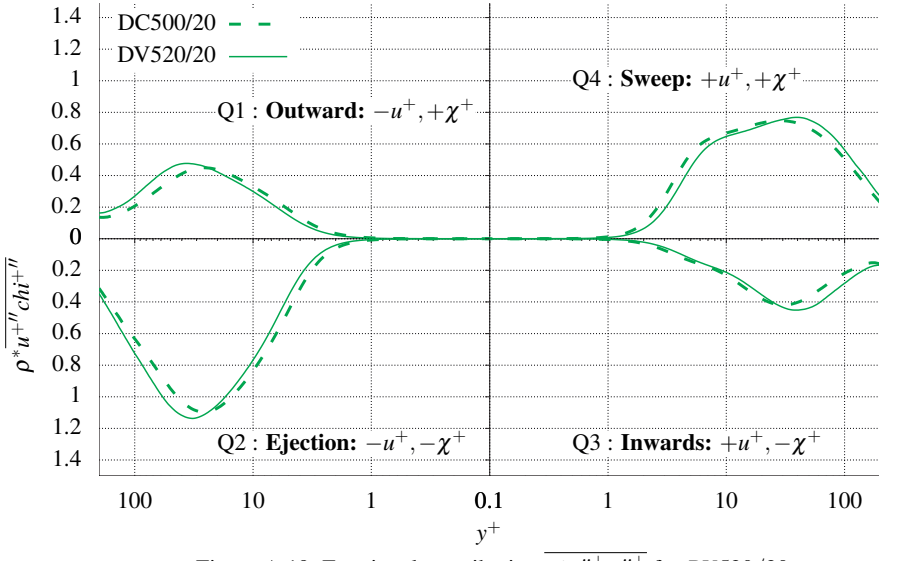

Figure A.19: Fractional contribution $\overline{\rho^* u''^+ \chi''^+}$ for $DV520/20$

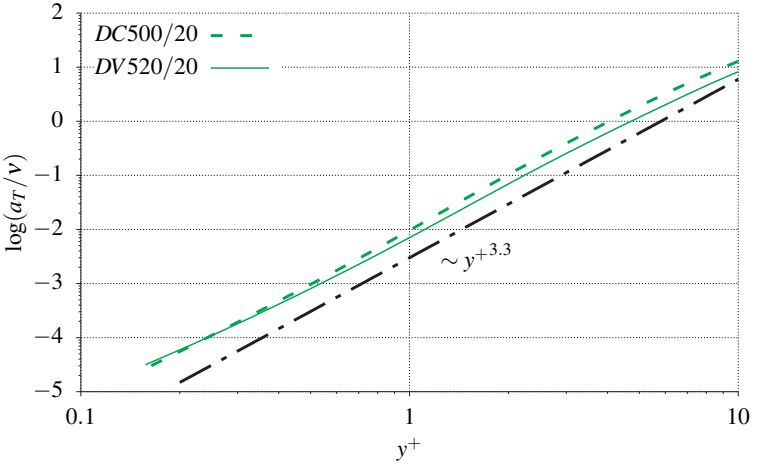

Figure A.20: Eddy diffusivity ratio vs. y^+ for the DC cases with $\mathrm{Re}_{\tau,w} = 500$

BIBLIOGRAPHY

Antonia, R. A. and J. Kim (1991). “Turbulent Prandtl number in the near-wall region of a turbulent channel flow”. In: *International Journal of Heat and Fluid Flow* 34.7, pp. 1905–1908.

Batchelor, G. (1959). “Small-scale variation of convected quantities like temperature in turbulent fluid Part 1. General discussion and the case of small conductivity”. In: *Journal of Fluid Mechanics* 5.01, pp. 113–133.

Blackwell, B. F., W. M. Kays, and R. Moffat (1972). “The turbulent boundary layer on a porous plate: an experimental study of the heat transfer behavior with adverse pressure gradients”. In: HMT-16.

Boersma, B. (1998). “Direct simulation of a jet diffusion flame”. In: *Annual Research Briefs, Center for Turbulence Research, Stanford, CA*, pp. 47–56.

Cebeci, T. (1973). “A model for eddy conductivity and turbulent Prandtl number”. In: *Journal of Heat Transfer* 95.2, pp. 227–234.

Chorin, A. J. (1967). “The numerical solution of the Navier-Stokes equations for an incompressible fluid”. In: *Bulletin of the American Mathematical Society* 73.6, pp. 928–931.

Courant, R., K. Friedrichs, and H. Lewy (1928). “Über die partiellen Differenzengleichungen der mathematischen Physik”. In: *Mathematische annalen* 100.1, pp. 32–74.

Durst, F., M. Fischer, J. Jovanovic, and H. Kikura (1998). “Methods to set up and investigate low Reynolds number, fully developed turbulent plane channel flows”. In: *Journal of Fluids Engineering* 120.3, pp. 496–503.

Durst, F., J. Jovanovic, and J. Sender (1995). “LDA measurements in the near-wall region of a turbulent pipe flow”. In: *Journal of Fluid Mechanics* 295, pp. 305–335.

Eggels, J., F. Unger, M. Weiss, J. Westerweel, R. Adrian, R. Friedrich, and F. Nieuwstadt (1994). “Fully developed turbulent pipe flow: a comparison between direct numerical simulation and experiment”. In: *Journal of Fluid Mechanics* 268, pp. 175–210.

Ghajar, A. J. and L.-M. Tam (1994). “Heat transfer measurements and correlations in the transition region for a circular tube with three different inlet configurations”. In: *Experimental Thermal and Fluid Science* 8.1, pp. 79–90.

Gnielinski, I. V. (2002). “Wärmeübertragung bei der Strömung durch Rohre”. In: *VDI-Wärmeatlas*. Springer, pp. 593–648.

Gnielinski, V. (1995). “Ein neues Berechnungsverfahren für die Wärmeübertragung im Übergangsbereich zwischen laminarer und turbulenter Rohrströmung”. In: *Forschung im Ingenieurwesen* 61.9, pp. 240–248.

Graeber, H. (1970). “Der waermeuebergang in glatten rohren, zwischen parallelen platten, in ringspalten und laengs rohrbuendeln bei exponentieller waermeflussverteilung in erzwungener laminarer oder turbulenter stroemung”. In: *International Journal of Heat and Mass Transfer* 13.11, pp. 1645–1703. ISSN: 0017-9310.

Grifoll, J. and F. Giralt (2000). “The near wall mixing length formulation revisited”. In: *International Journal of Heat and Mass Transfer* 43.19, pp. 3743–3746.

Harriott, P. and R. Hamilton (1965). “Solid-liquid mass transfer in turbulent pipe flow”. In: *Chemical Engineering Science* 20.12, pp. 1073–1078.

Hofmann, E. (1940). “Über die Gesetzmäßigkeiten der Wärme-und der Stoffübertragung auf Grund des Strömungsvorganges im Rohr”. In: *Forschung im Ingenieurwesen* 11.4, pp. 159–169.

Hollingsworth, D. K., W. M. Kays, and R. J. Moffat (Aug. 1989). “The measurement and prediction of heat transfer in a turbulent boundary layer in water”. In: *Symposium on Turbulent Shear Flows*. Vol. 2. 7th. Stanford, CA.

Hubbard, D. and E. Lightfoot (1966). “Correlation of heat and mass transfer data for high Schmidt and Reynolds numbers”. In: *Industrial & Engineering Chemistry Fundamentals* 5.3, pp. 370–379.

Irrenfried, C. and H. Steiner (2017). “DNS based analytical P-function model for RANS with heat transfer at high Prandtl numbers”. In: *International Journal of Heat and Fluid Flow* 66.Supplement C, pp. 217–225. ISSN: 0142-727X.

Jayatilleke, C. L. V. (1969). “The influence of Prandtl number and surface roughness on the resistance of the laminar sublayer to momentum and heat transfer”. In: *Progress Heat Mass Transfer* 1, pp. 193–321.

Jenkins, R. (1951). “Variation of the eddy conductivity with Prandtl modulus and its use in prediction of turbulent heat transfer coefficients”. In: *Heat Transfer and Fluid Mechanics Institute, Stanford*, pp. 147–158.

Kader, B. (1981). “Temperature and concentration profiles in fully turbulent boundary layers”. In: *International Journal of Heat and Mass Transfer* 24.9, pp. 1541–1544.

Kader, B. and A. Yaglom (1972). “Heat and mass transfer laws for fully turbulent wall flows”. In: *International Journal of Heat and Mass Transfer* 15.12, pp. 2329–2351.

Kármán, T. (1939). “The Analogy Between Fluid Friction and Heat Transfer”. In: *Transactions ASME* 61, pp. 705–710.

Kármán, T. et al. (1930). “Mechanische änlichkeit und turbulenz”. In: *Nachrichten von der Gesellschaft der Wissenschaften zu Göttingen, Mathematisch-Physikalische Klasse* 1930, pp. 58–76.

Kawamura, H., K. Ohsaka, H. Abe, and K. Yamamoto (1998). “DNS of turbulent heat transfer in channel flow with low to medium-high Prandtl number fluid”. In: *International Journal of Heat and Fluid Flow* 19.5, pp. 482–491.

Kays, W. M. (1994). “Turbulent Prandtl number - where are we?” In: *Journal of Heat Transfer* 116.2, pp. 284–295.

Kays, W. M. and M. E. Crawford (1980). *Convective heat and mass transfer*. Tata McGraw-Hill Education.

Kim, J. and P. Moin (Sept. 1987). *Transport of Passive Scalars in Turbulent Channel Flow*. Technical Memorandum 89463. Moffet Field, California: National Aeronautics and Space Administration.

Kim, J. and P. Moin (1985). "Application of a fractional-step method to incompressible Navier-Stokes equations". In: *Journal of Computational Physics* 59.2, pp. 308–323.

Konakov, P. K. (1954). "Eine neue Formel frue den Reibungskoeffizienten glatter Rohre". In: *Bericht der Akademie der Wissenschaften der UDSSR* 51.7, pp. 503–506.

Kozuka, M., Y. Seki, and H. Kawamura (2009). "DNS of turbulent heat transfer in a channel flow with a high spatial resolution". In: *International Journal of Heat and Fluid Flow* 30.3, pp. 514–524.

Lee, J., S. Y. Jung, H. J. Sung, and T. A. Zaki (2013). "Effect of wall heating on turbulent boundary layers with temperature-dependent viscosity". In: *Journal of Fluid Mechanics* 726, pp. 196–225.

Lemos, E., A. Secchi, and E. Biscaia Jr (2012). "Development of a high-order finite volume method with multiblock partition techniques". In: *Brazilian Journal of Chemical Engineering* 29.1, pp. 183–201.

Leschziner, M. (2000). "The computation of turbulent engineering flows with turbulence-transport closures". In: *Advanced Turbulent Flow Computations*. Springer, pp. 209–277.

Levich, V. G. (1962). *Physicochemical hydrodynamics*. Prentice hall.

Malin, M. (1987). "On the calculation of heat transfer rates in fully turbulent wall flows". In: *Applied Mathematical Modelling* 11.4, pp. 281–284.

Morris, F. and W. G. Whitman (1928). "Heat Transfer for Oils and Water in Pipes1". In: *Industrial & Engineering Chemistry* 20.3, pp. 234–240.

Na, T. and I. Habib (1973). "Heat transfer in turbulent pipe flow based on a new mixing length model". In: *Applied Scientific Research* 28.1, pp. 302–314.

Na, Y. and T. Hanratty (2000). "Limiting behavior of turbulent scalar transport close to a wall". In: *International Journal of Heat and Mass Transfer* 43.10, pp. 1749–1758.

Najm, H. N., P. S. Wyckoff, and O. M. Knio (1998). "A semi-implicit numerical scheme for reacting flow: I. stiff chemistry". In: *Journal of Computational Physics* 143.2, pp. 381–402.

Nemati, H., A. Patel, B. J. Boersma, and R. Pecnik (2016). "The effect of thermal boundary conditions on forced convection heat transfer to fluids at supercritical pressure". In: *Journal of Fluid Mechanics* 800, pp. 531–556.

Patel, A., B. J. Boersma, and R. Pecnik (2016). "The influence of near-wall density and viscosity gradients on turbulence in channel flows". In: *Journal of Fluid Mechanics* 809, pp. 793–820.

Patel, A., B. J. Boersma, and R. Pecnik (2017). "Scalar statistics in variable property turbulent channel flows". In: *Physical Review Fluids* 2.8, p. 084604.

Patel, A., J. W. Peeters, B. J. Boersma, and R. Pecnik (2015). "Semi-local scaling and turbulence modulation in variable property turbulent channel flows". In: *Physics of Fluids* 27.9, p. 095101.

Petukhov, B. S., A. Polyakov, and B. E. Launder (1988). *Heat transfer in turbulent mixed convection*. Hemisphere Publishing; New York, USA.

Petukhov, B. (1970). "Heat transfer and friction in turbulent pipe flow with variable physical properties". In: *Advances in Heat Transfer* 6, pp. 503–564.

Piller, M. (2005). "Direct numerical simulation of turbulent forced convection in a pipe". In: *International Journal for Numerical Methods in Fluids* 49.6, pp. 583–602.

Pope, S. B. (2001). *Turbulent flows*. IOP Publishing.

Popovac, M. and K. Hanjalic (2007). "Compound wall treatment for RANS computation of complex turbulent flows and heat transfer". In: *Flow, Turbulence and Combustion* 78.2, pp. 177–202.

Prandtl, L. (1910). "Eine Beziehung zwischen Warmeaustausch and Stromungswiderstand der Flussigkeiten". In: *Physikalische Zeitschrift* 11, pp. 1072–1078.

Redjem-Saad, L., M. Ould-Rouiss, and G. Lauriat (2007). "Direct numerical simulation of turbulent heat transfer in pipe flows: Effect of Prandtl number". In: *International Journal of Heat and Fluid Flow* 28.5, pp. 847–861.

Schwertfirm, F. and M. Manhart (2007). "DNS of passive scalar transport in turbulent channel flow at high Schmidt numbers". In: *International Journal of Heat and Fluid Flow* 28.6, pp. 1204–1214.

Sciacovelli, L., P. Cinnella, and X. Gloerfelt (2017). "Direct numerical simulations of supersonic turbulent channel flows of dense gases". In: *Journal of Fluid Mechanics* 821, pp. 153–199.

Shaw, D. A. and T. J. Hanratty (1977). "Turbulent mass transfer rates to a wall for large Schmidt numbers". In: *AIChE Journal* 23.1, pp. 28–37.

Sherwood, T. (1932). "Heat transmission to liquids flowing in pipes". In: *Industrial & Engineering Chemistry* 24.7, pp. 736–745.

Sirkar, K. K. and T. J. Hanratty (1969). "Limiting Behavior of Transverse Turbulent Velocity Fluctuations Close to a Wall". In: *Industrial & Engineering Chemistry Fundamentals* 8.2, pp. 189–192.

Sleicher, C. and M. Rouse (1975). "A convenient correlation for heat transfer to constant and variable property fluids in turbulent pipe flow". In: *International Journal of Heat and Mass Transfer* 18.5, pp. 677–683.

Spalding, D. (1961). "A single formula for the "law of the wall"". In: *Journal of Applied Mechanics* 28.3, pp. 455–458.

Spalding, D. (1967). "Monograph on turbulent boundary layers". In: *Imperical College: Mechanical Engineering Department Report TWF/TN* 33.

Stokes, G. G. (1851). *On the effect of the internal friction of fluids on the motion of pendulums*. Vol. 9. Pitt Press Cambridge.

Taylor, G. (1916). "Conditions at the surface of a hot body exposed to the wind". In: *British Advisory Committee for Aeronautics Reports and Memoranda* 272.

Tennekes, H. and J. L. Lumley (1972). *A first course in turbulence*. MIT press.

Tiselj, I., R. Bergant, B. Mavko, I. Bajsic, and G. Hetsroni (2001a). "DNS of turbulent heat transfer in channel flow with heat conduction in the solid wall". In: *Journal of Heat Transfer* 123.5, pp. 849–857.

Tiselj, I., E. Pogrebnyak, C. Li, A. Mosyak, and G. Hetsroni (2001b). "Effect of wall boundary condition on scalar transfer in a fully developed turbulent flume". In: *Physics of Fluids* 13.4, pp. 1028–1039.

Van Driest, E. R. (1956). "On turbulent flow near a wall". In: *Journal of the Aeronautical Sciences* 23.11, pp. 1007–1011.

van Driest, E. (1951). "Turbulent boundary layer in compressible fluids". In: *Journal of the Aeronautical Sciences* 18.3, pp. 145–160.

Vinokur, M. (1983). "On one-dimensional stretching functions for finite-difference calculations". In: *Journal of Computational Physics* 50.2, pp. 215–234.

Von Karman, T. (1939). "The analogy between fluid friction and heat transfer". In: *Transactions ASME* 61, pp. 705–710.

Wallace, J. M., H. Eckelmann, and R. S. Brodkey (1972). "The wall region in turbulent shear flow". In: *Journal of Fluid Mechanics* 54.1, pp. 39–48.

Wu, X. and P. Moin (2008). "A direct numerical simulation study on the mean velocity characteristics in turbulent pipe flow". In: *Journal of Fluid Mechanics* 608, pp. 81–112.

Zonta, F., C. Marchioli, and A. Soldati (2012). "Modulation of turbulence in forced convection by temperature-dependent viscosity". In: *Journal of Fluid Mechanics* 697, pp. 150–174.

Monographic Series TU Graz

Computation in Engineering and Science

Vol. 1 Steffen Alvermann
Effective Viscoelastic Behavior of Cellular Auxetic Materials
2008
ISBN 978-3-902465-92-4

Vol. 2 Sendy Fransiscus Tantono
The Mechanical Behaviour of a Soilbag under Vertical Compression
2008
ISBN 978-3-902465-97-9

Vol. 3 Thomas Rüberg
Non-conforming FEM/BEM Coupling in Time Domain
2008
ISBN 978-3-902465-98-6

Vol. 4 Dimitrios E. Kiousis
Biomechanical and Computational Modeling of Atherosclerotic Arteries
2008
ISBN 978-3-85125-023-7

Vol. 5 Lars Kielhorn
A Time-Domain Symmetric Galerkin BEM for Viscoelastodynamics
2009
ISBN 978-3-85125-042-8

Vol. 6 Gerhard Unger
Analysis of Boundary Element Methods for Laplacian Eigenvalue Problems
2009
ISBN 978-3-85125-081-7

Monographic Series TU Graz

Computation in Engineering and Science

Vol. 7 Gerhard Sommer

Mechanical Properties of Healthy and Diseased Human Arteries
2010
ISBN 978-3-85125-111-1

Vol. 8 Mathias Nenning

Infinite Elements for Elasto- and Poroelastodynamics
2010
ISBN 978-3-85125-130-2

Vol. 9 Thanh Xuan Phan

Boundary Element Methods for Boundary Control Problems
2011
ISBN 978-3-85125-149-4

Vol. 10 Loris Nagler

Simulation of Sound Transmission through Poroelastic Plate-like Structures
2011
ISBN 978-3-85125-153-1

Vol. 11 Markus Windisch

Boundary Element Tearing and Interconnecting Methods for Acoustic and Electromagnetic Scattering
2011
ISBN 978-3-85125-152-4

Vol. 12 Christian Walchshofer

Analysis of the Dynamics at the Base of a Lifted Strongly Buoyant Jet Flame Using Direct Numerical Simulation
2011
ISBN 978-3-85125-185-2

Monographic Series TU Graz

Computation in Engineering and Science

Vol. 13 Matthias Messner

Fast Boundary Element Methods in Acoustics
2012
ISBN 978-3-85125-202-6

Vol. 14 Peter Urthaler

Analysis of Boundary Element Methods for Wave Propagation in Porous Media
2012
ISBN 978-3-85125-216-3

Vol. 15 Peng Li

Boundary Element Method for Wave Propagation in Partially Saturated Poroelastic Continua
2012
ISBN 978-3-85125-236-1

Vol. 16 Andreas Jörg Schriefl

Quantification of Collagen Fiber Morphologies in Human Arterial Walls
2013
ISBN 978-3-85125-238-5

Vol. 17 Thomas S. E. Eriksson

Cardiovascular Mechanics
2013
ISBN 978-3-85125-277-4

Vol. 18 Jianhua Tong

Biomechanics of Abdominal Aortic Aneurysms
2013
ISBN 978-3-85125-279-8

Monographic Series TU Graz

Computation in Engineering and Science

Vol. 19 Jonathan Rohleder

Titchmarsh–Weyl Theory and Inverse Problems for Elliptic Differential Operators
2013
ISBN 978-3-85125-283-5

Vol. 20 Martin Neumüller

Space-Time Methods
2013
ISBN 978-3-85125-290-3

Vol. 21 Michael J. Unterberger

Microstructurally-Motivated Constitutive Modeling of Cross-Linked Filamentous Actin Networks
2013
ISBN 978-3-85125-303-0

Vol. 22 Vladimir Lotoreichik

Singular Values and Trace Formulae for Resolvent Power Differences of Self-Adjoint Elliptic Operators
2013
ISBN 978-3-85125-304-7

Vol. 23 Michael Meßner

A Fast Multipole Galerkin Boundary Element Method for the Transient Heat Equation
2014
ISBN 978-3-85125-350-4

Vol. 24 Lorenz Johannes John

Optimal Boundary Control in Energy Spaces
2014
ISBN 978-3-85125-373-3

Monographic Series TU Graz

Computation in Engineering and Science

Vol. 25 Hannah Weisbecker

Softening and Damage Behavior of Human Arteries
2014
ISBN 978-3-85125-370-2

Vol. 26 Bernhard Kager

Efficient Convolution Quadrature based Boundary Element Formulation for Time-Domain Elastodynamics
2015
ISBN 978-3-85125-382-5

Vol. 27 Christoph M. Augustin

Classical and All-floating FETI Methods with Applications to Biomechanical Models
2015
ISBN 978-3-85125-418-1

Vol. 28 Elias Karabelas

Space-Time Discontinuous Galerkin Methods for Cardiac Electromechanics
2016
ISBN 978-3-85125-461-7

Vol. 29 Thomas Traub

A Kernel Interpolation Based Fast Multipole Method for Elastodynamic Problems
2016
ISBN 978-3-85125-465-5

Vol. 30 Matthias Gsell

Mortar Domain Decomposition Methods for Quasilinear Problems and Applications
2017
ISBN 978-3-85125-522-5

Monographic Series TU Graz

Computation in Engineering and Science

Vol. 31 Christian Kühn

Schrödinger operators and singular infinite rank perturbations
2017
ISBN 978-3-85125-551-5

Vol. 32 Michael H. Gfrerer

Vibro-Acoustic Simulation of Poroelastic Shell Structures
2018
ISBN 978-3-85125-573-7

Vol. 33 Markus Holzmann

Spectral Analysis of Transmission and Boundary Value Problems for Dirac Operators
2018
ISBN 978-3-85125-642-0

Vol. 34 Osman Gültekin

Computational Inelasticity of Fibrous Biological Tissues with a Focus on Viscoelasticity, Damage and Rupture
2019
ISBN 978-3-85125-655-0

Vol. 35 Justyna Anna Niestrawska

Experimental and Computational Analyses of Pathological Soft Tissues – Towards a Better Understanding of the Pathogenesis of AAA
2019
ISBN 978-3-85125-678-9

Monographic Series TU Graz

Computation in Engineering and Science

Vol. 36 Marco Zank

Inf-Sup Stable Space-Time Methods for Time-Dependent Partial Differential Equations
2020
ISBN 978-3-85125-721-2

Vol. 37 Christoph Irrenfried

Convective turbulent near wall heat transfer at high Prandtl numbers
2020
ISBN 978-3-85125-724-3

Convective turbulent near wall heat transfer at high Prandtl numbers

The computational modelling of heat transfer in turbulent flow is of high importance for many industrial engineering applications, especially for fluids with high molecular Prandtl numbers, as typically met in cooling and heating applications. The present work performed Direct Numerical Simulations (DNS) of turbulent heated pipe flows at high molecular Prandtl numbers examining the effect of real fluid properties, and investigated experimentally heat transfer in pipe flows of high molecular Prandtl number fluids. One of the major findings of the simulations is the thickening of the diffusive thermal sublayer due to the increase of the molecular viscosity towards the colder flow core, which effectively reduces the heat transfer coefficient. An experimental test bench was specially designed and built for the considered pipe flow configuration, capable of validating the DNS simulations.

The gained knowledge was applied in the validation and development of thermal boundary conditions in Reynolds Averaged Navier-Stokes (RANS) simulations. The mathematically rather elaborate P-function approach was revisited and modified based on the DNS findings. The predictions of the proposed extended analytical model generally showed very good agreement with the DNS results and the experimental data.

MONOGRAPHIC SERIES TU GRAZ
COMPUTATION IN ENGINEERING AND SCIENCE

Verlag der Technischen Universität Graz
www.tugraz-verlag.at

ISBN 978-3-85125-724-3
ISSN 1990-357X

ISBN 978-3-85125-724-3
9 783851 257243